2011

Heavy-Duty Vehicles Modeling and Factors Impacting Fuel Consumption.

Lijuan Wang

Heavy-Duty Vehicles Modeling and Factors Impacting Fuel Consumption

Lijuan Wang

Dissertation submitted to the
College of Engineering and Mineral Resources
At West Virginia University
In Partial Fulfillment of the Requirements
For the degree of

Doctor of Philosophy
In
Mechanical Engineering

Nigel Clark, Ph.D., Chair
Jacky Prucz, Ph.D.
Hailin Li, Ph.D.
Scott Wayne, Ph.D.
Natalia Schmid, Ph.D.

Department of Mechanical and Aerospace Engineering

Keywords: PSAT, Modeling, Simulation, Validation, Conventional Heavy-Duty Truck, Engine Cooling Fan, Series Hybrid Bus

ProQuest LLC.
789 East Eisenhower Parkway
P.O. Box 1346
Ann Arbor, MI 48106 - 1346

Abstract

Heavy-Duty Vehicles Modeling and Factors Impacting Fuel Consumption

Lijuan Wang

A conventional heavy-duty truck PSAT model was validated and incorporated into the Powertrain System Analysis Toolkit (PSAT). The truck that was modeled was a conventional over-the-road 1996 Peterbilt tractor, equipped with a 550 hp Caterpillar 3406E non exhaust gas circulation (EGR) engine and an 18-speed Roadranger manual transmission. A vehicle model was developed, along with the model validation processes. In the engine model, an oxides of nitrogen (NO_x) emissions model and a fuel rate map for the Caterpillar 3406E engine were created based on test data. In the gearbox model, a shifting strategy was specified and transmission efficiency lookup tables were developed based on the losses information gathered from the manufacturer. As the largest mechanical accessory model, an engine cooling fan model, which estimates fan power demand, was integrated into the heavy-duty truck model. Experimental test data and PSAT simulation results pertaining to engine fuel rate, engine torque, engine speed, engine power and NO_x were within 5% relative error.

A quantitative study was conducted by analyzing the impacts of various parameters (vehicle weights, coefficients of rolling resistance and the aerodynamic drag) on fuel consumption (FC) for the Peterbilt truck. The vehicle was simulated over five cycles which represent typical vehicle in-use behavior. Three contributions were generated. First, contour figures provided a convenient way to estimate fuel economy (FE) of the Peterbilt truck over various cycles by interpolating within the parameter values. Second, simulation results revealed that, depending on the circumstances and the cycle, it may be more cost effective to reduce one parameter value (such as coefficient of aerodynamic drag) to increase FE, or it may be more beneficial to reduce another (such as the coefficient of rolling resistance). Third, the amount of the energy consumed by auxiliary loads was found to be highly dependent upon the driving cycles. The ratios between average auxiliary power and average engine power were found to be 71.0%, 17.1%, 15.3%, 12.4% and 11.43% for creep, transient, UDDS, cruise and HHDDT_s cycles, respectively.

A hybrid electric bus (HEB) also was modeled. The HEB that was modeled was a New Flyer bus with ISE hybrid system, a Cummins ISB 260H engine and a single-reduction transmission. Information and data were acquired to describe all major components of the HEB. The engine model was validated prior to modeling of the whole vehicle model. The load-following control strategy was utilized in the energy management system. Experimental data and PSAT simulated results were compared over four driving schedules, and the relative percent of errors of the FC, FE, CO_2 and NO_x were all within 5% except for the FE and NO_x of the Manhattan cycle, which were 6.93% and 7.13%, respectively. The high fidelity of this model makes it possible to evaluate the FE and NO_x emissions of series hybrid buses for subsequent PSAT users.

Acknowledgements

This research was supported by Argonne National Laboratory, under DUNS 19-151-0239. I would like to thank Aymeric Rousseau, Dominik Karbowski and their colleagues. Not only did they fund my research, but they were always ready to immediately provide information and guidance when it was needed.

I am extremely grateful to my advisor Dr. Nigel Clark for his guidance, support and encouragement throughout the research. He has supported me not only by providing a research assistantship over five years, but also academically and emotionally through the rough road to finish this dissertation. His broad knowledge, academic experiences, insightful comments, as well as his kindness have always inspired me. I would like to express my sincere appreciation to my other committee members Dr. Jacky Prucz, Dr. Scott Wayne, Dr. Hailin Li and Dr. Natalia Schmid for their invaluable comments and suggestions. I have benefitted greatly from their advice.

I would like to acknowledge Dan Carder, Ron Jarrett, Dave McKain, Petr Sindler, Chris Rowe, Brad Ralston and other staff who work at WVU Engine and Emissions Research Center and WVU Transportable Heavy-duty Vehicle Emission Testing Laboratory for helping me collect data during my experimental work.

I would like to thank all the graduate students of the excellent CAFEE group. The friendship and enlightening discussions have made my stay at CAFEE pleasant and enjoyable. Special thanks Clay Bell, Pingen Chen, Feng Zhen, Yuebin Wu, Shiyu Liu, Wei Qi, Jun Tu, Madhava Madireddy, Major Khan, Jario Sandoval, Francisco Posada, Idowu Olatunji, Derek Johnson, Clinton Bedick and all of the other graduate students who help me to complete my PhD study.

I must thank Dr. John Nuszkowski for the proofreading he has done and Dr. Marty French for being such a good friend who is always ready to help.

I would also like to thank Peterbilt Motor Company, Eaton Corporation, Caterpillar Inc. and New Flyer Industries for providing vehicles and components information.

My deepest gratitude goes to my family for their everlasting love and support throughout my life. I am grateful to my father for providing a lifetime of examples, encouragement and support for everything that I have done. I can't express my gratitude for my mother in words, whose unconditional love has been my greatest strength. Although she is no longer with us, she is forever remembered. I feel proud of my brother for his talents and kindness. He has been my role model and has always been my best counselor. My husband Jake, whose understanding, love and support, has taken the load off my shoulder. Thank you all for everything.

Table of Contents

List of Tables

List of Figures

Nomenclature and Abbreviations

A	Frontal Area of the Vehicle
a_{eco_dn}	Down-Shift Acceleration Pedal Position
a_{eco_up}	Up-Shift Acceleration Pedal Position
a_{perfo}	Performance Acceleration Pedal Position
ADVISOR	ADvanced VehIcle SimulatOR
AFV	Alternative Fuel Vehicle
ANN	Artificial Neural Network
APP	Accelerator Pedal Position
BSFC	Brake Specific Fuel Consumption
^{o}C	Degrees Celsius
CAFE	Corporate Average Fuel Economy
CAFFE	Center for Alternative Fuels, Engines and Emissions
C_d	Coefficient of Aerodynamic
CFD	Computational Fluid Dynamics
CFR	Code of Federal Regulations
C_{loss}	Countershaft Churn Losses
CO	Carbon Monoxide
CO_2	Carbon Dioxide
C_{pc}	Specific Heat of the Coolant
C_{pe}	Specific Heat of the Engine
$C_{p,UC}$	Thermal Heat Capacity of the Ultracapacitor
$\|\|dist\|\|$	Dot Products of Input Vector X and the Input Weight Matrix
DCM	Differential Coefficients Method
DOE	Department of Energy
ECU	Engine Control Unit
EGR	Exhaust Gas Recirculation
EISA	Energy Independence of Security Act
ESS	Energy Storage System
EPA	Environmental Protection Agency
FC	Fuel Consumption

FE	Fuel Economy
g	Acceleration due to Gravity
GREET	Greenhouse Gases, Regulated Emissions, and Energy Use in Transportation
GRNN	Generalized Regression Neural Network
GUI	Graphical User Interface
GVWR	Gross Vehicle Weight Rating
HC	Hydrocarbon
HEB	Hybrid Electrical Bus
HEV	Hybrid Electrical Vehicle
HHDDT	Heavy Heavy-Duty Diesel Truck
HHDDT_s	High Speed Cruise Short
i_{hs}	Ratio of the Input Gear to the Countershaft Gear
$I_{\max}$	Maximum Current
I_{UC}	Current of Ultracapacitor
k_1	1st Gear Ratio
k_2	2nd Gear Ratio
k_{fd}	Final Drive Ratio
K_p	Proportional Gain
K_i	Integral Gain
k_i	k^{th} Gear Ratio
ICE	Internal Combustion Engine
Li-ion	Lithium Ion
LR	Linear Regression
LSFC	Load-Specific Fuel Consumption
m	Vehicle Mass
m_{fuel}	Fuel Mass
$\dot{m}_{fuel}$	Fuel Rate Mass
$\dot{m}_{fuel\_eq}$	Equivalent Fuel Flow Rate Mass
M_c	Masses of the Coolant
M_e	Masses of the Engine
MAN	Manhattan

MTA	Metropolitan Transportation Authority
mpg	Mile Per Gallon
mph	Mile Per Hour
MY	Model Year
NGWBS	New Generation Wide-Base Single
NHTSA	National Highway Traffic Safety Administration
Ni-MH	Nickel Metal Hydride
NO_x	Oxides of Nitrogen
$N_{parallel}$	Number of Parallel Connected Ultracapacitor
NREL	National Renewable Energy Laboratory
N_{series}	Number of Series Connected Ultracapacitor
NYC	New York City
OCTA	Orange County Transportation Authority Cycle
P_{aux}	Auxiliary Load Including Engine Cooling Fan
$\%FC_{TechX}$	Percent FC Reduction of an Individual Technology
P_{fan}	Fan Power Loss
PI	Proportional Integral
P_{elect}	Electrical Power
$P_{engine\_\max\_effi}$	Engine Power at Maximum Engine Efficiency
$Perf\_Mode$	Performance Mode
P_{loss}	Lubricating Pump Losses
P_m	Motor Power
P_{motor_ave}	Average Motor Power
PM	Particulate Matter
P_{RL}	Engine Power Demanded to Propel the Vehicle
PSAT	Powertrain System Analysis Toolkit
P_{UC}	Ultracapacitor Discharge Power
P_{wh}	Power Demand at the Wheel
PTCM	Powertrain Controller Model

Q_{dis}	Heat Dissipated into the Air
Q_{gen}	Heat Generated
$\dot{Q}_e$	Heat Energy Flow Rates of the Engine
$\dot{Q}_r$	Heat Energy Flow Rates of the Radiator
$\dot{Q}_f$	Heat Energy Flow Rates of the Fuel
r_{acc1}/r_{acc0}	Vehicle Speed Difference between Up-and Down-Shifting Speed at Maximum Accelerator Pedal Position and the One at Zero Accelerator Pedal Position
RBF	Radial Basis Function
R_{charge}	Internal Resistance of the Ultracapacitor Pack during Charge
$R_{discharge}$	Internal Resistance of the Ultracapacitor Pack during Discharge
RMSE	Root Mean Square Error
RR	Rolling Resistance
$R_{thermal}$	Thermal Resistance of the System
R_{UC}	Internal Resistance of the Ultracapacitor
R_{wh}	Effective Radius of the Wheels
RWDC	Real World Drive Cycle
R^2	Square of Correlation Coefficients
SOC	State of Charge
SOC_{init}	Initial SOC of the Ultracapacitor
$SOC_{\max}$	SOC Maximum Threshold
$SOC_{\min}$	SOC Minimum Threshold
t	Time duration
T_c	Coolant Temperature
T_∞	Ambient Temperature
T_{air}	Surrounding Air Temperature
T_{Cd}	Torque of Aerodynamic Drag
T_{cont}	Continuous Torque
T_{cmd}	Torque Command
T_{dmd}	Torque Demand at the Wheels

T_{e_min}	Engine Minimum Throttle Torque Curve,
T_{e_max}	Engine Wide Open Throttle Torque Curve
T_{grade}	Torque Loss due to Grade
$T_{inertia}$	Torque of the Inertia of the Vehicle
TMA	Truck Manufacturers Association
$T_{\max}$	Maximum Torque
$T_{\max\_mechnical}$	Maximum Mechanical Torque
$T_{\max\_electrical}$	Maximum Torque Electrical
$t_{\min\_OFF}$	Minimum Duration Time to Turn the Engine OFF
$t_{\min\_ON}$	Minimum Duration Time to Turn the Engine ON
T_{out}	Torque Output
T_{peak}	Peak Torque
T_{PI}	Torque Converted from the Error between the Desired Vehicle Speed and the Actual Vehicle Speed
T_{RR}	Torque of Rolling Resistance
T_{UC}	Temperature of an Ultracapacitor Cell
T_{wheel_loss}	Torque Loss at the Wheel
UDDS	Urban Dynamometer Driving Schedule
$U(t)$	Unknown Input to the Analyzer
V	Velocity
$V_{i\rightarrow i+1}^{eco}$	Economical Up-Shifting Vehicle Speed
$V_{i\rightarrow i+1}^{perfo}$	Performance Up-Shifting Vehicle Speed
$V_{i+1\rightarrow i}^{eco}$	Economical Down-Shifting Vehicle Speed
$V_{i+1\rightarrow i}^{perfo}$	Performance Down-Shifting Vehicle Speed
V_{OC}	Open Circuit Voltage
$V_{OC\_\max}$	Maximum Open Circuit Voltage
$V_{OC\_\min}$	Minimum Open Circuit Voltage

WVU	West Virginia University
W	Vehicle Weight
w_i	Weight of the Linear Output Neuron
x	Dispersion Function of the Analyzer
x'	First Order Derivative of the Dispersion Function of the Analyzer
x''	Second Order Derivative of the Dispersion Function of the Analyzer
x_i	Center Vector for Neuron *i*
$Y(t)$	Measured Emission Data
$Y'(t)$	First Order Derivative of Measured Emission Data
$Y''(t)$	Second Order Derivative of Measured Emission Data
y_i	Measured Emission Data
$\hat{y}_i$	Predicted Emission Data
$\bar{y}$	Sample Mean of Measured Emission Data
$\bar{\hat{y}}$	Sample Mean of Predicted Emission Data
s_y	Standard Deviations of Measured Emission Data
$s_{\hat{y}}$	Standard Deviations of Predicted Emission Data
$0.5C_d\rho AV^3$	Aerodynamic Drag
$mV(dV/dt)$	Vehicle Inertia
ε_x	The Elasticity of Fuel Consumption with Respect to *x*
ρ	Air Density
ρ	Basis Functions in Artificial Neuron Network
μ	Coefficient of Rolling Resistance
θ	Grade
μmgV	Rolling Resistance
δ_{HI}	Heat Index
$\omega_{1\to2}^{eco}$	Economical Engine Speed of Up-Shifting to Lowest Gear
$\omega_{2\to1}^{eco}$	Economical Engine Speed of Down-Shifting from Lowest Gear

ω_{fan}	Engine Cooling Fan Speed
$\omega_{\max\_eff}$	Engine Speed at the Best Efficiency Point
ω_{idle}	Engine Idle Speed
ω_{iss}	Input Shaft Speed
ω_m	Motor Speed
$\omega_{N-1\to N}^{eco}$	Economical Engine Speed of Up-shifting to highest gear
$\omega_{N\to N-1}^{eco}$	Economical Engine Speed of Down-shifting from highest gear
η	Transmission Efficiency
η_m	Efficiency of the Motor
η_{UC}	Efficiency of Utracapacitors
α	Vector of the Constant Coefficients
β	Fuel Equivalent Factor with Unit g/J
ΔV	Error between the Desired Vehicle Speed and the Current Vehicle Speed
ΔV_i^{eco}	Difference of Vehicle Economical Up- and Down-Shifting Speeds
ΔV_i^{perfo}	Difference of Vehicle Performance Up- and Down-Shifting Speeds

Chapter 1: Introduction

1.1. Background

In the last two decades, heavy-duty vehicle engine design changes were driven primarily by emissions regulations. According to government and industry statistics, heavy-duty trucks account for approximately 20 percent of carbon dioxide (**CO_2**) emissions from all transportation sources in 2007 and the heavy-duty vehicle is the fastest-growing provider [1]. Heavy-duty vehicles are also responsible for 32 percent of NO_x emissions and 27 percent of transportation PM (particulate matter) emissions in 2004 [2]. NO_x and PM are significant sources of impact to public health. In December 2009, the Environmental Protection Agency (EPA) declared that CO_2 emissions endanger public health and proposed to regulate CO_2 standards for new vehicles, including heavy-duty trucks. In a U.S. Presidential memorandum, Barack Obama validated the EPA's findings and issued the following statement: "...medium- and heavy-duty trucks and buses continue to be a major source of fossil fuel consumption (FC) and greenhouse gas pollution. I therefore request that the Administrators of the EPA and the NHTSA immediately begin work on a joint rulemaking under the Clean Air Act (CAA) and the Energy Independence and Security Act of 2007 (EISA) to establish fuel efficiency and greenhouse gas emissions standards for commercial medium- and heavy-duty vehicles" [3]. The new European emissions regulation, which was introduced in July 2009 and will become effective in 2013, is comparable in stringency to the US 2010 standards [4, 5]. ADR80 (Australian Design Rule) also set emission limits for heavy-duty vehicles. ADR 80/02 requires heavy-duty vehicles to have OBD (on board diagnostics) systems that meet the European VI (or Japanese) requirements. ADR 80/03 requires vehicles to have OBD systems that meet the European V requirements [6]. The effects of vehicle model year (MY) on emissions have been addressed in the literature [7-10].

Separately, the request for high engine efficiency was driven by customer demand for reduced vehicle FC. At the time of writing, both regulation and customer demand are focused on increasing the efficiency of the whole vehicle, although the two thrusts may differ when overall operation economics and system efficiency are considered. The Energy Independence and Security Act (EISA) of 2007 puts forth the first-ever established fuel economy (FE) standards for vehicles in the Gross Vehicle Weight Rating (GVWR) range from 8,500 lbs to more than 80,000 lbs [11]. This standards will go into effect at the start of the 2014 model year[11].

To stay in business, Heavy-duty vehicle manufacturers find them under massive pressure to remain in compliance with regulations and anticipate the rising costs of developing new technologies. A tool that can accurately simulate multiple powertrain configurations without building costly physical prototypes is urgently needed. In order to meet this demand, the Argonne National Laboratory (ANL), cooperated with major automatic companies, developed the PSAT. PSAT is simulation tool that helps mitigate costs associated with vehicle system

design and validation of vehicle components and system [12]. Meanwhile, new control strategy and technologies including lightweight vehicle components, improved aerodynamics and tire rolling resistance have been attracted great attention. SmartWay transport partners commit to integrate new strategies and technologies that improve FE and reduce emissions and fuel cost for on-road freight fleets [13, 14].

1.2. Hypothesis and Objectives

The primary objective of this research was to validate of a conventional heavy-duty truck model. The central hypothesis of this proposed research was that vehicle modeling tools can provide sufficiently valuable insight into factors affecting emissions and fuel economy, provided that components within the models are adequately represented. Specific objectives included to acquire information and data which described all the major components of the vehicle, to improve the control strategy and to quantify the effects of factors on FE and emissions for the conventional heavy-duty truck. Another objective of this research is to model a series hybrid bus.

1.3. Technical Approaches

The first step of the study was to obtain information and prepare a set of component parameters of heavy-duty vehicles. Specific objectives were to determine the transient engine FE and emissions, define transmission efficiencies, model auxiliary loads (particularly fan loads) and shifting patterns. The intent, in turn, was that the heavy-duty truck model would then be used for the quantitative study for heavy-duty vehicles over different cycles and different terrains. In addition, a series hybrid heavy-duty bus was modeled over different driving schedules. The technical approaches used to meet the objectives of this research are summarized as follows.

Phase I: A conventional heavy-duty truck was first modeled and simulated by using the PSAT [15]. The truck was a 1996 MY Peterbilt tractor truck with a 550 hp Caterpillar 3406E non-EGR engine. It was equipped with an 18-speed Roadranger manual transmission and a tandem axle drive [16]. The Peterbilt truck has been operated through transient cycles on the chassis dynamometer to provide continuous emission data as well as engine speed and engine percent load at the West Virginia University (WVU) Transportable Heavy-duty Vehicle Emission Testing Laboratory.

First, the information and data used to describe the major components of the Peterbilt truck were incorporated into PSAT. For the engine model, the engine torque was estimated by interpolating between the maximum and minimum torque. The engine fuel rate was estimated by a fuel rate look-up table, which was developed based on experimental data and expressed in terms of the engine torque and the engine speed. For the NO_x emissions model, the data were examined first for time delay and diffusion. Two approaches, linear regression (LR) and artificial neural network (ANN) were provided to predict the NO_x emissions and the one with better predictive performance would be incorporated into PSAT. For the gearbox model, the shifting strategy was

elaborated and the transmission efficiency lookup tables were developed using the information from the manufacturer. In a conventional vehicle, the gear number is the most important factor to affect engine speed. It is thus essential to optimize the shifting strategy to validate the truck model. To find the gear number, the gear ratios, which were calculated from the measured engine and vehicle speed, were compared with the 18-speed Roadranger transmission equipped in the Peterbilt truck and the closest ratios were selected. As the largest mechanical accessory, an engine cooling fan model, which estimates fan power demand, was implemented into the heavy-duty truck model. Before modeling the whole vehicle model, it was necessary to validate each component model separately. This would help find problems with specific component models. In this dissertation, the engine was the only validated component model because of a lack of experiential data of other components.

Phase II: In this phase, the quantitative analysis of the impacts of various factors on FC was conducted. Three parameters, the vehicle weight, coefficients of rolling resistance and the aerodynamic drag were chosen to analyze their effects on FC. Since the aerodynamic drag, rolling resistance, and the truck mass are highly dependent on vehicle activities or duty cycles, the vehicle was simulated under typical in-use behavior which represents real world driving circumstances. In this dissertation, the Peterbilt PSAT model was simulated through the UDDS, HHDDT (including creep, transient, and cruise modes) and HHDDT_s (HHDDT Short, referring to a shortened high-speed cruise) schedules [17-20].

In order to examine the parametric effect of different engines on NO_x emissions, the 1996 Caterpillar 3406E engine of the Peterbilt truck was replaced by a 1999 Cummins ISM 370 hp non-EGR engine and a 2004 Cummins ISM 370 hp EGR engine, and then the truck model was simulated by PSAT over different cycles.

Phase III: A HEB was modeled in this phase. The HEB was a New Flyer bus with ISE hybrid system. First, information and data were acquired to describe all major components of the ISE hybrid bus, and these were incorporated as drivetrain components into PSAT. The main components that make up the ISE hybrid bus include the controller, engine, motor/generator, ultracapacitor, drive motor and the one-gear reduction transmission. Then the engine model was validated separately. The control strategy plays an important role in the FE of a hybrid electrical vehicle (HEV), because the FE is strongly dependent on the decision of how to split the power demand between the engine and the energy storage system at each instance in time. The control strategy in this dissertation was a load following method, in a way that the power flow of the engine, motor and ultracapacitors met the requirement of the power at the wheels while maintaining SOC at a reasonable level, with the engine operating on the optimal fuel efficiency curve.

1.4. Contributions

While PSAT has been widely used to predict the FC and exhaust emissions of conventional and hybrid light-duty vehicles, accurate modeling techniques for heavy-duty vehicles are still in its infancy. There remains a need to better understand real world factors and their impacts on FC and emissions.

The primary contribution of this study is the experimental validation of a conventional over-the-road heavy-duty Peterbilt truck model. The Peterbilt truck model developed in this research, in cooperation with ANL, has been integrated into the PSAT and in turn, the truck model was expanded to predict the FC and emissions for heavy-duty vehicles over different cycles and different terrains. The model has been sufficiently verified to use as the basis for parametric studies. The novelty of this study included the development of the predictive emissions model, transmission efficiency matrix and an engine cooling fan model.

The quantitative study of the impacts of factors on FE provided a way to estimate FE of heavy-duty vehicles over various cycles conveniently by interpolating within the factor values and extrapolating outside of them. Moreover, results suggest that depending on the circumstances, it may be more cost effective to reduce one parameter (such as coefficient of aerodynamic drag) to increase FE, or it may be more beneficial to reduce another parameter (such as the coefficient of rolling resistance).

A series HEB was modeled in this research. Main powertrain components were customized, the engine model was validated and the control strategy was improved. The PSAT simulated results were compared with the experimental data over four various driving schedules. The high fidelity of this model makes it possible to evaluate the FE and NO_x emissions of the series hybrid bus for future PSAT users.

Chapter 2: Literature Review

A review of relevant literature was performed, which provided basic information for completing the study. This section contains various sources in the area of vehicle simulation tools, types of truck activities, emissions modeling approach, HEV technologies and the control strategy.

2.1. Vehicle Simulation Tools

The business of heavy-duty vehicles is extremely competitive. To stay competitive, automakers have been forced to shift their focus to both remain in compliance with regulations and anticipate the rising costs of developing new technology. A tool that can accurately simulate multiple powertrain configurations without building costly physical prototypes is needed to optimize fuel efficiency and performance for next generation vehicles. Various vehicle simulation tools were developed in response to this requirement.

2.1.1. Greenhouse Gases, Regulated Emissions, and Energy Use in Transportation (GREET)

GREET is a fuel-cycle model developed by ANL in 1996, which evaluates various engine and fuel combinations on a constant fuel-cycle basis [21]. By inputting the user's own assumptions, the model generates energy and emission results for specific fuel and technology combinations. More than 100 organizations, including government agencies, the auto industry, the energy industry, research institutes, universities, and public interest groups in North America, Europe, and Asia were using GREET by 2005 [21].

2.1.2. AirCRED Model

AirCRED is a Graphical User Interface (GUI)-based calculation model developed by ANL. The model provides the interface for users to input information and then outputs data based on the inputs, which offers an easy and straightforward way to estimate the ozone precursor and winter season carbon monoxide (CO) emission reduction credit from Alternative Fuel Vehicles (AFVs) [22]. AirCRED is designed on the basis of the U.S. EPA's MOBILE model combined with test certification data for AFVs and their gasoline- or diesel-fueled counterparts [22, 23]. The difference between the tested certification emissions of AFVs and their conventional counterparts determines the magnitude of the credit (g/mile) [22].

2.1.3. Backward-Looking Model

The backward-looking approach works by assuming the vehicle meets the desired speed cycle. The tractive force and related wheel torque are calculated from the desired vehicle speed. The calculation migrates backward through the vehicle drivetrain all the way to the engine to finally determine how each component should respond to follow the speed [24]. The backward-looking model is relatively fast to run, but since the backward-looking models are static models which assume the vehicle speed cycle has already been met, transient effects are not accounted for realistically. Therefore, the backward-looking approach cannot complete an accurate control strategy. ADVISOR, which was originally developed by NREL in 1994 and was further developed by AVL in 2004, is representative of a backward-looking model. Other simulation programs, like Simple Electric Vehicle Simulation Software (SIMPLEV), also utilize backward-looking approaches [25].

2.1.4. Forward-Looking Model

PSAT is a forward-looking model which was originally developed by Argonne National Laboratory, under the direction of and with contributions from Ford, General Motors, and Daimler Chrysler. It works by imitating the driver to develop appropriate accelerator pedal and braking commands to meet the target vehicle speed [26]. PSAT is a state-of-the-art flexible and reusable vehicle simulation package and automotive engineering tool that evaluates a vehicle's FE and performance [26]. Users can build a vehicle model conveniently by selecting the drivetrain configuration, component models, initialization file and control strategy from the GUI. This simulation program allows the researchers to efficiently develop and optimize the vehicle performance, as well as help to reduce real-world emissions and FC. Currently, PSAT is licensed to more than 400 organizations, including automotive companies, major component suppliers, government researchers and universities [27]. The drawback of a forward-looking model is the relatively long simulation run time.

2.1.5. GT-DRIVE Simulation Tool

GT-DRIVE is a powertrain and vehicle simulation tool that conducts vehicle performance and cycle analysis for FE, emissions, and driveline component dynamics [28]. It is one of the applications of GT-SUITE [29]. GT-DRIVE can be run in both forward-looking mode and backward-looking mode. In a forward-looking mode, the vehicle response to the driver's inputs is calculated, and in a backward-looking model, the engine state and driver inputs are computed from a known vehicle state. The GT-DRIVE model includes an advanced driver model, HEV driveline components, strategy controller and characterizations of road conditions [28].

2.2. Metrics to Determine the Fuel Efficiency

2.2.1. Definition of Fuel Economy and Fuel Consumption

FC and FE are metrics used to determine the fuel efficiency of vehicles. FC is defined by the amount of fuel consumed in traveling a certain distance and is usually expressed in *gallon/100 miles* [14]. FE is the distance traveled per unit of fuel used (expressed in *mpg*). The relationship between FC and FE is nonlinear. A 10% increase in FE corresponds to 9.1% decrease in FC, whereas a 100% increase in FE corresponds to a 50% decrease in FC. A given percentage improvement in FE saves less and less fuel as the FE increases [14]. For example, the amount of fuel saved for a light-duty vehicle when FE is going from 20 *mpg* to 30 *mpg* for 12,000 miles traveled is 200 gallons. The amount of fuel saved for a heavy duty vehicle when FE is going from 5 to 6 *mpg* for the same 12,000 miles travels is 400 gallons. This example implies the importance of improving the FE of heavy-duty vehicles. A large amount of fuel can be saved by small improvements in FE.

2.2.2. Definition of Load-Specific Fuel Consumption

The vehicle load (gross weight) is an important input variable for a vehicle simulation when determining the vehicle's FE. The load has only a modest impact on FE for light-duty vehicles [14]. For most of the light-duty vehicles, the loaded weight is approximately 25 to 35 percent more than the empty weight [14]. The sales-weighted average of FC is used to convert into FE to compare with the standards of the corporate average fuel economy (CAFE). Whereas for heavy-duty trucks, the main purpose is to deliver payloads and it is common that the loaded weight accounts for a large proportion of the GVWR. So the metric related to the amount of work performed, FC per unit payload carried (termed as load-specific FC (LSFC)) with units of *gallon/ton-100 mile*, would be more meaningful. The LSFC is defined by Equation 2.1.

$$LSFC = \frac{FC}{W} \qquad \textit{Equation 2.1}$$

where FC is fuel consumption on a given cycle, in units of *gallon/100 miles*, W is the GVWR.

2.3. Types of Truck Activity

2.3.1. Heavy-Duty Diesel Truck Test Schedules

In characterizing the FE and emissions from heavy-duty vehicles, it is essential that the vehicle is tested or simulated under typical in-use behavior. In this study, several cycles which cover a wide range of driving conditions were used. The EPA's UDDS were developed for chassis dynamometer testing of heavy-duty vehicles [17]. It is also termed as "Cycle D". The UDDS includes both freeway and non-freeway driving activity, and is widely used for characterization

of performance of heavy-duty truck behavior. The speed-time characteristics of the UDDS are shown in appendices Figure A1. The basic parameters of the UDDS include a 1060 second duration trip, a 5.55 miles distance trip, an 18.86 mph average speed and a 58 mph maximum speed trip [17]. The HHDDT (Heavy Heavy-Duty Diesel Truck) schedule was originally created for the E55/59 study which represented real-world truck activity in California [17-20]. The HHDDT schedule included four modes, namely idle, creep, transient and cruise modes. The creation of the HHDDT has been discussed previously [17-20]. Each cycle has unique idle time, average speed, stop times, acceleration and deceleration. The creep mode has an average speed of less than two miles per hour, with a distance of 0.12 miles [19]. The transient mode has a higher average speed of 15.34 miles per hour, with a distance of 2.8 miles. The transient mode is the typical stop-and-go behavior for a heavy-duty truck in an urban area [19]. The cruise mode stands for freeway travel. The HHDDT_s represents both the high speed cruise that characterizes similar highway behavior that occurs in congested urban areas and south-north travel along Highway 99 and Interstate 55 [19]. The speed-time characteristics of the four modes (creep, transient, cruise and HHDDT_s) can be seen in Appendices Figures A2 through A5. The Manhattan (MAN) cycle was created from buses in-service used for the New York City (NYC) Metropolitan Transportation Authority (MTA). The speed-time trace consists of both conventional buses and HEBs over different NYC MTA bus routes [30]. The Manhattan cycle contains 20 micro-trips covering 2.1 miles in 1089 seconds, with an average speed of 6.78 mph [31].Vehicle speed over the duration of the Manhattan cycle is shown in Appendices Figure A6. The Orange County Transit Authority (OCTA) cycle is presented in Appendices Figure A7 [32, 33]. This cycle was derived from buses operating in Los Angeles and other California areas and reflects a wide variety of accelerations, decelerations and cruise operations. The Houston cycle (Appendices Figure A8) was another cycle developed using data logged from a real bus operation. These activities affect power demand from the vehicle and in turn affect FC and emissions [34]. Detailed statistics of these cycles are shown in Table 2.1.

Table 2.1: Test schedule statistics by modes

Parameters	Creep Mode	Trans Mode	UDDS	Cruise Mode	HHDDT_s	OCTA	MAN	HOU
Duration (s)	253*	671	1060	2083	760	1910	1089	1800
Distance (mile)	0.12	2.85	5.55	23.07	9.76	6.51	2.07	5.47
Average Speed (mph)	1.77	15.34	18.86	39.88	52.59	12.28	6.78	10.94
Maximum Speed (mph)	8.20	47.50	58.00	59.30	66.90	37.67	24.78	31.77
Maximum Accel (mph/s)	2.30	2.9	4.40	2.14	2.77	3.44	3.47	3.53
Maximum Decel (mph/s)	2.39	2.77	4.50	2.34	5.60	5.62	5.34	4.52
Percent Idle	41.11	15.57	32.92	7.73	8.03	15.30	26.91	28.89
Standard Deviation of Speed (mph)	2.04	13.39	19.65	22.01	22.68	10.08	7.22	11.52

*Note that usually a triple creep was run.

For a given cycle, it is important to use average speed when analyzing FC. The average speed of a real world cycle implies the extent to which the cycles are transient [35]. Low speed cycles (such as the creep mode) have high idle content implying more transient operation. Both the idle and stop-start behavior are more common at low speed modes than on highway. On a chassis dynamometer, the vehicle speed can be used for computing the aerodynamic drag and rolling resistance, provided the vehicle mass, gravitational acceleration, coefficients of aerodynamic drag and the rolling resistance are known. Figure 2.1 depicts the FC for a Line Haul Class 8 on real word drive cycles (RWDC). The real world drive cycle data used in Figure 2.1 were collected by Oak Ridge National Laboratory [36]. An interpolation among the collected FC was performed. The FCs of four test modes, transient mode, UDDS, creep mode and HHDDT_s modes for the Peterbilt truck (truck weight = 46,000 lbs, assumed the coefficient of rolling resistance $\mu = 0.00938$, assumed the coefficient of aerodynamic drag $C_d = 0.79$). The coefficients of aerodynamic drag and the rolling resistance are values presented in the Code of Federal Regulations [37]) which are also plotted in Figure 2.1. The FC (gallon/100 miles) is high at low average speed and decreases with the increase of average speed. Two factors might contribute to this phenomenon. First, a lot of energy is consumed by accelerating the vehicle from the idle or transient event. Second, powertrain efficiencies tend to be low at low speed. Figure 2.1 also shows that, after a certain speed, the FC increases as the average speed rises due to the fact that the aerodynamic drag increases significantly with the increase of the speed. This can be illustrated by Figure 2.2. Below 40 mph, the rolling resistance is much higher than aerodynamic drag, but after 60 mph, aerodynamic drag becomes significant. Figures 2.1-2.2 illustrate that the

FC has a minimum value at approximately 60 mph vehicle speed where the aerodynamic drag force is not yet extremely high.

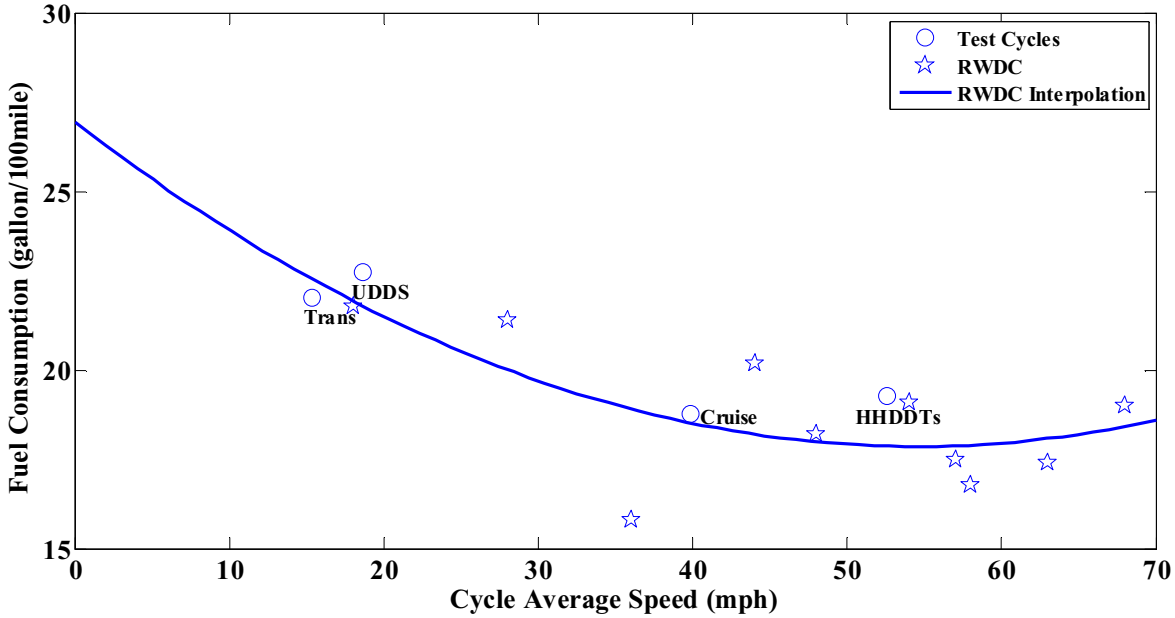

Figure 2.1: Fuel consumption as a function of average cycle vehicle speed for a sample of real world drive cycles for a Class 8 truck
(The FC of test cycles are PSAT 6.2 simulated results running over the UDDS, transient, cruise and the HHDDT_s modes at truck weight = 46,000 lbs, the coefficient of rolling resistance μ = 0.00938, the coefficient of aerodynamic drag C_d = 0.79) [36]

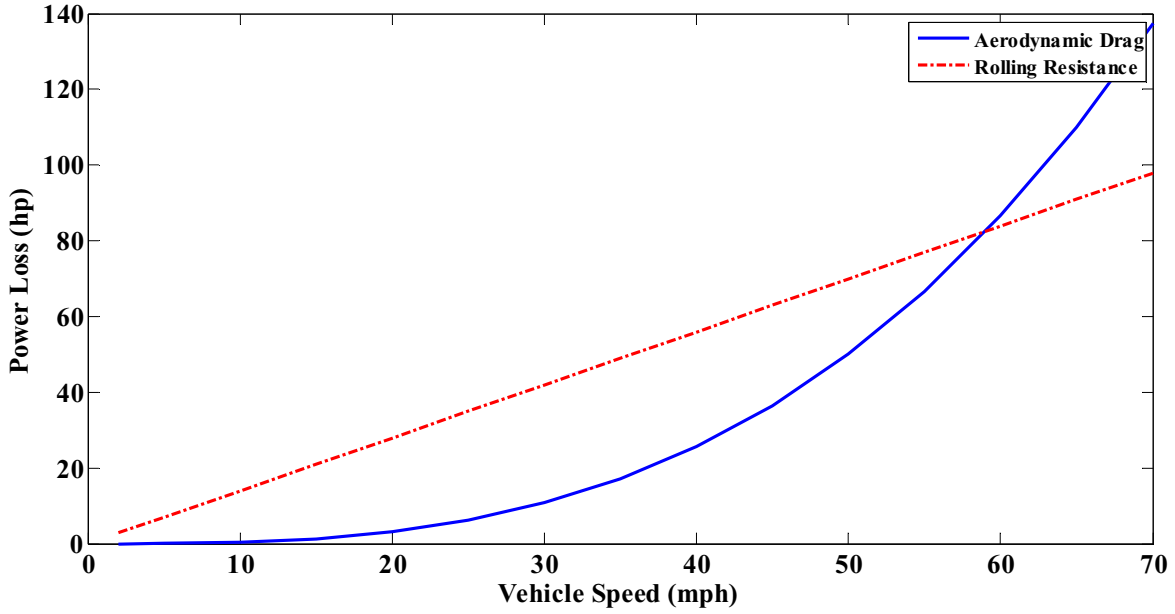

Figure 2.2: Power losses of aerodynamic drag and the rolling resistance for Peterbilt truck

(Truck test weight (with trailer) W = 46,000 lbs, the coefficient of rolling resistance μ = 0.00938, the coefficient of aerodynamic drag C_d = 0.79, frontal area A = 7.06 m^2)

2.3.2. Road Grade

Unlike duty cycles, the road grade effect on FC and emissions from heavy-duty vehicles has not received much attention. Limited literature was found to discuss the impact of the road load on FC. Khan and Clark addressed the effect of grades on FC over different cycles [34]. Kern et al. [38] specified that a grade less than 5% had little bearing while a steep grade had substantial effect on NO_x emissions. The CO, NO_x and hydrocarbon (HC) were observed increasing during uphill driving while PM did not change much.

Theoretically, the effect of the road grade on FC could be found from the road load equation, which is expressed by Equation 2.2 [39].

$$P_{RL} = P_{aux} + \frac{mV(dV/dt) + 0.5C_d\rho AV^3 + \mu mgV + mgV\sin(\theta)}{\eta} \qquad \textit{Equation 2.2}$$

where m is vehicle mass (kg), V is vehicle speed (m/s), C_d is the coefficient of aerodynamic drag, ρ is air density (kg/m^3), μ is the coefficient of rolling resistance, g is acceleration due to gravity (m/sec^2), θ is grade. P_{RL} denotes engine power demanded to propel the vehicle, P_{aux} denotes auxiliary load including the engine cooling fan, $mV(dV/dt)$ denotes vehicle inertia, $0.5C_d\rho AV^3$ denotes aerodynamic drag, μmgV denotes rolling resistance and $mgV\sin(\theta)$ denotes grade effect. The mathematical equation of the road gradient was calculated as the vertical rise (+) or fall (-) in meters (m) for every 100 m [40].

2.4. Emissions Modeling Approaches

It is essential to model instantaneous emissions because they can be incorporated into the vehicle simulation model [24, 26], support emission inventories and help develop engine after treatment control strategies. In the original PSAT initialization file, the emissions were estimated by lookup tables, which were expressed in terms of engine torque and speed, without including their derivations. Two modeling approaches, the LR and ANN methods have been reviewed because of their relevance to the dissertation topic. Both of these methods need actual engine data to be formulated.

2.4.1. Emissions Model by Linear Regression Method

LR method is an approach to model the relationship between two variables by fitting linear equations to the observed data. The most common method for fitting a regression line is the least-square approach [41, 42]. In the least square method, the best-fitting line for the observed data is computed by minimizing the sum of the squares of the vertical deviations from each data

point to the line [43]. LRs were widely used to fit a predictive model in many fields. Modeling engine emissions is one of the common applications.

The NO_x emissions related closely to engine power has been addressed earlier [53-55]. It has been shown that engine speed and torque are the primary input parameters in predicting emissions [45]. Most heavy-duty vehicles have manual transmissions, and so engine speed is determined by the vehicle speed and the selected gear, except during idle and shifting periods when the transmission is in neutral [47]. The engine torque is determined by the accelerator pedal position, the history of the acceleration pedal position, and the speed governor. Since the transient behavior may affect the emissions, their derivatives are also taken into account [47, 48]. By using the LR method, the emissions can be expressed as a linear combination of engine torque, engine speed and their derivatives.

2.4.2. Emissions Model by Artificial Neural Network

ANN is another predictive tool widely used in solving engineering problems. Application of ANNs includes regression analysis [49], classification [50] and data processing [51], etc. In predicting emissions, Jarrett and Clark indicated that engine speed and torque are the primary input variables [45]. Lucas et al. [52] pointed out the influence of the fuel composition parameters on PM with engine torque and speed as input variables using an ANN. The predicted NO_x emissions were found to be within 5% error by the ANN method using engine speed and torque as inputs [18]. In other instances, more variables were used to predict engine emissions. Hashemi [53] built an ANN to predict emissions using axle speed, torque and two other parameters which define a time span over 150 seconds. Hanzevack et al. [54] developed an ANN based on engine performance, fuel efficiency and an emissions prediction system. Bedick [55] used input variables of engine speed, engine torque, coolant and oil temperature to develop a NO_x model. Thompson et al. [56] exploited variables of engine speed, coolant temperature, oil temperature, exhaust temperature, intake air temperature, intake air pressure and accelerator position as inputs. By taking these variables, the emissions of CO_2, CO, NO_x, HC can be predicted to within 5% error over the FTP and two other random cycles [55, 56]. Desanteset et al. [57] proposed a mathematical model to predict NO_x, PM emissions and brake specific fuel consumption (BSFC) as a function of engine speed, fuel mass (g/cycle), air mass (g/cycle), fuel injection pressure, start of injection and EGR level. By using the ANN approach, the fuel mass, start of injection and EGR were found to be the most relevant parameters for NO_x, PM and BSFC. It was claimed that, the function performed successfully in minimizing BSFC, while maintaining the emission values below the demanded level. Krijnsen et al. [58] suggested the application of the ANN as a precise tool to predict NO_x emissions with the inputs of engine speed, rack position, intake air temperature, intake air pressure and their derivatives. By using these input variables, they were able to accurately predict NO_x emissions within 6% of measured values. Tehranian [59] demonstrated the ANN architecture and activation function on the

emissions predictions. A 3-Layer ANN with radial basis functions was suggested to predict five emissions of NO_x, PM, HC, CO, and CO_2.

2.5. Hybrid Electric Vehicle Technologies

According to statistics, buses in the United States provided more than 60 percent of the 9.7 billion transit passenger trips in 2005, approximately 84 percent of which were powered by diesel engines [60]. Hybridization technologies have demonstrated their ability to significantly reduce FC for various vehicle applications. Transit buses are especially suited for applying hybrid systems because they normally operate on predictable routes with frequent starts and stops [61]. An HEV uses multiple sources of energy that can be separately or simultaneously used to propel the wheels. Generally, the energy sources include an electric motor with energy from the energy storage systems (ESS), and a smaller than normal diesel engine that together provide the same power as a conventional bus while reducing FC and emissions.

The obvious advantages of a hybrid system include the following:

- Optimum engine operating region: The engine has an optimal region on the torque - speed panel. In an HEV, the engine operates closely to its best fuel efficiency line. As the engine and traction model are not coupled directly, the engine does not have to always follow the road load change. The engine can run in a less transient situation which results in significant reductions to FC and emissions [62].
- Engine shut off: Fuel efficiency is very low when the engine operates at a low speed. The engine is shut off when its speed is below a certain threshold thereby reducing FC and emissions.
- Regenerative braking: A regenerative brake recovers the kinetic energy produced when braking into electrical energy which can be stored in the ESS for future use. The kinetic energy is dissipated as heat in a conventional brake. In HEVs, up 50 percent of this energy could be recovered depending on the duty cycle and aerodynamic drag and rolling resistance [63].
- Better drivability: The electric motor reacts faster than an internal combustion engine (ICE), so the torque required to reach the desired vehicle speed can be achieved faster.
- Electrical accessories: the mechanical accessories are replaced by electric systems which will save some energy.

Disadvantages of an HEV include as following:

- The configuration is more complicated.
- The vehicle mass is heavier due to the addition of components.
- The cost is increased due to the complexity of the energy control strategy and the additional components.
- The reliability of the overall system is decreased due to the increased system complexity.

There are three basic architectures of HEVs, namely series, parallel and planetary transmission series/parallel. The ICE and ESS provide power to an electric motor that propels the vehicle in the series configuration. In the parallel configuration, both the electric motor and the ICE are contributors in powering the vehicle's wheels. Parallel HEVs intend to satisfy high speed and acceleration demands, whereas series systems are good for applications with large energy requirements [61]. For a public transit bus, where there are lots of accelerations, series HEBs have been generally favored by manufacturers [64].

2.5.1. Series Hybrid Electric Vehicle

As Figure 2.3 illustrates, in a series HEV, a ICE powers a generator, which either powers the electric drive motor or supplies power to charge the ESS when the ESS drop below a predefined minimum level. As the ICE and vehicle speed are decoupled and only the electric motor is connected with the wheels, the ICE does not have to to speed up or slow down as the vehicle speed changes. As a consequence, the system allows the power delivered by the engine to either follow engine speed and the load or not [22,65], which would theoretically allow the engine to be operated at maximal efficiency all the time and could increase a diesel engine's overall operation efficiency from 30% to nearly 40% [66].

The primary drawback of a series HEV is that the mechanical energy is first converted into electric energy and then changed back into mechanical energy. Some of the generated energy is lost as heat during the conversion process [66]. Another issue is that the propulsion devices (engine, generator and electric motor) need to be sized for the maximum sustained power [67]. The series hybrid system is more viable for city transit buses with lots of stop-and-go operations.

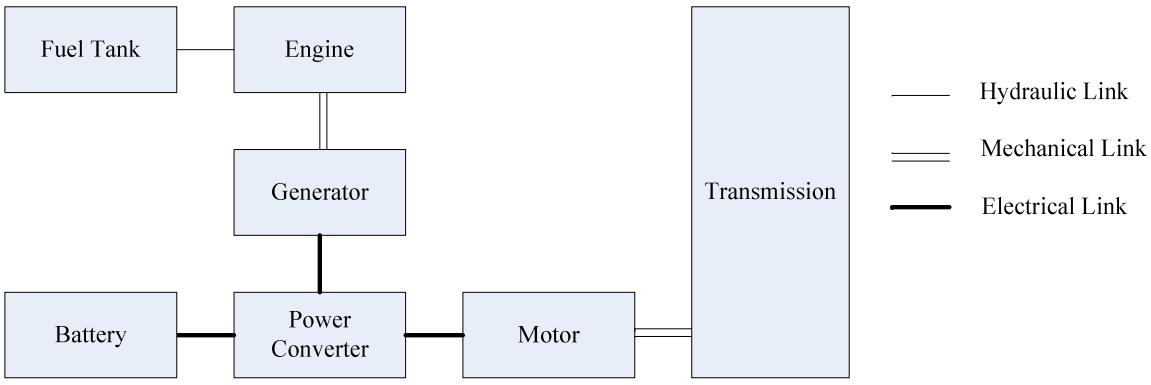

Figure 2.3: Series hybrid system

2.5.2. Parallel Hybrid Electric Vehicle

In the parallel hybrid configuration, the engine and electric motor are both connected to the vehicle drive wheels, shown in Figure 2.4. Both the engine and electric motor propel the drive

wheels simultaneously. The engine also drives the electric motor which is used as a generator to charge the ESS. Since the engine is capable of propelling the vehicle at cruise speed, as well as charging the ESS, the engine is larger and the motor is smaller compared with a series configuration [26]. In a series HEV, mechanical power from the engine is converted into electricity and then from electricity back into mechanical power in the drive motor, which results in a 15 percent loss of energy during the conversion [66]. Parallel HEVs get reduce of this loss while retaining the ability to recover regenerative braking energy. So a better FE is achieved in a parallel vehicle. However, in parallel HEVs, the engine and electric motor are directly coupled with drive wheels, which require a complex and expensive transmission [26].

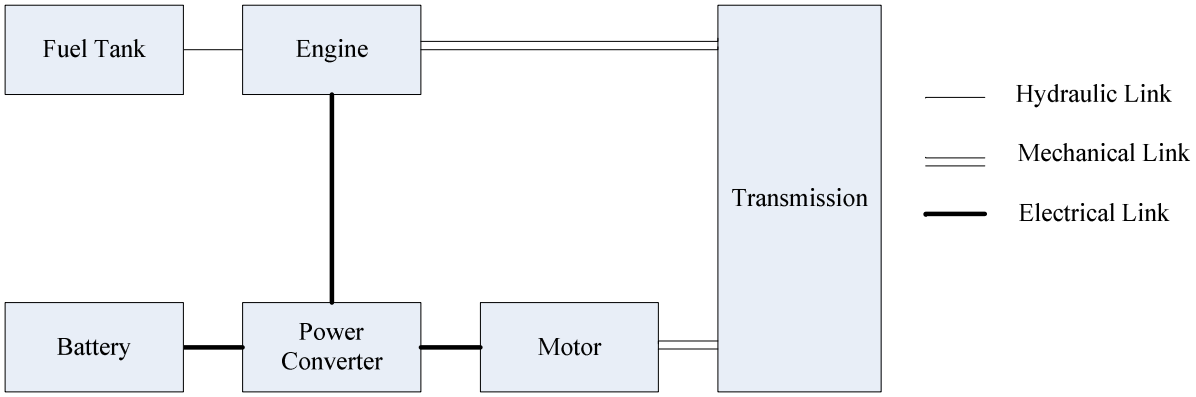

Figure 2.4: Parallel hybrid system

2.5.3. Planetary Transmission Series/Parallel Hybrid Electric Vehicle

It is known that a series propulsion system is more suitable for low-speed driving cycle whereas the parallel hybrid is more desirable during the highway driving condition [68]. The configuration of a planetary transmission series/parallel HEV (Figure 2.5) incorporates the features of both a series and parallel HEV. It has one more mechanical link compared with a series hybrid and one more generator compared with a parallel hybrid. The planetary hybrid electric propulsion system combines the benefits of both systems. However, this system suffers from its complexity and costliness. The GM-Allison Hybrid E^P50 System is a planetary transmission series/parallel system currently on the market [68, 69].

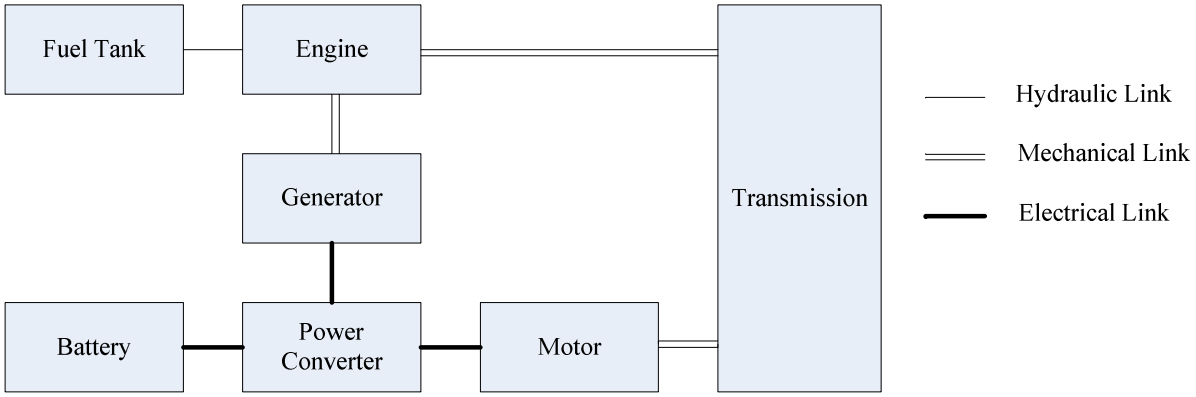

Figure 2.5: Series-parallel hybrid system

2.5.4. Energy Control Strategy in Hybrid Vehicles

The optimization of the energy control strategy is the key in obtaining a maximum reduction of FC from an HEV. The amount of fuel saved by using an HEV depends on the type of powertrain selected, the components, the energy control strategy and the driving cycles [14]. FC and emissions reduction can be realized by optimization of control strategy based on a certain driving cycle [14]. There are two basic energy control strategies, as outlined below.

2.5.4.1. Heuristic Rule-Based Control Strategy

Heuristic rule-based control strategy is designed based on "if-then-else" rules and uses the statically optimum efficiency map to achieve the best fuel efficiency. The heuristic rule is used to develop a set of event triggers which will be activated when certain conditions are met. The thermostatic control strategy is representative of a rule-based control approach. In a thermostatic control strategy hybrid system, the SOC is designed as an event trigger and the engine is turned ON/OFF when the SOC reaches the lower/upper limit. Rule-based strategies have been one of the most widely used energy management approaches [70]. The rule-based control strategy is simple, real-time implementable and has less computations to develop. The consequence of the simplicity is that this strategy cannot guarantee the best FE all of the time. A significant amount of parameters need to be tuned in order to find the maximum fuel efficiency point. A rule-based control strategy for a particular vehicle cannot be readily used for another [14].

2.5.4.2. Real Time Control Strategy

This control strategy utilizes the equivalent consumption minimization strategy that is based on equivalent fuel flow rate to minimize the overall FC over a given driving cycle [59, 71]. The equivalent fuel rate is given by:

$$\dot{m}_{fuel\_eq} = \dot{m}_{fuel} - \beta * P_{elect}$$ *Equation 2.3*

where $\dot{m}_{fuel\_eq}$ is the equivalent fuel flow rate, $\dot{m}_{fuel}$ is the actual fuel rate, β is the fuel equivalent factor with unit g/J, and P_{elect} is the actual electrical power. The equivalent energy from the ESS and the ICE is evaluated by comparing the cost of instantaneous energy generated. If the ICE produces power more efficiently than the ESS, then the ICE is used as power to propel the vehicle, otherwise, the ESS is favored. The key benefit of a real time control strategy is the optimization of the entire system as a whole instead of just the engine alone. This means that the overall efficiency that can be realized at the energy path is either from the ESS to the wheels or from both of the ICE and ESS to the wheels. In a real time control strategy, the modes of operation can be categorized as start, acceleration, cruise and deceleration (Figure 2.6).

- Start and acceleration: The ESS supplies power to propel the vehicle. The engine ON/OFF is linked to the available electric energy
- Cruise mode: The engine is ON and the engine power is used either to propel the wheel or charge the ESS.
- Large acceleration: The ICE and ESS are both connected to propel the vehicle. The engine provides additional torque to meet the large power demand.
- Braking: The regenerative braking recovers kinetic energy into a storable form for future use. The vehicle stops during this phase and the engine can be either run at idle speed or be turned off.

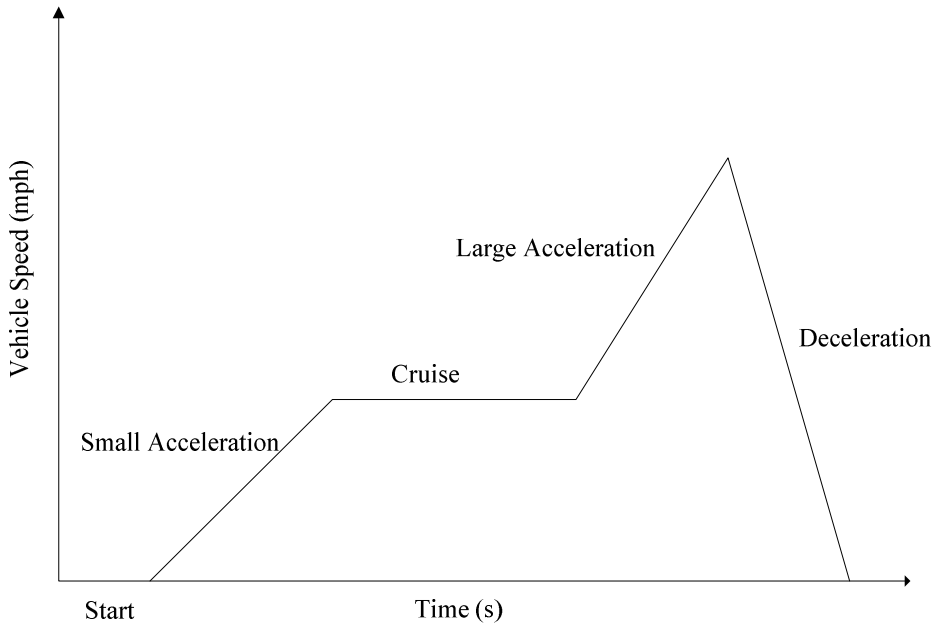

Figure 2.6: Analysis of operating modes for different stages of a driving cycle

The drawback of this approach lies in its complexity of the system due to the interactions of the drivertrain components (ICE, ESS and motor) [72].

2.5.5. Energy Storage System for Hybrid Vehicles

2.5.5.1. Batteries

It is important to choose the most appropriate battery technology as the battery affects the HEV in terms of cost, reliability, weight and "green" issues [14]. The most common battery technologies include lead-acid, nickel-metal hydride (Ni-MH) and lithium ion (Li-ion). Lead-acid batteries were used in the initial era of HEVs, but most of the current vehicles utilize Ni-MH and Li-ion [73]. Table 2.2 shows the comparison of two batteries [74].

Table 2.2: The comparison of two batteries [74]

	Ni-MH	**Li-ion**
Specific energy and specific power	50 Wh/Kg to 65 Wh/Kg	90 Wh/Kg- 95 Wh/Kg
Battery charging and discharging cycles	200-300 cycles	Above 1000 cycles
Cycle life the battery	The calendar life of Ni-MH batteries can be improved by full discharging to prevent crystalline formation [75]	Li-ion batteries are subject to aging, even if not in use.
State of charge	There exists a constant voltage profile for this battery from 80% - 30%	The battery should not be fully charged, high voltages stresses the battery [76]
Temperature dependent performance	Shows unsatisfactory performance at high or low temperatures	The performance erodes drastically at extreme high/low temperatures
Cost	NiMH batteries are priced at $250 to $1,500 per kWh in 2007. The total price of the battery pack for a hybrid car varies from $600 to $3,000 per vehicle.	The cost of the HEV batteries will be around $5,000 to $7,000 per car

2.5.5.2. Ultracapacitors

An ultracapacitor is an electrochemical capacitor that has a relatively high energy density while having the same characteristics of a normal capacitor [77]. The ultracapacitor contains two electrodes, which are separated by an insulator. This keeps current from flowing between the electrodes so that an electric potential is allowed to develop. The electrodes are typically built by a layer of activated carbon with metal foil. As the charge builds up on the electrodes, ions are attached to the surface of the activated carbon [78]. Ultracapacitors have obvious merits when compared with batteries, as described below:

- Can be charged or discharged in a very fast way, roughly ten times faster than a battery with the same weight
- Long lifetime, without degrading the performance with use, which extends the life of an HEVs' power source
- Ultralow internal resistance, which allows a high current to be drawn
- Low weight and volume
- Consistent performance at temperatures as low as -40 ^{o}F [78]

The HEV with the ultracapacitors is easier handled at rapid power transient due to its high power density, which allows an HEV with ultracapacitors to boost available power during acceleration [78]. Most of the existing ultracapacitor hybrids are aimed for use in transit buses where their frequent stop-and-go duty cycles match the operational characteristics of ultracapacitors [79]. Figure 2.7 shows a Maxwell ultracapacitor pack, which is used in the New Flyer ISE HEB model [80].

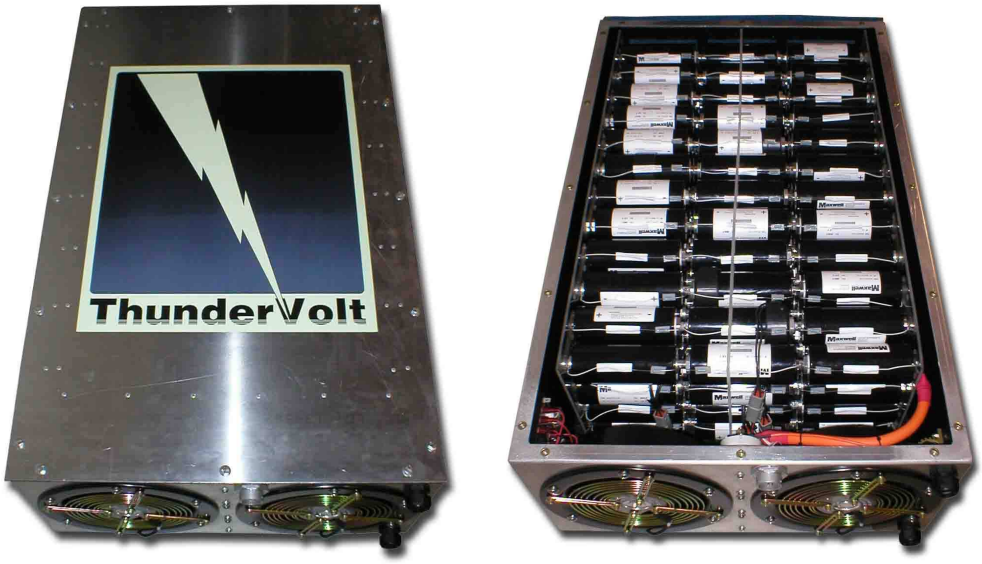

Figure 2.7: The Maxwell 2600 Farad Ultracapacitor
(Dimensions: 23.75" wide x 39.5" x 12", Pack weight: 245 lbs, Pack ESR resistance: 0.144Ohm, Pack capacitance: 18.05 Farad, Peak voltage: 345 volts (Each cell @ 2.5 volts), Peak/continuous current: 400/200 amps, Ambient air temperature rating: -35 to 50 deg. C) [80]

2.6. Summary

A comprehensive literature survey was performed to convey understanding of vehicle simulation tools, metrics to determine the FE, truck activities, emissions modeling approaches and HEV technologies. Eight cycles, UDDS, OCTA, Manhattan, Houston, creep, transient, cruise and high speed cruise schedules, which represented real-world truck activities were chosen in this research. Linear regression modeling and neural network modeling approaches were reviewed to determine the dominant input variables (like engine speed, torque and their derivatives). Basic architectures of HEVs, control strategies and the energy storage system were reviewed.

Chapter 3: PSAT Overview

PSAT is a forward-looking model that takes transient behavior and control strategies into account and thus simulates FE and performance in a realistic manner [22]. Figure 3.1 shows a PSAT vehicle model [81]. From the top down, four parts are included in the PSAT vehicle model: the driver, the powertrain controller (vehicle controller), the component controller and the powertrain component models. First, the driver model estimates the torque required to reach the desired speed and sends commands like accelerator pedal position (APP) for a diesel engine, gear number for the transmission, and mechanical braking for the wheels to the powertrain controller [82]. Then decisions about how different components are made based on the driver demand and the latest information from the component sensors. Eventually, the component controller commands (i.e., engine torque) are transformed and can then be used by the respective components' models (i.e., APP). The main disadvantage of PSAT is the relatively long simulation time compared with a backward-looking model [83, 84].

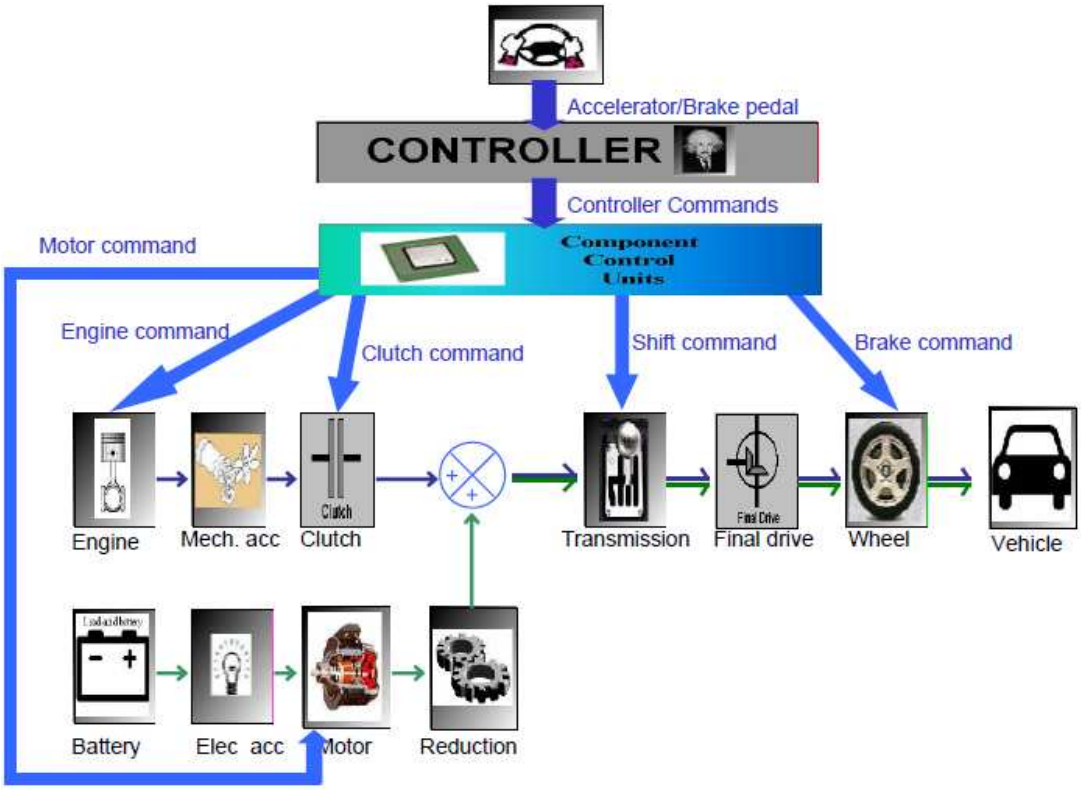

Figure 3.1: PSAT vehicle model
[81]

3.1. Driver Model

The driver model is used to simulate the accelerator or brake pedal position by estimating the torque at the wheels. Two components are included in this model. The first is a calculator, which is used to roughly calculate the torque demand at the wheel needed to achieve the desired vehicle speed. It also estimates torque losses due to the friction of braking, rolling resistance, aerodynamic drag and grade force [85]. The second component is a proportional and integral (PI) controller that requests more or less torque to the vehicle and converts the error between the desired vehicle speed and the current vehicle speed into a demand for torque at the wheels [85]. Fine adjustments are made by the PI controller. The schematic driver model is shown in Figure 3.2 [85].

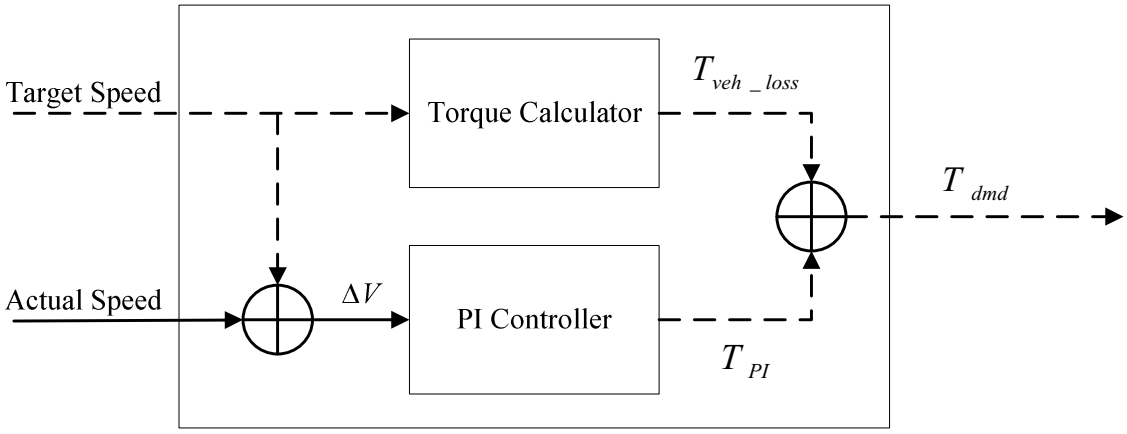

Figure 3.2: Schematic of the driver model

[16]

$$T_{dmd} = T_{wheel\_loss} + T_{PI} \qquad \textit{Equation 3.1}$$

where T_{wheel_loss} is the torque loss at the wheel and T_{PI} is the torque converted from the error between the desired vehicle speed and the current vehicle speed. Equations 3.2-3.3 [85] show these torque calculation methods.

$$T_{wheel\_loss} = T_{inertia} + T_{rolling} + T_{aero} + T_{grade} \qquad \textit{Equation 3.2}$$

$$T_{inertia} = m * dV/dt * R_{wh} \qquad \textit{Equation 3.2a}$$

$$T_{RR} = [(\mu_1 + \mu_2 * V + \mu_3 * V^2 + \mu_4 * V^3) * m * g * \cos(\theta)] * R_{wh} \qquad \textit{Equation 3.2b}$$

$$T_{Cd} = 0.5 * \rho * C_d * A * V^2 * R_{wh} \qquad \textit{Equation 3.2c}$$

$$T_{grade} = m * g * \sin(\theta) * R_{wh} \qquad \textit{Equation 3.2d}$$

where $T_{inertia}$ is the torque of the inertia of the vehicle *(Nm),* T_{RR} is torque of rolling resistance *(Nm),* T_{Cd} is torque of aerodynamic drag *(Nm),* T_{grade} is the torque loss due to grade *(Nm),* m is vehicle mass (*kg*), V is vehicle speed *(m/s),* R_{wh} is the effective radius of the wheels *(m),* μ are the coefficients of rolling resistance, C_d is the coefficient of aerodynamic drag, ρ is air density (kg/m^3), A is the frontal area of the vehicle (m^2), g is standard gravity (m/sec^2) and θ is grade.

$$T_{PI} = K_p * \Delta V + K_i * \int_0^t \Delta V * dt \qquad \textit{Equation 3.3[85]}$$

where K_p is proportional gain, K_i is integral gain, and ΔV is the error between the desired vehicle speed and the current vehicle speed, t is the time duration.

3.2. Powertrain Controller (Vehicle Controller) Model

The powertrain controller works as the brain of the vehicle by sending commands to the different components. The powertrain controller model (PTCM) includes 3 main blocks: propulsion (when positive torque is required at the wheels), brake (when negative torque is required at the wheels) and shift (to output gear ratio or gear number). The input parameters of PTCM are the command from the driver and feedback information from the powertrain model (Figure 3.1). Based on this information, the PTCM decides how each component of the powertrain should work to increase FE and decrease emissions. Eventually, commands are sent to the component control unit for the specific component to operate. For example, consider the engine in a conventional vehicle: the PTCM sends a torque request to the engine, and then the engine control unit (within the component control unit) converts torque into a load percentage command that can be processed by the engine model. The output parameters of the engine model are sent back to PTCM to make the next decision.

3.2.1. Propulsion Strategy

The propulsion model for a conventional vehicle outputs engine torque and engine ON/OFF command. In a conventional vehicle model, the engine is always ON. The engine torque is calculated based on the driver torque demand at the wheels and the gear ratio selected. The propulsion model for a hybrid vehicle outputs engine torque, generator torque, motor and engine ON/OFF command. In a hybrid vehicle model, the engine is either ON or OFF (or idle). The torques of the engine, motor and the generator are under the constraint of their maximum values [86].

3.2.2. Braking Strategy

In a conventional vehicle braking system, the wheels are slowed down by friction between the brake pads and brake rotors. The kinetic energy is turned into heat by friction and therefore wasted. In a hybrid vehicle, regenerative braking can help save fuel significantly by capturing

part of the kinetic energy when braking. The captured energy is converted into electrical energy and is stored in the ESS, which is used to power the vehicle in the future. With the regenerative brake, when the driver steps on the brake pedal, the traction motor is adjusted to reverse running mode, thus slowing down the vehicle and the energy captured is fed into the ESS. The actual amount of fuel savings is dependent on the operator driving behavior and the operating cycles [34]. The regenerative braking system is efficient in stop-and-go driving situations.

The braking model in PSAT outputs engine torque, generator torque and mechanical brake torque. In a conventional vehicle model, the engine torque demand is zero. The mechanical brake torque is calculated on the basis of the negative driver torque at the wheels and the gear ratio selected [86].

3.2.3. Shifting Strategy

In this study, the shifting strategy only happened in the conventional vehicle (as the hybrid bus has a single reduction transmission). The shifting strategy models the behavior of when and how a driver shifts the transmission by using gear maps that are a function of the accelerator pedal demand and the vehicle speed, which is shown in Figure 3.3 [16]. The accelerator pedal position is the ratio of desired torque at the wheels and the maximum torque at the wheels, a value between 0 and 1. The maximal torque (the maximum torque at each speed, which composes the maximum torque curve) at the wheels is a function of vehicle speed.

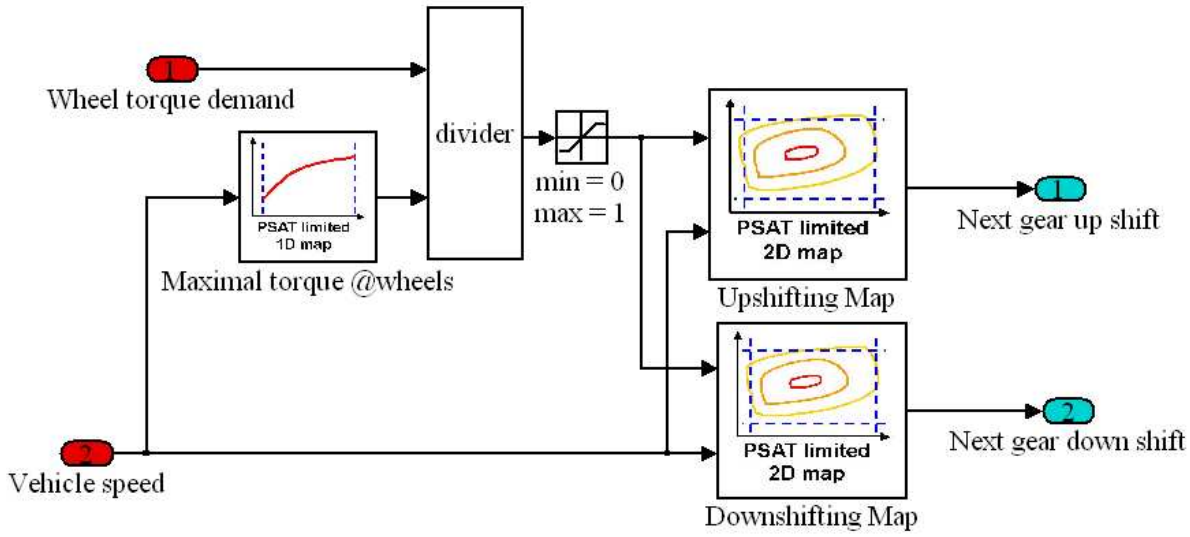

Figure 3.3: Diagram of vehicle shifting strategy model [16]

3.2.3.1. Economical Shifting Speed

The engine shifting speeds at low accelerator pedal positions are critical parameters in the shifting map definition. The so-called "economical" shifting speed is deemed as such because it is defined by the shifting strategy in a fuel saving mode. There are four key engine speeds in the shifting maps definition.

1) Engine speed of down-shifting to the lowest gear, which is the engine speed at which down-shifting is requested from 2nd to 1st for a zero accelerator pedal position.
2) Engine speed of up-shifting lowest gear, which is the engine speed at which up-shifting from 1st to 2nd for a zero accelerator pedal position.
3) Engine speed of down-shifting highest gear, which is the engine speed at which down-shifting is requested from the last gear to the second-to-the-last gear.
4) Engine speed of up-shifting highest gear, which is the engine speed at which up-shifting from the second-to-the-last gear (gear *N-1*) to the last gear (gear *N*).

In PSAT, these four speeds are defined in Equations 3.4-3.7 [86].

$$\omega_{2\to1}^{eco} = C * \omega_{idle} \qquad \textit{Equation 3.4}$$

where $\omega_{2\to1}^{eco}$ is the economical engine speed of down-shifting from lowest gear, C is a constant with a value of 1.15 is applied in this study and ω_{idle} is the engine idle speed.

$$\omega_{1\to2}^{eco} = \omega_{2\to1}^{eco} * C * \frac{k_1}{k_2} \qquad \textit{Equation 3.5}$$

where $\omega_{1\to2}^{eco}$ is the economical engine speed of up-shifting to the lowest gear, C is a constant with a value of 1.15 applied in this study, k_1 and k_2 are the 1st and the 2nd gear ratios respectively.

$$\omega_{N-1\to N}^{eco} = \omega_{\max\_eff} \qquad \textit{Equation 3.6}$$

where $\omega_{N-1\to N}^{eco}$ is the economical engine speed of up-shifting to the highest gear, $\omega_{\max\_eff}$ is the engine speed at best efficiency point.

$$\omega_{N\to N-1}^{eco} = \omega_{N-1\to N}^{eco} - 100 \qquad \textit{Equation 3.7}$$

where $\omega_{N\to N-1}^{eco}$ is the economical engine speed of down-shifting from the highest gear.

The engine down-shifting speeds from 2nd to 1st and from *N* to *N-1* are used to calculate the intermediate engine down-shifting speeds, which is defined by Equation 3.8 [86].

$$\omega_{i+1\to i}^{eco} = \frac{\omega_{N\to N-1}^{eco} - \omega_{2\to1}^{eco}}{N-2} * (i-1) + \omega_{2\to1}^{eco}, \quad 1 \le i \le N-1 \qquad \textit{Equation 3.8 [86]}$$

Correspondingly, the down-shifting vehicle speeds can be calculated using the engine down-shifting speed, the wheel radius, the gear ratio and the final drive ratio.

$$V_{i+1\to i}^{eco} = \frac{\omega_{i+1\to i}^{eco}}{k_{i+1} * k_{fd}} * R_{wh} \quad 1 \le i \le N-1 \qquad \textit{Equation 3.9 [86]}$$

where k_i is the k^{th} gear ratio, and k_{fd} is the final drive ratio.

Likewise, the intermediate up-shifting engine speeds and vehicle speeds are defined by Equations 3.10-3.11 [86].

$$\omega_{i\to i+1}^{eco} = \frac{\omega_{N-1\to N}^{eco} - \omega_{1\to 2}^{eco}}{N-2} * (i-1) + \omega_{1\to 2}^{eco}, \quad 1 \le i \le N-1 \qquad \textit{Equation 3.10 [86]}$$

$$V_{i\to i+1}^{eco} = \frac{\omega_{i\to i+1}^{eco}}{k_i * k_{fd}} * R_{wheel} \quad 1 \le i \le N-1 \qquad \textit{Equation 3.11 [86]}$$

3.2.3.2. Performance Shifting Speed

The performance up-shifting speed occurs at the maximum accelerator pedal positions (the maximum accelerator pedal position at each speed) and outputs the maximal torque at the wheels. The difference between performance up-shifting and down-shifting speeds is related to the difference of vehicle economical performance up-shifting and down-shifting speeds [86]:

$$\begin{cases} \Delta V_i^{eco} = V_{i\to i+1}^{eco} - V_{i+1\to i}^{eco} \\ \Delta V_i^{perfo} = V_{i\to i+1}^{perfo} - V_{i+1\to i}^{perfo} \\ \Delta V_i^{perfo} = r_{acc1} / r_{acc0} * \Delta V_i^{eco} \end{cases}, \quad 1 \le i \le N-1 \qquad \textit{Equation 3.12 [86]}$$

where ΔV_i^{eco} is the difference of vehicle economical up- and down-shifting speeds, ΔV_i^{perfo} is the difference of vehicle performance up- and down-shifting speeds, r_{acc1} / r_{acc0} is the vehicle speed difference between up-and down-shifting speed at maximum accelerator pedal position and the one at zero accelerator pedal position.

The down-shifting speeds can be found as described below.

$$V_{i+1\to i}^{perfo} = V_{i\to i+1}^{perfo} - r_{acc1} / r_{acc0} * (V_{i\to i+1}^{eco} - V_{i+1\to i}^{eco}), \quad 1 \le i \le N-1 \qquad \textit{Equation 3.13 [86]}$$

3.2.3.3. Shifting curve and map

After the economical and performance shifting speeds are computed, the shifting strategy can be defined. Figure 3.4 shows the up-and down-shifting curves for a 5-speed transmission [86]. It should be noted that the 5-speed transmission here is a demonstration for the up-and down-shifting curves of a control strategy and it is designed for light-duty vehicles.

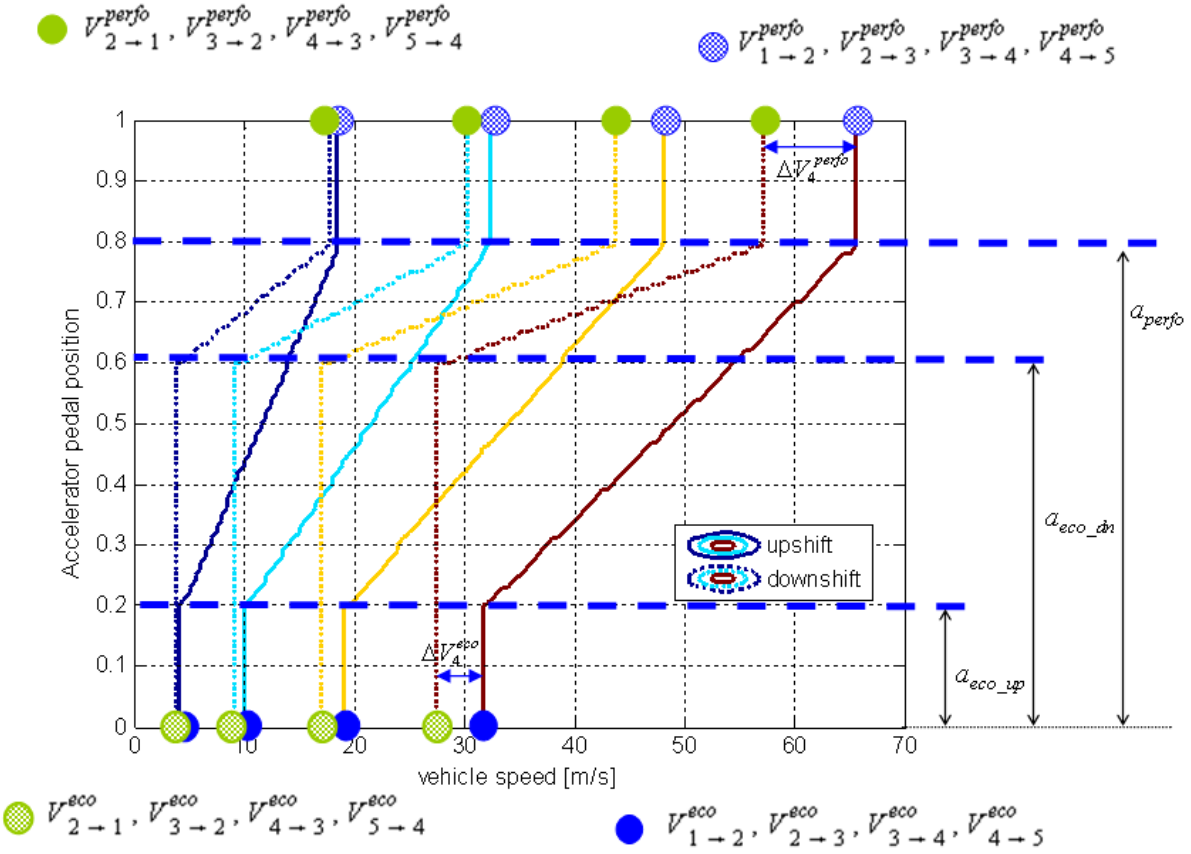

Figure 3.4: Up-and down-shifting curves for a 5-speed transmission [86]

The up-shifting strategy is defined in this manner: For accelerator pedal positions below a_{eco_up}, the up-shifting speed is the economical up-shifting speed. The up-shifting speed is the performance up-shifting speed when the accelerator pedal position is above a_{perfo}. The up-shifting speed is a linear interpolation of economical and performance up-shifting speeds for the accelerator pedal position between these two values [86].

Likewise, the down-shifting strategy is defined as follows: For accelerator pedal positions below a_{eco_dn}, the down-shifting speed is the economical down-shifting speed. The down-shifting speed is the performance down-shifting speed when the accelerator pedal position is above a_{perfo}. The

down-shifting speed is found by linear interpolation of economical and performance down-shifting speed for accelerator pedal position between these two values [86].

3.2.3.4. Shifting Logic and Steps

This shifting strategy model only outputs one parameter, the desired gear. The driver model initiates a gear up-shift when [86]: the up-shifting map outputs a gear that is higher than the current one and the engine speed at the higher gear is higher than the minimum acceptable engine speed or the current engine speed is higher than the maximum acceptable engine speed. The driver model initiates a gear down-shift when [86]: the down-shifting map outputs a gear that is lower than the current one and the engine speed at the lower gear is higher than the maximum acceptable engine speed or the current engine speed is lower than the minimum acceptable engine speed. A 1.5 seconds was applied in this research for each shifting.

After the shifting strategy is used to decide to shift gears with a manual transmission, up-shifting or down-shifting steps happen successively, shown in Figures 3.5 and 3.6.

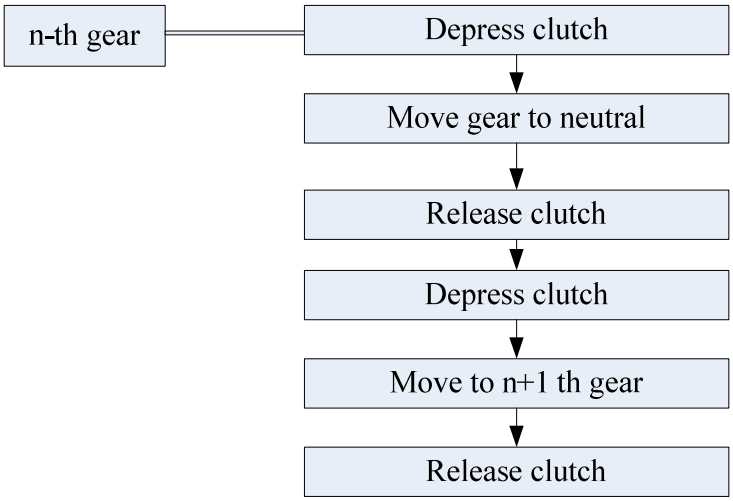

Figure 3.5: Up-shifting steps

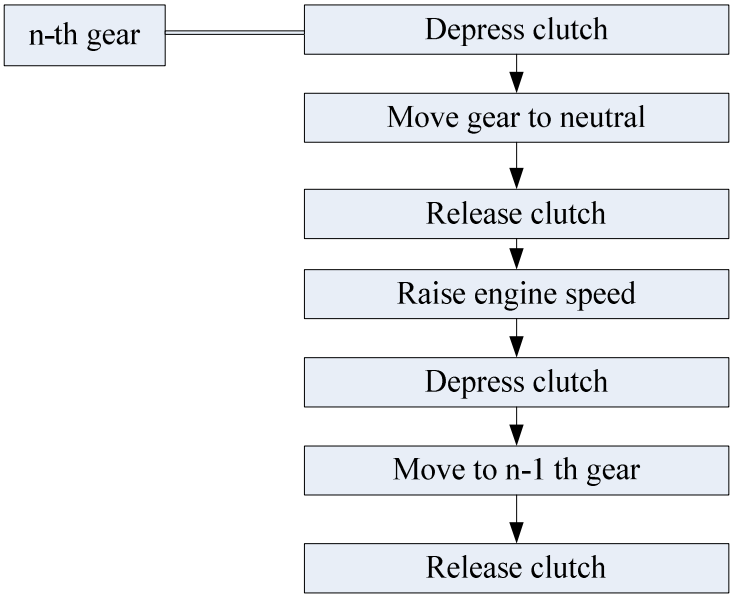

Figure 3.6: Down-shifting steps

3.3. Component Controller Model

The function of the component controller model is to transform the commands from the PTCM to the commands that can be used by the respective component models. For instance, the component controller model transforms engine torque from the PTCM to the throttle and sends it to the engine model and the output of engine power is used to propel the vehicle wheels.

3.4. Powertrain (Component) Model

Each powertrain model includes three parts: a constraint block which defines the components within the physical limits (for instance, the maximum engine torque at current speed), a signal conditioning block which sends commands to the component controller model and a component block which models the physics of the system [82].

To provide multiple options for the component model libraries, a generic format is designed for the input and output of the power ports by using the Bond Graph approach [87, 88]. There are 3 input ports and 3 output ports in this format model, as shown in Figure 3.7.

The input ports are used for the following information:

- Accept command (on/off engine, gear number) from PTCM
- Accept torque from upstream components
- Accept speed from downstream component

The output ports are used for the following information:

- Send component command (torque, rotational speed) to PTCM
- Send torque to downstream component
- Send speed to upstream component

It should be noticed that the first input and output ports are vectors and can be any size.

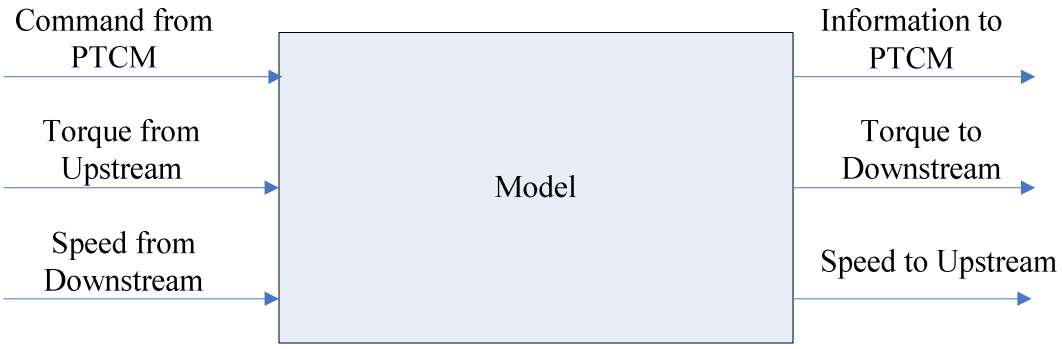

Figure 3.7: Schematic of the component model

The main components of the powertrain model (engine, mechanical accessories and transmission) will be discussed in the next chapter.

3.5. Summary

This section provides an overview of the PSAT program. Four sub-systems were included in the PSAT vehicle model: the driver, the powertrain controller, the component controller and the powertrain model. The driver model followed the driving cycle and sent torque demands to the vehicle controller by using a PI controller to estimate the torque at the wheels. The powertrain controller worked as the brain of the vehicle by processing commands from the driver and feedback signals from different components. The powertrain controller model consisted of three blocks: propulsion, braking and shifting strategy. Each block was reviewed, with an emphasis on shifting strategy. The commands from the powertrain controller model were transformed to commands that could be used by the respective components in the component controller model. The powertrain model provided a generic format of each component.

Chapter 4: Main Components of the Peterbilt Truck and Engine Emissions Model

4.1. The Peterbilt Truck Test Information

The heavy-duty vehicle used in this research was a Peterbilt truck, which was a conventional over-the-road tractor, with a non-EGR 550 hp (410 kW) 1996 Caterpillar 3406E engine, 18-speed Roadranger manual transmission and Peterbilt 379EXHD tandem axle drive. A test was performed at the WVU Transportable Heavy-duty Vehicle Emission Testing Laboratory in April 2006. The vehicle was operated over the UDDS on the chassis dynamometer to provide continuous emissions as well as engine speed and engine percent load data. Figure 4.1 shows the Peterbilt truck that was used in this study [16]. The drivetrain configuration used for the Peterbilt truck is shown in Figure 4.2. Detailed information about vehicle can be found in Table 4.1 [16].

Figure 4.1: Peterbilt truck

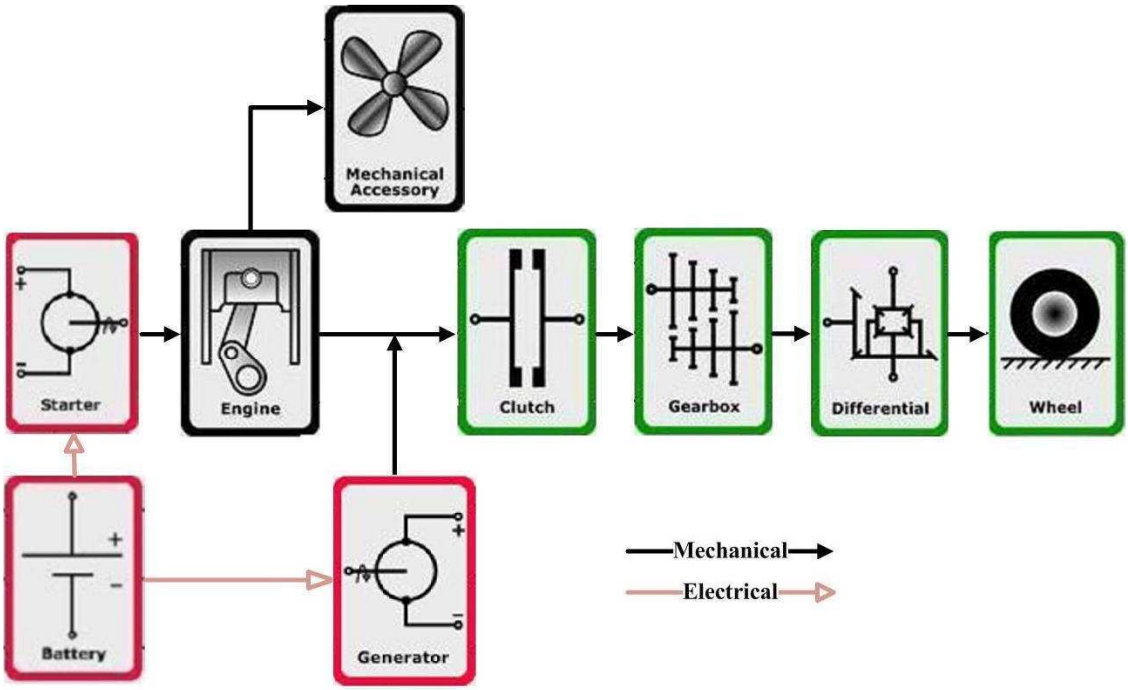

Figure 4.2: The Peterbilt truck drivertrain configuration in PSAT

Table 4.1: Details of the Peterbilt truck information

WVU Test Reference Number	WVU-Peterbilt-D2-TEST_D
Vehicle Type	Tractor
Vehicle Manufacturer	Peterbilt
Vehicle Model Year	1996
Vehicle Tested Weight (lb)	56,000
Odometer Reading (mile)	Started from 441,097
Transmission Type	18-Speed Manual Transmission
Final Drive Ratio	3.55
Tire Size	305/70R22.5
Coefficient of Rolling Resistance	0.00938
Coefficient of Aerodynamic	0.79
Engine Type	Caterpillar 3406E
Engine Model Year	1996
Engine Displacement (liter)	14.6
Number of Cylinders	6
Primary Fuel	Type 2 Diesel
Test Cycle	UDDS (also termed TEST_D)
Test Date	4/21/06

4.2. Engine Model

The engine used in this study was a Caterpillar 3406E. The engine model in PSAT includes three blocks: engine torque calculation, engine fuel rate calculation and engine emissions calculation. Figure 4.3 shows the general Simulink diagram of the engine model [16].

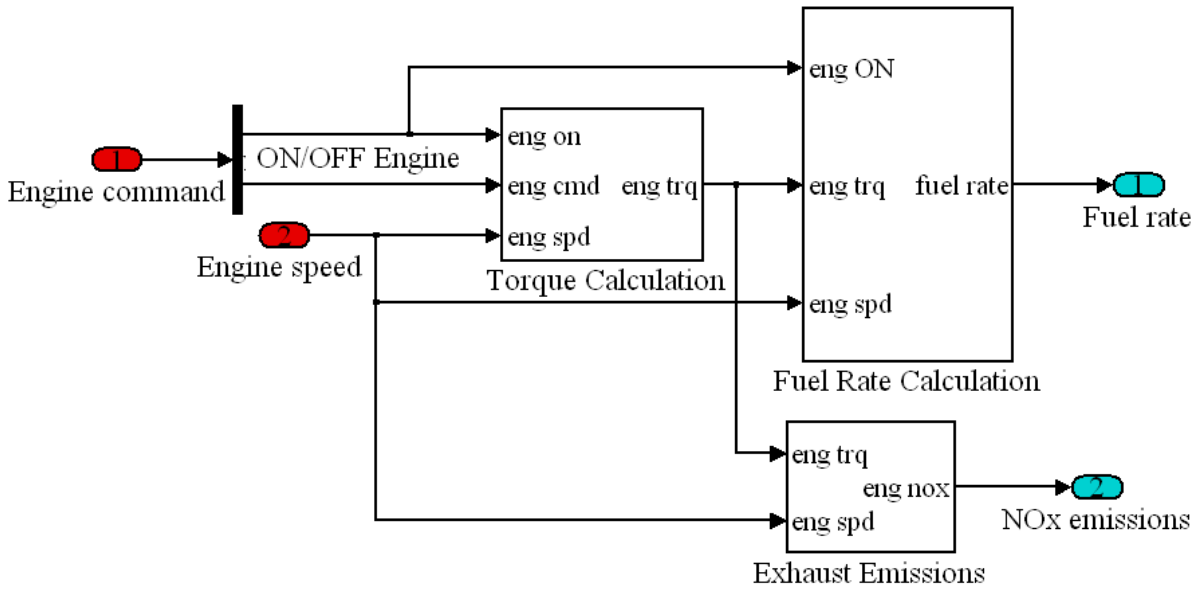

Figure 4.3: General Simulink diagram of the engine model in PSAT

4.2.1. Calculations of Engine Torque

Figure 4.4 shows the plot of the maximum and minimum torque of Caterpillar 3406E engine. The lower boundary refers to the case in which the fuel consumption is zero. The engine torque was calculated by interpolating between the maximum and minimum torque curves (the curve when the accelerator pedal position is zero). Equations 4.1 [85] show the calculations of engine torque.

$$T_{out} = \begin{cases} (1 - T_{cmd}) * T_{e\_\min} + T_{cmd} * T_{e\_\max}, & T_{cmd} >= 0 \,\&\, \omega_e > 0 \\ 0, & Otherwise \end{cases} \qquad \textit{Equation 4.1[85]}$$

where T_{out} is the output of engine torque, T_{cmd} is the engine command with value range [0 1], $T_{e\_\min}$ is the minimum torque curve, $T_{e\_\max}$ is the wide open the maximum torque curve, and ω_e is engine speed. Note that there may still be finite fueling when torque is less than zero (-50 ft-lb for the Caterpillar 3406E engine).

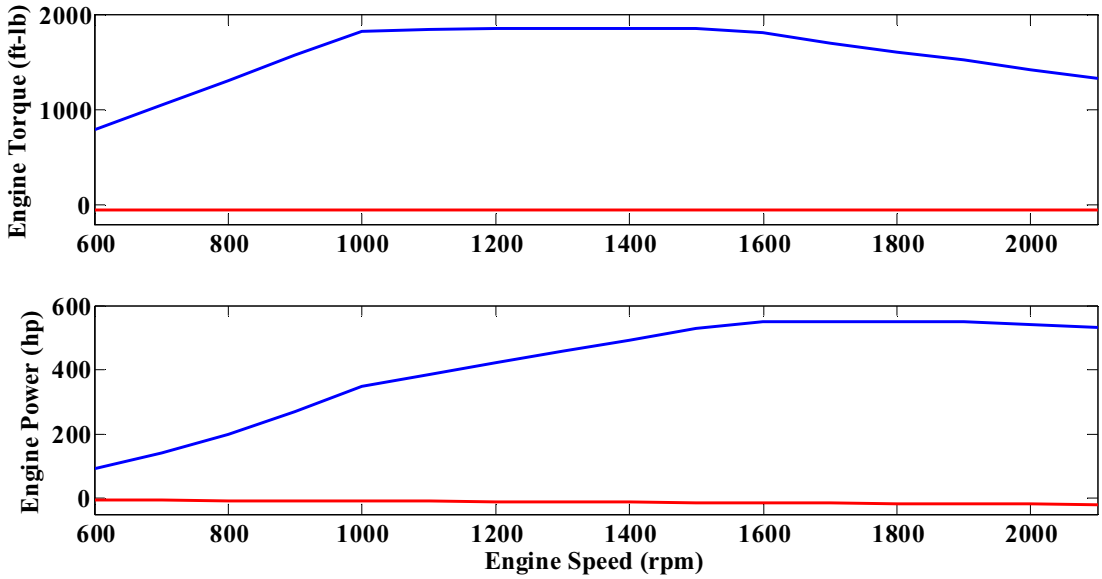

Figure 4.4: Plot of the maximum and minimum torque and power of the Caterpillar 3406E engine

4.2.2. Calculations of Engine Fuel Rate

The engine fuel rate was estimated by using a lookup table, which was a fuel rate matrix described in terms of engine torque and engine speed. The experimental Engine speed, engine percent load and engine fuel rate were all engine control unit (ECU) broadcasted data. The engine torque was the product of the broadcasted engine percent load and the maximum torque at a certain speed. The cumulative FC was obtained from scale measurements. The fuel rate matrix used in the PSAT initialization file was built based on the test data (fuel rate was interpolated at regions where no test data was available). Figure 4.5 shows the engine fuel rate map based on the data collected with the Peterbilt truck operating on the UDDS. In order to eliminate high frequency transient behavior for the fuel rate, a 5-second average window was applied. Transient behavior of non-EGR engines has little effect on fuel efficiency or brake specific NO_x. The newer engines with a variable geometry turbocharger, exhibit much higher dependence on the transient nature of the operation [47].

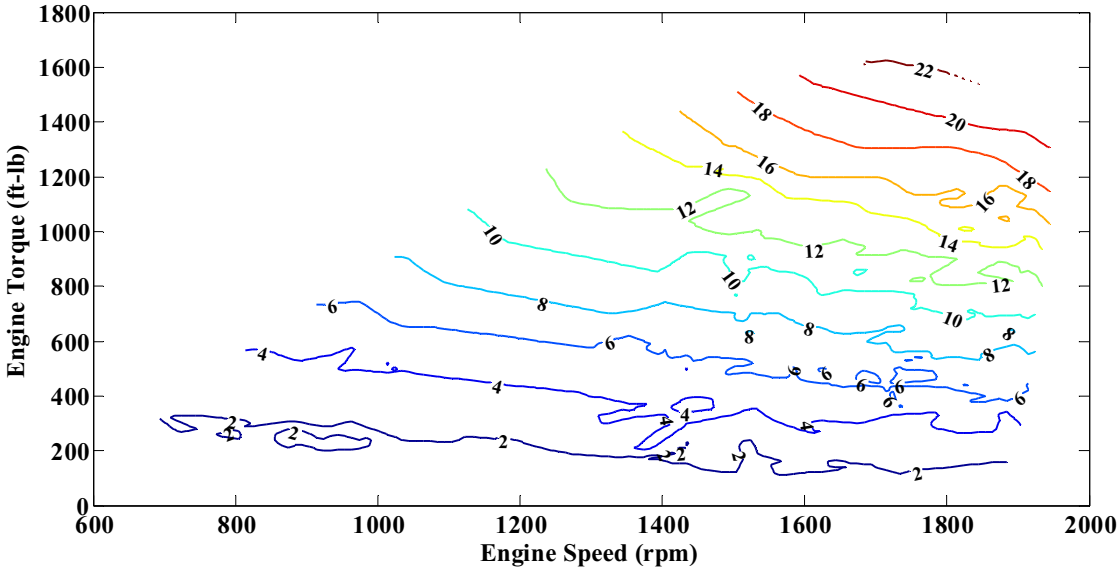

Figure 4.5: Caterpillar 3406E engine fuel rate (g/sec) operating on the UDDS

4.2.3. NO_x Emissions Model

The main emissions that are produced from a diesel engine include CO, CO_2, NOx, HC and PM are all regulated by the EPA [4, 89-91] as they all have negative effects on people or the environment. Of all the harmful emissions emitted from engines, legislation has focused on NO_x and PM because of their potential to endanger people and their contributions to emission inventories. The factors that influence emissions were addressed in the literature [47-48, 92-93]. The main goal of this section was to develop a NO_x emissions prediction model that took emissions as a function of engine power, engine torque, engine speed and their time derivatives.

4.2.3.1. Laboratory Description and Emissions Data Collection

West Virginia University currently possesses one WVU Transportable Heavy-duty Vehicle Emission Testing Laboratory and one Engine Emissions Laboratory which are capable of running transient and steady state testing on either heavy duty vehicles or engines [44, 94]. Detailed information about the design and operation of the laboratories has been discussed in technical papers [55, 95-98].

The WVU Transportable Heavy-duty Vehicle Emission Testing Laboratory collects emissions data from the vehicle while simulating the road condition without removing the engine from the vehicle [44]. The major components include a chassis dynamometer test bed, power absorber, flywheel, analyzer for emission gases and dilution tunnel. The dynamometer test bed is used for heavy duty vehicles driven on it to simulate the actual driving speed. A human driver operates the vehicle though the drive cycles. The aerodynamic drag and rolling resistance are simulated by the power absorber. Flywheels are used to mimic the vehicle weight and rotational inertia. To

analyze the emission constituents, the exhaust gas is channeled from the vehicle's exhaust system to a dilution tunnel where it is mixed with fresh air. The analyzers measure the exhaust gas that comes from the dilution tunnel. NO_x concentrations are measured using a chemiluminescent detector. CO and CO_2 concentrations are measured using non-dispersive infrared analyzers and HC concentrations are measured with a heated flame ionization detector [99]. Particulate matter (PM) is measured by a gravimetric approach.

4.2.3.2. Time Alignment

The gases traveling through the tunnel and the response of analyzers take time, so there was a time delay between the point in time when the engine operated and the point in time when the emissions related to that operating condition were measured [99]. However, the time delay caused by the response of analyzers was larger than other factors [44]. To compensate for the delay time, the emissions data should be time aligned with the engine operating variables (such as power, speed, and torque) [100, 101]. In general, the NO_x emissions correlate closely with engine power. The best result achieved for time alignment was obtained by performing a cross-correlation method between the NO_x emissions and the engine power [44, 102-104]. The time delays of emissions from the Peterbilt truck were found to be 14 seconds for CO_2 and 12 seconds for NO_x, which indicated there were different time delays among the different emission gases. This was due to the fact that different analyzers have different response times [44]. Figures 4.6-4.7 show the relationship between NO_x and engine power with and without time alignment. These data were collected from the Peterbilt truck with the Caterpillar 3406E engine operating on the UDDS. The two figures demonstrate that after time alignment the NO_x data are much less scattered and the coefficient of determination (R^2) between NO_x and power is much better than before time alignment, so it was important to perform the time shift before analyzing the data.

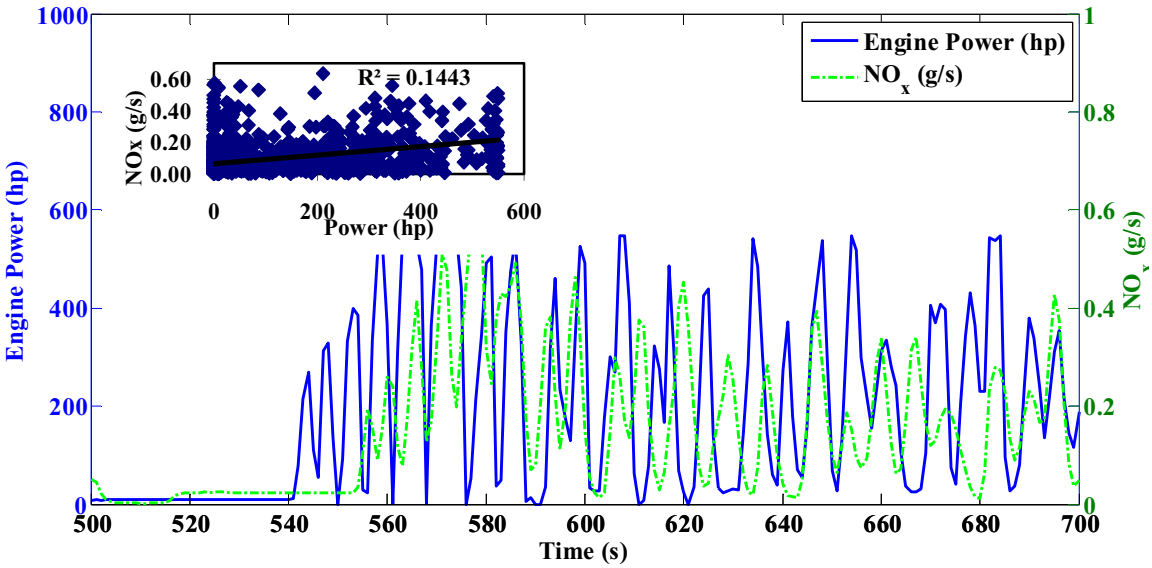

Figure 4.6: NO_x and engine power as a function of time before time alignment for the Peterbilt truck with a Caterpillar 3406E engine operating over the UDDS cycle

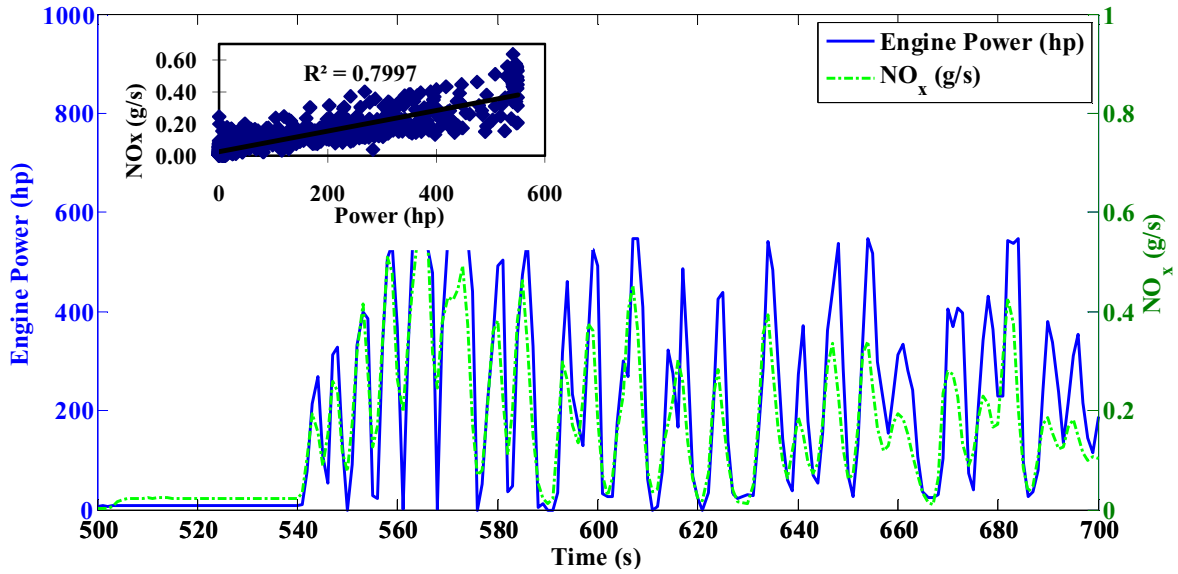

Figure 4.7: NO_x and engine power as a function of time after time alignment for the Peterbilt truck with a Caterpillar 3406E engine operating on a UDDS cycle

4.2.3.3. Dispersion and Reverse Transform

Apart from the time delay, the signal responses can also be distorted and spread over a period of time when measured by the analyzer. In other words, the measured signals were dispersed in

time with the amplitude of a peak smaller than what was actually experienced by the engine [99]. Even though the exhaust gas traveled through the dilution tunnel before it entered the analyzers, the majority of the dispersion was known to occur in the analyzer [99, 104]. Hence, the dispersion in the tunnel was negligible compared to the dispersion that resulted from the analyzer. The data collected by the analyzers were dispersed and do not represent the real instantaneous emissions. Different methods of reconstructing the instantaneous emissions signal from the measured signal were presented in the literature [44, 99, 105-106]. By compensating for the dispersion, the measured emissions data needed to be backwards transformed. Atjay and Weilenmann [106] developed the differential coefficients method (DCM) which reconstructed the true emission signal by reversely transforming the measured emissions. The DCM approach defined the real instantaneous data (before traveling to the analyzer) as a linear combination of the outputs (of the analyzer) and their first and second derivatives, shown in Equation 4.2 [106].

$$U(t) = Y(t) + a_1 * Y'(t) + a_2 * Y''(t) \qquad \textit{Equation 4.2 [106]}$$

where *U(t)* is the unknown input to the analyzer, *Y(t)* are the measured emission data (outputs of the analyzer) and $Y'(t)$ and $Y''(t)$ are its first and second derivatives, a_1 and a_2 are the coefficients of the linear combination. Equation 4.2 is based on a constraint that the integrated inputs are the same as the outputs over the duration of the observation [99]. The dispersion function proposed by Ramamurthy and Clark [93] is shown in Figure 4.8, which demonstrates the NO_x analyzer response to an instantaneous one second pulse signal. Note that different analyzers may differ in response.

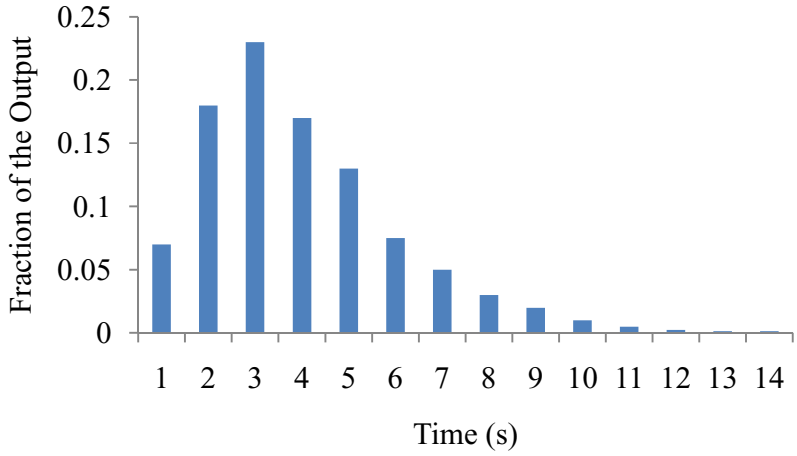

Figure 4.8: Analyzer response to a one second pulse
[93]

After the dispersion function is determined, the coefficients a_1 and a_2 in Equation 4.3 can be computed by applying the least-square method in Equation 4.3.

$$1 = x + a_1 * x' + a_2 * x'' \qquad \textit{Equation 4.3}$$

where x is the dispersion function of the analyzer, x' and x'' are its derivatives. The coefficients can be found by minimizing the least-square method and then using it to compute the inputs *U(t)* of the analyzer, defined in Equation 4.2. The reconstructed NO_x versus power is shown in Figure 4.9. The power was better correlated with the reconstructed NOx (R^2 of 0.86) than with the original measured NOx (R^2 of 0.80, Figure 4.7).

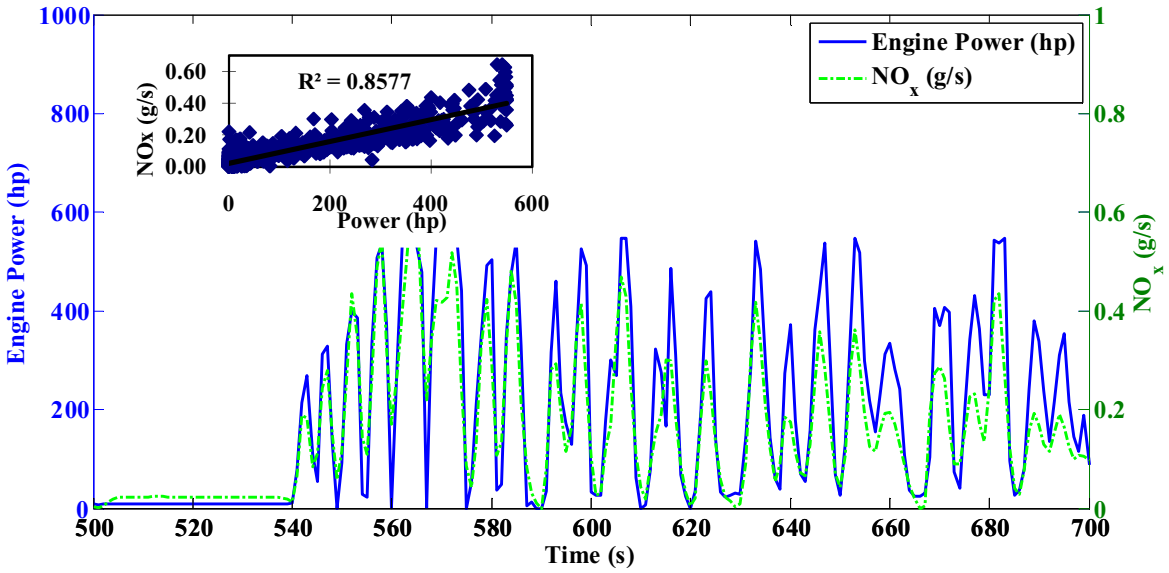

Figure 4.9: NO_x and engine power as a function of time after compensating the time delay and dispersion for the Peterbilt truck with a Caterpillar 3406E engine operating over the UDDS

4.2.3.4. NO_x Emissions Model-LR Method

After the data processing work of the time alignment and the backward transform, the emissions are ready to be modeled. NO_x emissions are closely related to engine power, engine torque and engine speed [47-48, 93]. Since the transient behavior also affects the emissions, their derivatives should also be included in the predictive emissions model. The predictive emissions are expressed as the real-time mass rate of emissions which are a function of engine power, speed, torque and their derivatives in a LR method [48] (Equation 4.4).

$$NO_{x\,\mathrm{Pre}} = a*P + b*\frac{dP}{dt} + c*T + d*\frac{dT}{dt} + e*\omega + f*\frac{d\omega}{dt} + g \qquad \textit{Equation 4.4}$$

where P is the engine power and T and ω are engine torque and engine speed respectively. The measured NO_x is used to train this linear model. The parameters *a, b, c, d, e, f* and *g* are constant coefficients with unit of g/hp-s, g/hp, g/ft-lb-s, g/ft-lb, g/s-rpm, g/rpm and g/s respectively. The constant coefficients are estimated by performing the least square method (Equation 4.5a-4.5b) [41, 42]. In matrix form the output Y is given by:

$$Y = P\alpha \qquad \textit{Equation 4.5a}$$

where Y is the dependent variable, in this case NO_x emissions.

$$P=\begin{bmatrix} P_1 & dP_1/dt & T_1 & dT_1/dt & \omega_1 & d\omega_1/dt & 1 \\ P_2 & dP_2/dt & T_2 & dT_2/dt & \omega_2 & d\omega_2/dt & 1 \\ \vdots & \vdots & \vdots & \vdots & \vdots & \vdots & \vdots \\ P_n & dP_n/dt & T_n & dT_n/dt & \omega_n & d\omega_n/dt & 1 \end{bmatrix}$$ and α is the vector of the constant coefficients.

By minimizing $\|Y - P\alpha\|^2$, the coefficients are estimated, which is given as:

$$\alpha = \left(P^T P\right)^{-1} P^T Y \qquad \textit{Equation 4.5b}$$

Once the coefficients are estimated, the predicted emissions data could be calculated by using Equation 4.4. The criteria used to evaluate the goodness of fit between the measured and predicted are the square of correlation coefficients (R^2) and the root mean square error (RMSE) defined in Equations 4.6-4.7 [47].

$$R^2 = \left(\frac{\sum_{i=1}^{N} (y_i - \bar{y})(\hat{y}_i - \bar{\hat{y}})}{(n-1) s_y s_{\hat{y}}} \right)^2 \qquad \textit{Equation 4.6 [47]}$$

$$RMSE = \sqrt{\frac{1}{n} \sum_{i=1}^{n} (\hat{y}_i - y_i)^2} \qquad \textit{Equation 4.7 [47]}$$

where y_i and $\hat{y}_i$ are measured and predicted emission data respectively, $\bar{y}$ and $\bar{\hat{y}}$ are their sample mean, s_y and $s_{\hat{y}}$ are their standard deviations respectively, and n is the number of measured data. The data used to illustrate the predictive emissions model were collected from two buses other than the Peterbilt truck because of a large quantity of experimental data available for these two buses over various cycles. The first bus was a 40 foot long 2005 MY Gllig transit bus, powered by a Cummins ISL 280 engine and operated over the UDDS, OCTA, Manhattan and Houston cycles. This bus was owned by LYNX Central Florida Regional Transportation Authority (abbreviated to LYNX transit bus) [107]. The test weight of the LYNX transit bus was 33,295 lb. Each schedule was considered as a training cycle and the other three cycles as testing cycles. By comparing the training and testing results, a representative training cycle can be chosen. Table 4.2 shows the summary of training and testing performance for NO_x emissions. The performance results indicate that there was not much difference when varying the training and testing cycles, which implies that the NO_x data can be translated among the four cycles. This was because each of the four schedules contains a variety of driving characteristics, such as accelerating, idling and decelerating. In this study, the UDDS was chosen as the training schedule and the other three were used as the testing schedules. The linear predictive emissions model was also applied in predicting an HEV, which was a 2007 MY New Flyer bus with an ISE hybrid system (abbreviated to ISE hybrid bus), powered by a Cummins ISB260H engine and operated on the same four schedules. The test weight of the ISE hybrid bus was 36,070 lb. Table 4.3 summarizes

the training and testing performance of the predictive NO_x emissions model for the ISE hybrid system bus. It is obvious that the performance of the predictive NO_x emissions model for the ISE hybrid system bus is better than that of the LYNX transit bus, which is due to the fact that the engine of the ISE hybrid system bus operates at an optimum performance range and is less transient for most of the time. Figures 4.10-4.11 depict the engine speed versus the derivative of engine speed and engine torque versus of the derivative of the engine torque over the UDDS. It can be seen that the engine in the hybrid bus was less transient than the engine in the LYNX conventional city transit bus.

The comparison and parity plots of the measured NO_x and predicted NO_x of the LYNX 2005 city transit bus using LR method from the training data of the UDDS and the testing data of the OCTA, Manhattan and Houston are shown in Appendix B1-B4 (A segment of time of the comparison plots are selected for better view). It should be noted that in all the parity plots in Appendix B1-B4, none of the predicted values of NO_x emissions was zero whereas measured NO_x was observed at zero when the vehicle was decelerating. This is because the torque was computed from broadcast engine percent load which was between 0 and 100 percent. In reality, the torque was negative when the vehicle goes downhill and the deceleration is large enough, whereas it was not broadcasting negative torque values in this study. Therefore, the data used to construct the predictive model were not entirely accurate. The result of this condition was that the predicted NO_x emissions were never zero. The comparison and parity plots of the measured NO_x and predicted NO_x of the New Flyer ISE hybrid system bus using LR method from the training data of the UDDS and the testing data of the OCTA, Manhattan and the Houston cycles are shown in Appendix B5-B8.

Table 4.2: Training and testing performance of NO_x emissions of a LYNX transit bus using the LR method

Testing \ Training		UDDS	OCTA	Manhattan	Houston
UDDS	**R^2**	**0.8047**	0.7967	0.8019	0.7986
	RMSE	**0.0218**	0.0227	0.0222	0.0227
OCTA	**R^2**	0.8275	**0.8388**	0.8199	0.8355
	RMSE	0.0190	**0.0179**	0.0200	0.0198
Manhattan	**R^2**	0.8467	0.8315	**0.8488**	0.8379
	RMSE	0.0152	0.0167	**0.0148**	0.0154
Houston	**R^2**	0.8242	0.8273	0.8198	**0.8303**
	RMSE	0.0164	0.0172	0.0162	**0.0156**

Table 4.3: Training and testing performance of NO_x emissions of an ISE hybrid bus using the LR method

Testing \ Training		UDDS	OCTA	Manhattan	Houston
UDDS	**R^2**	**0.9664**	0.9605	0.9418	0.9612
	RMSE	**0.0063**	0.0070	0.0090	0.0070
OCTA	**R^2**	0.9405	**0.9470**	0.9252	0.9468
	RMSE	0.0066	**0.0061**	0.0072	0.0061
Manhattan	**R^2**	0.9057	0.9097	**0.9208**	0.9109
	RMSE	0.0081	0.0077	**0.0071**	0.0076
Houston	**R^2**	0.9478	0.9530	0.9396	**0.9531**
	RMSE	0.0063	0.0059	0.0066	**0.0058**

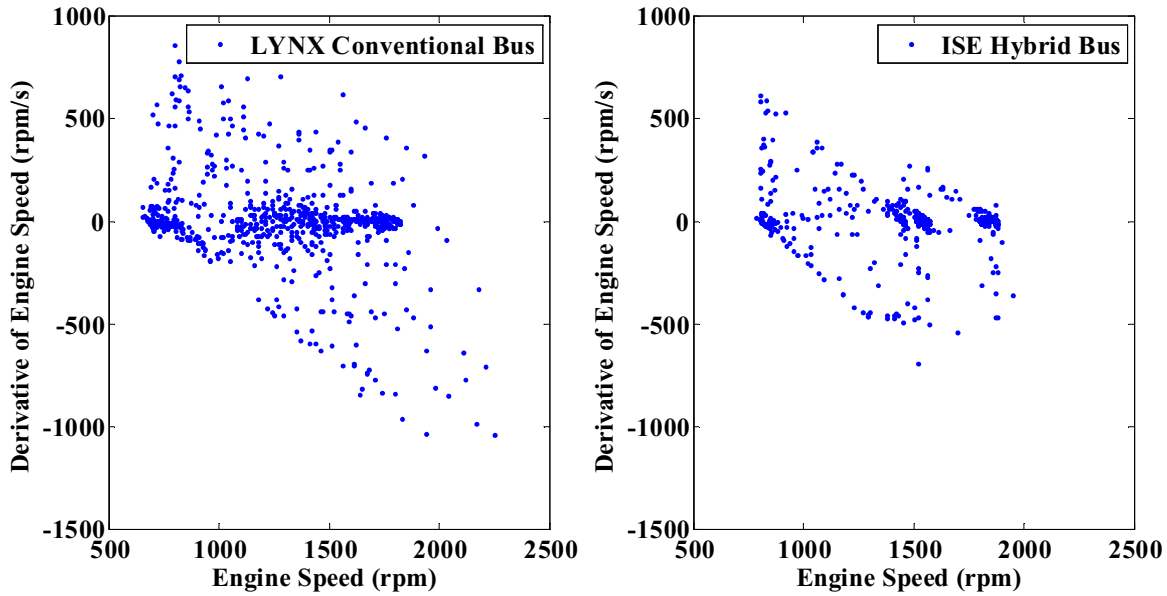

Figure 4.10: Engine speed versus derivative of the engine speed over the UDDS

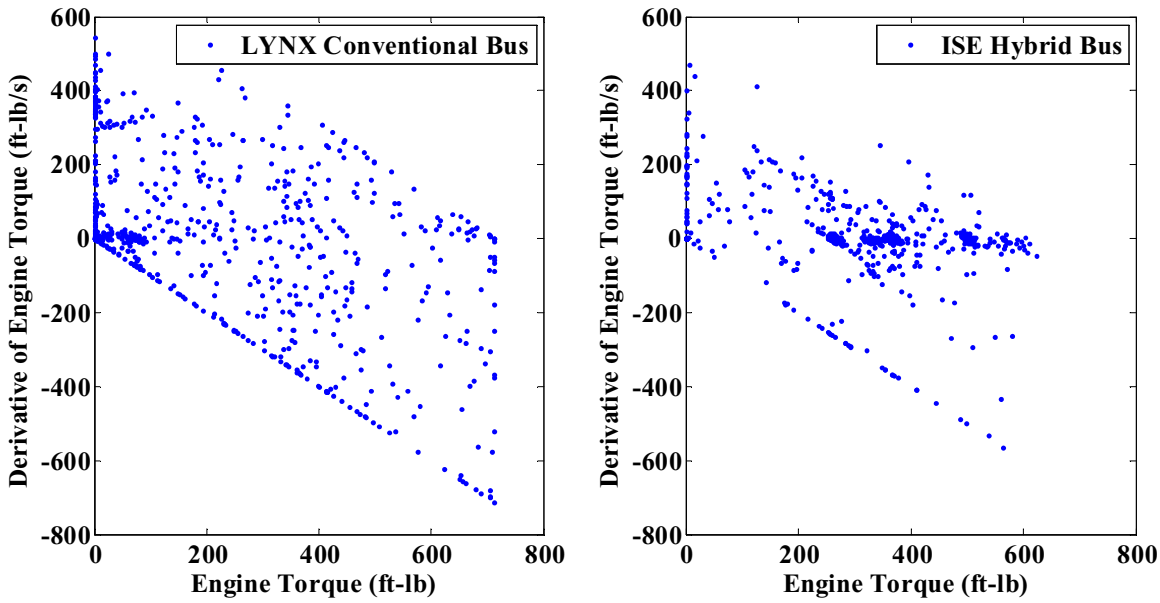

Figure 4.11: Engine torque versus derivative of the engine torque over the UDDS

4.2.3.5. NO_x Emissions Model-ANN Method

A NO_x predictive emissions model was also developed using the ANN approach. This approach to model emissions has been discussed in previous literature [45, 52-53, 56, 59, 92]. Historically, multiple parameters like engine speed, coolant temperature, oil temperature, exhaust temperature, intake air temperature, intake air pressure and accelerator position were chosen as input variables. By using these variables, the emissions of CO_2, CO, NO_x, HC were predicted within 5% error over different cycles [55, 56]. However, the intent of this NO_x predictive emissions model is to incorporate it into PSAT, so the engine power, engine torque, engine speed and their derivatives were chosen as inputs because of the constraint on PSAT vehicle model in this study.

The ANN model utilized the generalized regression neural network (GRNN) [108,109] which includes a radial basis function (RBF) layer and a linear layer to achieve the emissions prediction. A RBF neuron with R inputs is shown in Figure 4.12. The vector distance $//dist//$ is the dot products of input vector X and the input weight matrix. The input to the transfer function is the sum of weighted inputs and the scalar bias b [110]. The input to the i^{th} neuron can be expressed by Equation 4.8 [108].

$$n_i = \sum_i w_i * \rho(\| x - x_i \|) \qquad \textit{Equation 4.8 [108]}$$

where w_i is the weight of the linear output neuron, x_i is the center vector for neuron i, ρ is the basis functions which is described by ||dist||, the distance between input vector x and training

pattern x_i, and b_i is the bias, Correspondingly, the output to the transfer function for a radial basis neuron is shown in Equation 4.9 [108].

$$radbas(n_i) = \exp(-n_i^2) = \exp(-(\sum_i w_i * \rho(\| x - x_i \|))^2) \qquad \textit{Equation 4.9 [108]}$$

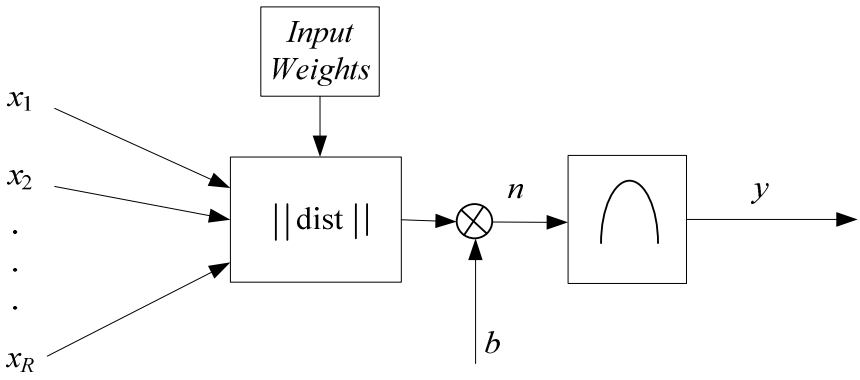

Figure 4.12: The RBF neuron architecture
[110]

GRNN consists of two layers: a hidden radial basis neuron layer and an output linear neuron layer. A diagram representing this architecture is shown in Figure 4.13 [111]. The output of the first layer, the radial basis neuron, serves as the input to the linear layer. The values in the *nprod* box (Figure 4.13) are inputs of the linear transfer function [92], calculated by the dot product of the outputs of the first layer and the output weights.

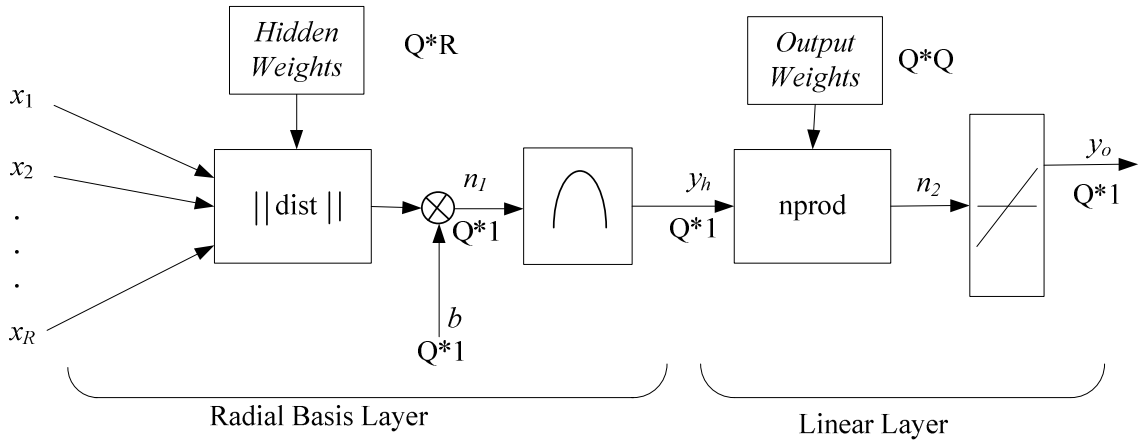

Figure 4.13: The GRNN architecture
[111]

In Matlab, the syntax of GRNN is given by [111]:

net = newgrnn(P,T,spread) *Equation 4.10*

where P is input vector, T is target vectors, and spread is the spread of RBF. All the input and target vectors were normalized before the training work. Consequently, the prediction data were also normalized and need to be de-normalized back. The normalization in this study was defined by:

$$y = x_i / x_{\max} \qquad \textit{Equation 4.11}$$

where y is the normalized inputs and targets, which all fall in the interval [-1, 1]. The value of the spread was varied during model development, with 0.1 providing the best match with target values.

Tables 4.4 and 4.5 summarize training and testing performance for NO_x emissions using the ANN for the LYNX city transit bus and the ISE HEB. The difference in performance when using the ANN to predict NO_x emissions compared to the LR method is relatively small. For both the ANN and the LR method, the predicted results are better for the ISE HEB than they are for the LYNX city transit bus. The comparison and parity plots of the measured and predicted NO_x of the LYNX 2005 city transit bus using the LR method from the training data of the UDDS and the testing data of the OCTA, Manhattan and the Houston cycles are shown in Appendix C1-C4. The comparison and parity plots of the measured and predicted NO_x of the ISE hybrid 2007 MY bus using LR method from the training data of the UDDS and the testing data of the OCTA, Manhattan and the Houston cycles are shown in Appendix C5-C8. Note that in all the parity plots in Appendix C5-C8, none of the predicted values of NO_x emissions is zero whereas measured NO_x was observed at zero when the vehicle was decelerating. This is due to the fact that the torque was computed from broadcasted engine percent load which was between 0 and 100 percent such that no negative torque was attained. In reality, the torque was negative when decelerating. Therefore the torque used to construct the predictive model did not entirely represent the real torque, which caused the predicted NO_x emissions to never be zero.

Table 4.4: Training and testing performance of NO_x emissions of a LYNX city transit bus using the ANN method

Testing \ Training		UDDS	OCTA	Manhattan	Houston
UDDS	**R^2**	**0.8938**	0.7942	0.7909	0.7865
	RMSE	**0.0162**	0.0226	0.0229	0.0230
OCTA	**R^2**	0.8128	**0.8791**	0.8120	0.8338
	RMSE	0.0210	**0.0158**	0.0216	0.0198
Manhattan	**R^2**	0.8261	0.8443	**0.8974**	0.8521
	RMSE	0.0161	0.0153	**0.0124**	0.0147
Houston	**R^2**	0.7857	0.8178	0.8021	**0.8629**
	RMSE	0.0178	0.0163	0.0171	**0.0142**

Table 4.5: Training and testing performance of NO_x emissions of an ISE hybrid bus using the ANN method

Testing \ Training		UDDS	OCTA	Manhattan	Houston
UDDS	**R^2**	**0.9804**	0.9516	0.9411	0.9514
	RMSE	**0.0048**	0.0076	0.0084	0.0076
OCTA	**R^2**	0.9480	**0.9617**	0.9393	0.9462
	RMSE	0.0061	**0.0052**	0.0066	0.0061
Manhattan	**R^2**	0.9115	0.9158	**0.9389**	0.9202
	RMSE	0.0076	0.0074	**0.0062**	0.0072
Houston	**R^2**	0.9576	0.9567	0.9507	**0.9710**
	RMSE	0.0056	0.0056	0.0060	**0.0046**

4.2.3.6. Linear Regression Method and Simulink Model Development

Compared with Tables 4.2-4.3 and Tables 4.4-4.5, it can be seen that there is not much improvement using the ANN method over the LR method to predict emissions when taking engine power, engine torque, engine speed and their derivatives as model inputs. It should be noted that when more input variables are considered, the ANN method has obvious advantages [55, 56]. In addition, because the LR method was more reliable and robust compared with ANN, the LR NO_x predictive emissions model was incorporated into the PSAT vehicle model. Figure 4.14 shows the Simulink block of the LR method. The constants shown in Figure 4.14 were calculated by performing the least-square method in Equation 4.5.

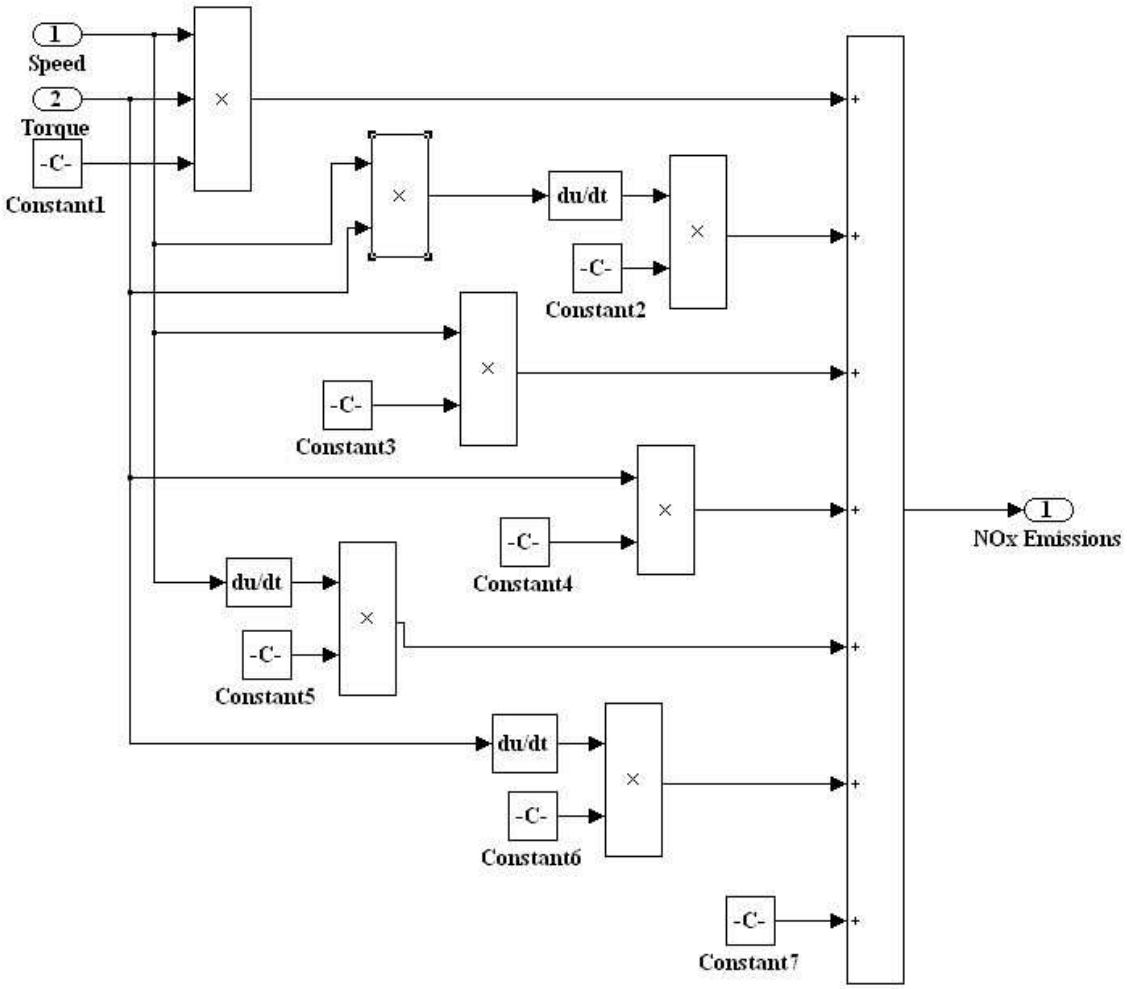

Figure 4.14: Simulink linear regression block

4.3. Transmission Model

The function of the transmission is to multiply or divide the engine torque/speed by the ratio for the selected gear. The transmission uses gears to achieve speed and torque conversion, which makes more effective use of the engine torque and keeps the engine operating at an appropriate rate of the speed and acceleration.

4.3.1. Development of 18-Speed Transmission Efficiency Lookup Tables

As part of the energy is lost in the transmission, it is important to model transmission efficiencies accurately. A manual 18-speed Eaton Fuller transmission was used in this study. The Eaton Fuller transmission shift pattern and shift control diagrams are shown in Figures 4.15-4.16 [112]. The transmission is a 5-speed unit with both a range change and a gear split. The range level works up for high range and down for low range and the splitter works rearward for "L" and

forward for “H”. The splitter control button (Figure 4.16) splits the ratios into low or high range. Table 4.6 shows the detailed performance for this Eaton Fuller transmission and the gear ratios. 16th gear is a direct drive, and both 17th and 18th gears provide overdrive operation [113]. Overdrive is a term used to describe a drivetrain that allows a vehicle at sustained speed to operate with reduced engine speed (the output shaft of the engine speed is larger than input shaft speed) which generally results in better FC [114].

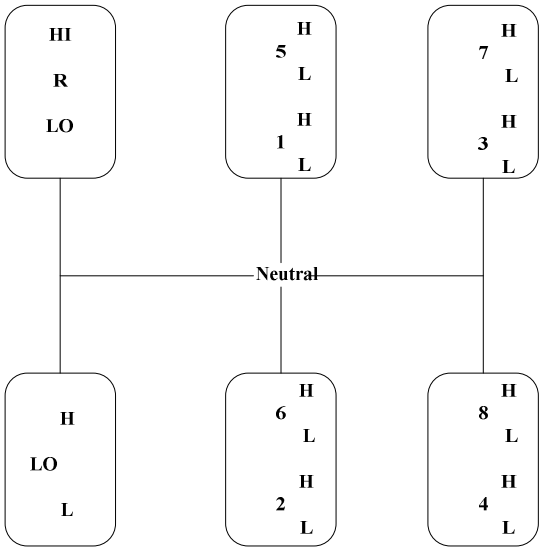

Figure 4.15: The Roadranger 18-speed transmission shift pattern of the Eaton Fuller transmission
[112]

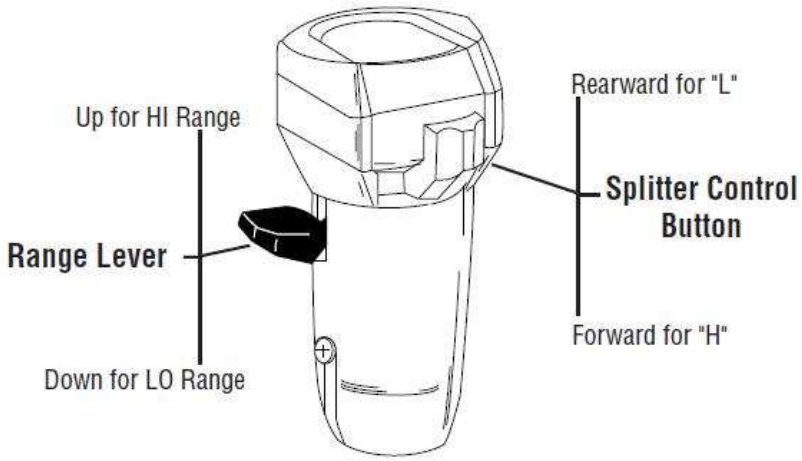

Figure 4.16: Shift controls diagram for the Roadranger 18-speed transmission
[112]

Table 4.6: Details for the Roadranger 18-speed transmission of Peterbilt truck [113]

Gear shift	Position	Ranger (High/Low)	Split (H/L)	Transmission Ratio	Gear Mesh	Maximum Efficiency (%)
1	LOL	Low	L	14.40	4	96
2	LOH	Low	H	12.29	4	96
3	1L	Low	L	8.56	4	96
4	1H	Low	H	7.30	4	96
5	2L	Low	L	6.05	4	96
6	2H	Low	H	5.16	4	96
7	3L	Low	L	4.38	2	97
8	3H	Low	H	3.74	2	97
9	4L	Low	L	3.20	4	96
10	4H	Low	H	2.73	4	96
11	5L	High	L	2.29	4	96
12	5H	High	H	1.95	2	97
13	6L	High	L	1.62	4	96
14	6H	High	H	1.38	2	97
15	7L	High	L	1.17	2	97
16	7H	High	H	1.00	0	99*
17	8L	High	L	0.86	4	96
18	8H	High	H	0.73	2	97

*Note that in the direct-drive gear (16th gear with gear ratio of 1) the efficiency is higher than the non- direct drive gears.

Few data sets are available to describe losses or efficiencies of manual transmissions, although general values are often suggested. In most cases, for typical vehicle activity, the efficiency of a manual transmission is quite high (usually above 90%) in comparison to automatic transmissions (usually about 80%) [115]. There were three major losses that were considered to calculate the transmission efficiencies in this study. First, churn losses are generated by moving lubrication oil in the transmission. All rotating components that are in direct contact with lubricant and move the oil due to their rotation contribute to the churn losses [116]. The deeper the components are submerged, the higher the losses are from the oil movement. The second category of the loss is lubrication pump losses, which is due to the forced pump lubrication of most heavy-duty transmissions, which consumes power. The third kind of the loss is mesh loss, which is the largest contributor to the total loss when the transmission is under load. Mesh losses are associated with the contact area of the gear teeth, which also is referred to as gear sliding [116]. Therefore, it is important to identify how many meshing gear pairs contribute to these losses. In direct drive, there are no significant mesh losses, which also can be seen in Table 4.6.

Detailed transmission efficiency maps were developed, which are defined as a function of the engine speed and torque in the transmission initialization file. The transmission efficiency information was gathered from the manufacturer [112,113]. Equation 4.12 shows the calculation of transmission efficiency:

$$\eta = \frac{(\frac{T*\omega}{5252})*\eta_{\max} - P_{loss} - C_{loss}}{(\frac{T*\omega}{5252})*\eta_{\max}} \qquad \textit{Equation 4.12}$$

where T is engine torque with a unit of *ft-lb*, ω is engine speed with a unit of *rpm*, $\eta_{\max}$ is the maximum efficiency which can be found from Table 4.6, C_{loss} is countershaft churn losses with a unit of *hp*, and P_{loss} is lubricating pump losses with a unit of *hp*. C_{loss} and P_{loss} were calculated by Equations 4.13-4.14 [113]:

$$C_{loss} = 5.3902*10^{-7}*i_{cs}^{\ 2} + 6.5734*10^{-4}*i_{cs} + 5.9420*10^{-3} \qquad \textit{Equation 4.13 [113]}$$

$$P_{loss} = 9.7314*10^{-5}*i_{cs} + 7.1389*10^{-7} \qquad \textit{Equation 4.14 [113]}$$

where $i_{cs} = {12.12*\omega_{iss}}/{i_{hs}}$, i_{hs} is the ratio of the input gear to the countershaft gear and ω_{iss} is the input shaft speed, with a unit rpm [113]. The headset ratio for this transmission is 0.7878 [113]. The units of C_{loss} and P_{loss} in Equations 4.13-4.14 are in *kW* [113], were converted to *hp* by dividing by 0.7457.

Combining the churn, mesh and lubrication pump losses yielded the matrix shown in Table 4.7 for 12th gear. Table 4.8 presents the sum of the churn and pump losses. The manual transmission has high efficiency at all but light load. In practice, losses will vary with wear of the transmission, and with the type and condition of the lubricant.

Table 4.7: Efficiencies of an 18-Speed Eaton Fuller transmission in 12th gear

Speed (rpm) / Torque (ft-lb)	200	400	600	800	1000	1200	1400	1600	1800	2000
200	0.317	0.648	0.758	0.814	0.847	0.869	0.885	0.896	0.906	0.913
400	0.648	0.814	0.869	0.896	0.913	0.924	0.932	0.938	0.942	0.946
600	0.758	0.869	0.906	0.924	0.935	0.942	0.948	0.952	0.955	0.957
800	0.814	0.896	0.924	0.938	0.946	0.952	0.956	0.959	0.961	0.963
1000	0.847	0.913	0.935	0.946	0.953	0.957	0.960	0.963	0.964	0.966
1200	0.869	0.924	0.942	0.952	0.957	0.961	0.963	0.965	0.967	0.968
1400	0.885	0.932	0.948	0.956	0.960	0.963	0.966	0.967	0.969	0.970
1600	0.896	0.938	0.952	0.959	0.963	0.965	0.967	0.969	0.970	0.971
1800	0.906	0.942	0.955	0.961	0.964	0.967	0.969	0.970	0.971	0.972

Table 4.8: Gear losses at different speed (including lube pump losses and churn losses)

Engine Speed (rpm)	**600**	**800**	**1000**	**1200**	**1400**	**1600**	**1800**	**2000**
Power Losses (hp)	1.198	1.781	2.457	3.226	4.089	5.044	6.093	7.235

4.4. Engine Cooling Fan Model

The mechanical accessory model represents all of the belt-driven as well as gear-driven loads on the engine. This includes the cooling fan, alternator, power steering pump air conditioner compressor and brake. In the Peterbilt truck with a 550 hp engine, the maximum of the auxiliary load (without a fan) was about 10 hp [117]. In the original PSAT file, the mechanical accessory model was a constant power loss model that draws constant power from the engine directly. The mechanical accessory model was redesigned in this study. The fan load was usually far greater than other loads when the fan is engaged and has received special attention. Here the mechanical accessory model was designed by adding a constant power (10hp, which represents the mechanical accessory loads other than the fan) to the fan power loss model.

A typical cooling system includes a thermostat, radiator, cooling fan, coolant pump, bypass tube and coolant path. The cooling fan's function is to dissipate the heat from the radiator. Figure 4.17 shows the simple coolant flow schematic of the Peterbilt truck [12]. The Peterbilt truck employs clutch driven fan that is thermostatically controlled via an air clutch, based on the temperature of the coolant [118]. When the coolant temperature is below the operating temperature (190 ^{o}F [117]), the coolant flows from the thermostat through the bypass tube to the

coolant pump directly. Once the temperature of the coolant goes above the set value, coolant flows through the radiator and the engine fan is turned on.

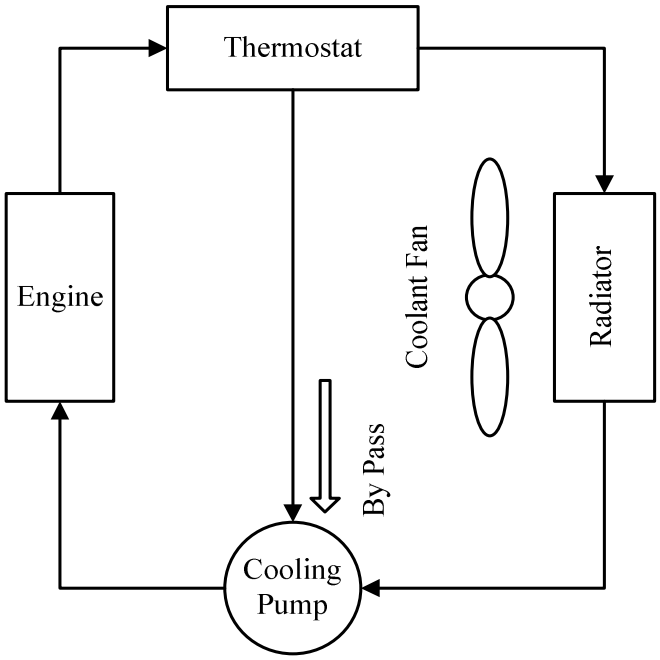

Figure 4.17: **Coolant flow schematic**

From a thermodynamic viewpoint, the engine cooling fan is undesirable. Because it consumes power when it is running and reduces thermal efficiency, thereby increasing the FC. However, the engine cooling fan is necessary because the engine materials cannot withstand very high temperatures [119]. Traditionally, an engine cooling system design was based on the worst vehicle operating conditions, such as high load, high ambient temperature and low vehicle speed. With the high demand for increasing FE and reducing emissions, it is imperative to build a cooling fan simulation model to evaluate the key parameters affecting fan power losses. Such a model should help designers with an inexpensive and convenient way to develop and improve the engine cooling system over steady state or transient operating conditions [120].

In this engine cooling system, the thermostat controls the coolant flow. The model assumed that the coolant temperature is determined by the linear, first order ordinary differential equation which is shown in Equation 4.15:

$$(M_c C_{pc} + M_e C_{pe}) * \frac{dT_c}{dt} = \dot{Q}_e - \dot{Q}_r \qquad \textit{Equation 4.15}$$

Where $\dot{Q}_r$ and $\dot{Q}_e$ are calculated from Equations 4.16-4.17.

$$\dot{Q}_r = UA*(T_c - T_\infty) \qquad \textit{Equation 4.16}$$

$$\dot{Q}_e = 0.4 * \dot{Q}_f \qquad \textit{Equation 4.17}$$

where $\dot{Q}_e$ and $\dot{Q}_r$ are the heat energy flow rates of the engine and the radiator, $\dot{Q}_f$ is the heat energy flow rate of the fuel from tested data (assuming fuel efficiency in the engine is 0.4), M_c and M_e are the masses of the coolant and the engine, C_{pc} and C_{pe} are specific heat of the coolant and the engine, T_c and T_∞ are the temperatures of the coolant in the radiator and the ambient air, U is the overall heat transfer coefficient of the radiator and A is the area associated with U.

Before Equation 4.15 may be solved, all the variables must be determined. The coolant used in this study was *50/50* water and glycol with a mass of *46 kg* [121]. The engine mass was *1470 kg* [121]. For a relatively simple engine cooling system model, *UA* is taken as one variable. First, the worst vehicle operating conditions were considered, which was at maximum power (*550 hp* (*410 kW*)), which happened at engine speed *1600* rpm (*167.55 rad/s*), very high coolant temperature (*220 ^oF* (*104.46 ^oC*)) and very high ambient air temperature (*120 ^oF* (*48.89 ^oC*)). Also assuming the heat energy dissipated into the coolant was equal to the maximum power, the *UA* was found by Equation 4.18:

$$410(kW) = UA * (377.59 - 322.04)(K) \qquad \textit{Equation 4.18}$$

Then *UA* can be solved by above equation, *UA* = 7.7394 (*kW/K*)

In a transient operating condition, *UA* is a function of the engine speed which can be expressed by Equation 4.19:

$$UA = UA_{(1600rpm)} * (\frac{\omega}{1600})^3 \qquad \textit{Equation 4.19}$$

where ω is engine speed with a unit of *rpm*.

After the value of *UA* is determined, all variables in Equation 4.15 are known. For a particular operating condition, the coolant temperature T_c in Equation 4.15 can be solved by using Runge-Kutta first order formula.

It was assumed that the coolant temperature T_c at $t = 0$ is at *190 ^oF* (*88 ^oC*) and the ambient temperature T_∞ is at *77 ^oF* (*25 ^oC*). A time increment of one second was used in this study. The coolant temperature at each second was used for calculating the next second. Another assumption was that the engine fan was off when T_c is below *189.5 ^oF* (*87.5 ^oC*), in this case *UA* is small and assumed to be zero and Equation 4.15 becomes:

$$(M_c C_{pc} + M_e C_{pe}) * \frac{dT_c}{dt} = \dot{Q}_e \qquad \textit{Equation 4.20}$$

When the fan is engaged (fan ON), engine speed is used to determine the fan power demands. Generally, as the fan speed increases, the resulting power losses on the engine increase significantly. Figure 4.18 shows the nature of a fan power loss curve [120]. The fan power loss was in proportion to the 2.7th power of the engine speed.

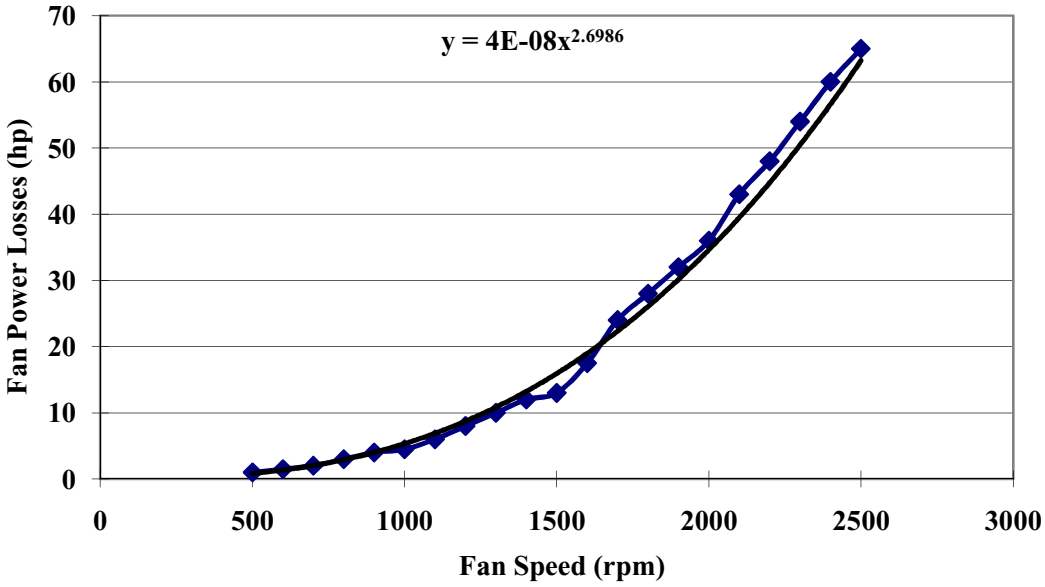

Figure 4.18: Engine fan power losses as a function of the fan speed for the heavy-duty vehicle (The points in the figure are from the reference [120])

The work flow chart of the engine cooling fan is demonstrated by Figure 4.19. A brief summary of its working process can be described in this way: After the coolant and ambient air temperatures were initialized, the coolant temperature was calculated by Equation 4.15, with the assumptions as stated. In the decision structure, the computed coolant temperature T_c was compared with the set one, 189.5 ^{o}F. If T_c is less than 189.5 ^{o}F, the fan is OFF, otherwise the fan is ON and the energy consumed by the engine fan was calculated. It should be noted that, to prevent the cooling fan from constantly turning ON and OFF at precisely 189.5 ^{o}F, a two second delay was imposed at the time of transition. For example, as the coolant temperature rises, it must maintain the temperature of 189.5 ^{o}F for at least two seconds before the fan will turn on. As the coolant temperature decreases, it must maintain a temperature below 189.5 ^{o}F for at least two seconds before the fan will turn off. Figure 4.20 illustrates the predicted coolant temperature when the Peterbilt truck is running over the UDDS. The comparison plot of the engine power and the power consumed by the engine cooling fan is shown in Figure 4.21.

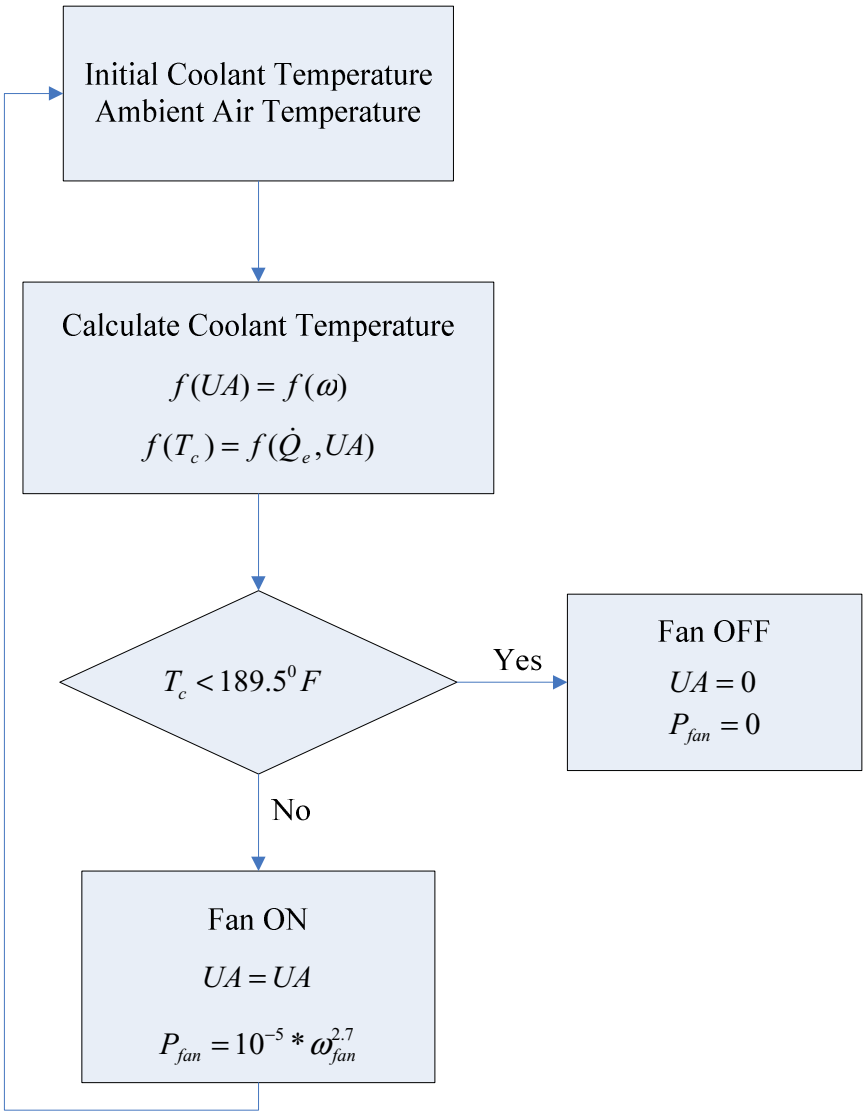

Figure 4.19: Work flow chart of engine fan power losses
(where P_{fan} is the fan power loss with a unit of *hp*, ω_{fan} is fan speed with unit of *rpm*)

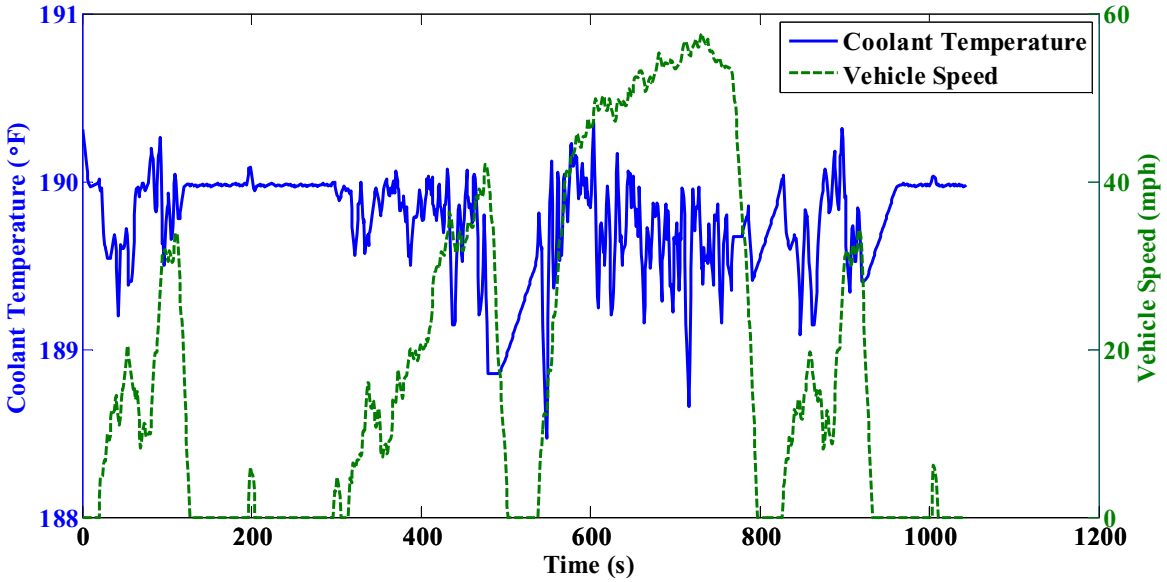

Figure 4.20: The predicted coolant temperature when the Peterbilt truck running over the UDDS

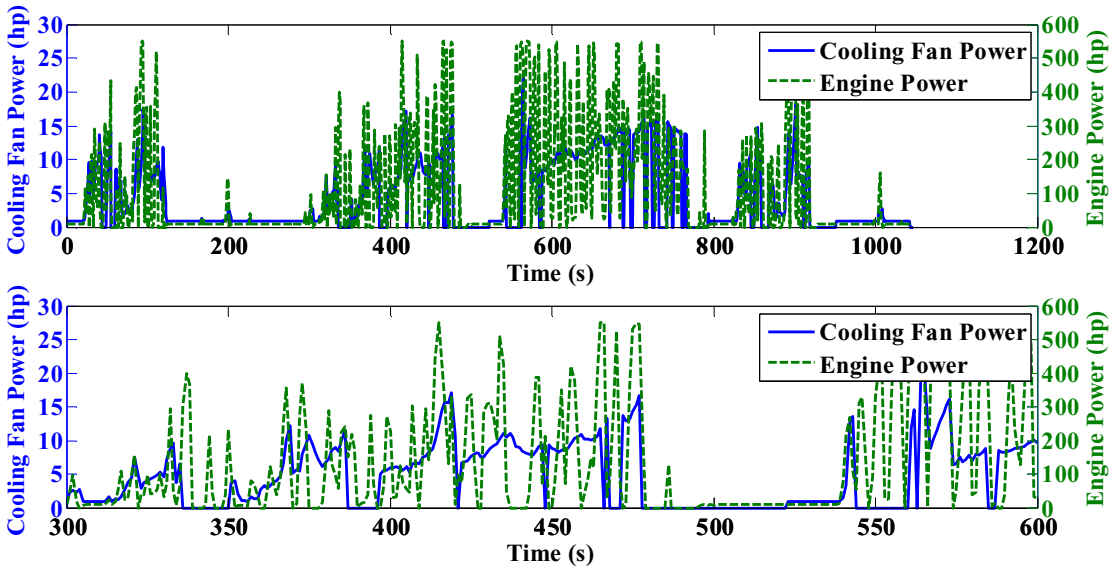

Figure 4.21: The comparison plot of the engine power and engine cooling fan power of the Peterbilt truck over the UDDS

4.5. Single Component Validation

After the component data have been integrated into PSAT, single component models need to be validated separately. The whole vehicle model is only as good as the most inaccurate component [122]. For example, if an HEB model has an accuracy of +/-3% for the engine, +/-2% for the traction motor and +/1% for the ESS, the whole HEB accuracy cannot be expected to be less than

+/-6%. When modeling and validating a whole vehicle model, it is often difficult to find where a specific error initiates. The single component validation allows for the finding of problems with specific components.

In order to validate a component model, first the measured input data of the real component needs to be integrated into the model. With experimental data as inputs, an ideal model should generate the experimental output. By comparing the experimental data and the PSAT simulated data, the accuracy of the component is determined. It should be noted that there is no feedback in single component model validation. The lack of feedback isolates problems caused by other components and the drivertrain controller.

Figure 4.22 shows the engine model in the single component model validation process, which takes the experimental engine command and speed as inputs (the ground signal in the input is the feedback signal of engine torque). The comparison results between the experimental data and simulated data is shown in Table 4.9. Both the experimental and the simulated data are average values. Figures 4.23-4.25 depict the instantaneous measured and simulated engine torque, engine fuel rate and NO_x emissions over the UDDS cycle. The engine torque was transformed from the engine command by interpolating between a closed throttle torque curve (minimum torque curve) and a wide opened throttle torque curve (maximum torque curve). The perfect match between the simulated torque and the experimental torque (Figure 4.23) confirms that the maximum and minimum torque curves are accurate and the PSAT model performs correctly. Figure 4.24 shows that the simulated instantaneous fuel rate matches the experimental fuel rate very well, which indicates that the fuel rate matrix developed on the basis of experimental data from the UDDS in the PSAT initialization file can be used for a generic fuel consumption study. The simulated NO_x emission data typically match the measured data well (Figure 4.25).

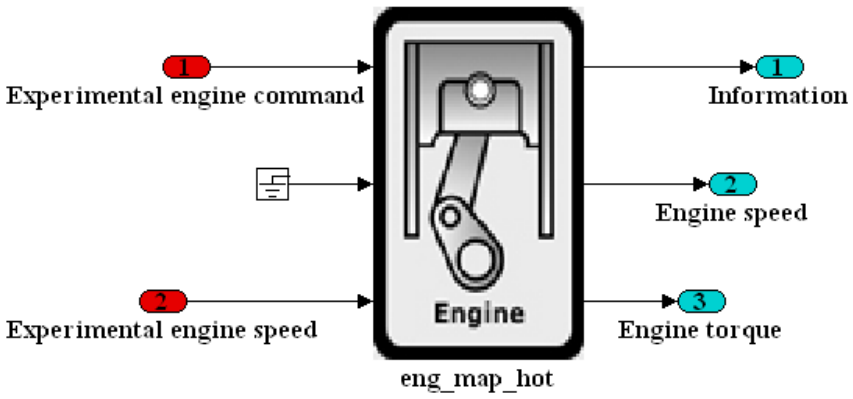

Figure 4.22: Engine model validation

Table 4.9: Comparisons of the experimental and PSAT simulated data over the UDDS in engine model validation of the Peterbilt truck

	Engine Speed	Engine Torque	Engine Fuel Rate	NO_x
	rpm	Nm	g/s	g/s
Experimental	1184.7	498.93	4.37	0.091
PSAT Simulated	1184.8	488.59	4.50	0.093
Relative Error (%)	-0.01	2.12	-2.89	-2.15

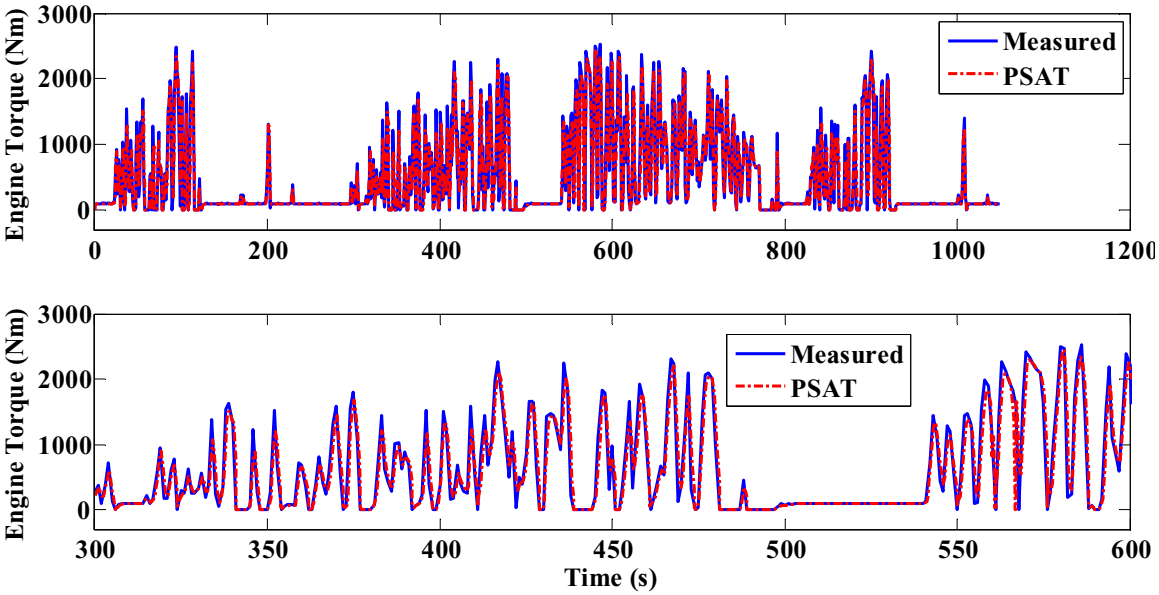

Figure 4.23: Comparisons of the measured and PSAT simulated engine torque in the validation of the Caterpillar 3406E engine model over the UDDS

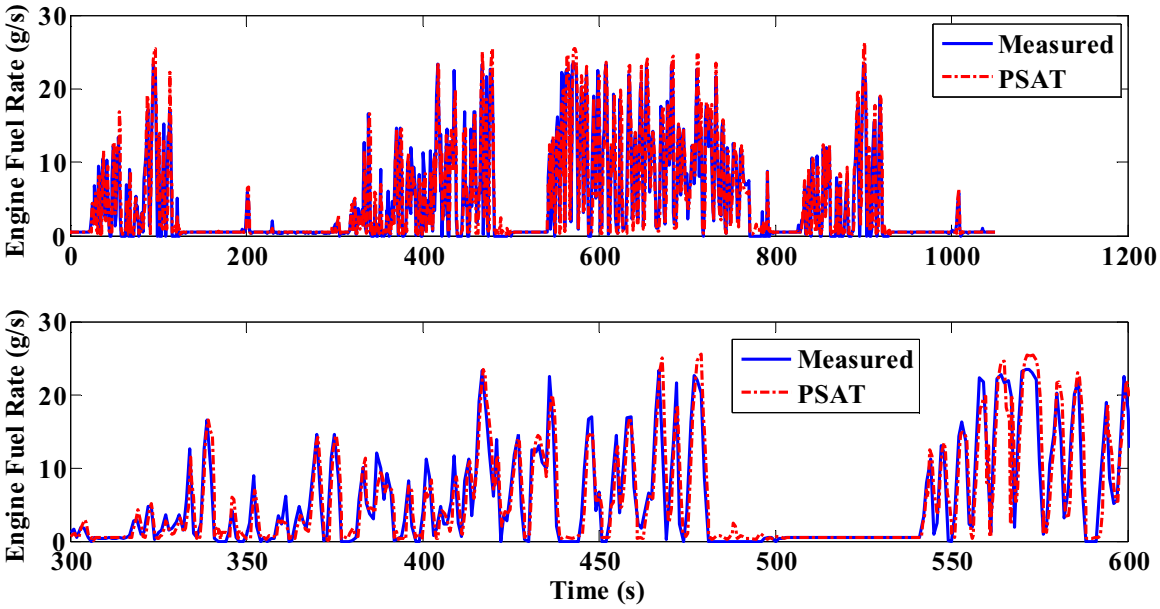

Figure 4.24: Comparisons of the measured and PSAT simulated engine fuel rate in the validation of the Caterpillar 3406E engine model over the UDDS

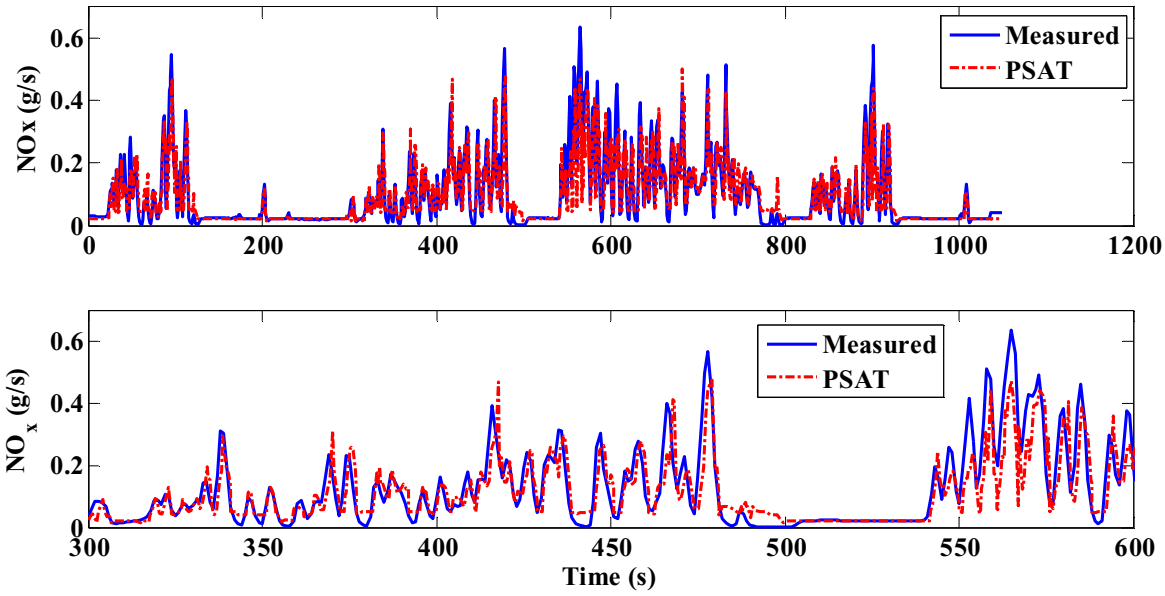

Figure 4.25: Comparisons of the measured and PSAT simulated NO_x emissions in the validation of the Caterpillar 3406E engine model over the UDDS

4.6. Validation Results of the Peterbilt Truck Model

Two criteria were used to evaluate the goodness of the fit between the PSAT simulated and test engine torque, engine speed, engine power, fuel consumptions and NO_x emissions. (i) the square

of correlation coefficients (R^2) which is defined in Equation 4.6 and (ii) the relative error, defined in Equation 4.21.

$$RE = \frac{(\bar{y} - \bar{\hat{y}})}{\bar{y}} * 100\% \qquad \textit{Equation 4.21}$$

where *RE* is the relative error, $\bar{y}$ and $\bar{\hat{y}}$ are the means of the measured and PSAT simulated data. In this study, "validation," as defined by the Argonne National Laboratory, referred to the PSAT simulated results compared with the test data [123]. Table 4.10 shows the validation results of the Peterbilt truck model. The FE (mpg) was calculated by dividing the distance the vehicle traveled by the amount of fuel consumed. The engine fuel rate, speed, torque, power, vehicle speed and emissions were all average values. The measured CO_2 data were background corrected data. From Table 4.10, it can be seen that the relative percent of errors between the measured and PSAT simulated values are all within 5%.

Table 4.10: The comparison of measured and PSAT simulated results of Peterbilt truck over the UDDS

Parameter	**Measured**	**PSAT Simulated**	**R^2**	**Relative Error (RE)(%)**
UDDS Distance(mile)	5.44	5.38	------	1.10
Vehicle Speed (mph)	18.67	18.68	1.00	-0.12
Fuel Economy (MPG)	3.82	3.82	------	0.00
Fuel Consumption (kg/cycle)	3.57	3.67	------	-2.80
Engine Fuel Rate (g/s)	4.37	4.54	0.94	-3.89
Engine Speed (rpm)	1184.69	1160.05	0.89	2.08
Engine Torque (lb-ft)	367.94	360.41	0.89	2.05
Engine Power (hp)	106.73	103.64	0.93	2.89
CO_2 (g/mile)	2640.49	2690.98	0.94	-1.91
NO_x (g/mile)	18.19	17.81	0.89	2.09

To further illustrate the PSAT simulation results, the continuous data of vehicle speed, engine fuel rate, engine speed, torque power and NO_x emissions, are plotted with their corresponding parity regression plots of measured and PSAT simulated values. In order to eliminate tiny transient problems, a 5-second average window was applied to both measured and PSAT simulated data to evaluate simulation performance. Figure 4.26 shows the vehicle speed target and the results from testing and PSAT simulation. From the left graph, it can be seen that the PSAT simulated speed is closer to the target speed than the measured one. Figure 4.27a-b illustrates the measured and simulated engine fuel rate (Figure 4.27b shows the selected 200 seconds). The experimental engine fuel rates were acquired from the engine ECU broadcast. The fuel rate signal comparison shows a satisfying result, with a R^2 value of 0.94 between the test

and PSAT simulated data (Figure 4.27c). Figures 4.28-4.30 compare the experimental and simulated engine speed, engine torque and engine power, correlation coefficients of 0.89, 0.89 and 0.93 respectively were found between the measured engine speed, torque and power and the PSAT simulated values. Figure 4.31 demonstrates the measured and the PSAT simulated NO_x emissions. The PSAT NO_x emissions model is given by:

$$NO_{x\Pr e} = -2.63*10^{-5}*P - 3.42*10^{-5}*\frac{dP}{dt} + 0.0012*T - 0.00028*\frac{dT}{dt} - 7.67*10^{-5}*\omega + 0.00094*\frac{d\omega}{dt} + 0.021$$

Equation 4.22

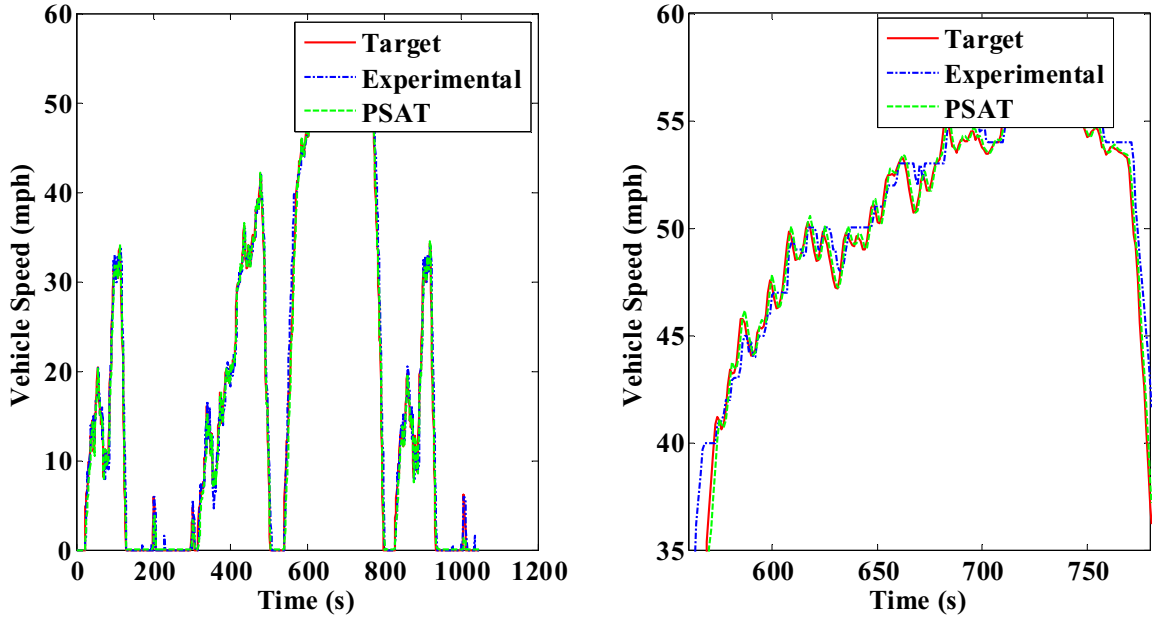

Figure 4.26: Comparison of the target, experimental and PSAT simulated vehicle speed over the UDDS

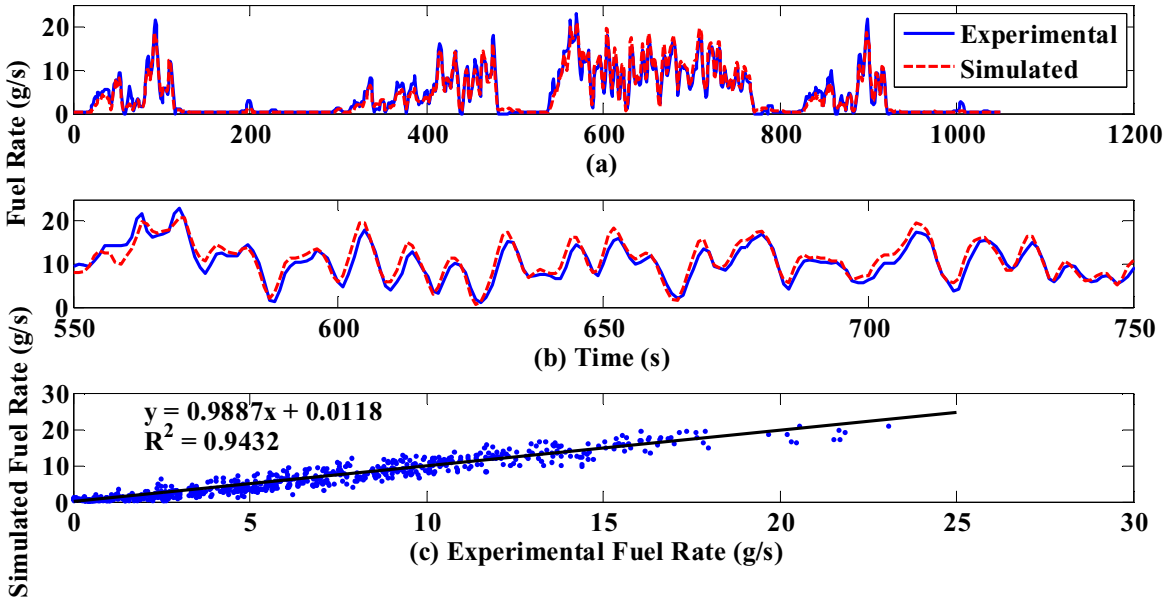

Figure 4.27: Comparison of the experimental and PSAT simulated engine fuel rate and the parity plot over the UDDS

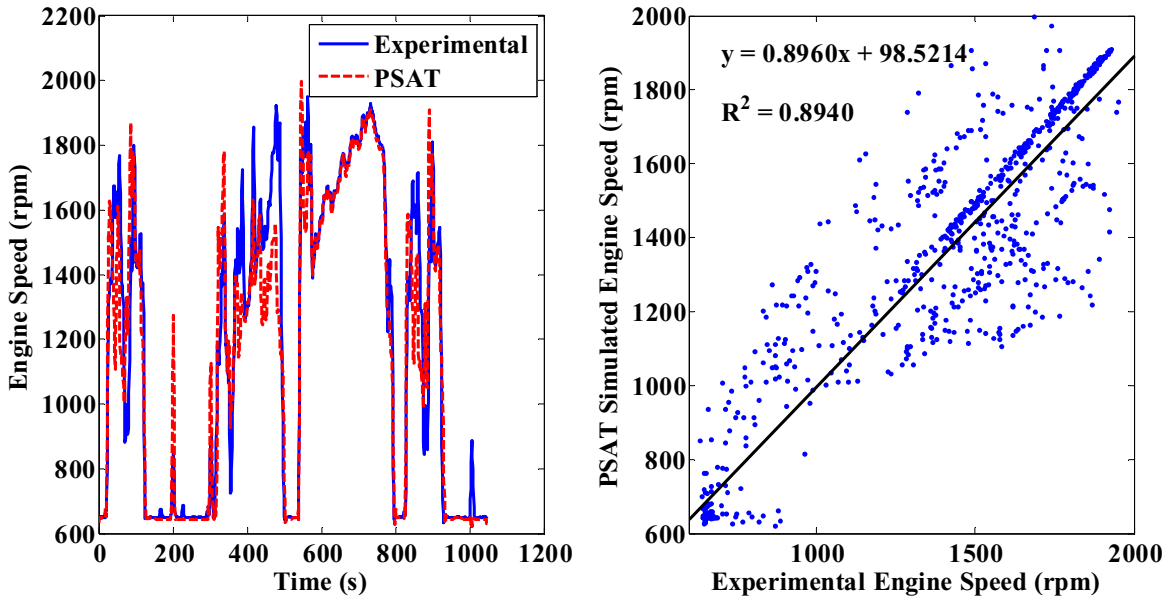

Figure 4.28: Comparison of the ECU broadcast engine speed and the PSAT simulated engine speed and the parity plot over the UDDS

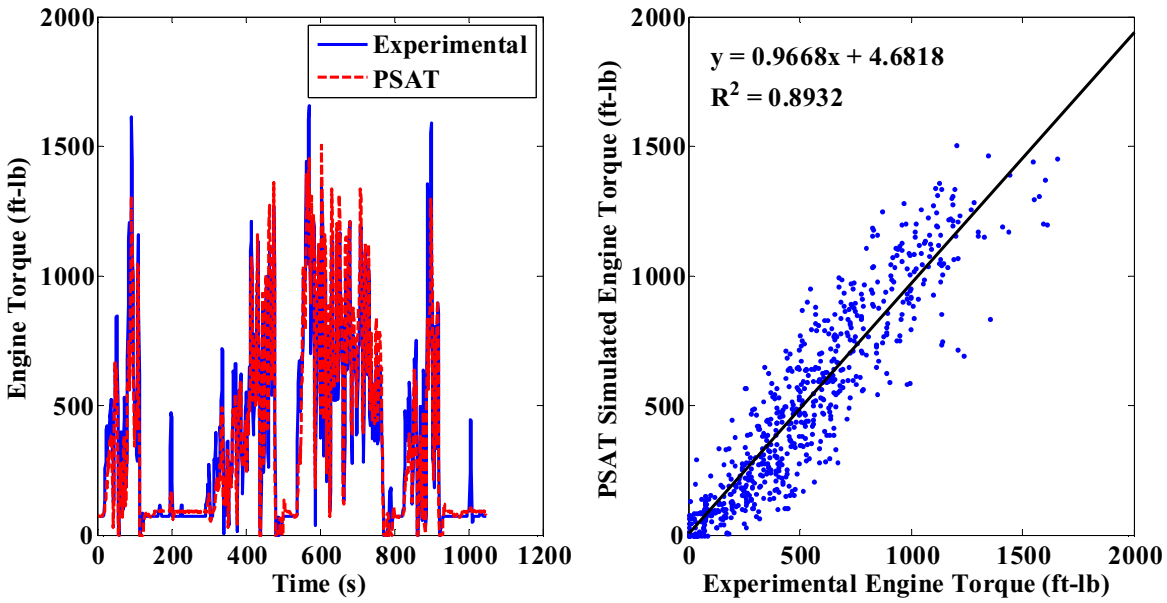

Figure 4.29: Comparison of the ECU Broadcast engine torque and the PSAT simulated engine torque and the parity plot over the UDDS
(The experimental engine torque is converted from broadcast engine percentage load, so there is no negative torque).

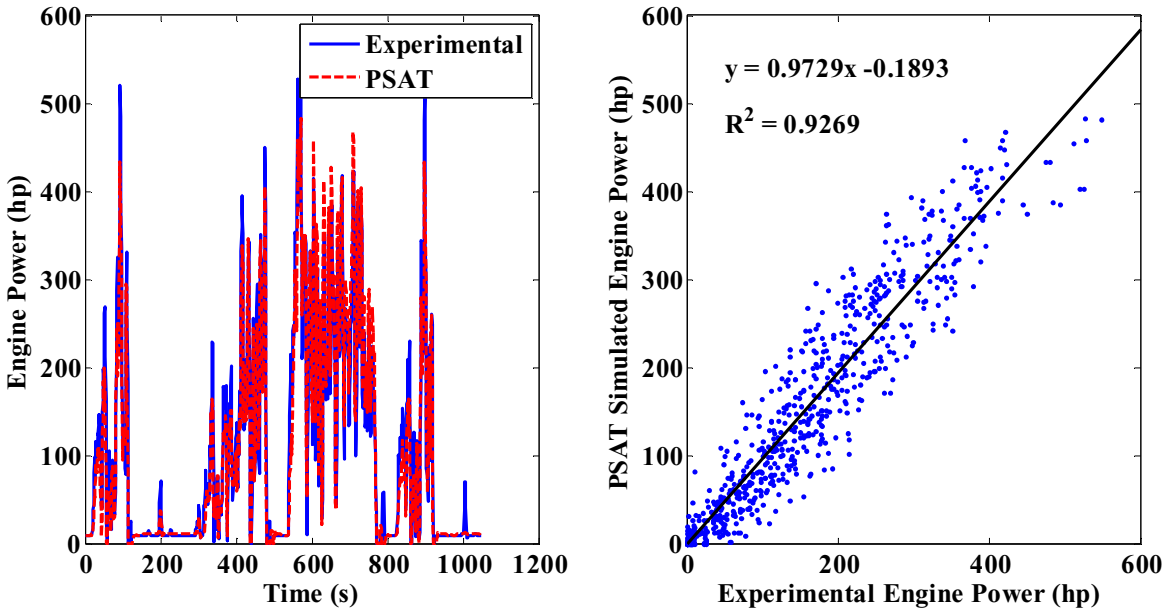

Figure 4.30: Comparisons of the experimental and PSAT simulated engine power and the parity plot over the UDDS
(The experimental engine power is the product of the engine speed and engine torque which are broadcasted parameters)

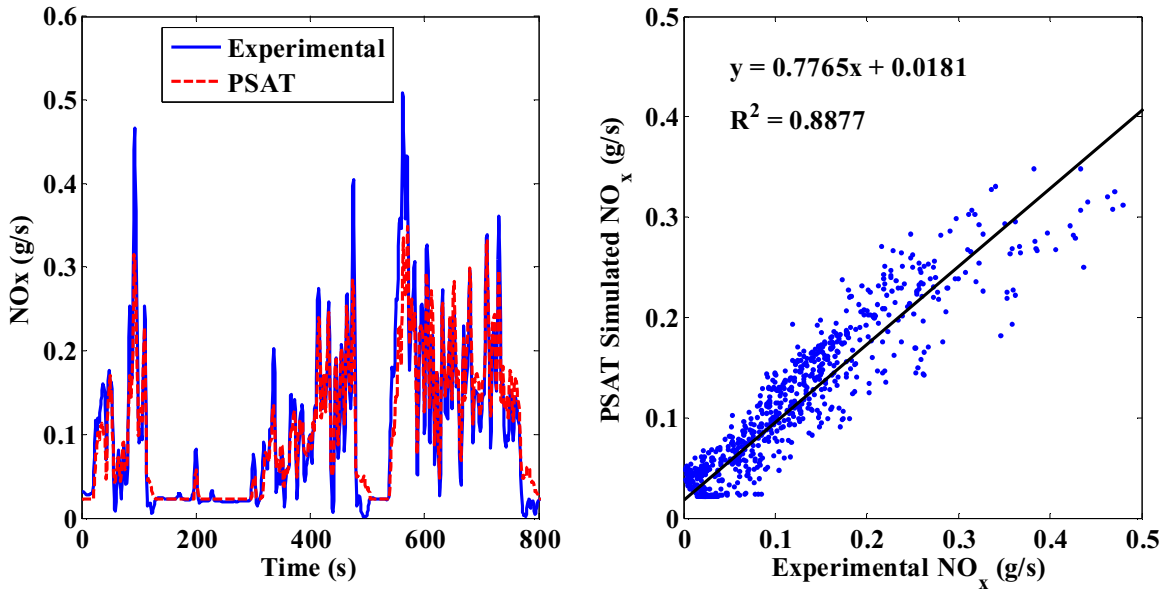

Figure 4.31: Comparison of the measured and PSAT simulated NO_x and the parity plot over the UDDS

4.7. Summary

Detailed information and data utilized to elaborate the major components of the Peterbilt truck and NO_x emissions model approaches were presented in this section. The Peterbilt truck modeled was a conventional over-the-road tractor, equipped with a 550 hp non-EGR Caterpillar 3406E engine, 18-speed Roadranger manual transmission and tandem axle drive. In the engine model, the calculation of the engine torque, fuel rate and emissions were described. The engine torque was estimated by interpolating the curve at the maximum and zero accelerator pedal positions. The engine fuel rate was estimated by using a fuel rate look-up table which was developed based on experimental data and expressed in terms of the engine torque and engine speed. The emissions were estimated by using an LR and an ANN approach, with engine power, speed, torque and their derivatives as inputs. The emissions models were trained and validated using experimental data running over the UDDS, OCTA, Manhattan and the Houston schedules from two different buses. Before developing the predictive emissions model, the data were examined first for time delay, which is mainly caused by the response of the analyzer. To compensate the delayed time, the emissions were aligned with engine power by performing cross-correlation method. In addition, the emissions signals were also spread over a period of time when measured by the analyzers. By compensating for the dispersion, the measured emissions data were backwards transformed by using the differential coefficients method. It was indicated that the power was much better correlated with the reconstructed NO_x emissions than with the directly measured NO_x emissions. The performance of both predictive emissions models was reasonably accurate. However, the LR method was more reliable and robust compared with the ANN

method, The LR NO_x predictive emissions model was eventually determined to be one that would be incorporated into the PSAT vehicle model. In the transmission model, transmission efficiency matrixes were developed on the basis of loss information gathered from the manufacturer. As the largest mechanical accessory model, an engine cooling fan model, which estimated fan power demand based on many thermal assumptions, was incorporated into the heavy-duty truck model. The engine model was validated separately before the validation of the whole vehicle model.

The validation performance by comparing the PSAT simulated data and experimental data among the engine fuel rate, speed, torque, power, vehicle speed and emissions were summarized. The results showed that the relative percent of the error between the experimental and PSAT simulated values were all within 5%. This showed that the Peterbilt truck model was sufficiently validated and could be used as the basis for future parametric studies.

Chapter 5: Quantitative Effect of Factors on Fuel Efficiency and Emissions

The desire for high vehicle efficiency was driven by customer demand for reducing vehicle FC and the regulations for reducing emissions. At the time of writing, both regulation and customer demand were focused on increasing the efficiency of the whole vehicle, although the two thrusts may differ when overall operation economics and system efficiency are considered. The objective of this chapter was to estimate the FC of the Peterbilt truck over various cycles as a function of key parameters from a parametric analysis.

5.1. Impact of Single Technologies on Fuel Consumption

5.1.1. Aerodynamic Drag

Aerodynamic drag is a force opposing the motion of the vehicle caused by the resistance of the ambient air. Quantitatively, the aerodynamic drag is proportional to the product of the coefficient of aerodynamic drag, the frontal area and the square of vehicle velocity, as shown in Equation 2.2. The coefficients of aerodynamic drag for current heavy-duty vehicles with smooth-sided van trailers are about 0.6-0.65, which is higher than the value found from light-duty vehicles, normally about 0.3-0.4 [14]. The higher aerodynamic drag values in a heavy-duty vehicle are due to the fact that they are equipped with large boxes (with larger frontal area than that of light-duty vehicles) to carry freight. The metric for evaluating aerodynamic losses is the coefficient of aerodynamic drag. Reducing frontal area usually sacrifices the interior size and thus has limited value in reducing aerodynamic drag. Driving slower can also reduce the drag force. However, changing actual road speed is not realistic, so reducing the drag coefficient is the main way to reduce aerodynamic drag. The Peterbilt truck was simulated by PSAT over various driving cycles at different weights, coefficient of aerodynamic drag and rolling resistance. Figure 5.1 depicts the impact of the coefficient of aerodynamic drag on FE at a constant test weight and rolling resistance. Five different driving schedules, UDDS, transient, creep, cruise and high speed cruise were chosen to represent various driving conditions. It can be seen that the FCs are approximately linear functions of the coefficient of aerodynamic drag over the UDDS, transient, cruise and high speed cruise modes. At the creep mode, the impact of aerodynamic drag on FC is negligible. So it is no benefit to reduce aerodynamic drag during the creep mode. Conversely, there is some benefit for aerodynamic drag reduction from medium speed cycles (UDDS and Transient) and a large benefit can be achieved during high speed cycles (cruise and high speed cruise mode). If the coefficient of aerodynamic drag is reduced from 0.6 to 0.5 (16.7 percent reduction), a 4.2 percent FC savings is achieved for the Peterbilt truck during cruise mode.

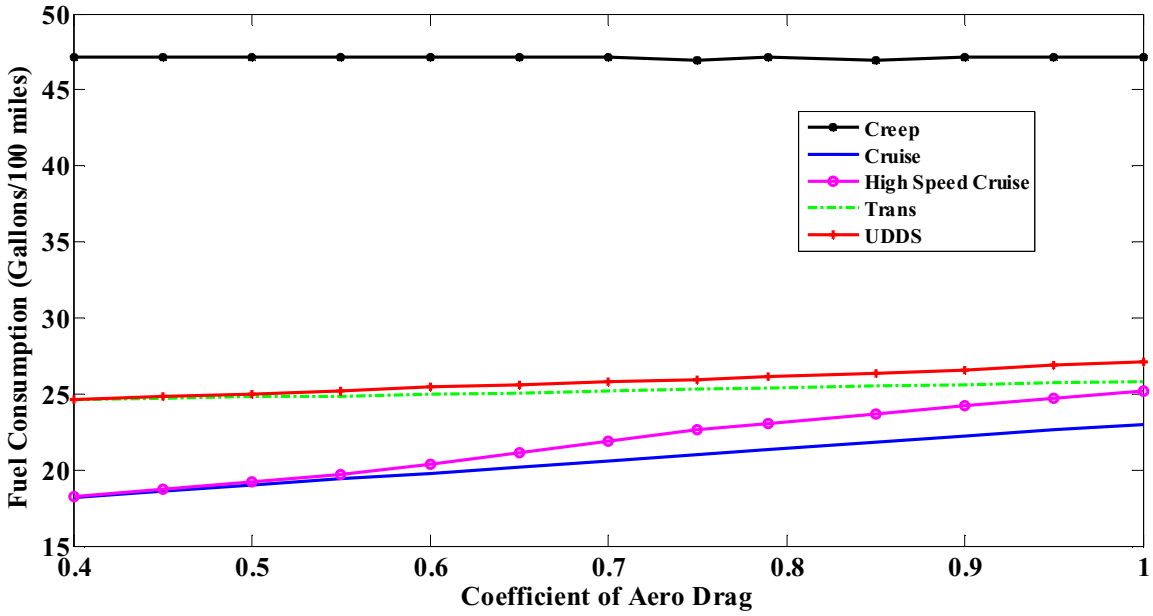

Figure 5.1: The impact of coefficients of aerodynamic drag on fuel consumption for Peterbilt truck over various driving cycles
(Truck weight = 56000 lbs, Frontal area = 7.06 m^2, Coefficient of rolling resistance $\mu = 0.00938$)

5.1.1.1. Technologies for Tractor Aerodynamic Improvement

The truck manufacturers seek technologies to minimize the coefficient of aerodynamic drag in order to reduce FC. Technologies used to reduce the aerodynamic drag of the tractors include a streamlined hood, faired bumper, fuel tank fairings, side fairing, cap extender and more aerodynamic mirrors [14]. Figure 5.2 shows common aerodynamic improvement technologies [14]. One characteristic of the aerodynamically optimized tractors is that the sleeper cab tractor is equipped with many fairings [14]. The cab extenders which reduce the gap between tractors and trailers play an important role in determining the overall coefficients of aerodynamics drag. The recommended maximum distance is typically 30 inches between the rearmost portion of the tractor to the trailer face [14]. Figure 5.3 shows a traditional Peterbilt truck (left) and a SmartWay Peterbilt truck (right). Table 5.1 shows the market shares and improvement of various aerodynamic technologies on tractors [124] in the 2012 time frame. The FC reduction of the combined technologies is calculated multiplicatively according to the following equation.

$$\%FC_{Package} = 1-(1-\%FC_{Tech1})(1-\%FC_{Tech2})(1-\%FC_{TechN}) \qquad \textit{Equation 5.1[14]}$$

where $\%FC_{TechX}$ is the percent FC reduction of an individual technology, and therefore $\%FC_{TechX}$ is FC associated with the reduction.

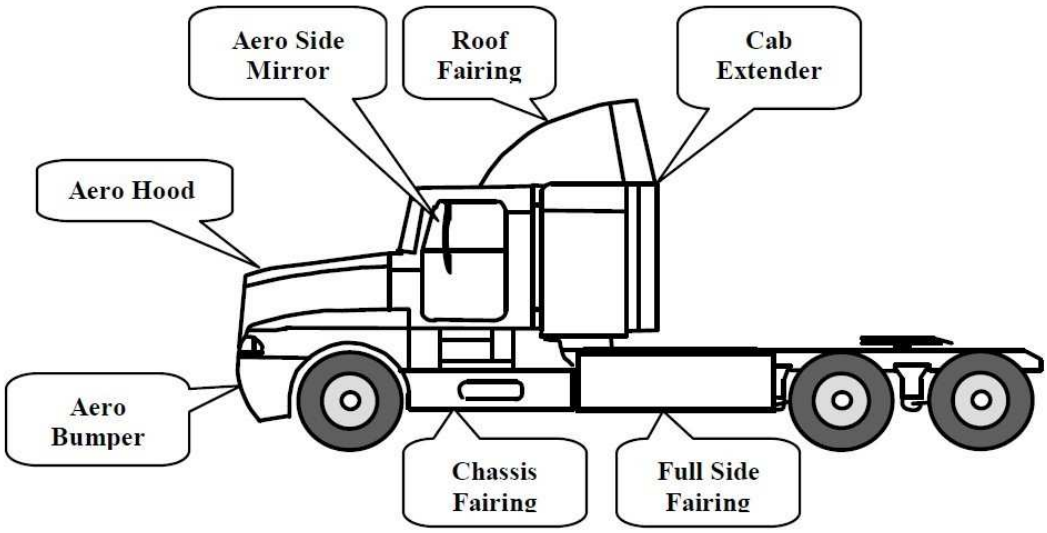

Figure 5.2: The identification of the common aerodynamic improvement technologies [14]

Figure 5.3: The traditional Peterbilt truck (left) and the SmartWay Peterbilt truck (Source: Peterbilt Truck manufacturer's website)

Table 5.1: Class 8 tractor aerodynamic technologies
[124]

Technology	FC % Reduction	C_d % Improvement	Cost	Industry Adopt Rate (%)
Sleeper Roof Fairing	7-10	25-20	$500-$1000	Standard
Day Cab Roof Deflector	4-7	13	$1000-$1300	30
Chassis Skirt	3-4	4-7	$1500-$2000	50-60
Cab Extender	2-3	4-5	$300-$500	80-90
Next Generation Package	3-4	6-8	$2750	2012 Introduction

5.1.1.2. Technologies for Trailer Aerodynamic Improvement

Significant progress has been made to improve the aerodynamics by adding boat tails, a nose cone, vortex stabilizer and a bogie cover to trailer [14] (Figure 5.4). However, two reasons impede the widespread use of these new technologies. One is that most of time, the owners of tractor and trailer are not same, so the trailer owner does not benefit from the FC reduction by making expensive adaptations to the trailer in the interest of improving aerodynamics. Another reason is that there are more trailers than there are tractors, as a result, the cost in aerodynamic improvement needs to be compensated for the less miles traveled [14]. Table 5.2 gives the summaries of supplier's information for FE improvement by applying various aerodynamic technologies [14].

Figure 5.4: Trailer technologies
(Upper left: trailer skirt, upper right: boat tail, lower left: nose cone, lower right: bogie covers [14])

Table 5.2: The FE improvement by utilizing various aerodynamic technologies [14]

Trailer Aerodynamic Technology	Trailer Skirts	Boat Tails	Nose Cone	Vortex Stabilizer	Bogie Cover
Range of FE Improvement (%)	5.6-7.5	2.9-5.0	2.0-4.0	1.0	1.0
Range of Cost	$1600-$2400	n/a	$800-$1260	$500	n/a

5.1.2. Rolling Resistance

Figure 5.5 shows the impacts of coefficients of rolling resistance on FC for the Petertilt truck over different cycles at a constant test weight and aerodynamic drag. It can be seen that the FC is linearly proportional to the coefficients of rolling resistances over the different duty cycles. The FC was calculated by dividing the volume of fuel consumed by 100 miles distance traveled. A "jumping" was observed in the creep mode because of the precision at which PSAT simulates the trip. This causes rounding errors due to the very short distance traveled and the very small

amount of fuel consumed. If the coefficient of rolling resistance was reduced from 0.006 to 0.005 (16.7 percent reduction), a 4.5 percent FC savings would be achieved for the Peterbilt truck over the cruise mode.

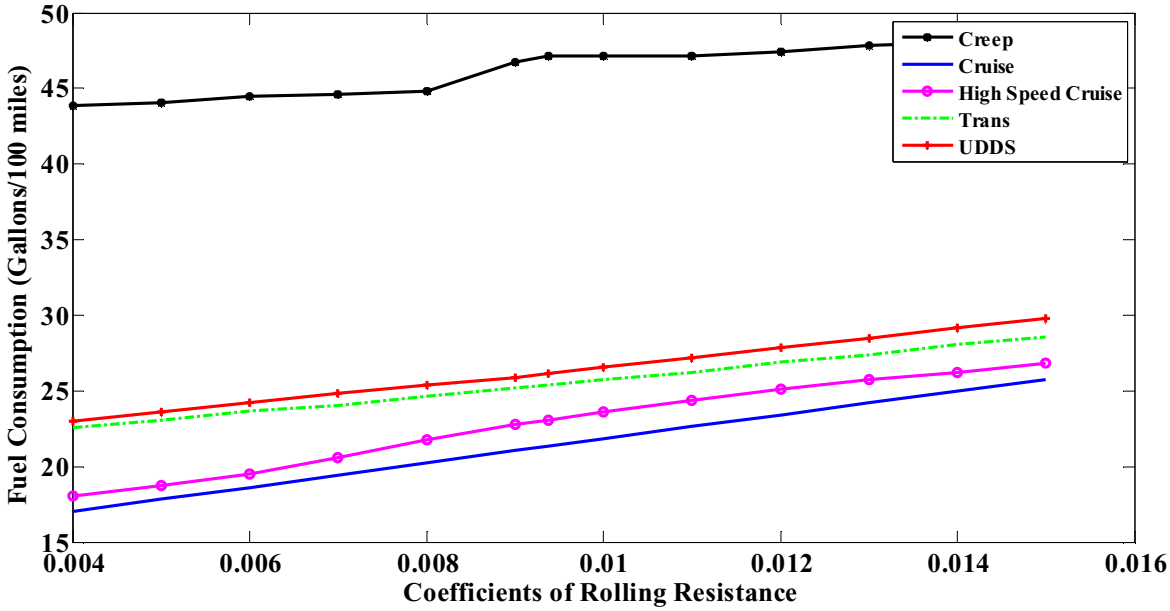

Figure 5.5: The impact of coefficients of rolling resistance on fuel consumption for Peterbilt truck over various driving cycles
(Truck weight = 56,000 lbs, Coefficient of aerodynamic drag C_d = 0.79, Frontal area = 7.06 m^2)

One of the most imposing technology achievements in reducing rolling resistance is to replace the dual tires by wide-based single tires. The pressure in the tires is another factor that affects rolling resistance significantly. For Class 8 truck tires, a 20 percent pressure reduction can cause a 5-8 percent increase in rolling resistance, which yields a 2-3 percent loss in FE [125]. Using nitrogen instead of air for tire inflation is an effective technology that can be used to reduce the pressure loss rate [126]. The coefficient of rolling resistance also mildly depends on temperature, tread wear, vehicle speed and pronouncedly on the tire inflation pressure as well as wheel alignment [14, 127].

5.1.3. Vehicle Weight

The vehicle weight affects the engine power required to propel the vehicle through acceleration, rolling resistance, and hill climbing. Figure 5.6 depicts the simulated performance taking into account the influence of the weight on fuel consumption over various cycles. The results of this simulation show a 9 percent FC reduction over the cruise mode when decreasing the vehicle weight from 76,000 lbs to 66,000 lbs (13 percent weight reduction). In other words, it is expected to see a 0.9 percent fuel saving for every 1,000 lbs of vehicle weight reduction. Obviously, the reduction of truck weight will benefit FC. The "jumping" in the creep mode could again be

attributed to the rounding errors of the very short distance traveled and the very small amount of the fuel simulated. However, the main purpose of heavy-duty vehicles is to deliver payloads. Therefore the metric related to the amount of work performed would be more meaningful. The LSFC (Load-Specific Fuel Consumption) with unit gallon/ton-100 mile as a performance metric was applied in this research. Figure 5.7 demonstrates the PSAT simulation results of LSFC. It shows that the LSFC actually decreases when adding payload to a vehicle. Figure 5.7 also indicates that the LSFC does not change much after the payload is greater than 40 tons. This analysis is for flat land and when the grade is included, the weight may play an even greater role.

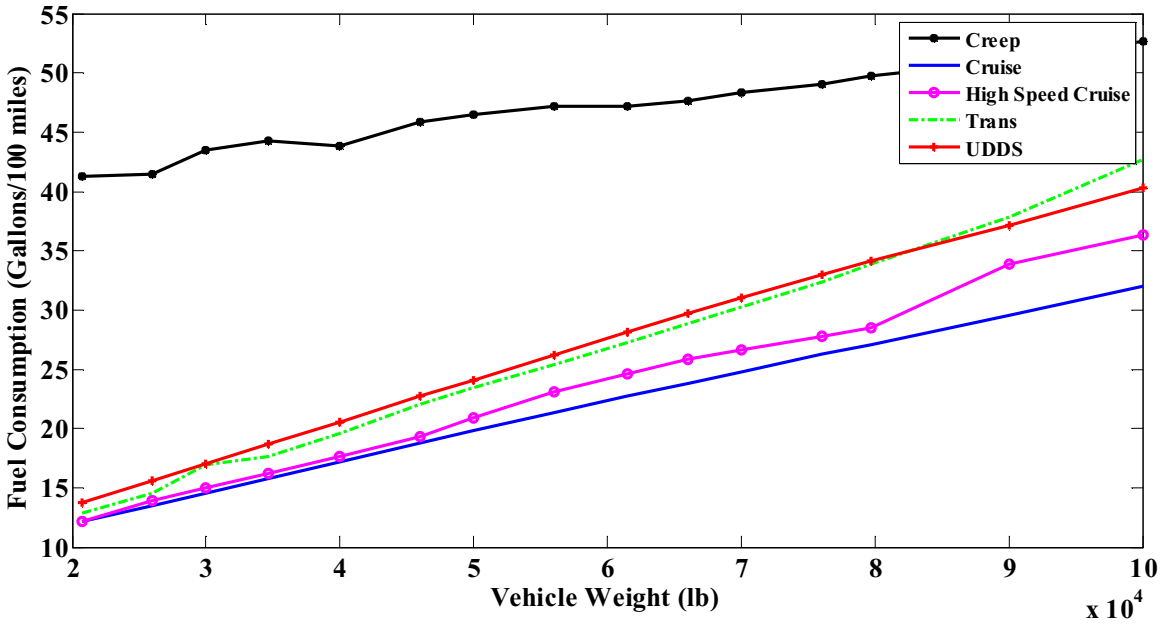

Figure 5.6: The impact of vehicle weight on fuel consumption for Peterbilt truck over various driving cycles
(Coefficient of rolling resistance μ = 0.00938, Coefficient of aerodynamic drag C_d = 0.79, Frontal area = 7.06 m^2)

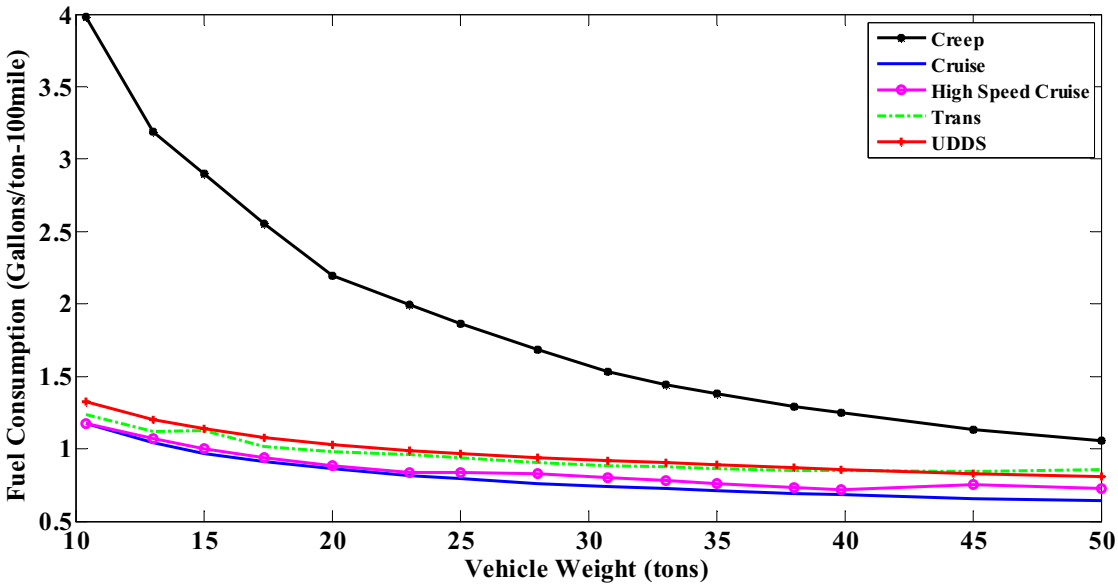

Figure 5.7: The impact of vehicle weight on load-specific fuel consumption for Peterbilt truck over various driving cycles
(Coefficient of rolling resistance μ = 0.00938, Coefficient of aerodynamic drag C_d = 0.79, Frontal area = 7.06 m^2)

When considering fuel-saving technologies through light-weighing, it is necessary to review the empty truck weight. The distribution of the weight among main components of a Class 8 tractor is shown in Figure 5.8 [128]. Table 5.3 shows the summary of weight reduction estimates [14]. Besides the FC benefits from weight reduction, another advantage of light-weighting technology is the ability afforded by the truck manufacturers to maintain the axle load limits imposed by regulation. By using light-weighting technology the tractors can either carry more freight or reduce FC with the same payload capacity.

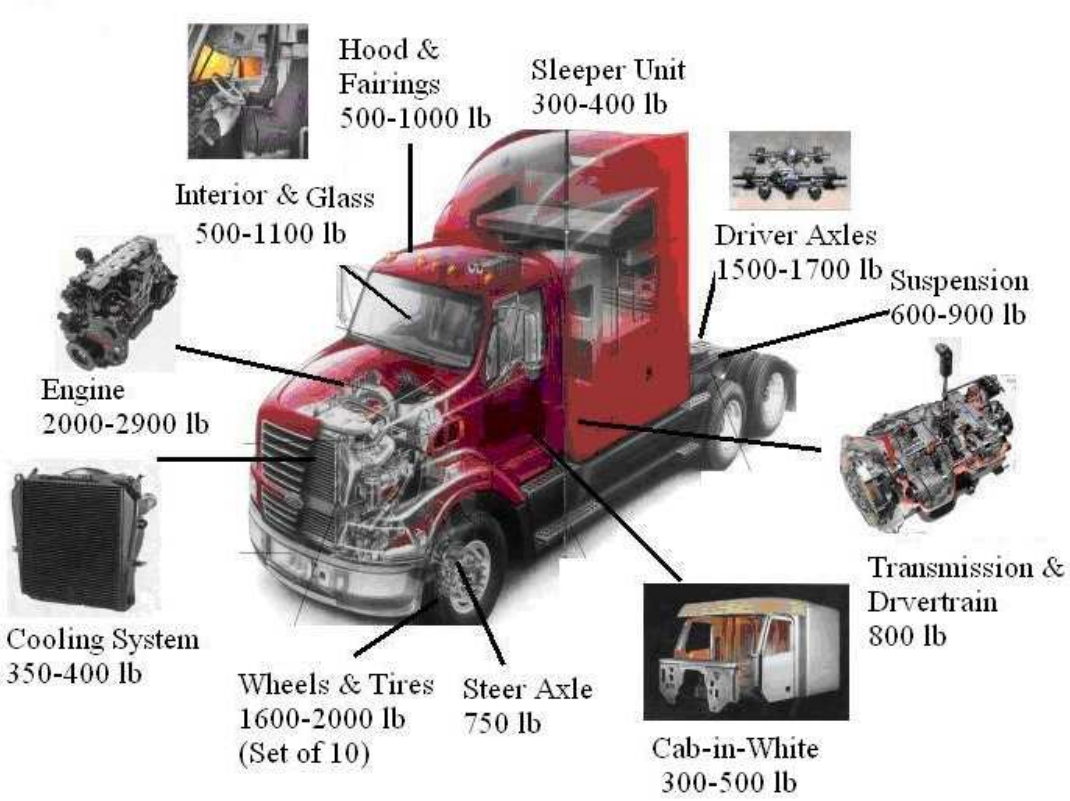

Figure 5.8: Typical weights of specific components in Class 8 sleeper tractor [128]

Table 5.3: Summary of weight reduction estimates [14]

	Weight Reduction Potential
Tractor for Class 8	Wide single wheels affords up to 340 kg total weight saving over dual wheels [129]
	3,000 lbs weight saving was achieved by engine downsize, wide single tires and light trailers [130]
	The 21st Century Truck Partnership agreed on a 20% weight reduction [131]
	Recent Volvo press release said 20% reduced weight feasible in 10 years [132]
	25% weight reduction estimate by American Iron & Steel Institute [133]
Trailer for Class 8	The trailer with new materials and composite structures are approximately 1,000 lbs lighter than previous generation [14]

5.2. The Elasticity of Fuel Consumption

There is another way to view the impacts of parametric variation on FC. Table 5.4 shows the variations of FC over different cycles keeping some parameters constant while varying others by subtracting 5 percent from the base and adding 5 percent to the base numbers. The base numbers used were as follows:

Weight: 56,000 lbs.
Coefficient of aerodynamic drag: 0.79
Coefficient of rolling resistance: 0.00938

Elasticity describes the relation between the proportional change in the dependent variable (FC) in response to a proportional change in the independent variable (weight, rolling resistance or aerodynamic drag) [134, 135]. For example, the elasticity of fuel consumption with respect to weight describes the percentage change in FC in response to a given percentage change of the weight. The formula for the elasticity of fuel consumption with respect to the variables can be expressed by equation 5.2.

$$\varepsilon_x = \frac{dFC/FC}{dx/x}$$ *Equation 5.2 [134]*

where ε_x represents the elasticity of fuel consumption with respect to x, and x represents vehicle weight (abbreviated to W), coefficient of rolling resistance (abbreviated to RR) and coefficient of aerodynamic drag (abbreviated to C_d). Table 5.5 shows the elasticity of fuel consumption with respect to weight, rolling resistance and aerodynamic drag. From Table 5.5, it can be seen that the FC varies with truck weight with an elasticity of 0.6-0.7 over transient, UDDS, cruise, and high speed cruise modes, which indicates that a 10 percent reduction in weight can produce 6-7 percent decrease in FC. Similarly, a 10 percent reduction in rolling resistance can produce 2-3 percent decrease in FC. The elasticity of fuel consumption with aerodynamic drag is highly dependent on the driving cycle. The elasticity of fuel consumption was 0.34 over high speed cruise mode while it was only 0.007 over the creep mode. Overall, the weight has the largest elasticity of fuel consumption of all the parameters and the elasticity increases with the increase of the speed of duty cycles.

Table 5.4: Fuel consumption over different cycles by subtracting 5 percent from the base and adding five percent to the base numbers
(The base numbers: Weight = 56,000 lbs, Coefficients of aerodynamic drag = 0.79, Coefficients of rolling resistance = 0.00938)

Cycle	Weight (lb)	FC (kg/cycle)	Coefficient of Rolling Resistance	FC (kg/cycle)	Product of Aero Drag and Frontal Area (A = 7.06 m^2)	FC (kg/cycle)
Creep	53200	0.1502	0.00891	0.1514	5.3010	0.1517
	56000	0.1517	0.00938	0.1517	5.5774	0.1517
	58800	0.1520	0.00985	0.1521	5.8590	0.1518
Transient	53200	2.2355	0.00891	2.2877	5.3010	2.3055
	56000	2.3164	0.00938	2.3164	5.5774	2.3164
	58800	2.3977	0.00985	2.3450	5.8590	2.3250
UDDS	53200	4.3788	0.00891	4.4902	5.3010	4.5058
	56000	4.5418	0.00938	4.5418	5.5774	4.5418
	58800	4.7159	0.00985	4.6087	5.8590	4.5755
Cruise	53200	15.3122	0.00891	15.5519	5.3010	15.5933
	56000	15.8275	0.00938	15.8275	5.5774	15.8275
	58800	16.3539	0.00985	16.1071	5.8590	16.0662
HHDDTs	53200	7.4250	0.00891	7.5921	5.3010	7.5792
	56000	7.7106	0.00938	7.7106	5.5774	7.7106
	58800	7.9769	0.00985	7.8342	5.8590	7.8437

Table 5.5: The elasticity of fuel consumption with respect to weight, rolling resistance and aerodynamic drag

Cycle	Weight (lb)	εW	Coefficient Of Rolling Resistance	εRR	Product of Aero Drag and Frontal Area (A = 7.06 m^2)	εC_d
Creep	55720	0.1187	0.00891	0.0461	5.3010	0.0066
	56000		0.00938		5.5774	
	56280		0.00985		5.8590	
Transient	55720	0.7002	0.00891	0.2474	5.3010	0.0842
	56000		0.00938		5.5774	
	56280		0.00985		5.8590	
UDDS	55720	0.7422	0.00891	0.2609	5.3010	0.1535
	56000		0.00938		5.5774	
	56280		0.00985		5.8590	
Cruise	55720	0.6582	0.00891	0.3508	5.3010	0.2988
	56000		0.00938		5.5774	
	56280		0.00985		5.8590	
HHDDT_s	55720	0.7158	0.00891	0.3140	5.3010	0.3430
	56000		0.00938		5.5774	
	56280		0.00985		5.8590	

5.3. Impact of Multiple Technologies on Fuel Consumption

As seen from the above section, the FC significantly differs when the different parameters are chosen. This section will provide a method to estimate the FC of the Peterbilt truck over various cycles as a function of multiple parameters (such as coefficients of aerodynamic drag and rolling resistance, vehicle weight and coefficient of rolling resistance). Figures 5.9-5.13 show a parametric sweep conducted on the Peterbilt truck model over the creep, transient, UDDS, cruise, and high speed cruise modes. The FE contours are a function of coefficients of aerodynamic drag and rolling resistance at a constant weight (56,000 lbs). The fuel economy was not affected by aerodynamic drag during the creep mode, as shown in Figure 5.9. The next four figures (Figures 5.10 through 5.13) indicate a very similar relationship between fuel economy and the individual variables (coefficients of rolling resistance and aerodynamic drag) used to construct the chart. A trend can be seen from these grouped fuel economy contour lines. In the high fuel economy region, the line spaces are closer and have deep gradients, while the gradient was lower at low fuel economy, which was believed to lie with the definition of FE [136]. FE is the amount of fuel

consumed over a given distance. The rate of change of FE can be obtained with a derivative, as shown by Equation 5.3.

$$\frac{d(D/V)}{dV} = -\frac{D}{V^2} \qquad \textit{Equation 5.3}$$

where D is a constant distance traveled, V is volume of the FC over this distance, and D/V is the fuel economy. Figures 5.10 -5.13 also demonstrate how fuel economy is influenced relatively by parameters. In Figure 5.12, cruise mode for example, when the coefficient of aerodynamic drag is 0.55 and the coefficient of rolling resistance is 0.0055, it could be concluded that decreasing the coefficient of aerodynamic drag by 0.09 has the same effect as reducing the coefficient of rolling resistance by 0.0008. This suggests that, depending on the circumstances, it may be more cost effective to reduce one parameter (such as coefficient of aerodynamic drag) to increase fuel economy, or it may be more beneficial to reduce another (such as the coefficient of rolling resistance). Another function of these contour figures is to provide a way to estimate FE conveniently by interpolating within the parameter values and extrapolating outside of them.

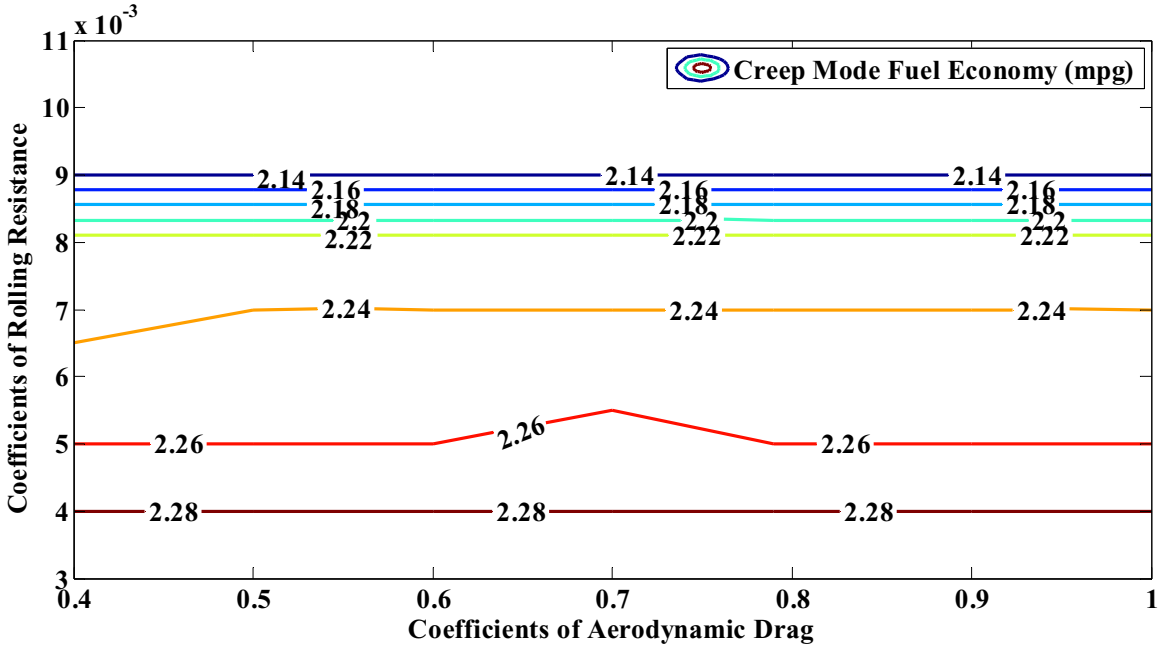

Figure 5.9: Fuel economy contour map for Peterbilt truck for various coefficients of rolling resistance and aerodynamic drag over the creep mode
(Truck weight = 56,000 lbs, Frontal area = 7.06 m^2)

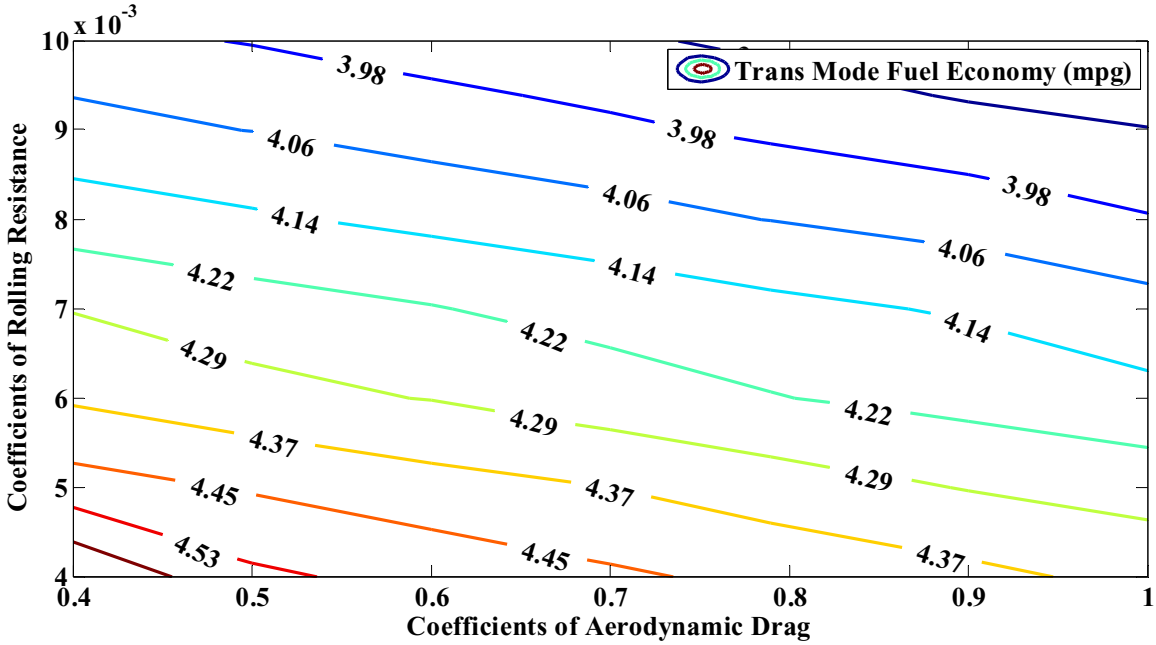

Figure 5.10: Fuel economy contour map for Peterbilt truck for various coefficients of rolling resistance and aerodynamic drag over the Transient mode
(Truck weight = 56,000 lbs, Frontal area = 7.06 m^2)

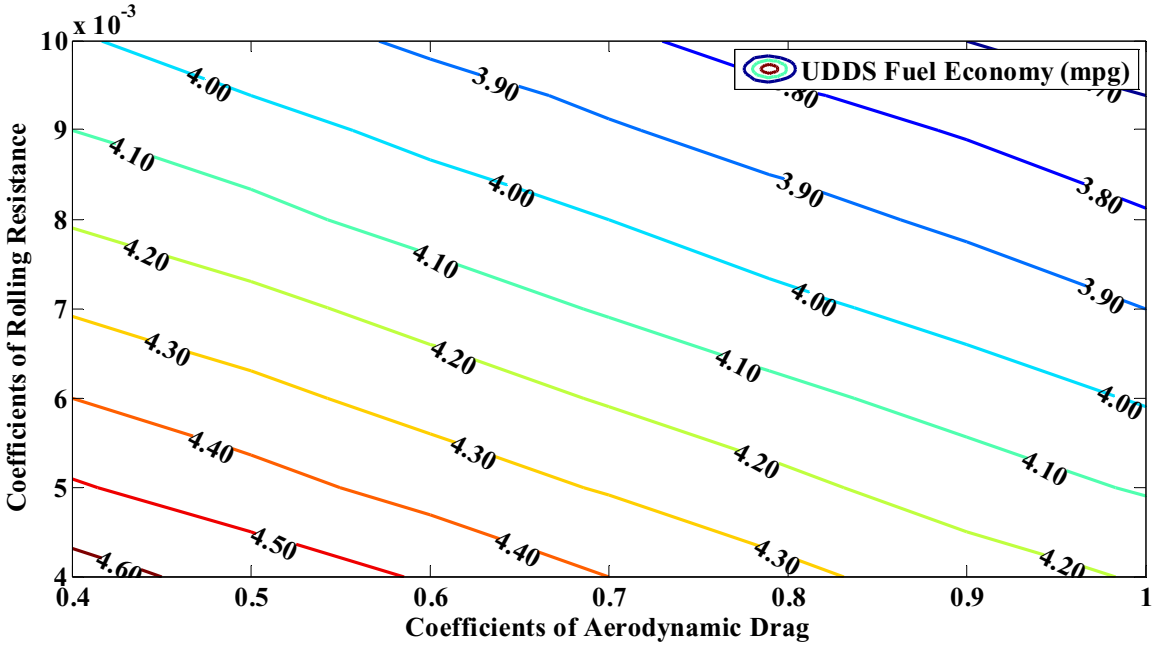

Figure 5.11: Fuel economy contour map for Peterbilt truck for various coefficients of rolling resistance and aerodynamic drag over the UDDS mode
(Truck weight = 56,000 lbs, Frontal area = 7.06 m^2)

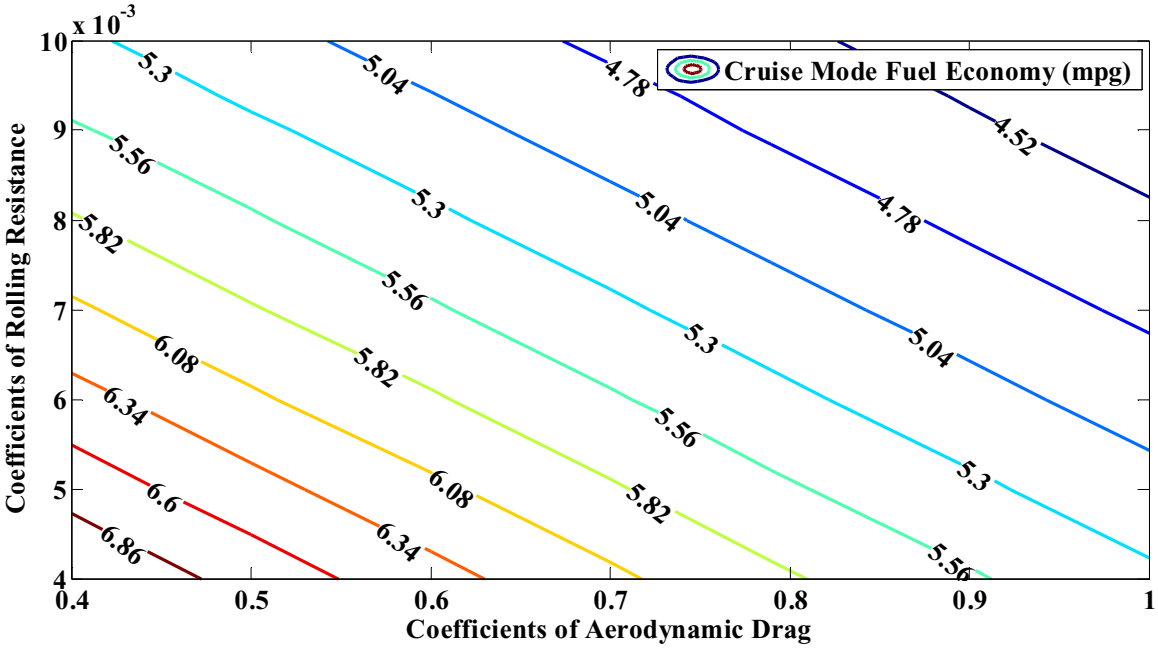

Figure 5.12: Fuel economy contour map for Peterbilt truck for various coefficients of rolling resistance and aerodynamic drag over the cruise mode
(Truck weight = 56,000 lbs, Frontal area = 7.06 m^2)

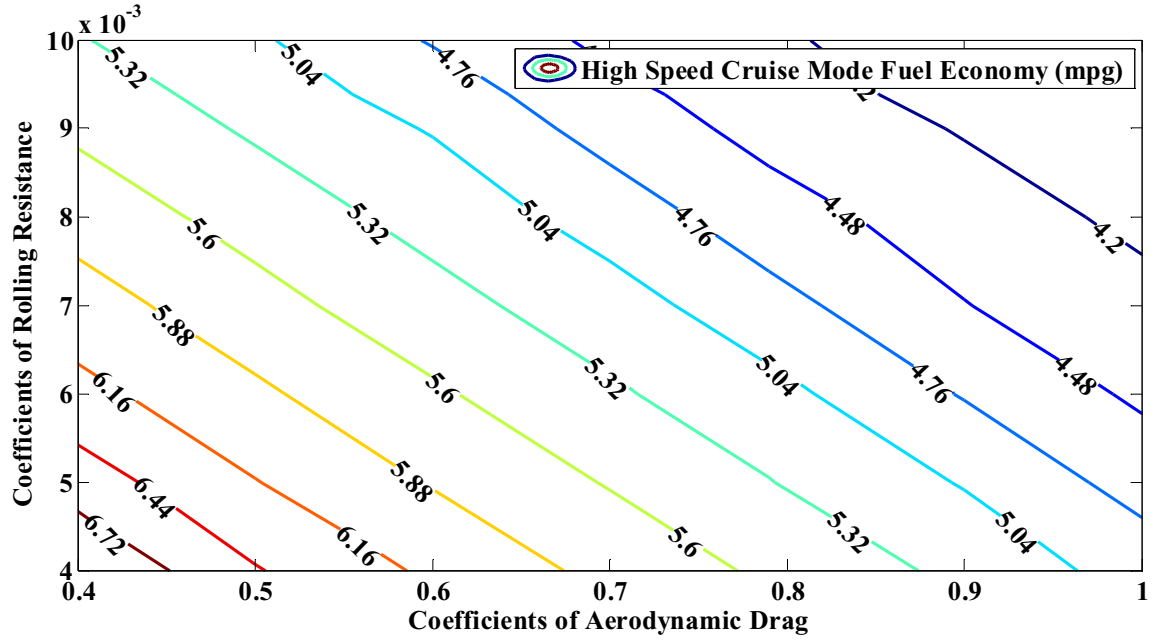

Figure 5.13: Fuel economy contour map for Peterbilt truck for various coefficients of rolling resistance and aerodynamic drag over the high speed cruise mode
(Truck weight = 56,000 lbs, Frontal area = 7.06 m^2)

Other cases to analyze how FE can be influenced by multiple parameters are shown in Figures 5.14-5.18, which demonstrate the FE contour figures on various coefficients of rolling resistance and truck weight at a constant coefficient of aerodynamic drag (C_d = 0.79) over the creep, transient, UDDS, cruise, and high speed cruise modes. Irregular lines shown in Figure 5.14 are caused by two facts. The first reason, as addressed in former research, is the fact that the weight influences the ability of the truck to follow the trace closely in the creep mode [20]. Another reason is because of the rounding errors of the very short distance traveled and the very small amount of fuel consumed. Another area to pay attention to is the irregular contour lines at low weight in transient mode (Figure 5.15). This might be caused by the influence of gear shifting behavior on FC. Figures 5.15-5.18 illustrate a similar trend between fuel economy and the individual variables (vehicle weight and coefficients of rolling resistance) used to construct the contour maps. The contour lines are closer and the gradients are larger at high FE. In contrast, contour lines spread and the gradients are smaller at low FE. As stated, the contour maps can be used to find the relative change in FE by parameters. For instance, examine the FE in Figure 5.17 for the cruise mode, it was observed that reducing the truck weight from 27,000 lbs to 24,000 lbs (11 percent weight reduction) had the same impact on reducing coefficients of rolling resistance from 0.0085 to 0.0062 (27 percent reduction). And likewise, Figures 5.15-5.18 can be used to estimate FE by interpolating within the parameter values and extrapolating outside of them.

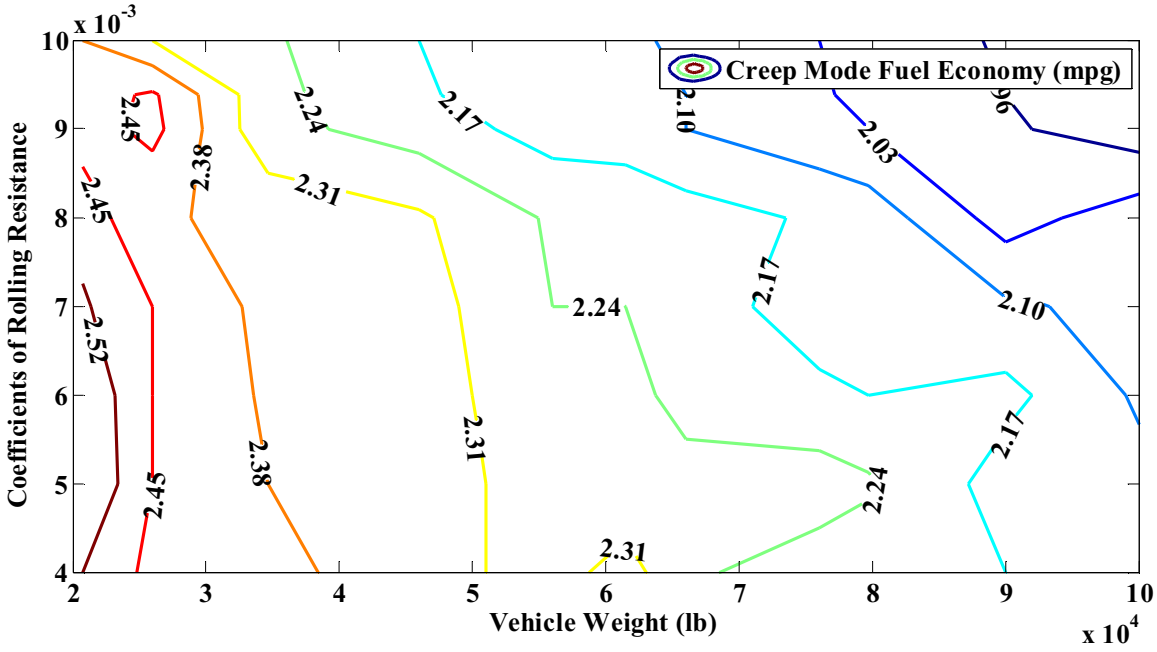

Figure 5.14: Fuel economy contour map for Peterbilt tuck on various coefficients of rolling resistance and truck weight over the creep mode
(Coefficient of aerodynamic drag C_d = 0.79, Frontal area = 7.06 m^2)

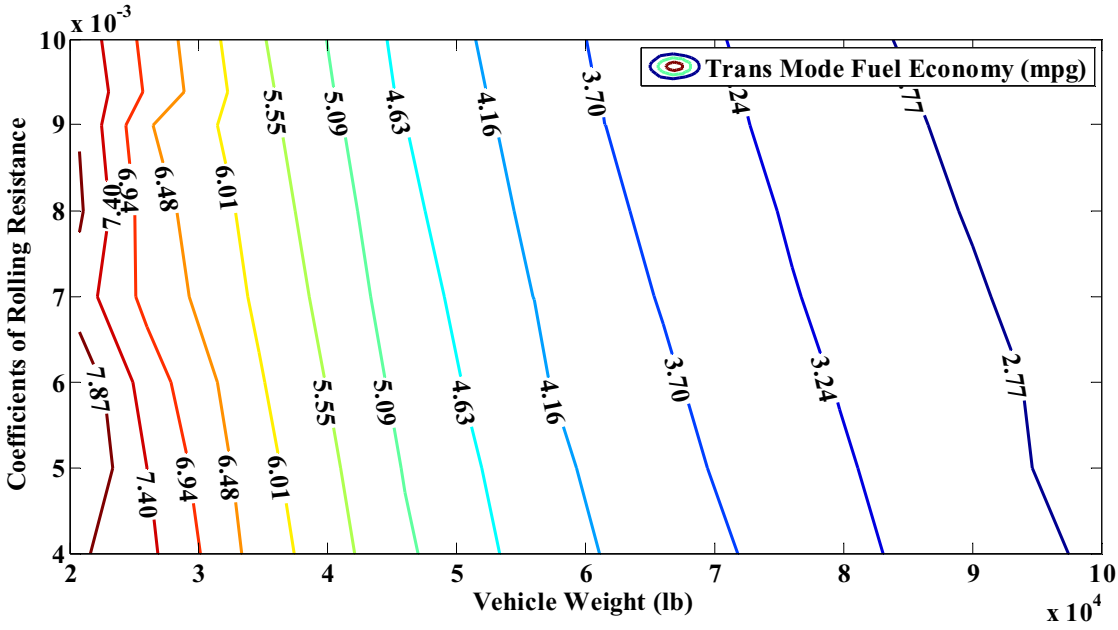

Figure 5.15: Fuel economy contour map for Peterbilt tuck on various coefficients of rolling resistance and truck weight over the transient mode
(Coefficient of aerodynamic drag C_d = 0.79, Frontal area = 7.06 m^2)

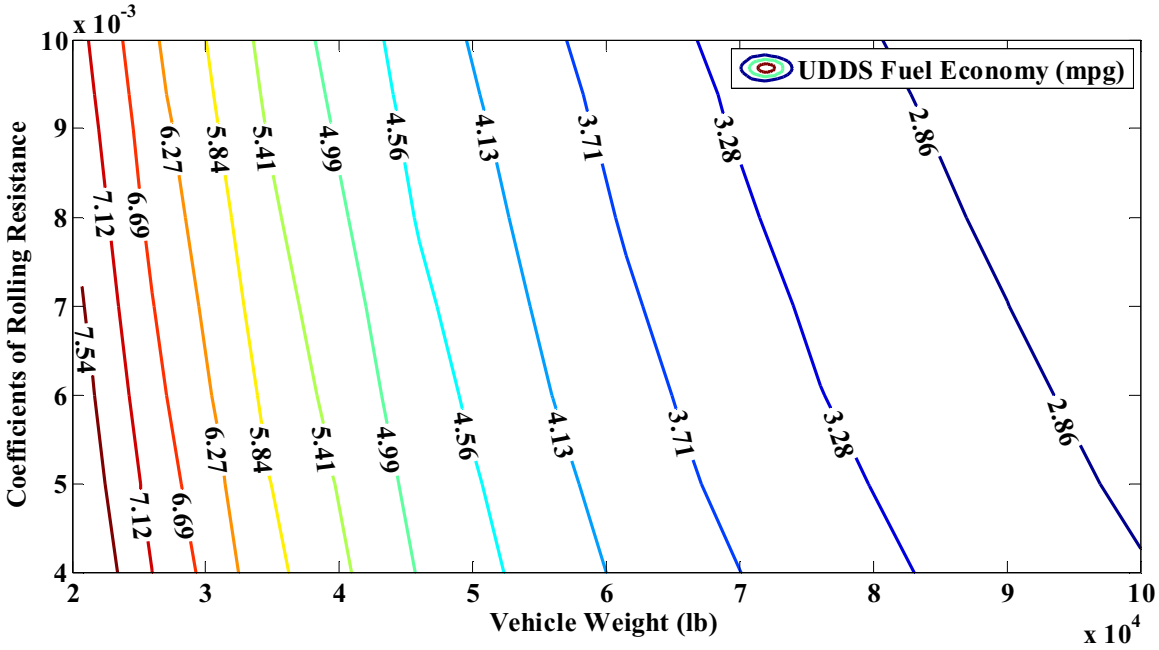

Figure 5.16: Fuel economy contour map for Peterbilt tuck on various coefficients of rolling resistance and truck weight over the UDDS
(Coefficient of aerodynamic drag C_d = 0.79, Frontal area = 7.06 m^2)

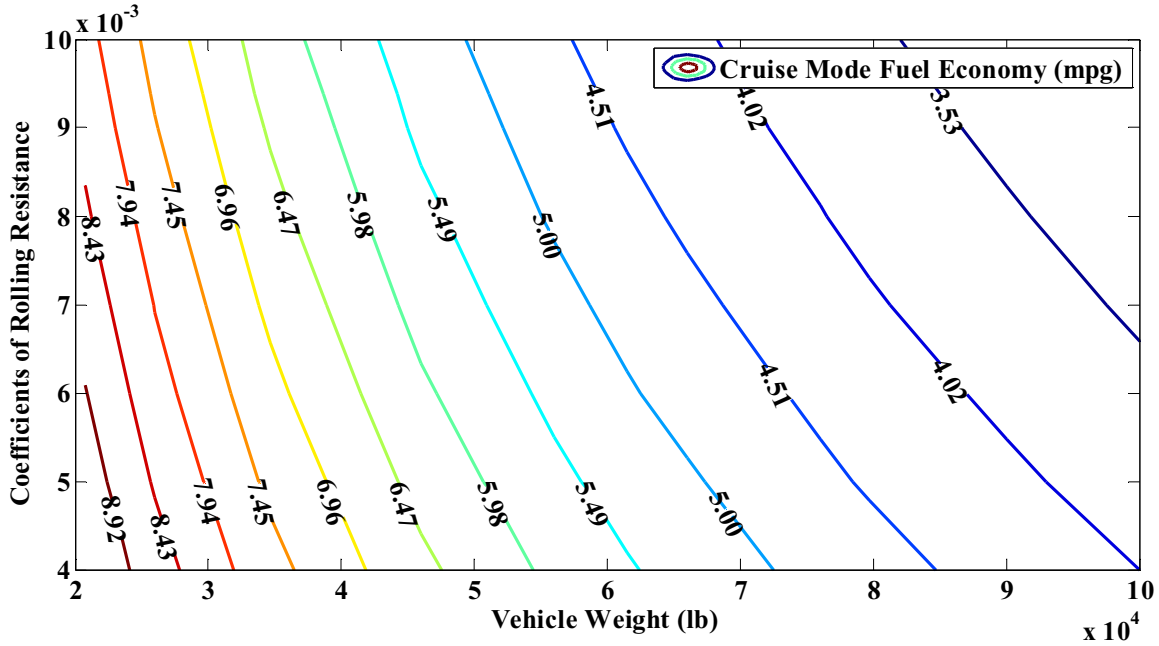

Figure 5.17: Fuel economy contour map for Peterbilt tuck on various coefficients of rolling resistance and truck weight over the cruise mode
(Coefficient of aerodynamic drag C_d = 0.79, Frontal area = 7.06 m^2)

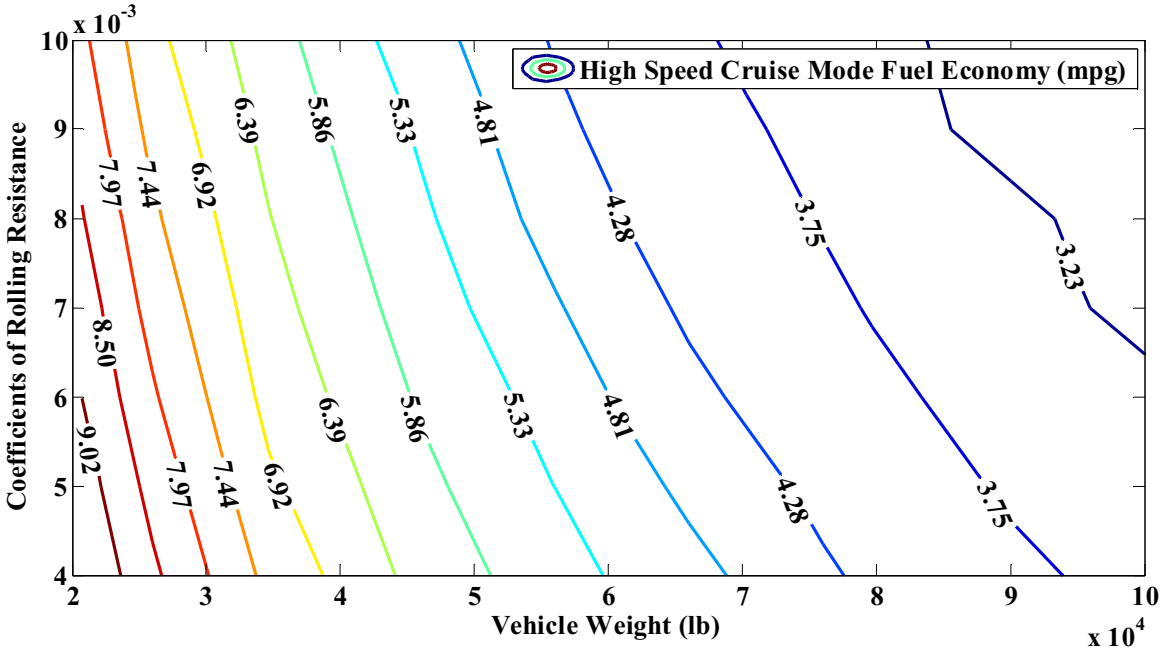

Figure 5.18: Fuel economy contour map for Peterbilt tuck on various coefficients of rolling resistance and truck weight over the high speed cruise mode
(Coefficient of aerodynamic drag C_d = 0.79, Frontal area = 7.06 m^2)

5.4. Grade Effect on Fuel Economy and NO_x Emissions

The effect of road grade on FC and NO_x emissions has been addressed [34, 38]. The Peterbilt truck model was simulated over the UDDS with a uphill grade ranging from 1% to 5% on PSAT. The truck could overcome a 3% uphill grade without compromising its speed (Table 5.6), whereas the truck had difficulty following the target speed during high acceleration with a grade of more than 3%. This was due to the fact that the peak power rating of the truck was not high enough for the UDDS with more than a 3% road grade. Figure 5.19 shows the vehicle target speed and the PSAT simulated speed over the UDDS with 4% (left) and 5% (right) road grade. Table 5.6 indicates that the UDDS with a 3% grade produces a 22.51% decrease in FE while at the same time it generates 16.00% more NO_x emission when compared to the UDDS with no grade.

Table 5.6: The road grade effects on FE and NOx emissions

Grade (%)	0	1	2	3	4	5
FE (mpg)	3.82	3.52	3.23	2.96	2.73	2.47
Cycle (mile)	5.41	5.41	5.41	5.41	5.37	5.23
NO_x (g/mile)	17.81	18.21	19.39	20.66	22.08	23.05

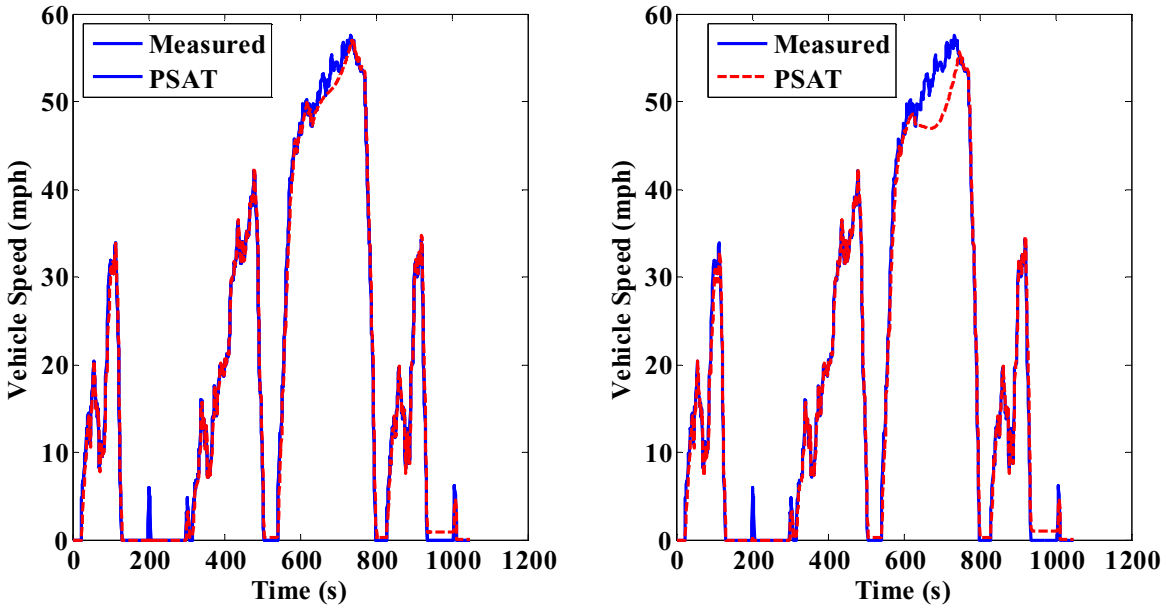

Figure 5.19: The target and PSAT simulated vehicle speed with 4% uphill road grade (left) and 5% uphill road grade (right)

In the real world, terrains were classified into three types by the American Association of State Highway and Transportation Officials (AASHTO) [137]: flat terrain, rolling terrain and mountain terrain. Road elevation in rolling terrain consistently rises above and falls below the

road grade [34]. Graphical representations of road grade with rolling terrains on the UDDS are demonstrated in Figures 5.20-5.21. The road grade on rolling terrain was mimicked by a sine wave with a 3% wave crest road grade, which implied that ascending a rolling hill in a sinusoidal way reaching a 3% maximum grade followed by descending 3% to level in the same way [34]. In Figure 5.20, the grade of rolling terrain was determined with respect to the distance traveled on the UDDS. The straight line stood for idle time. So no distance was traveled and no change in grade occurred. An alternate way to generate the road grade was proposed by Khan [34]. The road grade was produced with respect to time instead of distance, as shown in Figure 5.21. As a result, the road grade was characterized as a continuous function of cycle time traveled [34].

The Peterbilt truck model was simulated over the UDDS with the road grade based on distance traveled duration and road grade based on time traveled duration. A 2.96 mpg FE was acquired for the two types of grades.

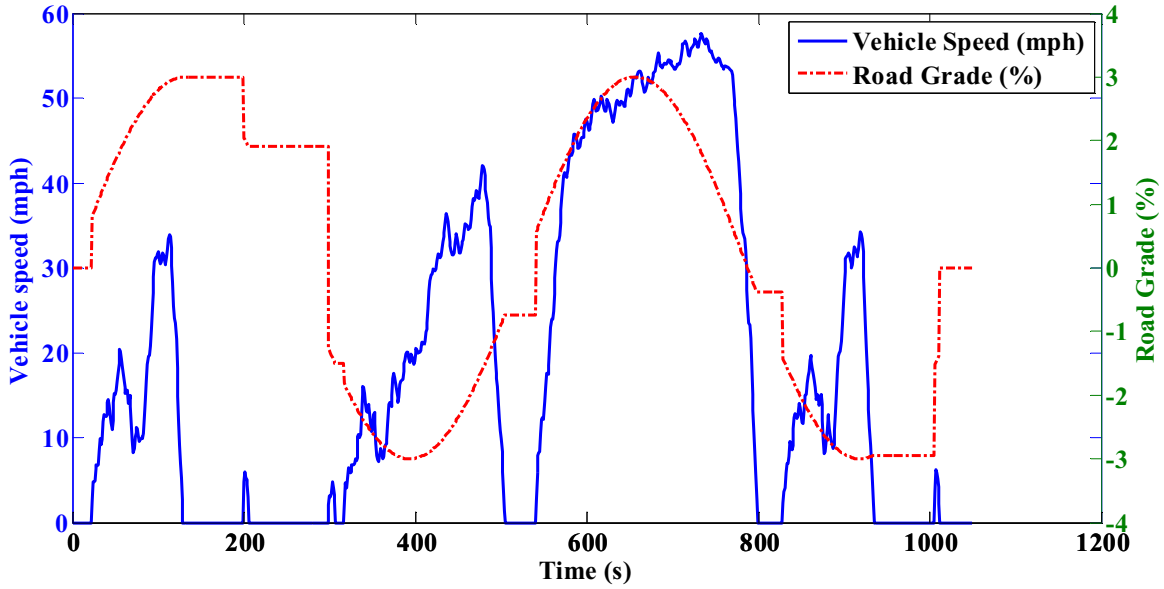

Figure 5.20: Road grade on the UDDS against cycle distance duration for rolling terrains

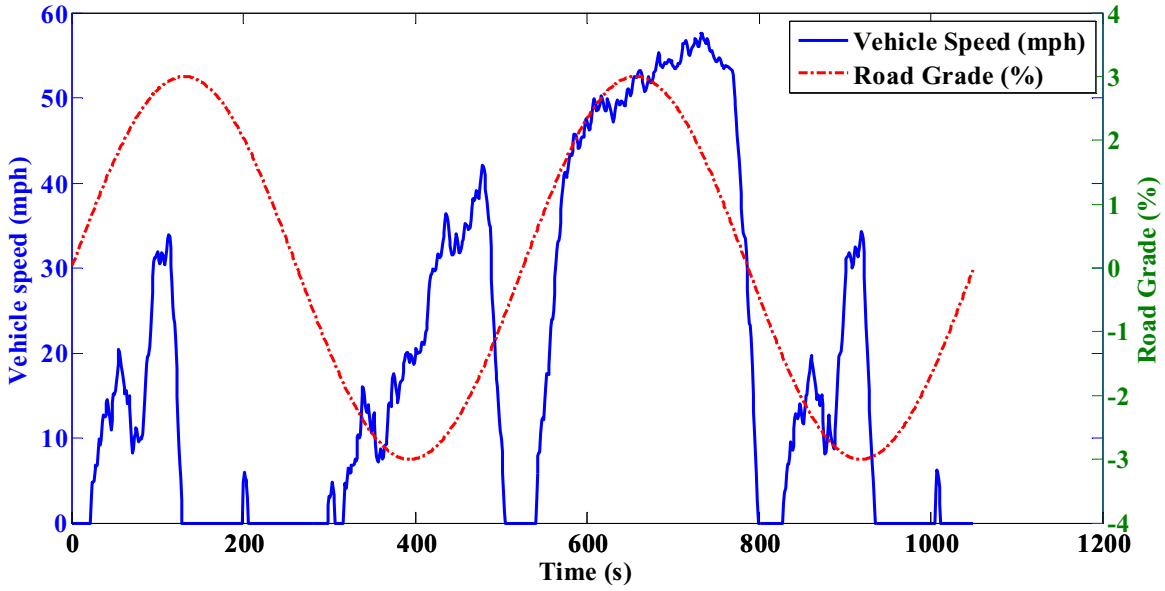

Figure 5.21: Road grade on the UDDS against cycle time duration for rolling terrains

5.5. Impact of Auxiliary Load on Fuel Consumption

In addition to powering the wheels, auxiliary loads also contribute to energy consumption. The engine cooling fan is used for cooling the coolant in the radiator; the engine oil pump is used for pumping motor oil for circulation around the engine; compressed air is used for the braking system; the air conditioner is used for driver and passengers' comfort; the alternator is used to charge the vehicle's ESS and the power steering systems require power to drive the associated pumps and compressors [14]. The amount of energy consumed by auxiliary loads highly depends on the vehicle operating cycle. Table 5.7 demonstrates the average engine power and auxiliary power required during various driving conditions. At high speed cruise, auxiliary load accounts for about 11 percent of engine power (assuming ambient temperature is 75 ^{o}F). While in the creep mode, most of the power generated by the engine is consumed by the auxiliary loads.

Table 5.7: Average engine power and auxiliary power over various driving cycles (C_d = 0.79, μ = 0.00938, weight = 56,000 lbs)

	Creep	Transient	UDDS	Cruise	HHDDT_s
Average Engine Power (hp)	13.94	80.74	98.30	180.25	258.04
Average Auxiliary Power (hp)	10.31	14.41	15.33	22.45	29.5

5.6. Parametric Study on Oxides of Nitrogen

As the NO_x emissions are closely related the power output of engines, changes in the power requirement should also be expected to result in a corresponding change in NO_x emissions. It is essential to convey the quantitative effects of factors on NO_x emissions from parametric analysis. Clark et al. [138] explored the vehicle weight effect on emissions and FC from a diesel bus. The NO_x emissions from this bus varied considerably on all cycles at all vehicle weights that were addressed. Some efforts were made to understand the effect of aerodynamic drag and rolling resistance on NO_x emissions and FC [139]. The Peterbilt truck was simulated by PSAT over transient, UDDS, cruise and high speed cruise modes at various weights, coefficients of rolling resistance and aerodynamic drag. The simulation results are shown in Figures 5.22-5.24. Overall, the impacts of rolling resistance, aerodynamic drag and weight on NO_x emissions had a similar effect as FC. These figures show that there are nearly linear relationships between NO_x emissions and the rolling resistance, aerodynamic drag, and vehicle weight. There is a 2.8 percent NO_x emissions reduction when reducing the coefficient of rolling resistance from 0.007 to 0.006 (14 percent reduction) over the cruise mode. A 1.8 percent of NO_x emissions reduction was obtained over the cruise mode by reducing the coefficient of aerodynamic drag from 0.7 to 0.6 (14 percent reduction) and a 6.8 percent of NO_x emissions reduction was achieved by reducing the truck weight from 70,000 lbs to 60,000 lbs (14 percent reduction).

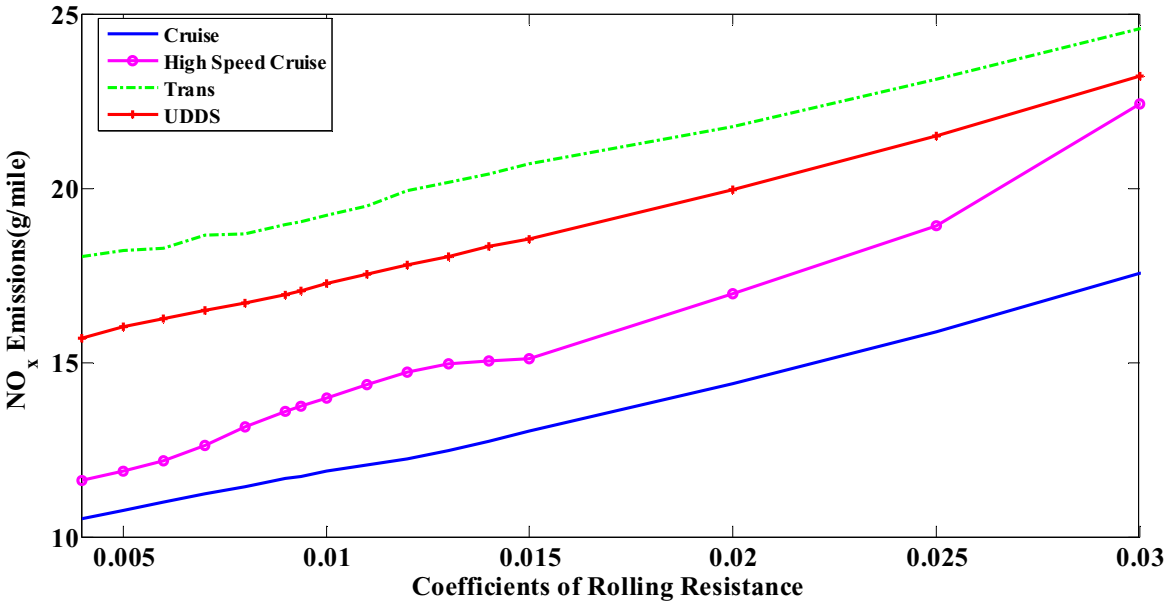

Figure 5.22: The impact of coefficients of rolling resistance on NO_x emissions for Peterbilt truck over various driving cycles
(Truck weight = 56000 lbs, Coefficient of aerodynamic drag C_d = 0.79)

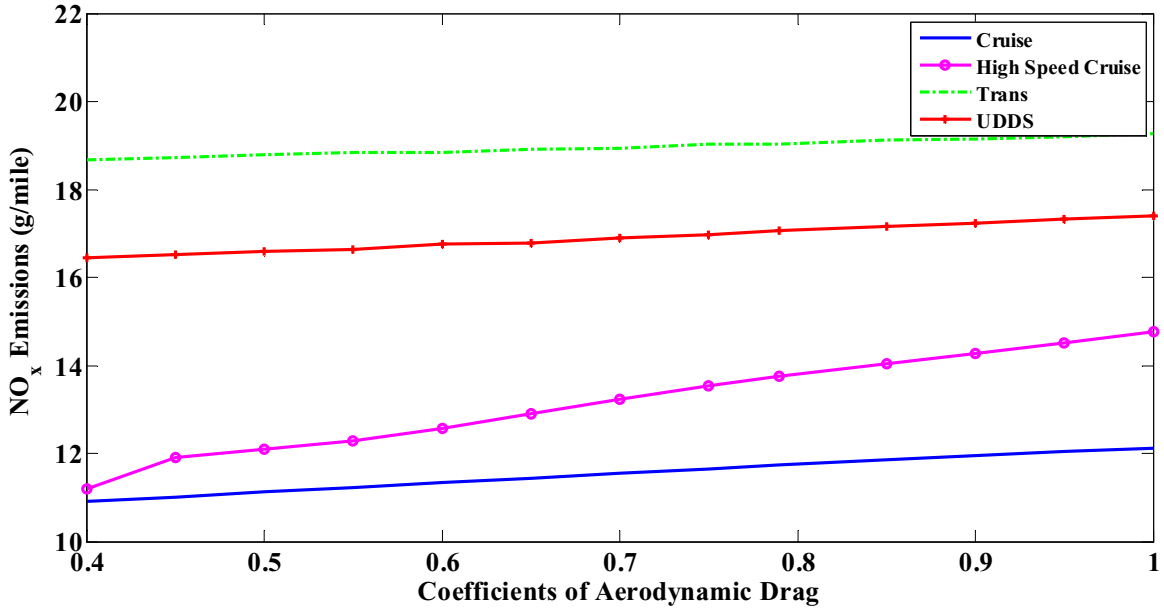

Figure 5.23: The impact of coefficients of aerodynamic drag on NO_x for Peterbilt truck over various driving cycles
(Truck weight = 56,000 lbs, Coefficient of Rolling Resistance μ = 0.00938, Frontal area = 7.06 m^2)

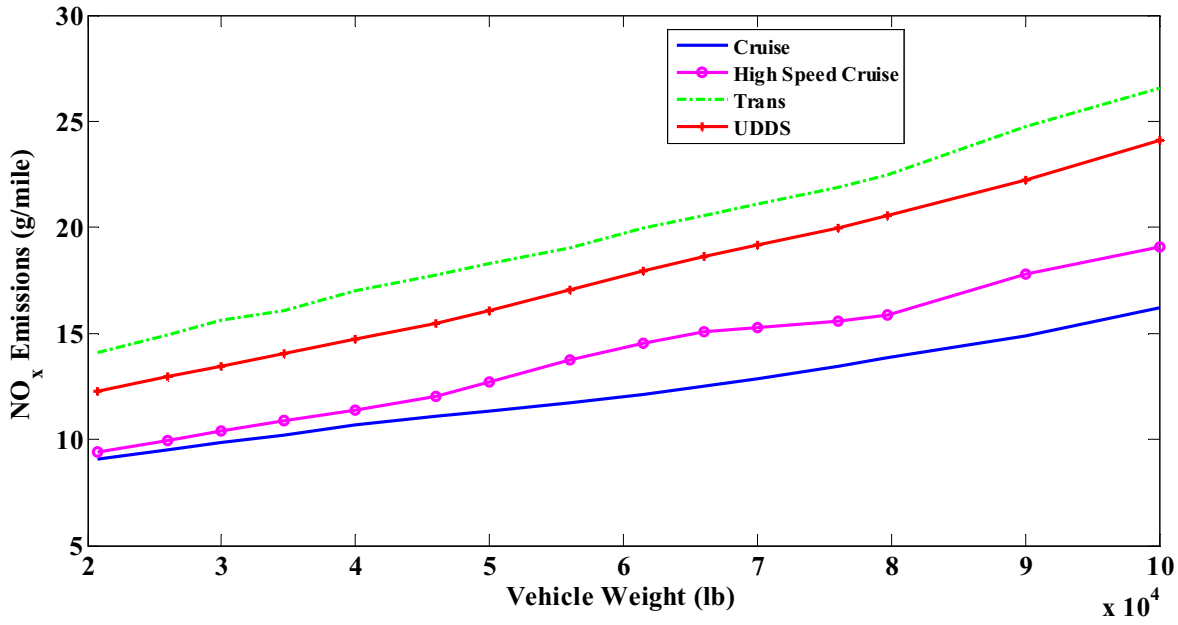

Figure 5.24: The impact of coefficients of vehicle weight on NO_x for Peterbilt truck over various driving cycles
(Coefficient of aerodynamic drag $C_d = 0.79$, Coefficient of rolling resistance $\mu = 0.00938$, Frontal area = 7.06 m^2)

5.7. The Impact of Different Engines on Oxides of Nitrogen Emissions

The effect of different engines on NO_x emissions was also examined in this dissertation. In the conventional truck model, the original 1996 Caterpillar 3406E engine of the Peterbilt truck was substituted by a model of two other engines: a 1999 Cummins ISM 370 hp non-EGR engine, and a 2004 Cummins ISM 370 hp EGR engine. The truck models then were simulated in PSAT over different cycles. Table 5.8 summarizes the PSAT simulation results for NO_x with different engines. The 2004 Cummins engine has the least NO_x emissions, which was due to the fact that the EPA adopted new emission regulations for MY 2004 and later heavy duty vehicles and engines. It should be noticed that the vehicle with the new replaced engines (1999 Cummins ISM 370 and 2004 Cummins ISM 370) could not follow the target vehicle speed at high accelerations due to the lack of engine power.

Table 5.8: NO_x emissions (g/mile) when different engine was replaced on Peterbilt truck over different driving modes
($C_d = 0.79$, $\mu = 0.00938$, weight = 56,000 lbs)

Mode / Engine	Creep	Transient	UDDS	Cruise	HHDDT_s
1996 Caterpillar	70.75	19.03	17.06	11.74	13.74
1999 Cummins	77.40	21.13	20.88	16.23	16.71
2004 Cummins	65.65	13.82	11.25	7.96	8.09

5.8. Summary

This section quantified the impacts of factors on FC by simulating the Peterbilt truck using PSAT. Factors used in this section included vehicle weight, road grade, coefficient of rolling resistance and aerodynamic drag. The simulation results indicated that there was no benefit for aerodynamic drag reduction on the creep mode, there was some benefit for aerodynamic drag reduction from medium speed cycles and a large benefit could be achieved from high speed cycles. The results further revealed that reducing the coefficient of aerodynamic drag from 0.6 to 0.5 with the same frontal area led to a 4.2 percent FC reduction, and reducing the coefficient of rolling resistance from 0.006 to 0.005 lead to a 4.5 percent FC reduction for the Peterbilt truck over the cruise mode. Among the three parameters, the truck weight had the largest effect on FC as the weight affected FC through acceleration, rolling resistance, and hill climbing. A 9 percent FC reduction over the cruise mode was found with reducing the vehicle weight by 10,000 lb. However, due to the fact that the primary purpose of heavy-duty vehicles is to carry freight, the metric related to the amount of work performed, LSFC with unit gallon/ton-100 mile was suggested in this research. Simulation results showed that the LSFC tended to decrease when adding payload to the vehicle. A new term, elasticity of fuel consumption, which described the relation between the proportional change in the dependent variable in response to a proportional change in the independent variable was introduced for further reviewing the impacts of parametric variation on FC. The impacts of factors on FC were further verified by the elasticity of fuel consumption.

To examine the road grade effect on FE and NO_x emissions, the Peterbilt truck model was simulated over the UDDS with a grade ranging from 1% grade to a 5% grade on PSAT. The results showed that the truck can overcome 3% grade without sacrificing its speed, but had difficulty following the target speed at high acceleration when the grade is greater than 3%. The simulation also indicated that the UDDS with a 3% grade produces a 22.51% decrease in FE while at the same time it generates 16% more NO_x emissions compared to the UDDS with no grade.

Auxiliary loads also contributed to FC. Simulation results indicated that the amount of energy consumed by auxiliary loads was highly dependent upon the driving cycles. Auxiliary loads consumed about 11 percent of engine power at the high speed cruise mode. While in the creep mode, auxiliary loads accounted for most of the power generated by the engine. As for the effects of factors on NO_x emissions, simulation results showed that there were approximate linear relationships between NO_x emissions and given factors, as well as FC and given factors.

Chapter 6: Hybrid Bus Modeling and Simulation

6.1. Overview of the Series Hybrid Bus

The HEB modeled in this study was a New Flyer bus with a series ISE hybrid system. The specific hybrid system design included a Cummins ISB 260H diesel ICE, a permanent magnet synchronous 221 hp at peak power electric generator, 7 phase inverters, a Maxwell BCAP0010 2600 Farad ultracapacitor package, a traction motor inverter and an AC induction 201 hp at peak power traction motor/brake [80]. Like most series hybrid buses, there is a one-gear reduction transmission and a rear axle differential reduction in the New Flyer HEB. The energy flow schematic of the ISE system is shown in Figure 6.1 [80]. The engine is not directly coupled to the vehicle drviertrain, but it is connected to a generator that supplies power to motor to propel the wheel. When the power required from the wheels is lower than the engine supplied, part of the power is used for charging the ultracapacitors until the ultracapacitors reach the maximum threshold. During braking, the traction motor acts as a generator to transform the kinetic energy into electricity which is used to charge the ultracapacitors. The auxiliary loads, such as the air conditioning system and compressors are electrically powered. The PSAT drivetrain configuration of the New Flyer ISE HEB is shown in Figure 6.2. Detailed specification used for the New Flyer bus with series ISE hybrid system can be found in Table 6.1 [80].

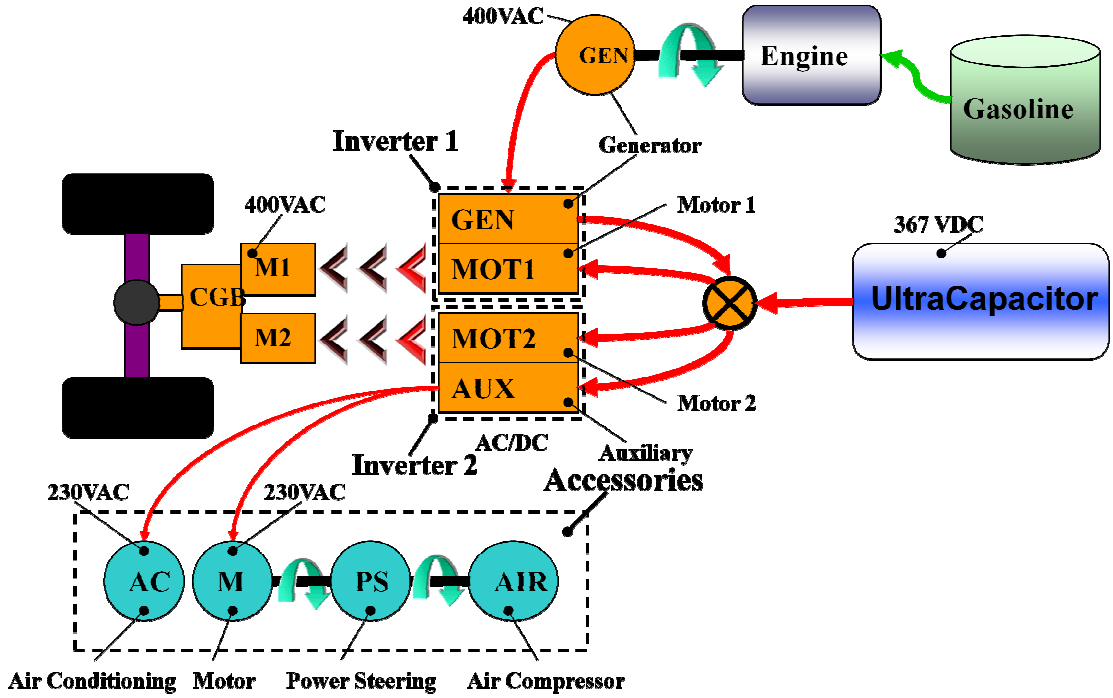

Figure 6.1: The energy flow schematic of the New Flyer Bus with an ISE hybrid system [80]

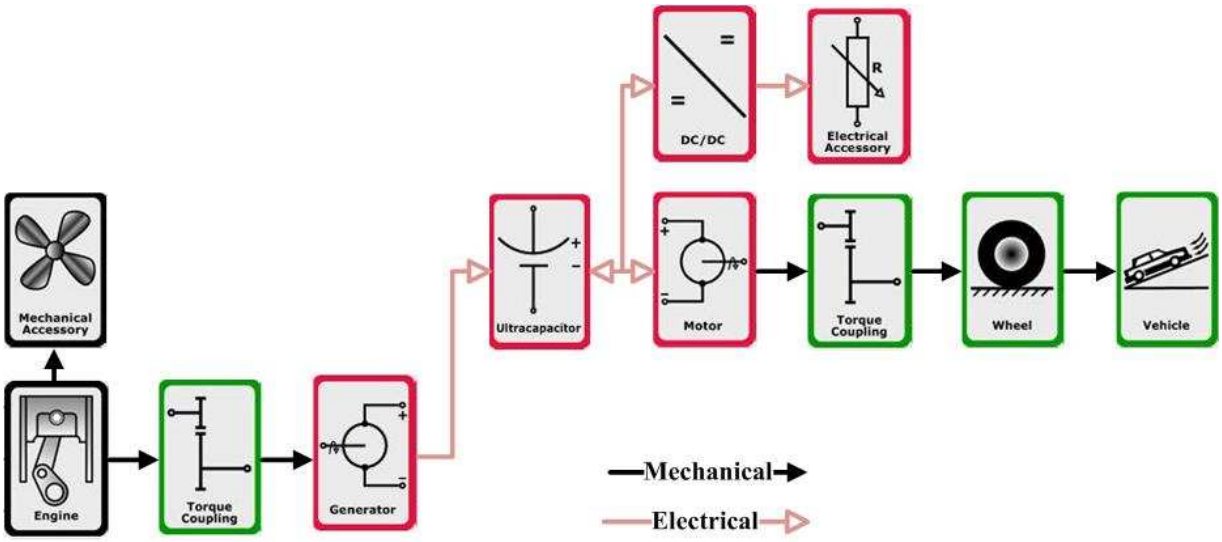

Figure 6.2: The drivertrain configuration of the New Flyer hybrid bus in PSAT

Table 6.1: The detail information of the New Flyer bus with series ISE hybrid system [80]

Vehicle	**Type**	Series Hybrid Bus
	Manufacturer	New Flyer of America
	Model Year	2007
	Gross Weight	42,540 lb (19,296 kg)
	Curb Weight	32,540 lb (14,760 kg)
	Tested Weight	36,070 lb (16,361kg)
	Odometer Reading	29,036 Miles
Single Reduction Transmission Gear Ratio		4.05
Final Drive Ratio		4.08
Tire Size		305/70R22.5
Coefficient of Rolling Resistance		0.008
Coefficient of Aerodynamic		0.79
Engine	**Type**	Cummins ISB260H
	Model Year	2006
	Power	260 hp (194 kW)
	Engine Displacement	5.9 L
	Number of Cylinders	6
Motor	**Type**	AC Induction Motor
	Rated Power	114 hp (85 kW)
	Peak Power	201 hp (150 kW)
	Rated Torque	162 ft-lb (220 Nm)
Generator	**Type**	PM synchronous generator
	Rated Power	114 hp @2500 rpm (85 kW @2500 rpm)
	Peak Power	221 hp (165 kW)
	Rated Torque	236 ft-lb (320 Nm)
ESS	**Type**	Maxwell BCAP0010 2600 Farad
	Cell number	144
	Peak Voltage	345 Volts
Primary Fuel		D2
Test Cycle		UDDS, OCTA, Houston and Manhattan
Test Date		September 2009

6.2. Main Components Model

6.2.1. Engine Model

The engine model simulates engine torque, FC and emissions. The engine torque was calculated by interpolating between the maximum torque curve and the minimum torque curve (zero curve in this study) by the engine torque demand from the controller. Figure 6.3 shows the plot of the maximum and minimum torque and power generated by the Cummins ISB 260H engine [140]. The lower boundary refers to the case in which the fuel consumption is zero. The detailed calculation of engine torque has been addressed in Chapter 4. The engine fuel rate was determined by a static lookup table described in terms of engine torque and engine speed. The engine fuel rate was interpolated within the boundaries. There is no fuel rate when the engine speed is below the starting speed and when the engine is brought up to starting speed by the starter motor that all happens before fuel is injected into the engine [85]. It should be noticed that the engine starting speed is much lower than the engine idle speed. In a similar way, the NO_x emissions are estimated by a lookup table of NO_x emission rate. Both the fuel rate lookup table and NO_x emissions lookup table were developed from the experimental data collected at WVU Transportable Heavy-duty Vehicle Emission Testing Laboratory. Four test cycles (UDDS, OCTA, Manhattan and Houston) were used to build the look up tables. Figures 6.4-6.5 show the engine fuel rate map and emission rate map expressed as a function of engine speed and engine torque.

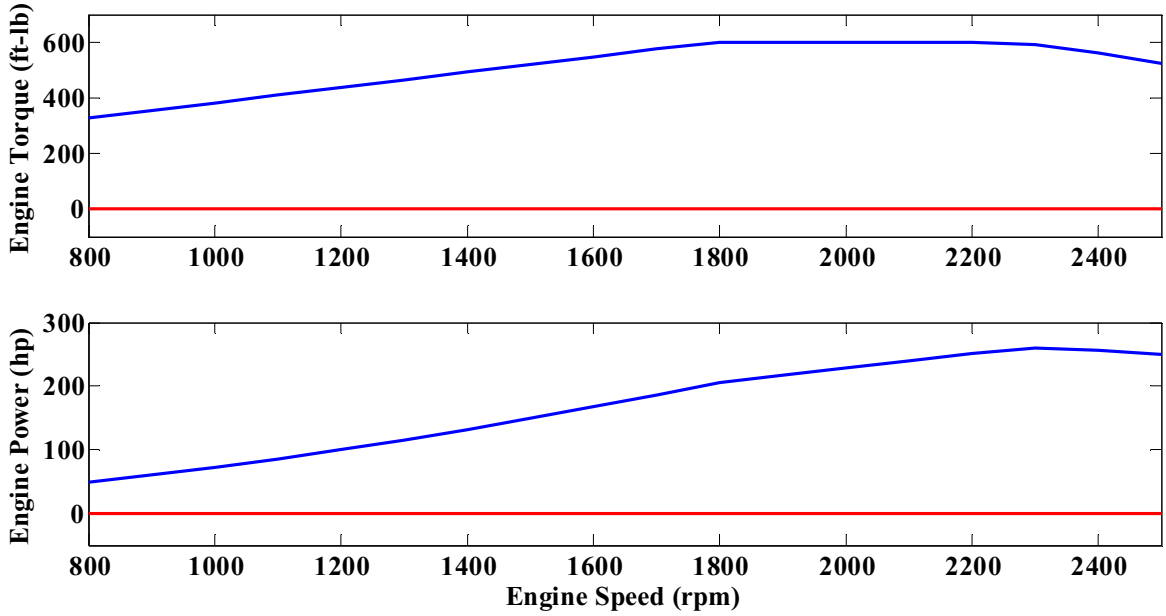

Figure 6.3: The maximum and minimum torque and power generated by the Cummins ISB 260H engine
[140]

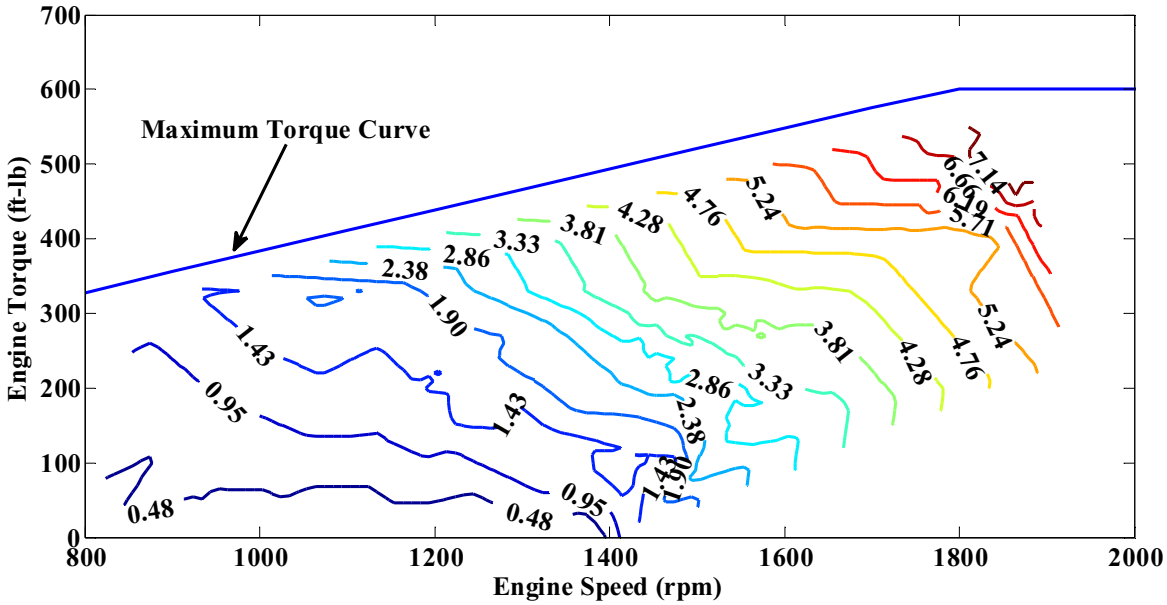

Figure 6.4: Cummins ISB 260H fuel rate map (g/s) over the UDDS
(Constructed from the experimental data collected at WVU Transportable Laboratory)

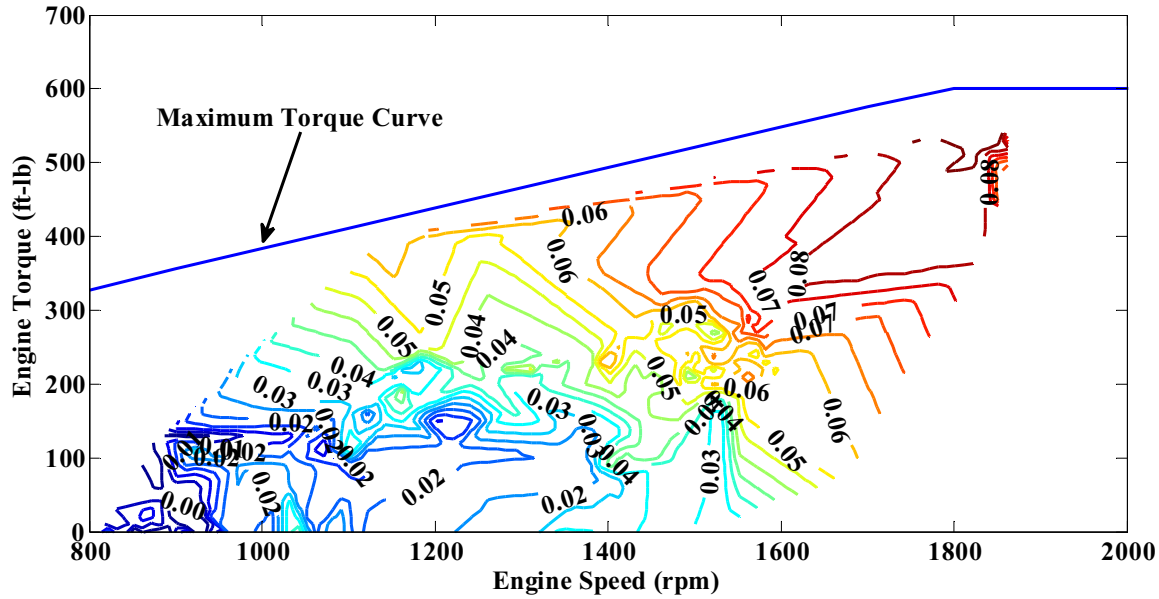

Figure 6.5: Cummins ISB 260H NO_x emission rate (g/s) over the UDDS
(Constructed from the experimental data collected at WVU Transportable Laboratory)

6.2.2. Generator Model

In a series hybrid, the engine powers a generator and the generator either charges the energy storage system or propels the traction motor. The torque of the generator is calculated by using the commands sent by the controller and the maximum torque curve. The angular speed of the generator can be computed by dividing the total torque from the engine and the generator by their respective inertias. Figure 6.6 shows the torque performance and the efficiency map of the permanent magnet synch generator used in the New Flyer ISE HEB.

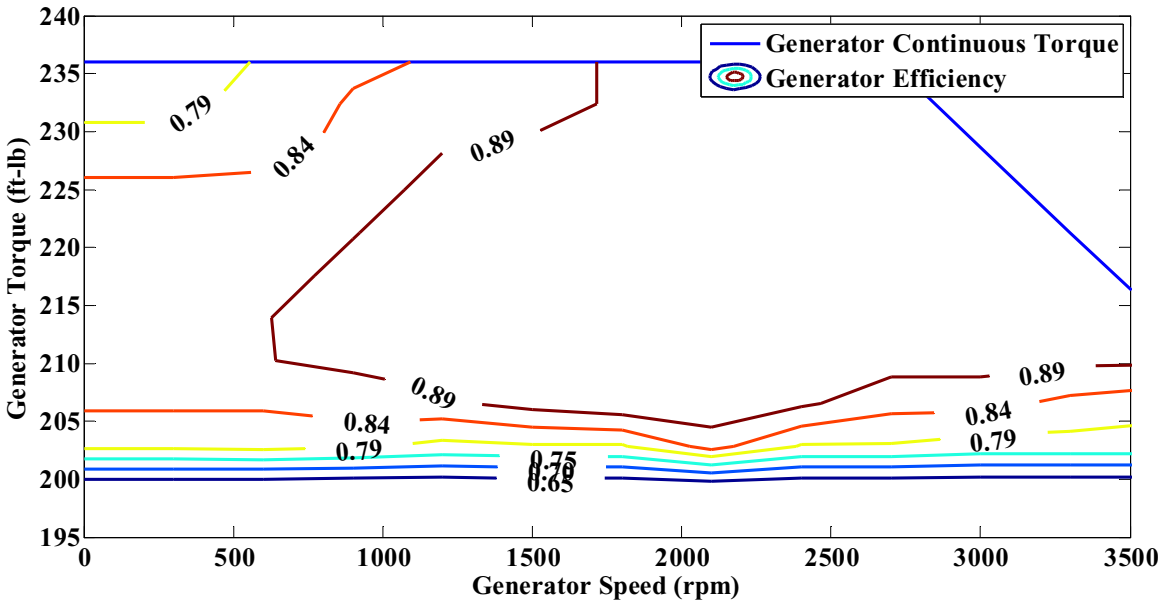

Figure 6.6: The continuous torque and the efficiency map of the generator used in the New Flyer HEB

(The generator continuous torque was acquired from the manufacturer and the generator efficiency map were plotted by using the empirical data from the PSAT generator initialization file)

6.2.3. Motor Model

The motor model converts the commands ([-1 1]) sent by the controller into motor torque by using its maximum and continuous torque curve. A positive command causes the motor to output positive torque and propels the vehicle while a negative command causes the motor to output negative torque and charges the ultracapacitors. Figure 6.7 shows the general Simulink diagram of the PSAT motor model. The motor output torque was computed by multiplying the motor command for the controller and the maximum available torque of the motor at a given speed.

$$T_{out} = T_{\max} * T_{cmd} \qquad \textit{Equation 6.1}$$

where T_{out} is the output of motor torque, T_{cmd} is the motor command with value range [-1, 1], T_{max} is maximum torque, which is constrained both electrically and mechanically.

$$T_{\max} = \min(T_{\max\_mechnical}, T_{\max\_electrical}) \qquad \textit{Equation 6.2}$$

where $T_{max\_mechnical}$ can be computed by Equation 6.3, which interpolates between the continuous torque curve and the maximum torque curve by using the heat index of the motor. If the motor is hot, then the continuous torque curve is used (that is, the heat index is 1), and the maximum torque curve is used when the motor is at its operating temperature.

$$T_{\max\_mechnical} = T_{cont} * \delta_{HI} + T_{peak} * (1 - \delta_{HI}) \qquad \textit{Equation 6.3 [85]}$$

where T_{cont} and T_{peak} are continuous and peak torques, which is dependent on the current shaft speed, as shown in Figure 6.8 [80]. δ_{HI} denotes the heat index, which is a term corrected to adjust the available torque between the continuous and peak torques during operation. Equation 6.4 gives its empirical calculation formula.

$$\delta_{HI} = -0.3 + \int_0^T \frac{0.3}{\tau} * (\frac{T_{out}}{T_{cont}} - 1) * dt \qquad \textit{Equation 6.4 [85]}$$

The motor is allowed to operate at peak torque for a short time. But will be forced towards the continuous torque curve after sustained operation.

The output torque is also constrained by the electrical power $T_{max\_electrcal}$, which was computed by:

$$T_{\max\_electrical} = \begin{cases} \dfrac{U * I_{\max}}{\omega_m} & motoring \\ -\dfrac{U * I_{\max}}{\omega_m} & generating \end{cases} \qquad \textit{Equation 6.5}$$

where U and I_{max} are the voltage and the maximum available current of the motor, ω_m is the speed of the motor.

The current of the motor was computed by:

$$I_m = \frac{P_m}{U} \qquad \textit{Equation 6.6}$$

where

$$P_m = \begin{cases} T_m * \omega / \eta_m & motoring \\ T_m * \omega * \eta_m & generating \end{cases} \qquad \textit{Equation 6.7}$$

where η_m is the efficiency of the motor, which is a function of motor torque and speed, as shown in Figure 6.9. Instead of multiplying the motor torque and speed, and adding a loss term, the

motor electrical power was computed directly from the output torque and speed, with losses taken into account.

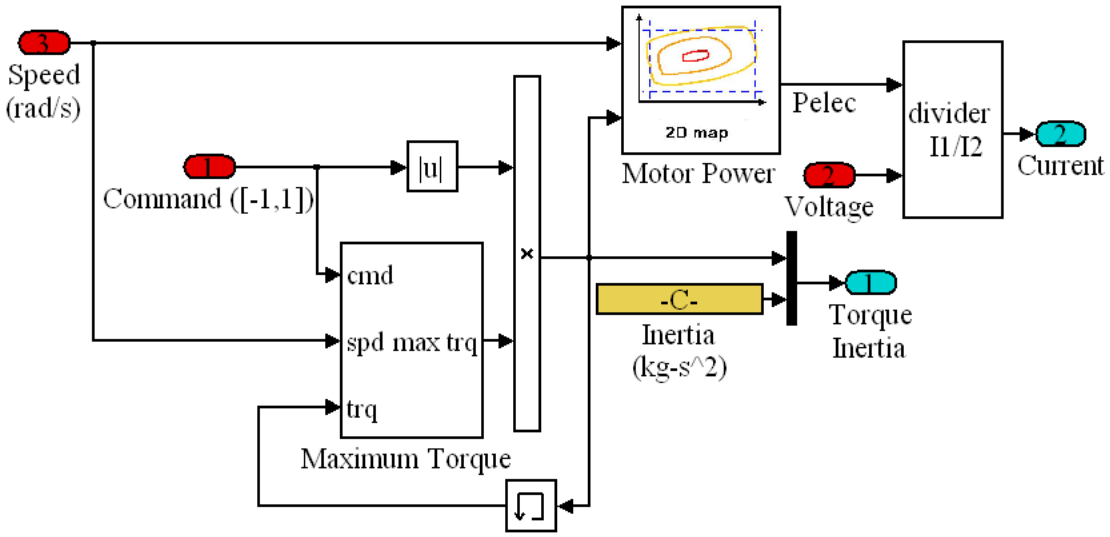

Figure 6.7: The general Simulink diagram of the PSAT motor model

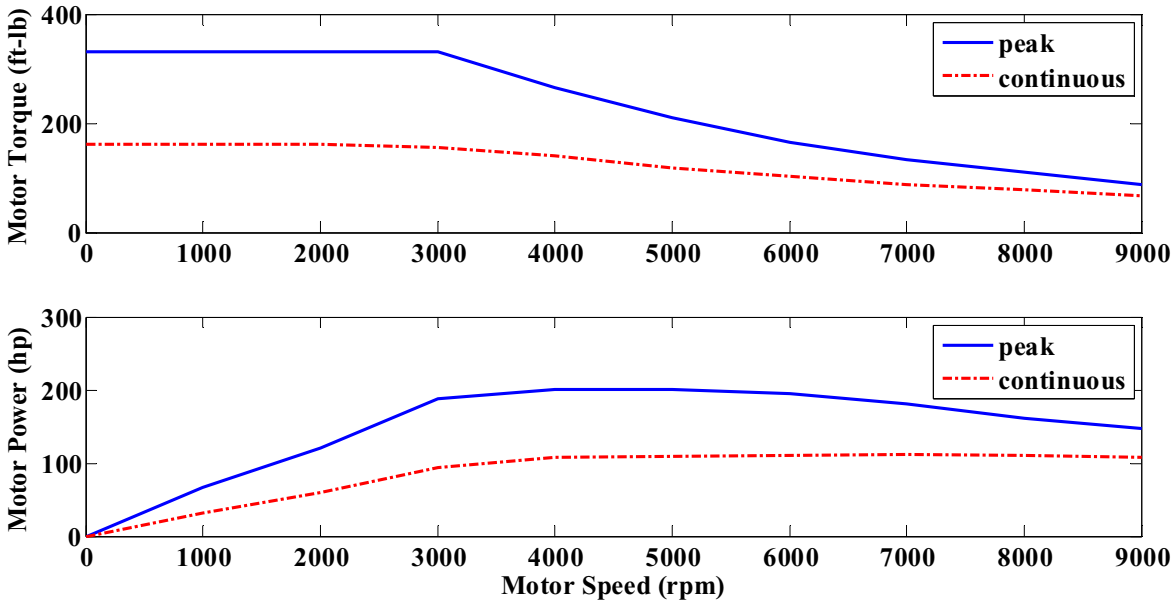

Figure 6.8: The peak and continuous torque and power of the motor used in the New Flyer HEB

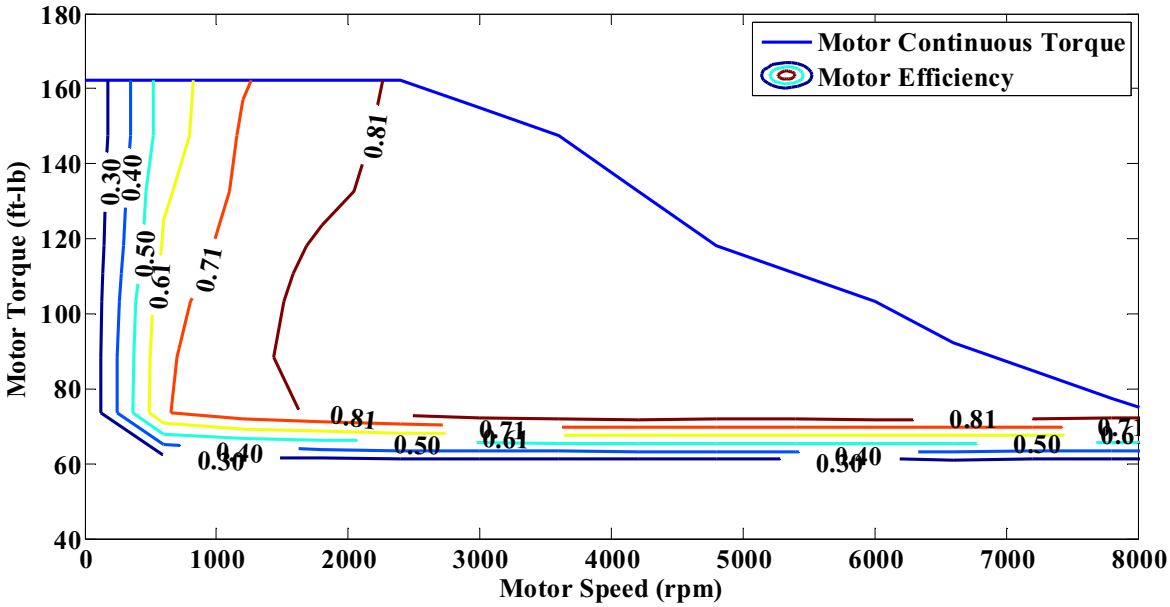

Figure 6.9: The continuous torque and the efficiency map of the motor used in the New Flyer HEB

(The motor continuous torque was derived by the manufacturer and the motor efficiency map were plotted by using the empirical data from the PSAT motor initialization file)

6.2.4. Ultracapacitors

The ultacapacitors provide electric power to the motor. The ultracapacitor model in PSAT utilizes current as an input and constrains its operation within the maximum and minimum voltage. Power delivered by ultracapacitors is constrained by the maximum value which the equivalent circuit provides or the motor controller can accept [85]. The general Simulink diagram of the PSAT ultracapacitor model is shown in Figure 6.10.

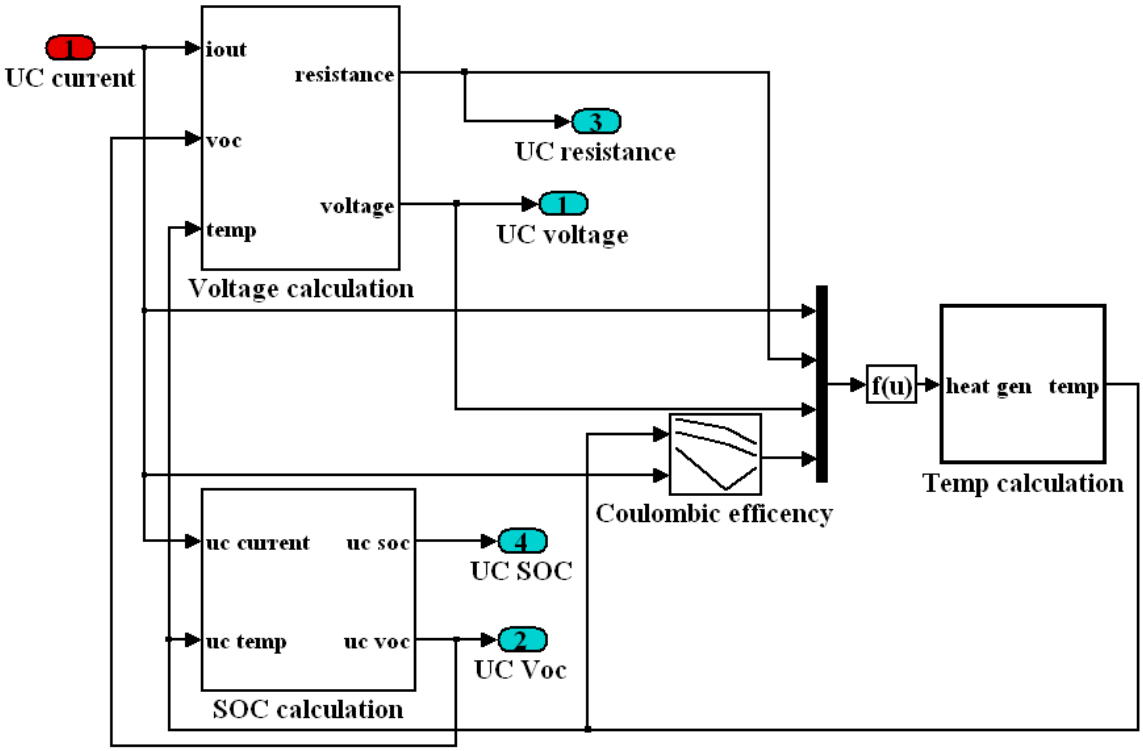

Figure 6.10: The general Simulink diagram of the PSAT ultracapacitor model

The voltage calculation block computes the voltage at the terminal of the ultracapacitor, which is given by:

$$V_{out} = V_{OC} - I_{UC} * R_{UC} \qquad \textit{Equation 6.8}$$

where V_{OC} and I_{UC} is the open circuit voltage and current flowing out of the ultracapacitor, R_{UC} is internal resistance of the ultracapacitor pack and can be computed by:

$$R_{UC} = \begin{cases} R_{charge} * \dfrac{N_{series}}{N_{parallel}} & I_{UC} < 0 \\ R_{discharge} * \dfrac{N_{series}}{N_{parallel}} & I_{UC} > 0 \end{cases} \qquad \textit{Equation 6.9 [85]}$$

where R_{charge} is the internal resistance of the ultracapacitor pack during charging and $R_{discharge}$ is the internal resistance of the ultracapacitor pack during discharging, which vary with the current and temperature, as shown in Figure 6.11 (on left). N_{series} is number of cells in the ultracapacitor module that are connected in series, $N_{parallel}$ is the number of series connected modules that are then connected in parallel.

The open circuit voltage V_{OC} is given by:

$$V_{OC} = \int \frac{I_{UC}}{C(T_{UC}, I_{UC})} * \frac{N_{series}}{N_{parallel}} dt + SOC_{init} * C_{\max} * (V_{OC\_\max} - V_{OC\_\min}) + V_{OC\_\min} \qquad \textit{Equation 6.10 [85]}$$

where T_{UC} is the temperature of an ultracapacitor cell. $C\ (T_{UC},I_{UC})$ is the cell capacitance as a function of cell temperature and cell current, which varies slightly with the current and temperature, as shown in Figure 6.11 (on right). The SOC_{init} is the initial SOC of the ultracapacitor, C_{max} is the maximum capacitance of a single cell, V_{OC_max} and V_{OC_min} are maximum and minimum open circuit voltages of a single cell.

The SOC was calculated by determining the remaining Coulombs of the charge in the ultracapacitors and dividing by the maximum Coulombs the battery can store. Since the voltage is proportional to the stored charge for an ultracapacitor, the SOC can be computed from the voltage, as shown in Equation 6.11.

$$SOC = \frac{V_{OC} - V_{OC\_\min}}{V_{OC\_\max} - V_{OC\_\min}} \qquad \textit{Equation 6.11 [85]}$$

As the capacitance and resistance are dependent on temperature, it is essential to model the thermal dynamics of the ultracapacitors. The heat generation is given by:

$$Q_{gen} = \begin{cases} R_{UC} * I_{UC}^2 - V_{OUT} * I_{UC} * (1 - \eta_{UC}) & I_{UC} < 0 \\ R_{UC} * I_{UC}^2 & I_{UC} > 0 \end{cases} \qquad \textit{Equation 6.12 [85]}$$

Heat is also dissipated by convection heat transfer between the ultracapacitor case and its surrounding air. The temperature difference between the ultracapacitors and surrounding air was used to compute heat dissipated.

$$Q_{dis} = \frac{T_{air} - T_{uc}}{R_{thermal}} \qquad \textit{Equation 6.13}$$

where Q_{dis} is the heat dissipated into the air, $R_{thermal}$ is the thermal resistance of the system, T_{air} is the surrounding temperature, which needs to be determined from the previous time step.

$$T_{air} = T_{\infty} - \frac{Q_{dis}}{2\dot{m} * C_{p,air}} \qquad \textit{Equation 6.14}$$

where T_{∞} is the ambient temperature, $\dot{m}$ and $C_{p,air}$ are the mass flow rate and the heat capacity of air. The heat generated by the ultracapacitors minus the heat dissipated into the air is utilized to compute the temperature of ultracapacitor pack.

$$T_{UC} = \int \frac{Q_{gen} - Q_{dis}}{m_{UC} * C_{P,UC}} dt \qquad \textit{Equation 6.15 [85]}$$

where m_{UC} is the mass of the ultracapacitors, $C_{p,UC}$ is the thermal heat capacity of the ultracapacitor.

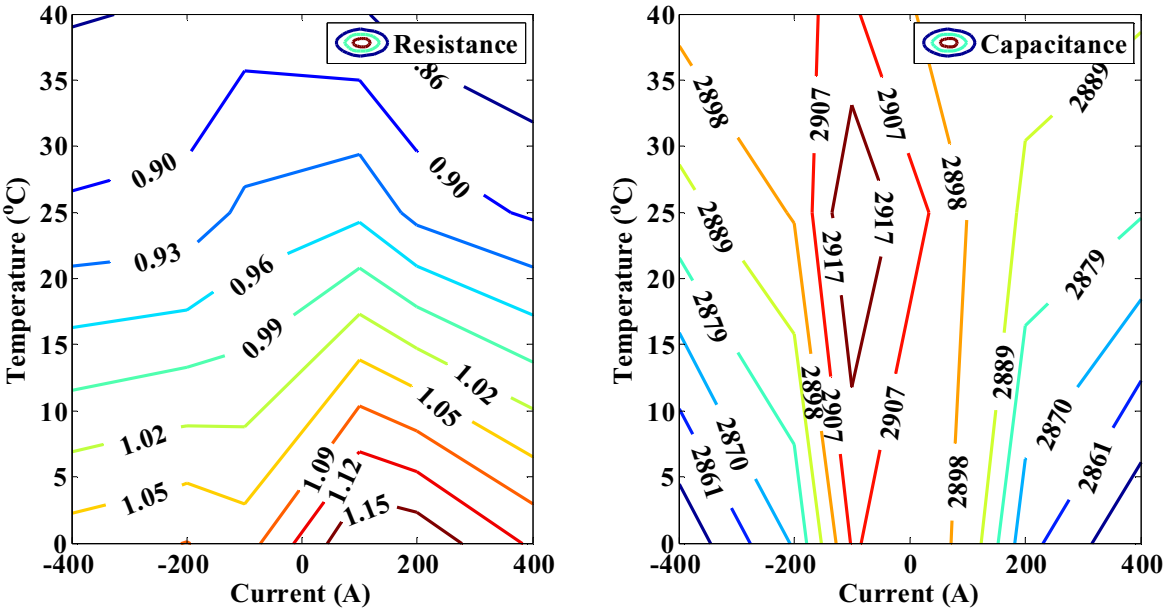

Figure 6.11: The ultracapacitor resistance (left, in mΩ) and capacitance (right, in Farads) as a function of current and temperature
(These maps were plotted by using empirical data from PSAT component initial files)

6.3. Single Component Validation

After the component data had been integrated into PSAT, the Cummins ISB 260H engine model was validated. The validation process was the same as stated in Chapter 4. By comparing the experimental data and the PSAT simulated data, the accuracy of the engine model was determined. The comparison results between the experimental data and simulated data is shown in Table 6.2. Both the experimental and the simulated data are average values. Figures 6.12-6.14 depict the instantaneous measured and simulated engine torque, engine fuel rate and NO_x emissions over the OCTA cycle. The engine torque was transformed from the engine command by interpolating between a minimum torque curve and a maximum torque curve. The perfect match between the simulated torque and the experimental torque (Figure 6.12) confirms that the maximum and minimum torque curves are accurate and the PSAT model performs correctly. Figure 6.13 shows that the simulated instantaneous fuel rate matches the experimental fuel rate very well, which indicates that the fuel rate matrix developed on the basis of experimental data from four transient cycles (UDDS, OCTA, Manhattan and Houston) in the PSAT engine initialization file can be used for a generic fuel consumption study. The simulated NO_x emission data typically match the measured data very closely except for very transient situations (Figure 6.14). This is because the NO_x emissions are estimated by a lookup table, which is expressed as a function of engine speed and engine torque, without considering their derivatives.

Table 6.2: Comparisons of the experimental and PSAT simulated data in validation of the engine model

Cycle		Engine Speed	Engine Torque	Engine Fuel Rate	NO_x
		rad/s	Nm	g/s	g/s
UDDS	Experimental	135.45	230.30	2.42	0.039
	PSAT Simulated	135.45	225.77	2.41	0.037
	Relative Error (%)	0	1.97	2.85	5.12
OCTA	Experimental	134.48	204.64	2.02	0.037
	PSAT Simulated	134.47	199.90	2.07	0.036
	Relative Error (%)	0.01	2.32	0.74	1.48
Houston	Experimental	128.11	177.57	1.72	0.032
	PSAT Simulated	128.11	172.27	1.77	0.032
	Relative Error (%)	0	2.99	3.24	1.30
Manhattan	Experimental	123.92	153.88	1.51	0.028
	PSAT Simulated	123.92	148.19	1.57	0.029
	Relative Error (%)	0	3.38	2.28	1.79

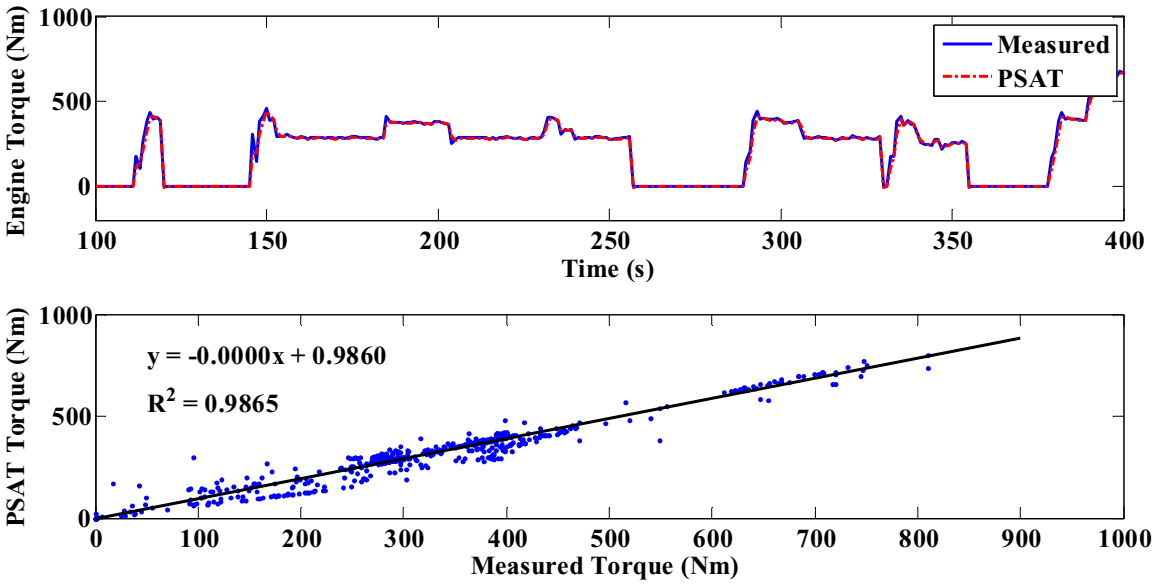

Figure 6.12: The comparison plot (over a selected 300 seconds) and parity plot of the measured and PSAT engine torque in the validation of the Cummins ISB 260H engine model over the OCTA cycle

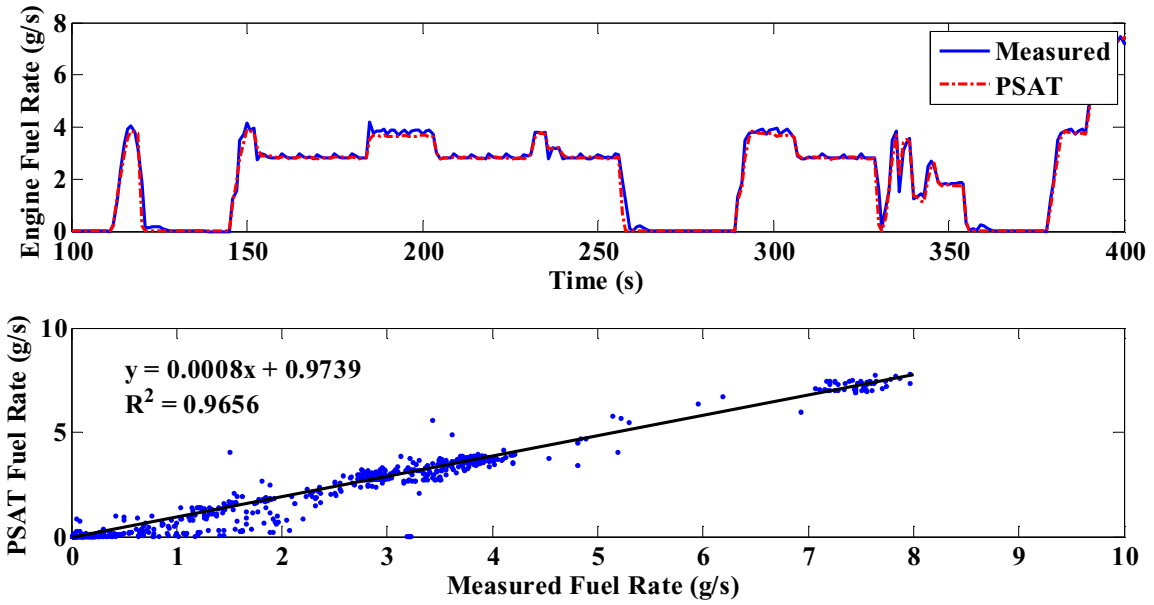

Figure 6.13: The comparison plot (over a selected 300 seconds) and parity plot of the measured and PSAT engine fuel rate in the validation of the Cummins ISB 260H engine model over the OCTA cycle

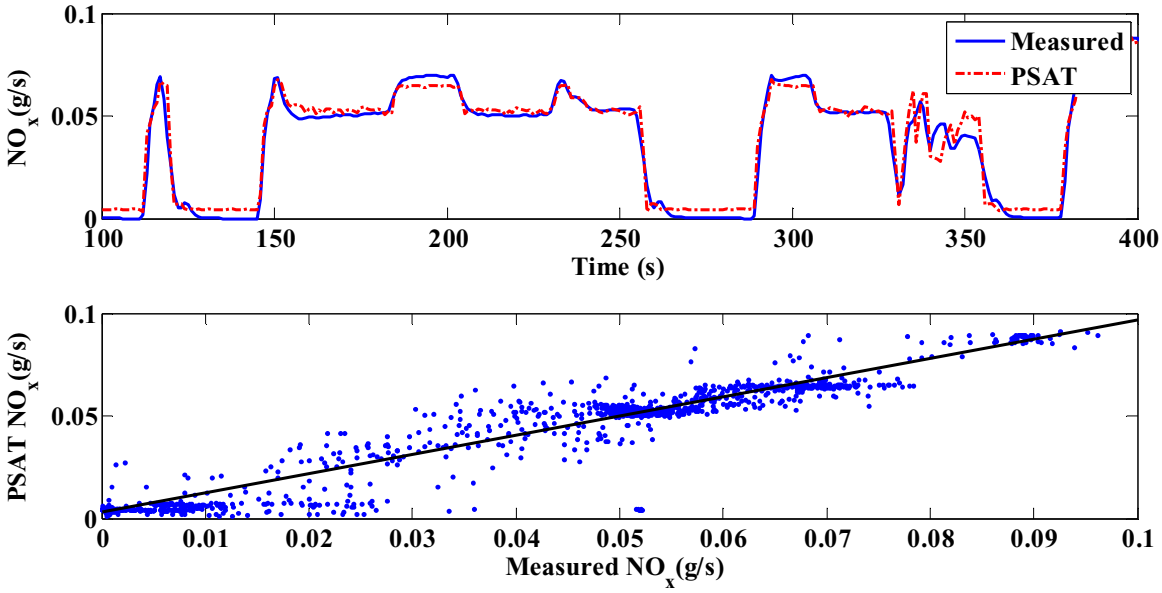

Figure 6.14: The comparison plot (over a selected 300 seconds) and parity plot of the measured and PSAT NO_x in the validation of the Cummins ISB 260H engine model over the OCTA cycle

6.4. Control Strategy

A control strategy model receives operation commands (such as acceleration pedal position, braking) from the driver and the real-time feedback information (such as currents and voltage of the ultracapacitors, engine speed and torque, etc.) of powertrain components. The control strategy model generates control signals and sends them to each powertrain component for the next step. The control strategy for energy management plays a critical role in FC and emissions of a hybrid vehicle. The instantaneous FC and emissions are highly dependent upon how well the power demand is distributed between the engine and ultracapacitors instantaneously.

6.4.1. Control Strategy Approaches

Two control strategy approaches are normally utilized in the energy management system: the thermostatic control method and the load-following method.

6.4.1.1. Thermostatic Control

Thermostatic control strategy utilizes a rule-base approach that event triggers are activated when certain conditions are met. In a thermostatic control strategy system of an HEV, the engine operates at an optimum point where maximum fuel efficiency can be reached, with the ultracapacitors SOC varying between upper and lower limits. The engine is turned off when the SOC reaches the upper limit, and the motor power is provided by the ultracapacitors. The engine turns on when the SOC reaches the lower limit. The controller balances the engine speed and the

battery current in this case such that the engine operates at its most efficient point. The most efficient point needs to be set up preliminarily for a specific engine. The original New Flyer ISE hybrid bus utilized thermostatic control strategy. The optimum point in the Cummins ISB 260H engine equipped in the ISE hybrid bus was found at a speed of 1500 rpm and a torque of 320 ft-lb (about 92 kW). Motor power is supplied by the engine, any extra (or shortage) power is consumed (or supplied) by the energy storage system. As it is a single-parameter control, the thermostatic control strategy is simple and easy to manipulate. However, the limitation of the thermostat control is constrained by Equation 6.16 [142], which indicates that the thermostat control only works if the average demanded power is less than the engine power at maximum engine efficiency. Therefore, thermostatic control cannot be considered optimized for all drive cycles and for all applications.

$$P_{motor\_ave} \leq P_{engine\_\max\_effi} \qquad \textit{Equation 6.16 [142]}$$

6.4.1.2. Load-Following Control

In an engine map, there is a minimum FC (g/s) point at a given speed and these points consist of the optimum speed-torque curve which shows the highest efficiencies at different speeds. In the load-following strategy, the engine is adjusted to operate on the optimum speed-torque curve, in a way that engine power required is not directly related to road load demand. The best fuel efficiency in a load-following control strategy is given by:

$$\eta(\omega, T) = \frac{\omega' \cdot T}{LHV \cdot \frac{dm_{fuel}}{dt}(\omega, T)} \qquad \textit{Equation 6.17 [86]}$$

where ω' represents the transposition of the engine speed with minimum fuel consumption and T is the corresponding torque, and m_{fuel} is the minimum FC mass at the given speed. In the hybrid mode, the engine power demand was the difference between road load demand and the ultracapacitor power demand. The ultracapacitors were either charging or discharging and the engine in this study either operated at optimum curve to provide power or operated in an idle state. If the SOC of the ultracapacitors was above the threshold value, the ultracapacitor power was positive and supplied part of the road load demand, which reduced the load demand from the engine. The ultracapacitors consumed energy from the engine when charging, which increased the load demand from the engine. During a special situation where the sum of the engine power supplied and ultracapacitors supplied was less than the road load demand, the engine would leave the maximal efficiency curve to satisfy the demanded power [143]. The SOC threshold value of the ultracapacitors was kept between 0.9 and 0.1. The upper limit of 0.9 provided a buffer to absorb energy from the engine or regenerative braking. The lower limit of the SOC of the ultracapacitors could be set much lower than that of batteries due to their ultralow internal resistance. The control strategy utilized in this study is the load-following technique.

6.4.2. Propelling Strategy

For the propelling strategy model, the necessary inputs were as follows:

- Ultracapacitors: SOC, propulsion and regenerative power limits
- Engine: The output of engine speed and the engine torque limit
- Motor: The input of motor speed, the output of motor current, voltage and the motor torque limit
- Generator: The input of generator speed, torque, the output of generator current, voltage propulsion and regenerative torque limit.
- The vehicle speed and the wheel torque demand

The system outputs three parameters, motor torque, engine torque, and generator torque.

6.4.2.1. Motor Torque and Power

The motor torque was calculated by dividing the wheel torque demand by the final drive ratio. But the motor torque needed to be constrained for the case when the ultracapacitors have reached the maximum SOC. When the maximum SOC was reached, the energy was only allowed to be pulled out of the ultracapacitors, which was not allowed during charging of the ultracapacitors. Therefore, no regenerative motor torque was allowed when the SOC reached its maximum value. The calculation of electrical power demand of the motor is illustrated by Figure 6.15. The motor torque is first saturated with the motor maximum propelling torque, which is then used to compute the mechanical power and the power losses in the motor by a predefined lookup table which was developed based on the motor efficiency map in Figure 6.9. The sum of the mechanical power and the losses power in the motor was the electrical power demand of the motor. The electrical power demand was used to compute the generator power demand, which was finally used to compute the engine power demand to achieve the target vehicle speed.

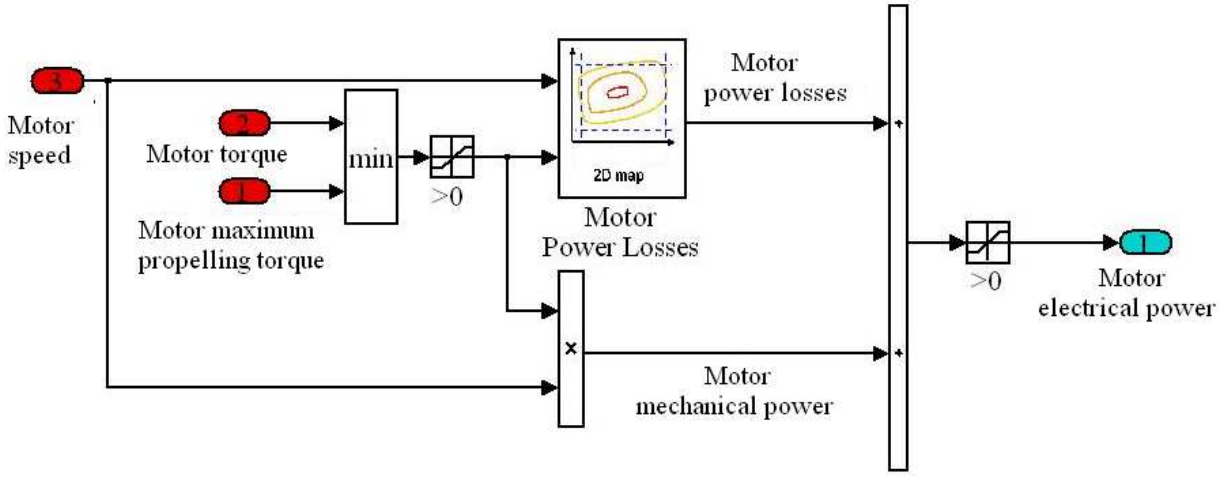

Figure 6.15: The electrical power demand of the motor

Figure 6.16 illustrates a simulink diagram to depict the calculation of the maximum motor torque. The generator either powers the motor or generates power to charge the ultracapacitors depending on the sign of generator torque. If it is positive, the generator power is used to propel the vehicle. Otherwise, it is used to charge the ultracapacitors.

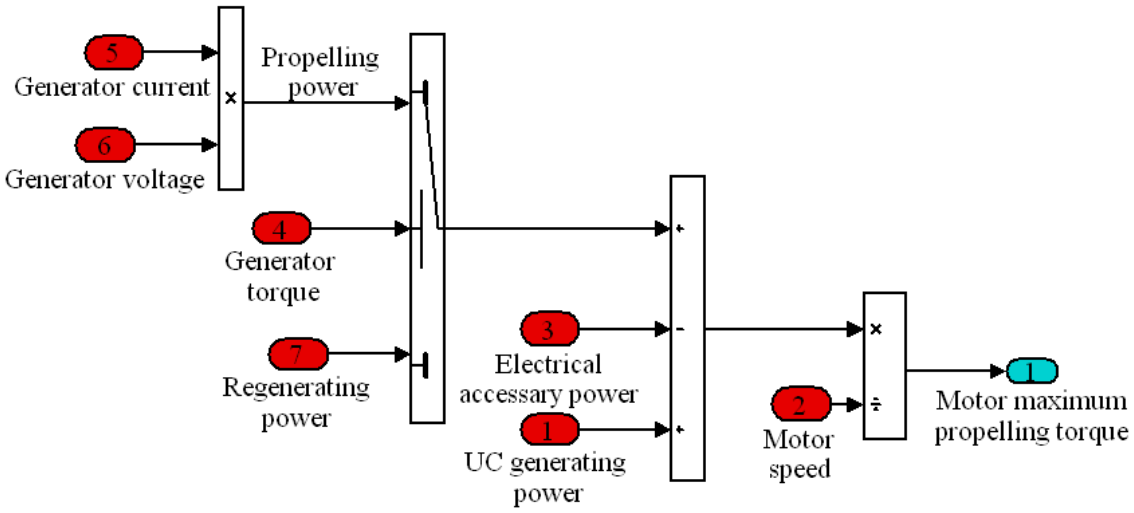

Figure 6.16: The maximum motor torque attained

6.4.2.2. Engine Power and Torque

The calculation of the engine power demand in an HEV is illustrated by Figure 6.17, consisting of three blocks. In block A1, the total motor electrical power demand was obtained by adding electrical accessory power to the motor electric power.

The sum of total motor electrical power demand and generator electrical power equaled the total ultracapacitor power needed by the motor to propel the vehicle. Adding the ultracapacitors power demand to the generator mechanical power gave the power demand from the engine to propel the vehicle (block A2). In other words, the engine power demand was the difference between the vehicle load demand and the ultracapacitors power demand. If the SOC of the ultracapacitors was above the minimum set value, the energy discharged from the ultracapacitors was positive and provided a fraction of the road load power which reduced the load on the engine. In this way, the engine power demand was directly related to the power required at the wheels, as shown in Equation 6.18. As the road demand increases, the engine power demand also increases.

$$P_{eng} = P_{wheel} - P_{UC} \qquad \textit{Equation 6.18}$$

where P_{eng} is the power demand from the engine, P_{wheel} is the power demand at the wheels. P_{UC} is the ultracapacitors discharged power, which is a function of the SOC and is found by a predefined lookup table. If the SOC of the ultracapacitors was below the minimum set value, the ultracapacitors needed to be charged and the maximum charging power was utilized as part of the engine calculation. At performance mode, where the accelerator pedal position exceeded 0.8,

all the powers of each component were set to their maximum valves. At this moment, the engine did not follow the optimum fuel efficiency curve anymore.

The sum of the total power demand from the engine to propel the vehicle and the mechanical accessories gave the total power needed from the engine (block A3). The engine torque was computed by dividing the engine power demand by the current engine speed, with the saturation of maximum engine torque and generator torque.

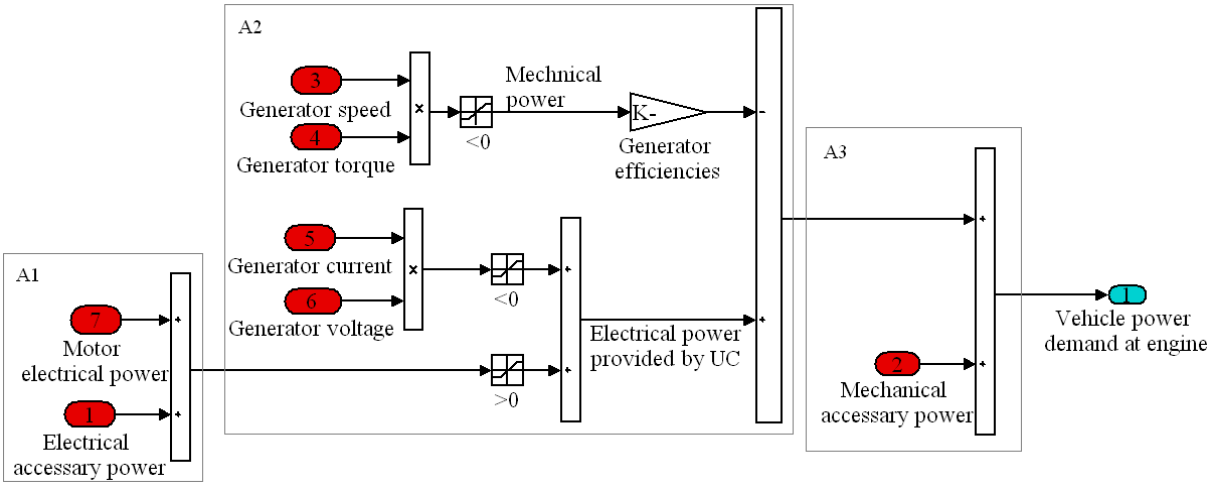

Figure 6.17: The power demand to reach the target vehicle speed at the engine

6.4.3. The HEB Operation State

The vehicle operating state is composed of six distinct transient states, shown in Figure 6.18.

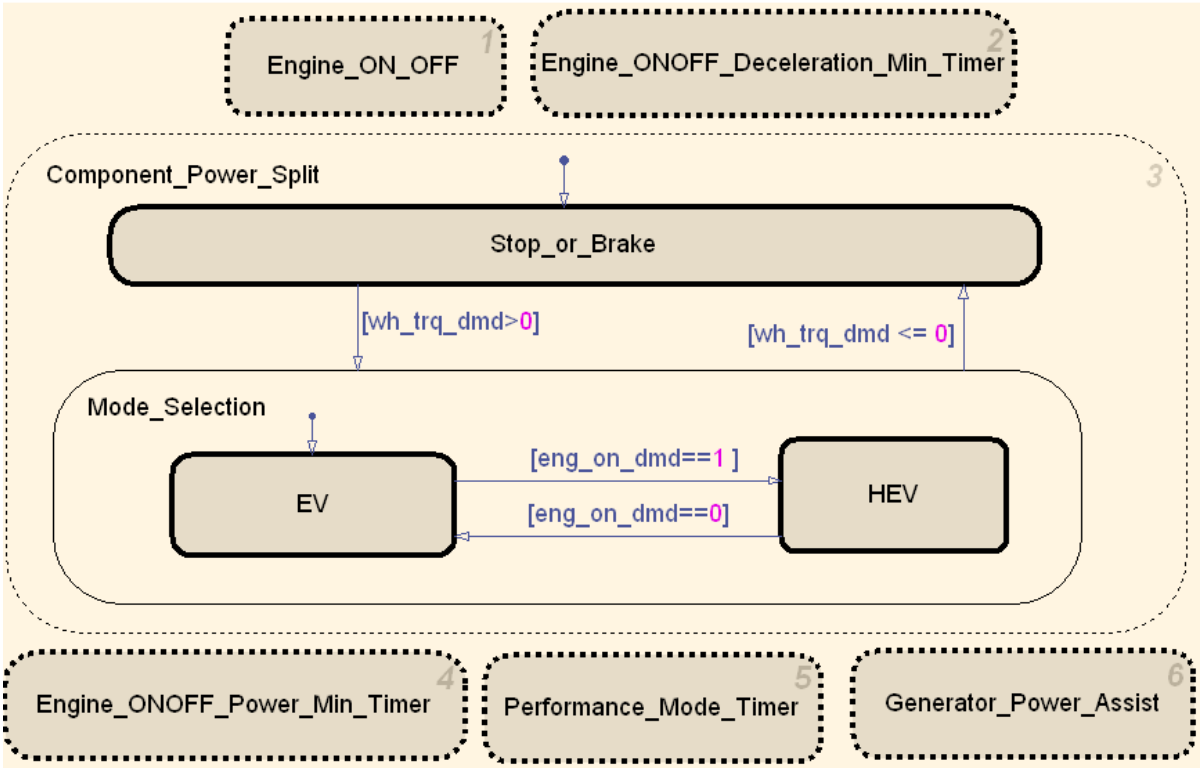

Figure 6.18: Vehicle operating state

(1) Engine ON/OFF Block

This block sends the engine ON/OFF command. The controller turns the engine ON when,

$$\begin{cases} SOC < SOC_{\min} \quad OR \\ t_{\min\_ON} = 1 \quad OR \\ P_{\max\_UC} = 1 \quad OR \\ Perfo\_Mode \end{cases}$$

where $soc_{\min}$ is the SOC minimum threshold, $t_{\min\_ON}$ is the minimum duration time at a power threshold to turn the engine ON. It is a binary parameter which is determined by engine ON/OFF minimum power timer in Block 4. $P_{\max\_UC}$ is the maximum power demand of the ultracapacitors. When the vehicle power needed exceeds the maximum power of the ultracapacitors, the engine will turn ON. $Perf\_Mode$ denotes performance mode when the accelerator pedal position is more than 0.8.

The control strategy turns the engine OFF when,

$$\begin{cases} T_{\min\_OFF} = 1 \quad OR \\ \left(\begin{array}{ll} SOC > SOC_{\max} & AND \\ t_{\min\_OFF} = 1 & AND \\ P_{elec} < P_{UC} & AND \\ Not\_Perfo\_Mode & \end{array} \right) \end{cases}$$

where $t_{\min\_OFF}$ denotes the minimum duration of time at sufficient deceleration to turn the engine OFF, which is a binary parameter that is determined by the engine ON/OFF minimum deceleration timer in Block 2. $SOC_{\max}$ is the SOC maximum threshold. $t_{\min\_OFF}$ is the minimum duration of time at a power threshold to turn the engine OFF. It is a binary parameter which is determined by the engine ON/OFF minimum power timer in Block 4. P_{elec} denotes the electrical power demand and P_{UC} Puc denotes the ultracapacitor's power in pure electric mode. Not_Perf_Mode denotes performance mode when the accelerator pedal position is less than 0.8.

In the New Flyer ISE HEB model design, the engine was not turned off during driving for the maximum degree of comfort for the passengers. Moreover, it was better for emissions as the engine was warm all the time. The vehicle deceleration torque demand to turn the engine OFF was set to its largest value (occurred in engine ON/OFF deceleration timer block), which resulted in the engine always being in the ON state.

(2) Engine ON/OFF Minimum Deceleration Timer Block

The engine ON/OFF deceleration timer block determines if the vehicle is decelerating sufficiently to turn the engine OFF. When the wheel torque demand is negative, the timer is active. The engine is shut off with the negative threshold of wheel torque demand for a sufficient duration of time (two seconds were utilized in the ISE HEB model). If the wheel torque demand went above zero, the timer was reset. In this study, the engine was either on or idle, so the $t_{\min\_OFF}$ was never set to one.

(3) Component Power Split Block

The component power split block includes three sub-states: stop or brake, pure electric vehicle mode and HEV mode.

- Stop and brake state: which was active when the vehicle was stopping or braking. Regenerative braking helped capture part of the kinetic energy that was normally lost as heat via friction during mechanical braking. For safety reasons, the New Flyer ISE HEB model utilized a combination of mechanical braking and regenerative braking to slow down or stop the vehicle. The mechanical braking was activated by the brake command from the driver as the brake pedal was directly connected to the friction

brake. The operating state of regenerative braking was dependent on the SOC. Regenerative braking was disabled if the ultracapacitors SOC reached its maximum threshold.

- Electric mode: which was active when the ultracapacitors supplied all the power necessary to propel the vehicle and the engine was idle.
- HEV mode: This state was active when the engine either charged the ultracapacior or powered the motor for propelling the wheels. The engine power in the HEV was not directly associated with its wheel power demand, and it was therefore possible for the engine to operate in its optimum efficiency curve. The power required at the wheels was the sum of power demand from the engine and the ultracapacitors. In the HEV, the ultracapacitors acted as a "buffer" and supplied power to the engine to ensure the engine operated at its optimum efficiency torque curve by storing some power for future use. Vice versa, the ultracapacitors supply part of the energy when the power demand increased thereby reducing the load on the engine such that the engine still operated at its optimum efficiency torque curve.

(4) Engine ON/OFF Minimum Power Timer Block

This block controlled the minimum power threshold timer for the engine ON/OFF logic. When the power difference between the engine power demand and the ultracapacitors power demand was less than the engine OFF threshold for a minimum amount of time, the engine was shut down or kept at idle (in this case $t_{\min\_OFF} = 1$). When the power difference between the engine power demand and the ultracapacitors power demand was higher than the engine ON threshold for a minimum amount of time, the engine was either charging the ultracapacitors or powering the motor (in this case $t_{\min\_ON} = 1$).

(5) Performance Mode Block

When the accelerator pedal demand exceeded a threshold (0.8 assumed) for a minimum period of time, this mode was activated.

(6) Generator Power Assist

The generator was only motoring when the engine was ON and propeled the motor. When the engine was ON, the assist mode timer was active and the generator started to motor for the duration of the predefined time.

6.4.4. Tuning of Parameters

A significant amount of the parameter tuning was required to match the experimental data. Table 6.3 shows the values of parameters tuned in the load-following control strategy for the New Flyer ISE HEB.

Table 6.3: The values of parameters tuning in the road load control strategy for the New Flyer HEB model

Parameters	**Values**
SOC below which the engine is charging the ultracapacitor	0.1
SOC above which the engine is idling	0.9
Accelerator pedal for the performance mode	0.8
Vehicle speed below which the engine is idling	1.5 mph
Minimum engine power demand to charge the ultracapcior or power the motor	48 hp
Maximum engine power demand to turn it idle	40 hp
Maximum generator power to start the engine spinning	10 hp
Minimum time duration at sufficient decelerating to turn the enging OFF	2 seconds
Minimum time duration at power threshold to turn the engine ON/OFF	2 seconds
Other parameters	PSAT default

6.5. HEB Simulation Results

After all the powertrain components were customized, the engine model validated and the road load control strategy improved, the New Flyer ISE HEB model was operated on four driving schedules, UDDS, OCTA, Manhattan and Houston schedules. The evaluation was performed by comparing the driving schedule duration, and cycle-averaged FC, FE and NO_x between the PSAT simulated results and experimental data, as presented in Table 6.4. It can be seen that the relative percent of errors between the experimental and PSAT simulated values of FC, FE, CO_2, NO_x are all within 5% except for the FE and NO_x of the Manhattan cycle, which were 6.93% and 7.13% respectively.

Table 6.4: The comparison of tested and cycle-averaged PSAT simulated results of New Flyer HEB

Cycle		Cycle Distance	Fuel Consumption	Fuel Economy	CO_2	NO_x
		mile	kg	mpg	g/mile	g/mile
UDDS	Experimental	5.33	2.57	6.58	1683.6	7.80
	PSAT Simulated	5.31	2.54	6.60	1663.6	7.81
	Relative Error (%)	0.38	1.17	-0.30	1.19	-0.12
OCTA	Experimental	6.51	3.85	5.34	2098.8	10.76
	PSAT Simulated	6.31	3.68	5.42	2028.3	10.71
	Relative Error (%)	3.07	4.41	-1.50	3.36	0.46
HOU	Experimental	5.47	3.10	5.57	1987.7	10.42
	PSAT Simulated	5.35	3.00	5.64	1949.2	10.13
	Relative Error (%)	2.19	3.23	-1.26	1.94	2.78
MAN	Experimental	2.07	1.65	4.04	2793.8	14.87
	PSAT Simulated	1.96	1.65	3.76	2923.9	15.93
	Relative Error (%)	5.31	0	6.93	-4.66	7.13

The vehicle speed, SOC, engine speed and the engine torque over the UDDS, CTA, Houston and the Manhattan Schedules were depicted in Figures 6.19-6.22. From these Figures, it can be seen that the PSAT simulated HEB could follow the target vehicle speed well while it maintained SOC at a reasonable level. Therefore, it can be concluded that the New Flyer hybrid bus model could be used for FC and emissions evaluation for future PSAT users.

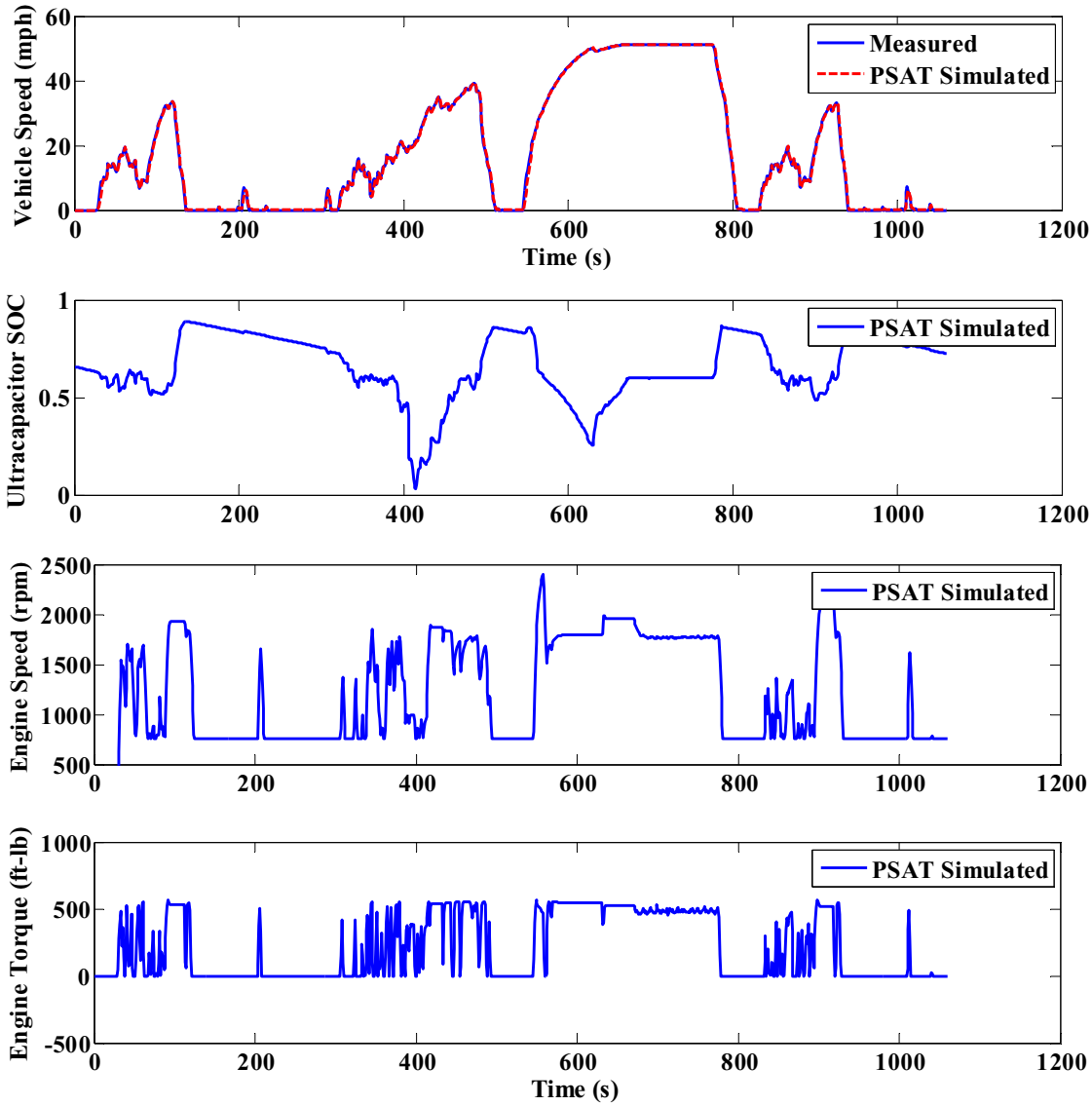

Figure 6.19: PSAT simulation results for New Flyer HEB over the UDDS

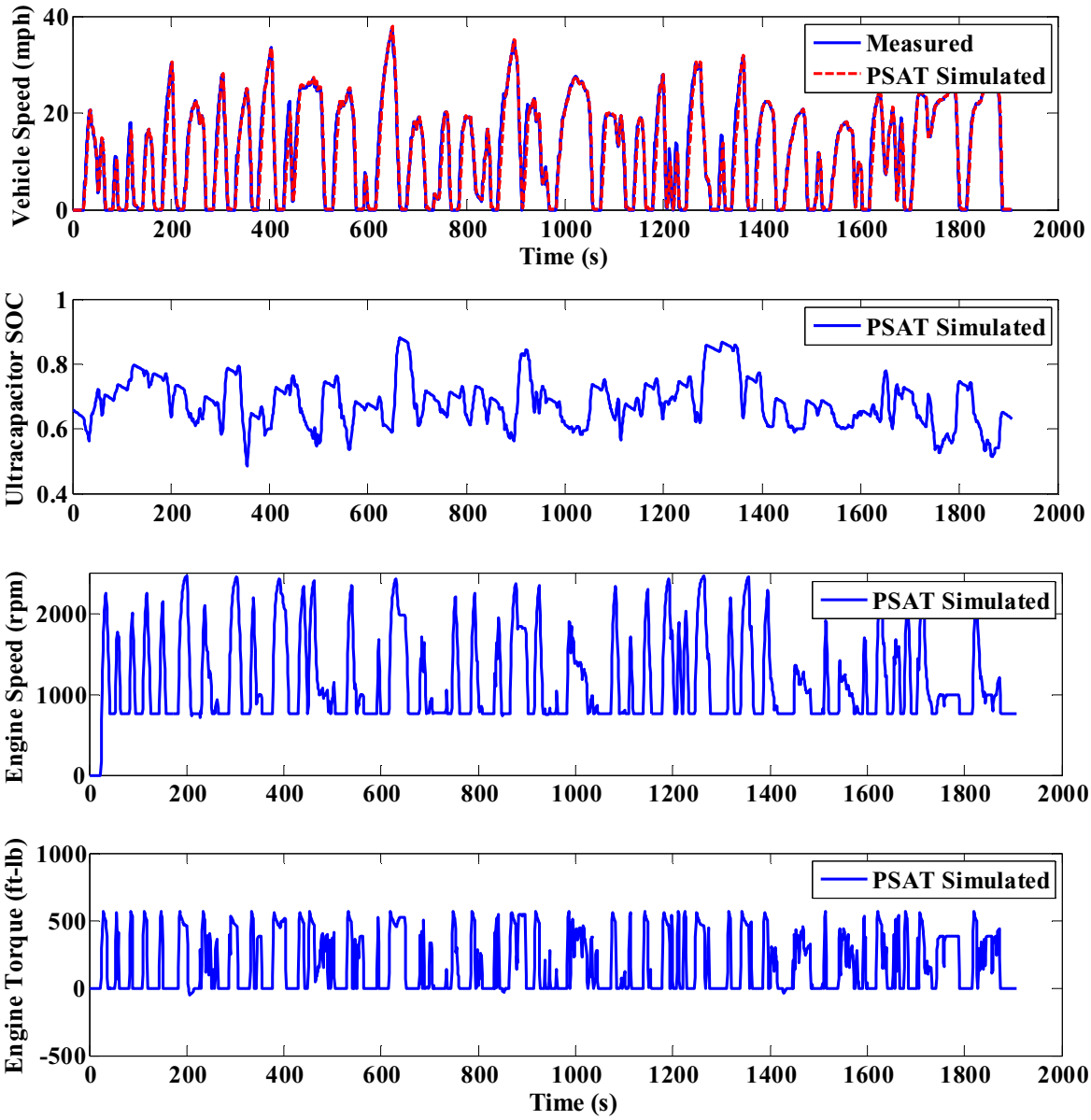

Figure 6.20: PSAT simulation results for New Flyer HEB over the OCTA cycle

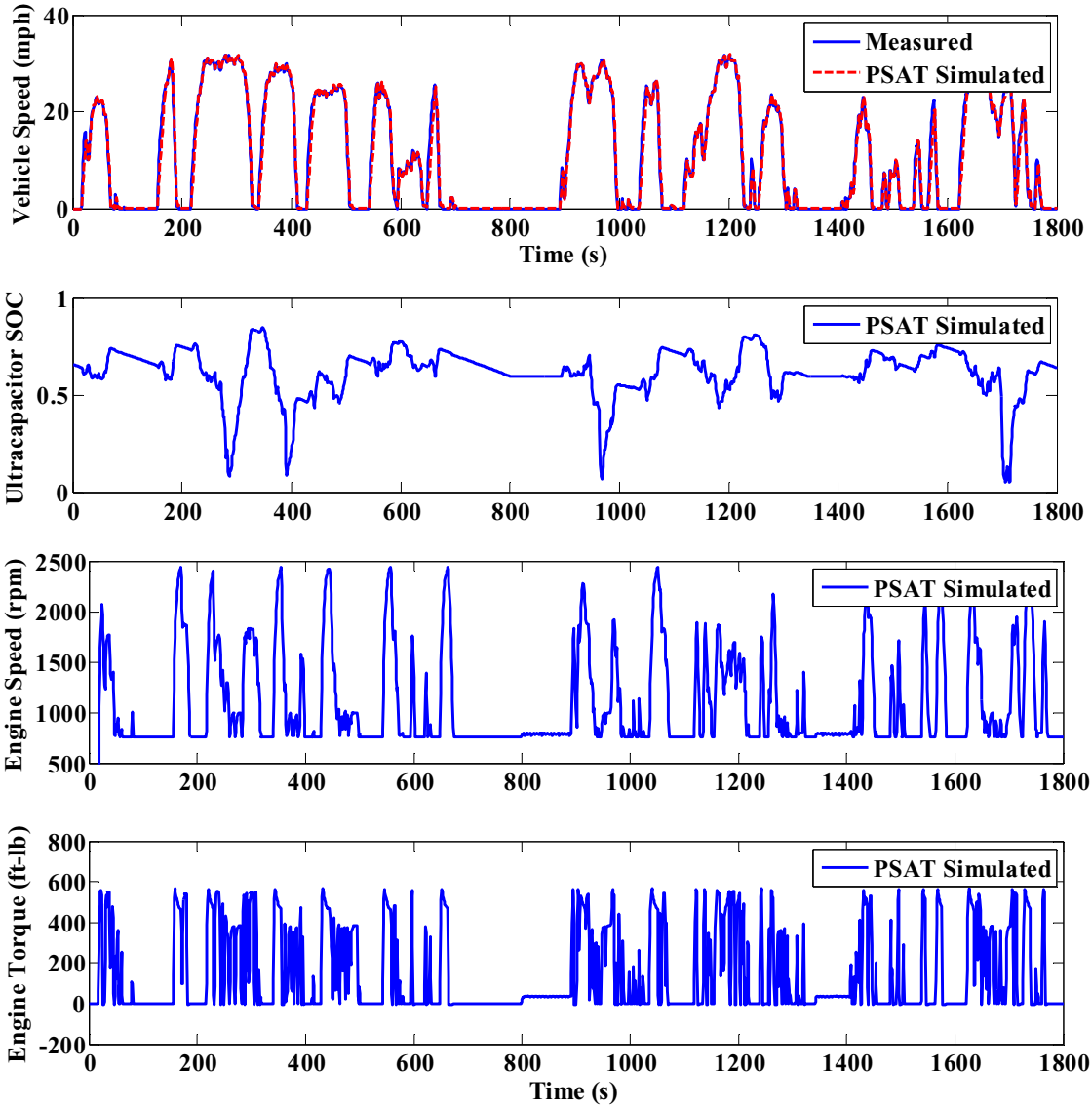

Figure 6.21: PSAT simulation results for New Flyer HEB over the Houston cycle

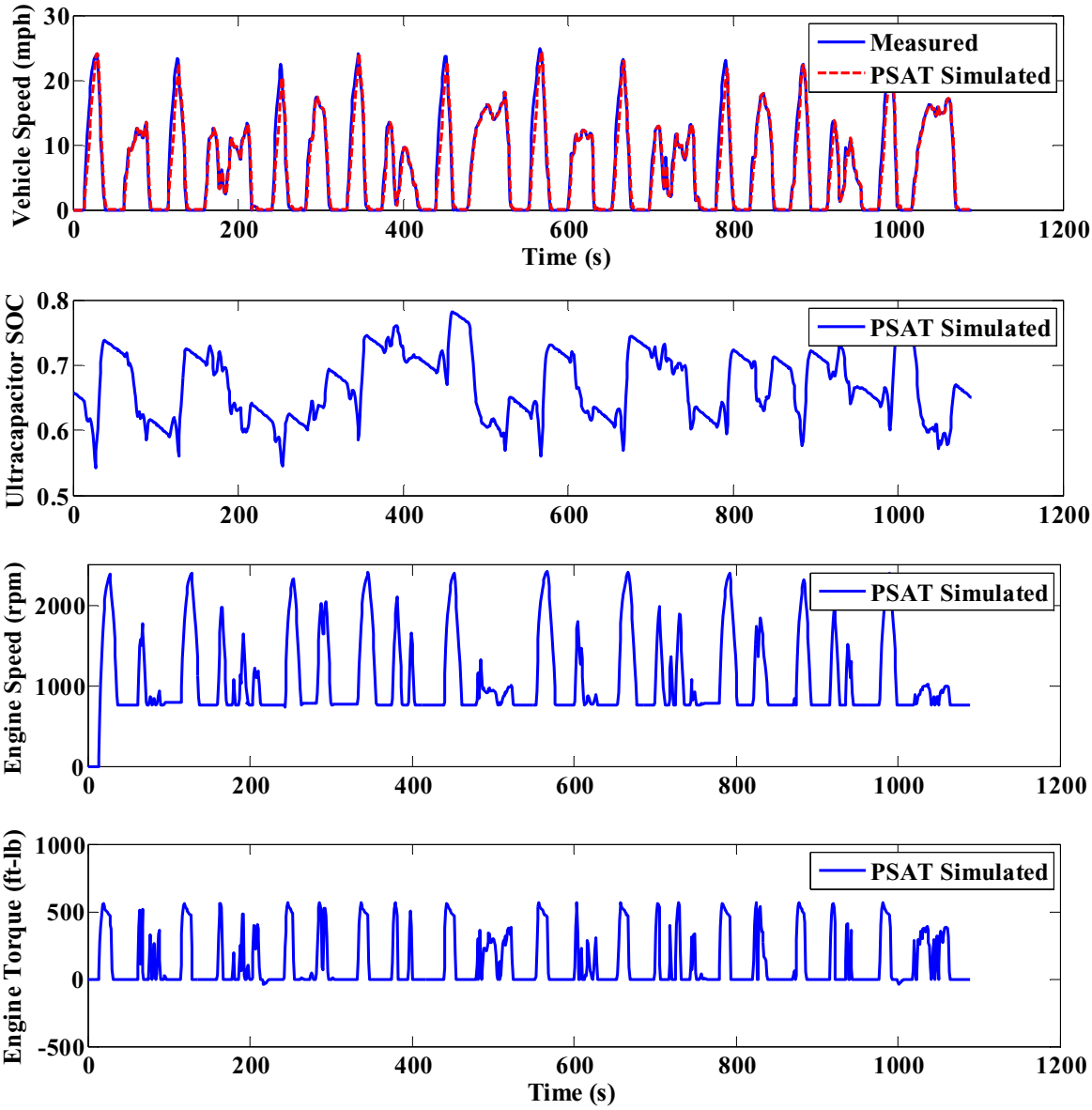

Figure 6.22: PSAT simulation results for New Flyer HEB over the Manhattan cycle

6.6. Summary

A generic methodology proposed to model the HEB was presented in this section. The specific HEB includes an ICE, an electric generator, ultracapacitors and a traction motor/brake. Three important aspects of the HEB modeling process were discussed in this study: modeled the main components, validated the engine model and improved the control strategy. The first part of the work was dedicated to the component data collection. The main components of the powertrain pertaining to the engine, the generator and motor, were mapped on the basis of information from the manufacturer [80] and data collected from the WVU Transportable Heavy-duty Vehicle

Emission Testing Laboratory. After the component information was implemented into PSAT, the engine model was validated. Results indicated that the maximum and minimum torque curves, fuel rate matrix, and NO_x emission rate matrix developed on the basis of experimental data from the four transient cycles (UDDS, OCTA, Manhattan and Houston) in the PSAT initialization file were sufficiently accurate and could be used to represent the Cummins ISB 260H engine model.

Two different control strategies, thermostatic control and load-following control were described. In a thermostatic control strategy, the engine operated at a maximum fuel efficiency point, with the ultracapacitors SOC varied between the upper and lower limits. In the load-following control strategy, the engine operated at an optimum speed-torque curve which consisted of the maximum efficiencies at different speeds. The load-following control strategy was utilized in this study. Once each individual component model was validated and the control strategy was improved, PSAT simulated results were compared with the experimental data over four various driving schedules. The relative percent of errors between the experimental and PSAT simulated values of the FC, FE, CO_2 and NO_x emissions were all within 5% except for the FE and NO_x of the Manhattan cycle, which were 6.93% and 7.13% respectively.

Chapter 7: Conclusions and Recommendations

7.1. Conclusions

The first objective was to validate a conventional heavy-duty truck model. The truck was an over-the-road 1996 Peterbilt tractor, equipped with a 550hp Caterpillar 3406E non-EGR engine and an 18-speed Roadranger manual transmission. This objective was achieved by acquiring the information and data described the components precisely, validating the engine model separately, as well as validating the whole vehicle model. The model developed in cooperation with ANL during this research, has been integrated into the PSAT model for its application to heavy-duty trucks. The central hypothesis, that "vehicle modeling tools can provide sufficiently valuable insight into factors affecting emissions and FE, provided that components within the models are adequately represented", was proven to be true. The difference between tested data and PSAT simulated data pertaining to average engine fuel rate, average engine torque, average engine speed, average engine power and the average NO_x were within 5% relative error. The comparison results indicated that the PSAT model was sufficiently accurate to use as the basis for parametric studies. The novelty of this research included the development of a predictive emissions model, transmission efficiency matrix for a manual 18-speed transmission based on information from manufacturer and a method to explore the engine cooling fan power losses.

The hypothesis of this research, that vehicle model can provide sufficiently insight into factors affecting on emissions and FE has been further proved by quantitatively analyzing the impact of the factors on emissions and FE. As the emissions and the FE were strongly dependent upon vehicle activities or duty cycles, the Peterbilt truck was simulated over five cycles: UDDS, creep, transient, cruise and high speed cruise short modes, which represented typical real world in-use behavior. Overall, the FC increased approximately linearly with the increase of the weight, coefficients of rolling resistance and aerodynamic drag over the schedules used. Among the three parameters, the truck weight had the largest effect on FC. A 0.9 percent fuel saving was found for every 1,000 lbs vehicle weight reduction over the cruise mode. The quantitative study also revealed how FE was influenced by multiple parameters. The FE contour figures were plotted as functions of multiple parameters, (such as coefficients of aerodynamic drag and rolling resistance, vehicle weight and the coefficient of rolling resistance), which generated two contributions: first, it provided a convenient way to estimate FE of the Peterbilt truck over various cycles by interpolating within the parameter values. Secondly the results showed that, depending on the circumstances, it may be more cost effective to reduce one parameter (such as coefficient of aerodynamic drag) to increase FE, or it may be more beneficial to reduce another parameter (such as the coefficient of rolling resistance). The simulation of the effect of the road grade on FE and emissions revealed that the Peterbilt truck model can overcome 3% uphill grade with speed loss but had difficulty following the target speed at high acceleration when the grade

is greater than 3% over the UDDS. The simulation also indicated that the UDDS with a 3% upgrade hill produced a 22.51% decrease in FE while at the same time it generated 16% more NO_x emissions compared to the UDDS with no grade.

Another objective of this research, to model a hybrid bus, was also achieved successfully. Information and data were acquired to describe all major components of the New Flyer hybrid bus, and these were incorporated as drivetrain components into PSAT. The engine model was validated separately before modeling the whole vehicle, which helped find problems with the specific model. The control strategy was improved in a way that the power flow of the engine, motor and ultracapacitors met the requirement of the power at the wheels while maintaining SOC at a reasonable level with the engine operating on the optimum fuel efficiency curve. The PSAT simulated results were compared with the experimental data over four various driving schedules. The relative percent of errors between the experimental and cycle averaged PSAT simulated values of FC, FE, CO_2, NO_x were all within 5% except for the FE and NO_x of the Manhattan cycle, which were 6.93% and 7.13% respectively. The high fidelity of this model made it possible to evaluate the FE and NO_x emissions of series hybrid buses for later PSAT users.

7.2. Recommendations

1. In the conventional Peterbilt truck model, the most crucial issue to computing fan power loss is to estimate the coolant temperature which controls the switching of the fan. When the fan is engaged, the fan power loss is the cube of fan speed (the same as engine speed in Peterbilt truck). In this study, the instantaneous coolant temperature was calculated by thermodynamic and heat transfer equations with some assumptions. A different method to predict the coolant temperatures is suggested as following. During a test, the vehicle speed, engine torque, engine speed, the coolant temperature, ambient temperature and the engine cooling fan's ON/OFF time fraction are collected. The coolant temperature predictive model is trained by using the LR or the ANN method, taking the vehicle speed, engine torque, speed (or even their derivatives) and ambient temperature as input parameters. The predicted coolant temperature is then expressed as a function of vehicle speed, engine torque, engine speed and ambient temperature. The predicted time fraction of fan ON/OFF can be found, providing the critical coolant temperature set by the manufacturer for fan ON/OFF is known. The engine coolant temperature model can be validated by comparing the predicted time fraction of fan ON/OFF with the tested time fraction of fan ON/OFF. The validated predictive coolant temperature model is integrated into the PSAT for estimating fan engine power loss.
2. In the HEB model, the electrical accessories model is taken from the PSAT original electrical accessory model, which is a constant power model. When the engine speed is above idle, a constant power loads the engine. In reality, the power of electrical accessories varies according to the ambient temperature, vehicle speed and operating load. The power consumption of an air conditioning system in a bus can be significant for riding comfort. It is

essential to accurately model the power consumption of air conditioning systems in PSAT for buses in the future.

3. As the average FE is strongly dependent on the power distribution between the engine and the energy storage system, optimizing the control strategy in a vehicle model would be worthwhile. In the road load control strategy, the engine operates in the optimum efficiency torque curve without considering the efficiencies of the motor and the energy storage system. An overall system optimized control strategy [142] which includes optimizing both the efficiency of the engine and the efficiency of the ESS is recommended for future work.

References

1. "EPA and NHTSA Propose First-Ever Program to Reduce Greenhouse Gas Emissions and Improve Fuel Efficiency of Medium- and Heavy-Duty Vehicles: Regulatory Announcement," EPA-420-F-10-901, October 2010, Available Online, http://www.epa.gov/otaq/climate/regulations/420f10901.pdf, Accessed 30 March 2011.
2. SmartWay^{SM} Transport Partnership, "U.S. EPA & NRCan (Natural Resource of Canada) Official Signing of the Memorandum of Understanding and Licensing Agreement," Fact Sheet, EPA420-F-05-041, September 2005.
3. "EPA to Release Draft Greenhouse Gas Emission Limits for Heavy Trucks," The New York Times - Breaking News, World News & Multimedia, Available Online, http://www.nytimes.com/gwire/2010/08/16/16greenwire-epa-to-release-draft-greenhouse-gas-emission-l-78469.html, Accessed 2 February 2011.
4. "Emission Standard, European Union: Heavy-Duty Diesel Truck and Bus Engine," DieselNet: Diesel Emissions Online, http://www.dieselnet.com/standards/eu/hd.php, Accessed 24 January 2011.
5. "Emission Standard, United States: Heavy-Duty Diesel Truck and Bus Engine," DieselNet: Diesel Emissions Online, http://www.dieselnet.com/standards/us/hd.php, Accessed 24 January 2011.
6. "Emission Standard, Australia: On-Board Vehicle and Engine," DieselNet: Diesel Emissions Online, http://www.dieselnet.com/standards/au/, Accessed 24 January 2011.
7. Clark, N.N., Gautam, M., Wayne, W.S., Lyons, D.W. and Thompson, G.J., "Heavy-Duty Vehicle Chassis Dynamometer Testing for Emissions Inventory, Air Quality Modeling, Source Apportionment and Air Toxics Emissions Inventory," Short Title: E-55/59, Final Report, Prepared by Center for Alternative Fuels, Engines, and Emissions (CAFEE), West Virginia University, WV, August 2007.
8. Clark, N.N., Wayne, W.S., Nine, R.D., Buffamonte, T., Hall, T., Rapp, B.L., Thompson, G.J. and Lyons, D.W., "Emissions from Diesel-Fueled, Heavy-Duty Vehicles in Southern California," 2003 SAE Transactions: Journal of Fuels & Lubricants, Vol. 112, pp. 1688-1699, May 2003.
9. Clark, N.N., Wayne, W.S., Buffamonte, T., Hall, T., Lyons, D.W. and Lawson, D., "The Gasoline/Diesel PM Split Study: Heavy Duty Vehicle Regulated Emissions," Coordinating Research Council On-Road Emissions Meeting, San Diego, CA, May 2003.
10. Clark, N.N., Gautam, M., Wayne, W.S., Thompson, G.J., Nine, R.D., Lyons, D.W., Buffamonte, T., Xu, S. and Maldonado, H., "Regulated Emissions from Heavy Heavy-

Duty Diesel Trucks Operating in the South Coast Air Basin," Powertrain and Fluid Systems Conference and Exhibition, Toronto, Ontario, Canada, SAE Paper 2006-01-3395, October 2006.

11. Duleep, K.G., "Emission and Energy Characteristics of Heavy-Duty Diesel-Powered Trucks and Buses," Energy and Environmental Analysis, Inc., 1995, Available Online, http://www.nap.edu/openbook.php?record_id=9676&page=237, Accessed 3 February 2011.

12. "Hybrid Electric Systems: Goals, Strategies and Top Accomplishment," Available Online, http://www1.eere.energy.gov/vehiclesandfuels/pdfs/hybrid_elec_sys_goals.pdf, Accessed 2 June 2011.

13. "SmartWay Transport," Available Online, http://www.epa.gov/smartwaytransport/transport/, Accessed 2 June 2011.

14. Committee to Assess Fuel Economy Technologies for Medium- and Heavy-Duty Vehicles; National Research Council; Transportation Research Board, Technologies and Approaches to Reducing the Fuel Consumption of Medium- and Heavy-Duty Vehicles, The National Academies Press, 2010, ISBN-10: 0-309-14982-7, Washington, D.C..

15. The MathWork™, "Argonne National Laboratory Develops Powertrain System Analysis Toolkit with MathWorks™ Tools," User Story, 91552v00, March 2008.

16. Wang, L., Clark, N.N. and Chen, P., "Modeling and Validation of an Over-the-Road Truck," SAE 2010 Commercial Vehicle Engineering Congress, Chicago, IL, SAE Paper 2010-01-2001, October 2010.

17. Clark, N.N., Gautam, M., Wayne, W.S., Thompson, G.J. and Lyons, D.W., "California Heavy Heavy-Duty Diesel Truck Emissions Characterization for Project E-55/E-59 Phase 1.5," CRC Project E-55/E-59 Report, August 2004.

18. Protection of the Environment, Code of Federal Regulations, CFR Appendix I to Part 86- Urban Driving Dynamometer Schedule, Title 40, U.S. Government Printing Office, Washington, D.C., 2005.

19. Clark, N.N., Tehranian, A., Nine, R.D. and Jarrett, R.P., "Translation of Distance-Specific Emissions Rates between Different Chassis Test Cycles using Artificial Neural Networks," SAE Spring 2002 Fuels & Lubricants Meeting, Reno, NV., SAE Paper 2002-01-1754, January 2002.

20. Clark, N.N., Gautam, M., Wayne, W.S., Nine, R.D., Thompson, G.J., Lyons, D.W., Maldonado, H., Carlock, M. and Agrawal, A., "Creation and Evaluation of a Medium Heavy-Duty Truck Test Cycle," 2003 SAE Transactions: Journal of Fuels & Lubricants, Vol. 112, pp. 2654-2667, October 2003.

21. Wang, M., "The Greenhouse Gases, Regulated Emissions, and Energy Use in Transportation (GREET) Model Version 1.5," August 1999, Available Online, http://www.transportation.anl.gov/pdfs/TA/264.pdf, Accessed 2 April 2011.

22. "AirCRED: Calculating Ozone Emission Reduction Credits for Clean Cities Vehicles," Available Online, http://www.transportation.anl.gov/modeling_simulation/AirCred/index.html, Accessed 30 March 2011.

23. U.S. Environmental Protection Agency, "Description and History of the MOBILE Highway Vehicle Emission Factor Model," Available Online, http://www.epa.gov/otaq/models/mob-hist.htm, Accessed 28 March 2011.

24. Markel, T., Brooker, A., Hendricks, T., Johnson, V., Kelly, K., Kramer, B., O'Keefe, V., Sprik, S. and Wipke, K., "ADVISOR: A Systems Analysis Tool for Advanced Vehicle Modeling," Journal of Power Sources, Vol. 110, No. 2, pp. 255-266, August 2002.

25. Cole, G.H., "SIMPLEV: A Simple Electric Vehicle Simulation Program, Version 1.0," Technical Report, DOE Contract Number: AC07-76ID01570, June 1991.

26. Ciccarelli, T., Toossi, R. and Goodarzi, A., "Assessment of Hybrid Configuration and Control Strategies in Planning Future metropolitan/Urban Transit Systems," SAE Future Transportation Technology Conference and Exposition, Costa Mesa, CA, SAE Paper 2001-01-2502, August 2001.

27. ECOCAR & Vehicle Technologies Program, "PSAT Accurately Simulates Advanced Vehicles," Available Online, http://www1.eere.energy.gov/vehiclesandfuels/pdfs/success/psat.pdf, Accessed 28 March 2011.

28. Gamma Technologies Inc., "Vehicle & Drivetrain Dynamics for Performance, Fuel Economy & Emissions," Available Online, http://www.gtisoft.com/img/broch/broch_gtdrive.pdf, Accessed 28 March 2011.

29. Gamma Technologies Inc., "GT-SUITE: Virtual Engine/Powertrain/Vehicle Simulation," Available Online, http://www.gtisoft.com/products/p_GT_SUITE.php, Accessed 28 March 2011.

30. Chen, D., "The Effects of Drive Cycle Accessory Load and Degree of Hybridization on Fuel Economy and Emissions for Hybrid Electric Buses," M.S. Thesis, University of Alabama, AL, 2010.

31. Nennelli, A.D., "Simulation of Heavy-Duty Hybrid Electric Vehicles," M.S. Thesis, West Virginia University, WV, 2001.

32. "SAE Standard J-2711: Recommended Practice for Measuring Fuel Economy and Emissions of Hybrid-Electric and Conventional Heavy-Duty Vehicle," SAE Standard

for Works in Process, September 2002, Available Online, http://subscriptions.sae.org/content/j2711_200209/, Accessed 30 January 2011.

33. Clark, N.N, Wayne, W.S. and Lyon D.W., "Transit Bus Life Cycle Cost and Year 2007 Emissions Estimation," Final Report to Federal Transit Administration (FTA), FTA-WV-26-7004.2007.1, July 2007.

34. Khan, ABM.S., "Route and Grade Sensitive Modeling of Fuel Efficiency and Emissions for Diesel Buses," Ph.D. Dissertation, West Virginia University, WV, 2010.

35. Barth, M. and Boriboonsomsin, K., "Real-World CO2 Impacts of Traffic Congestion," Transportation Research Record: Journal of the Transportation Research Board, Washington, D.C., No. 2058, pp. 163-171, November 2008.

36. Delorme, A., Karbowski, D. and Sharer, P., "Evaluation of Fuel Consumption Potential of Medium and Heavy Duty Vehicles through Modeling and Simulation," Report to National Academy of Sciences, Washington, D.C., Contract Number: DEPS-BEES-001, October 2009.

37. Protection of the Environment, Code of Federal Regulations, Part 86, Subpart N, Title 40, U.S. Government Printing Office, Washington, D.C., 2005.

38. Kern, J., Clark, N.N., and Nine, R.D., "Factoring Terrain Effects into Vehicle Emissions Modeling and Inventory," 10th CRC On-Road Vehicle Emissions Workshop, San Diego CA, March 2000.

39. Simpson, A.G., "Parametric Modeling of Energy Consumption in Road Vehicles," Ph.D. Dissertation, the University of Queensland, Australia, 2005.

40. American Association of State Highway and Transportable Official, A Policy on Geometric Design of Highways and Streets, AASHTO, Fifth Edition, Washington, D.C., 2004.

41. Rao, C.R., Toutenburg, H., Fieger, A., Heumann, C., Nittner T. and Scheid, S., Linear Models: Least Squares and Alternatives, Second Edition, Springer Series in Statistics, New York, NY, 1999.

42. Wolberg, J., Data Analysis Using the Method of Least Squares: Extracting the Most Information from Experiments, Springer, New York, NY, 2005.

43. Saville, D.J. and Wood, G.R., Statistical methods: the geometric approach, Third Edition, Springer, Springer, New York, NY, 1991.

44. Ramamurthy, R., Clark, N.N., Atkinson, C.M. and Lyons, D.W., "Models for Predicting Transient Heavy Duty Vehicle Emission," SAE International Fall Fuels and Lubricants Meeting and Exhibition, San Francisco, CA, SAE paper 982652, October 1998.

45. Jarrett, R.P. and Clark, N.N., "Weighting of Parameters in Artificial Neural Network Prediction of Heavy-Duty Diesel Engine Emissions," Powertrain and Fluid Systems Conference and Exhibition, San Diego, CA, SAE Paper 2002-01-2878, October 2002.

46. "Reduce NO_x Emissions on the Road," European Conference of Ministers of Transport (ECMT), 2006, Available Online, http://internationaltransportforum.org/pub/pdf/06NOx.pdf, Accessed 4 February 2011.

47. Chen, X., Schmid, N.A., Wang, L. and Clark, N.N., "Regression-Based Oxides of Nitrogen Predictors for Three Diesel Engine Technologies," Journal of the Air & Waste Management Association, Vol. 60, No. 1, pp. 72-90, January 2010.

48. Clark, N.N., Bedick, C.R., Wang, L., Thompson, G.J., McKain, D. and Ralston, B., "Emissions from a Legacy Diesel Engine Exercised through the ACES Engine Test Schedule," SAE International Powertrains, Fuels and Lubricants Congress, Shanghai, China, SAE Paper 2008-01-1679, June 2008.

49. Arsie, I., Marotta, F., Pianese, C. and Rizzo, G., "Information-Based Selection of Neural Networks Training Data for S.I. Engine Mapping," SAE 2001 World Congress, Detroit, MI, SAE Paper 2001-01-0561, April 2001.

50. Vincent, D., McCardle, J. and Stroud, R., "Classification of Metal Transfer Mode Using Neural Networks," Neural Networks, IEEE International Conference, Perth, WA, Vol. 1, pp. 522-525, December 1995.

51. Luo, F., Applied Neural Networks for Signal Processing, Cambridge University Press, New York, NY, March 1999.

52. De Lucas, A., Duran, A. Carmona, M. and Lapuerta M., "Modeling Diesel Particulate Emissions with Neural Networks," Fuel, Vol. 80, No. 4, pp. 539-548, March 2001.

53. Hashemi, N. and Clark, N.N., "Artificial Neural Network as a Predictive Tool for Emissions from Heavy-Duty Diesel Vehicles in Southern California," International Journal of Engine Research, Vol. 8, No. 4, 2007.

54. Hanzevack, E.L., Long, T.W., Atkinson, C.M. and Traver, M.L., "Virtual Sensors for Spark Ignition Engines Using Neural Networks," Proceedings of the American Control Conference, Albuquerque, NM, Vol. 1, pp. 669-673, June 1997.

55. Bedick, C.R., "Optimization of a Retrofit Urea-SCR System," Ph.D. Dissertation, West Virginia University, WV, 2009.

56. Thompson, G.J., Atkinson, C.M., Clark, N.N., Long, T.W. and Hanzevack, E., "Neural Network Modeling of the Emissions and Performance of a Heavy-Duty Diesel Engine," Proceedings of the Institution of Mechanical Engineers, Part D: Journal of Automobile Engineering, Vol. 214, No. 2, pp. 111-126, 2000.

57. Desantes, J.M., López, J.J., García, J.M. and Hernández, L., "Application of Neural Networks for Prediction and Optimization of Exhaust Emissions in a H.D. Diesel Engine," SAE 2002 World Congress, Detroit, MI, SAE Paper 2002-01-1144, March 2002.

58. Krijnsen, H.C., Van Kooten, W.J., Calis, H.A., Verbeek, R.P. and Van Den Bleek, C.M., "Prediction of NO_x Emissions from a Transiently Operating Diesel Engine Using an Artificial Neural Network," Chemistry Engineering Technology, Vol. 22, pp. 601-607, July 1999.

59. Tehranian, A., "Effects of Artificial Neural Networks Characterization on Prediction of Diesel Engine Emissions," M.S. Thesis, West Virginia University, WV, 2004.

60. "Hybrid Buses Cost and Benefits," Available Online, http://www.eesi.org/files/eesi_hybrid_bus_032007.pdf, Accessed 5 February 2011.

61. Haddadi,S., Esfahanian, V., Nehzati, H., Sangtarash, F. and Akhgari, A., "Effects of Drivetrain Hybridization on Fuel Economy and Dynamic Performance of a Series Hybrid Electric Transit Bus," SAE International Powertrains, Fuels and Lubricants Congress, Shanghai, China, SAE Paper 2008-01-1562, June 2008.

62. Burke, A.F., "Hybrid/electric Vehicle Design Options and Evaluations," SAE International Congress and Exposition, Detroit, MI, SAE paper 920447, February 1992.

63. Zhang, J., Lu, X., Xue, J. and Li, B., "Regenerative Braking System for Series Hybrid Electric City Bus," The World Electric Vehicle Journal, Vol. 2, No. 4, pp. 128-134, 2008.

64. Ehsani, M., Gao, Y. and Emadi, A., Modern Electric Hybrid Electric, and Fuel Cell Vehicles: Fundamentals, Theory and Design, Second Edition, CRC Press, ISBN, 9781420053982, September 2009.

65. Chu, L., Wang, Q., Liu, M. and Li, J., "Parametric Design of Series Hybrid Powertrain for Transit Bus," SAE International Truck and Bus Meeting and Exposition, Fort Worth, TX, SAE Paper 2003-01-3371, November 2003.

66. Northeast Advanced Vehicle Consortium, Bradley, M.J. and Associates, TCRP Report 59: Hybrid-Electric Transit Buses: Status, Issues, and Benefits, National Academy Press, Washington, D.C., 2000.

67. Wong, Y.S., "System Design and Energy Management Strategy for Hybrid Electric Vehicle," Ph.D. Dissertation, University of Hong Kong, China, 2008.

68. Xiong, W.W. and Yin, C.L., "Design of Series-Parallel Hybrid Electric Propulsion Systems and Application in City Transit Bus," WSEAS Transactions on System, Vol. 8, No. 5, May 2009.

69. Chandler, K. and Walkowicz, K., "King County Metro Transit Hybrid Articulated Buses: Final Evaluation Results," Technical Report, NREL/TP-540-40585, December 2006.

70. Jalil, N., Naim, A.K. and Salman, M., "A Rule-Based Energy Management Strategy for a Series Hybrid Vehicle," Proceedings of the American Control Conference, Albuquerque, NM, Vol. 1, pp. 689-693, June 1997.

71. Sciarretta, A., Back, M. and Guzzella, L., "Optimal Control of Parallel Hybrid Electric Vehicles," IEEE Transactions on Control Systems Technology, Vol. 12, No. 3, pp. 352-363, May 2004.

72. Turlapati, V.K., "Modeling and Optimization of a Plug-in Hybrid Electric Vehicle," M.S. Thesis, Clemson University, SC, 2010.

73. Karden, E., Ploumen, S., Fricke, B., Miller, T. and Snyder, K., "Energy Storage Devices for Future Hybrid Electric Vehicles," Journal of Power Sources, December 2006, Available Online http://spinnovation.com/sn/Batteries/Energy_storage_devices_for_future_hybrid_electric_vehicles.pdf, Accessed 6 April 2011.

74. Aditya, J.P. and Ferdowsi, M., "Comparison of NiMH and Li-Ion Batteries in Automotive Applications," IEEE Vehicle Power and Propulsion Conference, Harbin, China, September 2008.

75. "The Nickel-Metal Hydride (NiMH) Battery," Available Online, http://buchmann.ca/chap2-page4.asp, Accessed 30 March 2011.

76. "Charging Lithium-Ion Batteries", Available Online, http://batteryuniversity.com/learn/article/charging_lithium_ion_batteries, Accessed 30 March 2011.

77. "Capacitor Characteristics," Rod Elliott (ESP), September 2005, Available Online, http://sound.westhost.com/articles/capacitors.htm, Accessed 30 March 2011.

78. Rotenberg, D., "Ultracapacitor Assisted Powertrains: Modeling, Control, sizing, and the impact on fuel economy," M.S. Thesis, Clemson University, SC, 2008.

79. Major, J., "Hybrid Shuttle Bus Using Ultracapacitors," Proceedings of Electrical Insulation Conference and Electrical Manufacturing Expo, Indianapolis, IN, pp. 275-278, October 2005.

80. Personal Communication, New Flyer Industries Inc., August 2010.

81. Rousseau, A., "PSAT Training: Part 02: Capabilities," Argonne National Laboratory, Available Online, http://www.transportation.anl.gov/pdfs/HV/298.pdf, Accessed 23 February 2011.

82. Rousseau, A., Sharer, P. and Besnier, F., "Feasibility of Reusable Vehicle Modeling: Application to Hybrid Vehicles," SAE 2004 World Congress and Exhibition, Detroit, MI, SAE Paper 2004-01-1618, March 2004.

83. Baglione, M.L., "Development of System Analysis Methodologies and Tools for Modeling and Optimizing Vehicle System Efficiency," Ph.D. Dissertation, University of Michigan, MI, 2007.

84. Maxoulis, C.N., Tsinoglou, D.N. and Koltsakis, G.C., "Modeling of Automotive Fuel Cell Operation in Driving Cycles," Energy Conversion and Management, Vol. 45, No. 4, pp. 559-573, March 2004.

85. PSAT Documentary, Book 2-Components, Packaged with PSAT Software.

86. PSAT Documentary, Book 3-Controllers, Packaged with PSAT Software.

87. Paynter, H.M., Analysis and Design of Engineering Systems, MIT Press, Cambridge, MA, 1961.

88. Karnopp, D., Margolis, D. and Rosenberg, R., System Dynamics: A Unified Approach, Second edition, John Wiley & Sons, Inc., New York, NY, 1990.

89. United States Environmental Protection Agency, "Emissions Standards Reference Guide for Heavy-Duty and Nonroad Engines," EPA420-F-97-014, Washington, D.C., September 1997.

90. United States Environmental Protection Agency, "Greenhouse Gas Emissions," Available Online, http://www.epa.gov/climatechange/emissions/index.html, Accessed 8 January 2011.

91. California Environmental Protection Agency Air Resources Board (CARB), "Health Effects of Diesel Exhaust Particulate Matter," Available Online, http://www.countyofglenn.net/govt/departments/air_pollution/documents/8-19-07/fact_sheet_health_effects_of_diesel_exha.pdf, Accessed 15 February 2011.

92. Perhinschi, M.G., Wayne, W.S., Clark, N.N. and Lyons, D.W., "Neural Network Modeling of Emissions from Medium-Duty Vehicles Operating on Fisher-Tropsch Synthetic Fuel," SAE 2007 World Congress, Detroit, MI, SAE Paper 2007-01-1080, April 2007.

93. Ramamurthy, R. and Clark, N.N., "Atmospheric Emissions Inventory Data for Heavy Duty Vehicles," Environmental Science & Technology, Vol. 33, No. 1, pp. 55-62, December 1988.

94. Vora, K.A., "Cycle and Weight Effects on Emissions and Development of Predictive Emissions Model for Heavy-Duty Trucks," M.S. Thesis, West Virginia University, WV, 2006.

95. Lyons, D.W. (Principal Investigator), “Transportable Heavy Duty Emissions Testing Laboratory and Research Program,” Prepared under Task No. DE-FG26-90CH10451, the U.S. Department of Energy, Prepared by Center for Alternative Fuels, Engines, and Emissions (CAFEE), West Virginia University, WV, December 2008.

96. Wu, Y., Carder, D. and Shade, B., “A CFR1065-Compliant Transportable/On-Road Low Emissions Measurement Laboratory with Dual Primary Full-Flow Dilution Tunnels,” ASME 2009 Internal Combustion Engine Division Spring Technical Conference, Milwaukee, WI, Paper No. ICES2009-76090, pp. 399-410, May 2009.

97. Clark, N.N., McKain, D., Barnett, R., Wayne, W.S., Gautam, M., Thompson, G.J. and Lyons, D.W., “Evaluation of Crankcase Emissions Abatement Device,” Presented to: New Condensator, Inc., Prepared by Center for Alternative Fuels Engines and Emissions (CAFEE),West Virginia University, WV, August 2006.

98. Olatunji, I., Clark, N.N., Sindler, P., McKain, D., Thompson, G.J., Gautam, M., Wayne, W.S. and Nuszkowski, J., “Biodiesel Blend Emissions of a 2007 Medium Heavy Duty Diesel Truck,” SAE Commercial Vehicle Engineering Congress, Rosemont, IL, SAE Paper 2010-01-1968, October 2010.

99. Madireddy, M.R. and Clark, N.N., “Sequential Inversion Technical and Differential Coefficient Approach for Accurate Instantaneous Emission Measurement,” International Journal of Engine Research, Vol. 7, No. 6, pp. 437-446, July 2006.

100. Kamarianakis, Y. and Gao, H.O., “Accounting for Exhaust Gas Transport Dynamics in Instantaneous Emission Models via Smooth Transition Regression,” Environmental Science & Technology, Vol. 44, No. 4, pp. 1320-1326, January 2010.

101. Madireddy, M.R., “Methods for Reconstruction of Transient Emissions from Heavy-Duty Vehicles,” Ph.D. Dissertation, West Virginia University, WV, 2008.

102. Hashemi, N. and Clark, N.N., “Artificial neural network as a predictive tool for emissions from heavy-duty diesel vehicles in Southern California,” International Journal of Engine Research, Vol. 8, No. 4, pp. 321-336, August 2007.

103. Messer, J.T, Clark, N.N. and Lyons, D.W., “Measurement Delays and Modal Analysis for a Heavy-Duty Transportable Emissions Testing Laboratory,” SAE International Congress and Exposition, Detroit, MI, SAE paper 950218, February 1995.

104. Clark, N.N., Jarrett, R.P. and Atkinson, C.M., “Field Measurements of Particulate Matter Emissions and Exhaust Opacity from Heavy Duty Vehicles,” Journal of the Air & Waste Management Association, Vol. 107, pp. 84-93, 1999.

105. Ganesan, B. and Clark, N.N., “Relationship between instantaneous and measured emissions in heavy-duty applications,” SAE International Fall Fuels and Lubricants Meeting and Exhibition, San Antonio, TX, SAE Paper 2001-01-3536, September 2001.

106. Atjay, D. and Weilenmann, M., "Compensation of the Exhaust Gas Transport Dynamics for Accurate Instantaneous Emission Measurements," Environmental Science and Technology, Vol. 38, No. 17, pp. 5141-5148, August 2004.

107. Available Online, http://www.golynx.com/?id=1156140, Accessed 31 March 2011.

108. Buhmann, M.D., Radial Basis Functions: Theory and Implementations, Cambridge University Press, Cambridge, U.K., 2003.

109. Celikoglu, H.B., "Application of Radial Basis Function and Generalized Regression Neural Networks in Non-Linear Utility Function Specification for Travel Mode Choice Modeling," Mathematical and Computer Modeling, Vol. 44, No. 7-8, pp. 640-658, October 2006.

110. The MathWorks Online help toolbox, http://www.mathworks.com/help/toolbox/nnet/radial_3.html#45, Accessed 20 February 2011.

111. The MathWorks Online help toolbox, http://www.mathworks.com/help/toolbox/nnet/radial_3.html#45, Accessed 20 February 2011.

112. Eaton Fuller Transmission Manual, September 2007, Available Online, http://www.roadranger.com/Roadranger/productssolutions/transmissions/low-inertiasuper18/index.htm, Accessed 20 February 2011.

113. Personal Communication, Eaton Corp., July 2008.

114. Setright, L. J. K. (Edited by Ian Ward), Anatomy of the Motor Car, St. Martin's Press, New York, NY, pp. 93-95, 1976.

115. Leo, A.M. and Dongen, V., "Efficiency Characteristics of Manual and Automatic Passenger Car Transaxles," SAE Passenger Car Meeting and Exposition, Troy, MI, SAE Paper 820741, June 1982.

116. Heingartner, P. and Mba, D., "Determining the Power Losses in the Helical Gear Mesh," ASME 2003 International Design Engineering Technical Conferences and Computers and Information in Engineering Conference, Chicago, IL, Paper No. DETC2003/PTG-48118, pp. 965-970, September 2003.

117. Personal Communication, Peterbilt Motors Company, January 2009.

118. Nunney, M.J., Light and Heavy Vehicle Technology, Fourth Edition, Butterworth-Heinemann, Burlington, MA, November 2006.

119. Arici, O., Johnson, H.J. and Kulkarni, J.A., "The Vehicle Engine Cooling System Simulation Part 1 - Model Development," SAE International Congress and Exposition, Detroit, MI, SAE Paper 1999-01-0240, March 1999.

120. Hawkins, J.S., Avery, R.M. and Super, L., "Method of Estimating Engine Cooling Fan Power Losses," US Patent 6904352, June 2005.

121. Personal Communication, Caterpillar Inc., January 2010.

122. Rousseau, A., Sharer, P. and Pasquier, M., "Validation Process of an HEV System Analysis Model: PSAT," SAE 2001 World Congress, Detroit, MI, SAE Paper 2001-01-0953, March 2001.

123. Rousseau, A., Kwon, J., Sharer, P., Pagerit, S. and Duoba, M., "Integrating Data, Performing Quality Assurance, and Validating the Vehicle Model for the 2004 Prius Using PSAT," SAE 2006 World Congress, Detroit, MI, SAE Paper 2006-01-0667, April 2006.

124. TIAX, LLC, "Assessment of Fuel Economy Technologies for Medium- and Heavy-Duty Vehicles," Final Report to the National Academy of Sciences, Cambridge, MA, pp. 4-3, September 2009.

125. Goodyear Tire and Rubber Company, "Radial Truck Tire and Retread Service Manual," Manual No. 700-862-932-505, 2003.

126. Evans, L., Harris, J., Terrill, E. and MacIsaac, J.D., "The Effects of Varying the Levels of Nitrogen in the Inflation Gas of Tires on Laboratory Test Performance," Report prepared by NHTHA Vehicle Research and Test Center, Report No. DOT HS 811 094, Washington, D.C., March 2009.

127. Schuring, D.J., "The Rolling Loss of Pneumatic Tires," Rubber Chemistry and Technology, Vol. 53, No. 3, pp. 600-720, 1980.

128. Smith, M. and Eberle, C., "Heavy Vehicle Mass Reduction Goals and Manufacturing Challenges," Presentation at the U.S. Department of Energy Workshop on Tooling Technology for Low Volume Vehicle Production, Seattle, WA, October 2003.

129. Melson, J., "Progress in Tires." Presentation by Michelin at the International Workshop on the Use of Wide-Base Tires**,** Federal, McLean, VA, October 2007.

130. Ogburn, M., Ramroth, L. and Lovins A.B., "Transformational Trucks: Determining the Energy Efficiency Limits of a Class-8 Tractor-Trailer," July 2008, Available Online, http://www.rmi.org/rmi/Library/T08-08_TransformationalTrucksEnergyEfficiency, Accessed 3 March 2011.

131. Sullivan, R., "Parasitic Energy Loss Reduction," Presentation to the National Academy of Sciences Committee on Review of the 21st Century Truck Partnership, Washington, D.C., February 2007.

132. "Super-Light Trucks are Coming," June 2009, Available Online, http://fleetowner.com/trucking_around_world/building-lighter-trucks-0625/, Accessed 3 March 2011.

133. "Financial and Operating Information for America's 100 Largest for Hire and Private Fleets," September 2009, Available Online, http://www.ttnews.com/tt100/TT100_web_FH09.pdf, Accessed 3 March 2011.

134. Landau, L.D. and Lifshitz, E.M., Theory of Elasticity, Third Edition, Butterworth-Heinemann, Oxford, UK, 1986.

135. O'Keefe, M.P. and Vertin, K., "An Analysis of Hybrid Electric Propulsion Systems for Transit Buses," National Renewable Energy Laboratory, Milestone Completion Report, Contract No. DE-AC36-99-GO10337, October 2002.

136. Wohlecker, R., Johannaber, M. and Espig, M., "Determination of Weight Elasticity of Fuel Economy for Conventional ICE Vehicles, Hybrid Vehicles and Fuel Cell Vehicles," SAE World Congress & Exhibition, Detroit, MI, SAE Paper 2007-01-0343, April 2007.

137. American Association of State Highway and Transportable Official (AASHTO), A Policy on Geometric Design of Highways and Streets, Fifth Edition, 2004, Available Online, http://www.knovel.com/web/portal/browse/display?_EXT_KNOVEL_DISPLAY_bookid=2528&VerticalID=0, Accessed 23 February 2011.

138. Clark, N.N., Khan, ABM.S., Wayne, W.S., Gautam, M., Thompson, G.J., McKain, D., Lyons, D.W. and Barnett, R., "Weight Effect on Emissions and Fuel Consumption from Diesel and Lean-Burn Natural Gas Transit Buses," 14th Asia Pacific Automotive Engineering Conference, Hollywood, CA, SAE Paper 2007-01-3626, August 2007.

139. Bachman, L., Erb, A. and Bynum, C., "Effect of Single Wide Tires and Trailer Aerodynamics on Fuel Economy and NO_x Emissions of Class 8 Line-Haul Tractor Trailers." Commercial Vehicle Engineering Congress and Exhibition, Chicago, IL, SAE Paper 2005-01-3551, November 2005.

140. Personal Communication, Cummins Inc., August 2010.

141. Rousseau, A., Sharer, P. and Pasquier, M., "Validation Process of an HEV System Analysis Model: PSAT," SAE 2001 World Congress, Detroit, MI, SAE Paper 2001-01-0953, March 2001.

142. Cross, P.W., "System Modeling and Energy Management Strategy Development for Series Hybrid Vehicles," M.S. Thesis, Georgia Institute of Technology, GA, August 2008.

143. Wang, Z., Li, W. and Xu, Y., "A Novel Power Control Strategy of Series Hybrid Electric Vehicle," 2007 IEEE/RSJ International Conference on Intelligent Robots and Systems, San Diego, CA, October-November 2007.

Appendix A: Driving Schedules

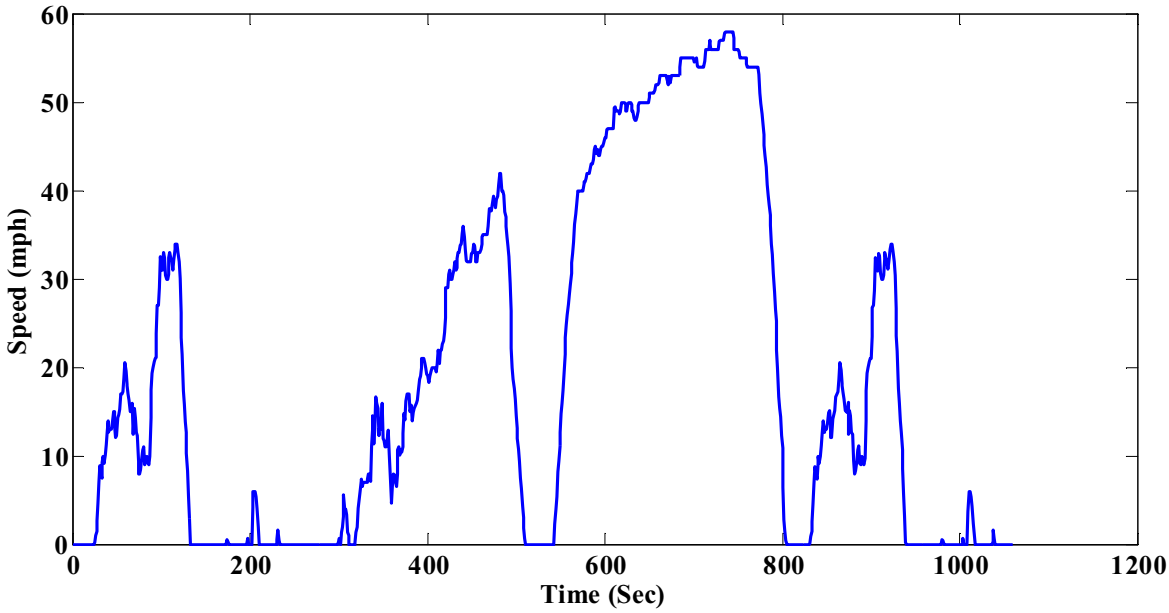

Figure A1: UDDS

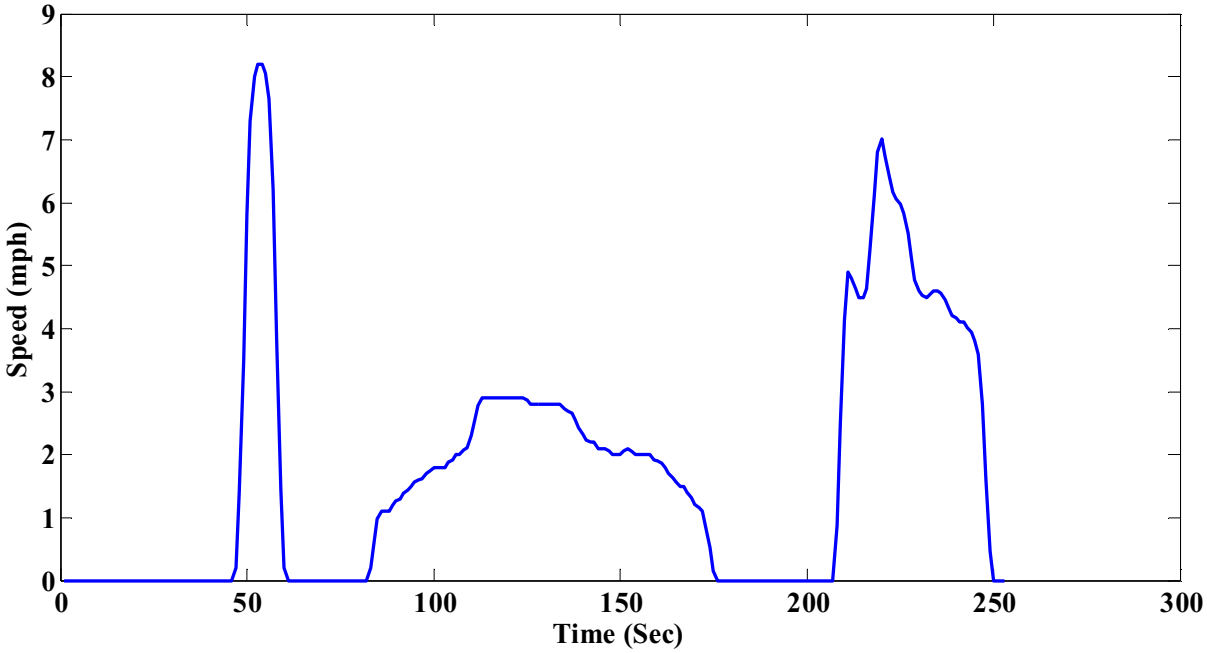

Figure A2: Creep Mode

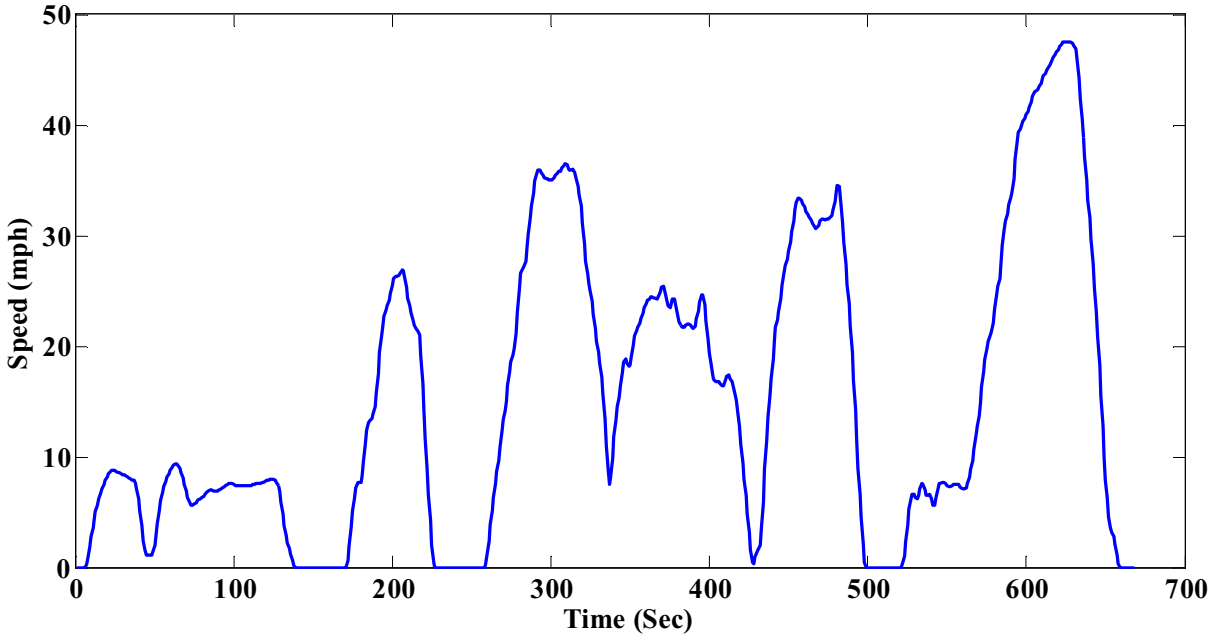

Figure A3: Transient Mode

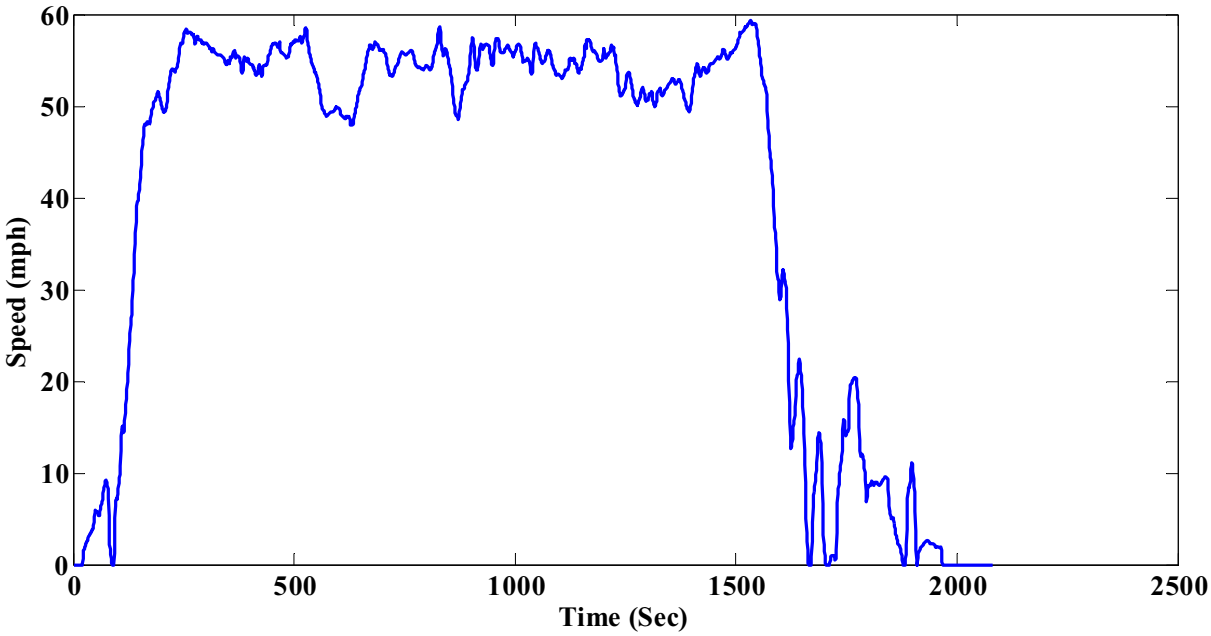

Figure A4: Cruise Mode

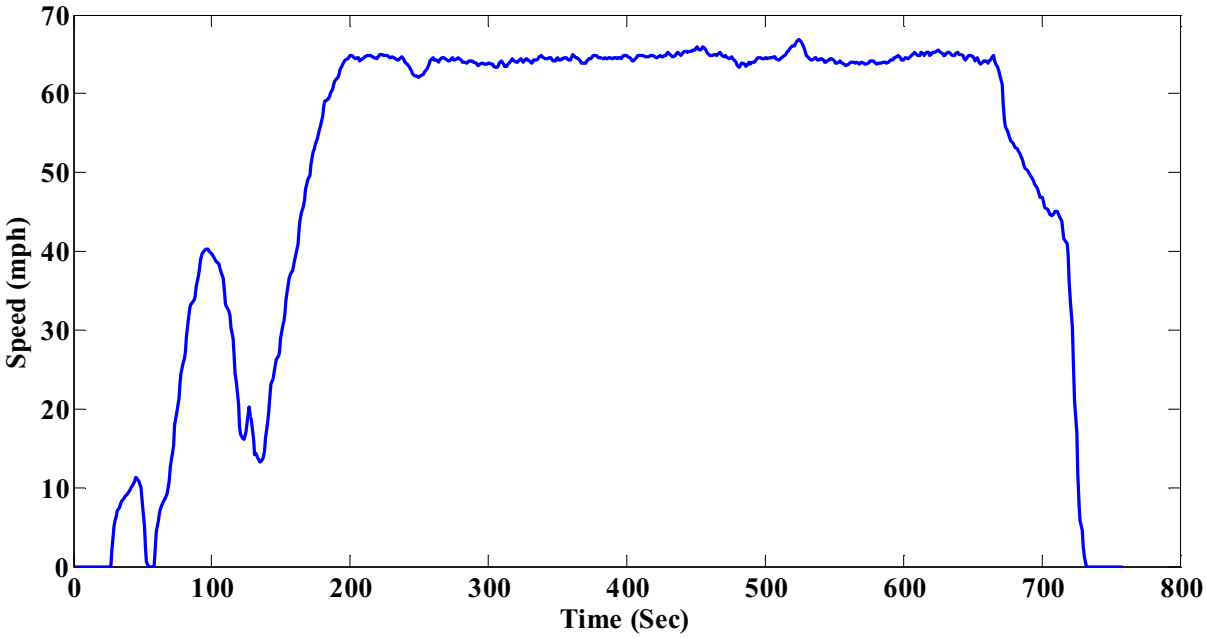

Figure A5: HHDDT_s Mode

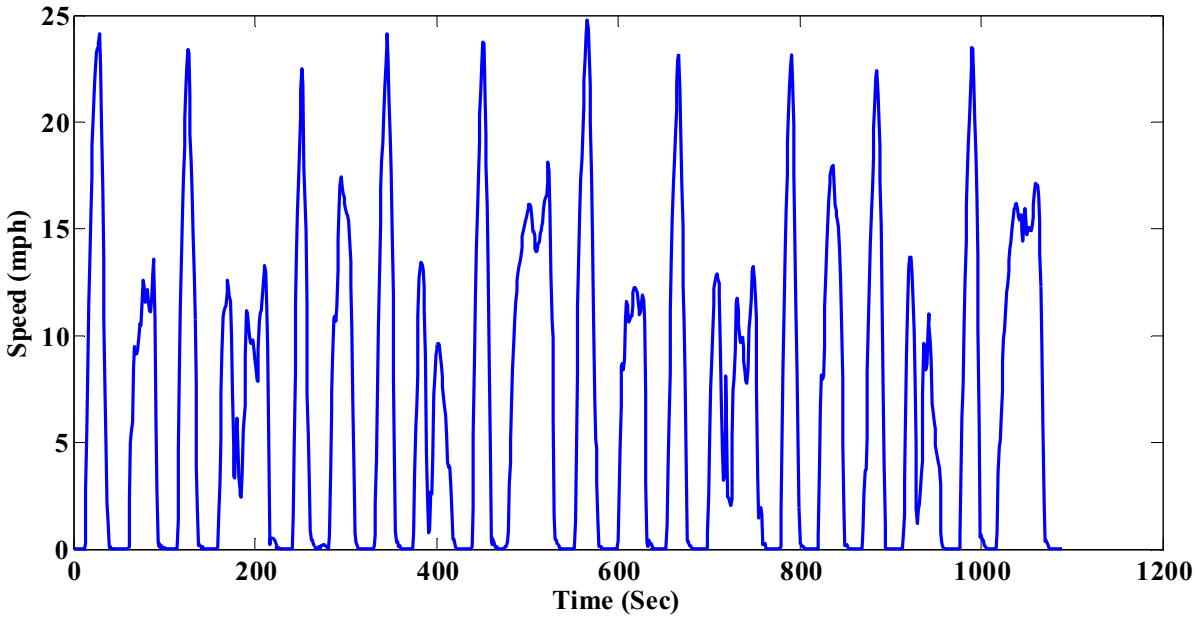

Figure A6: Manhattan Cycle

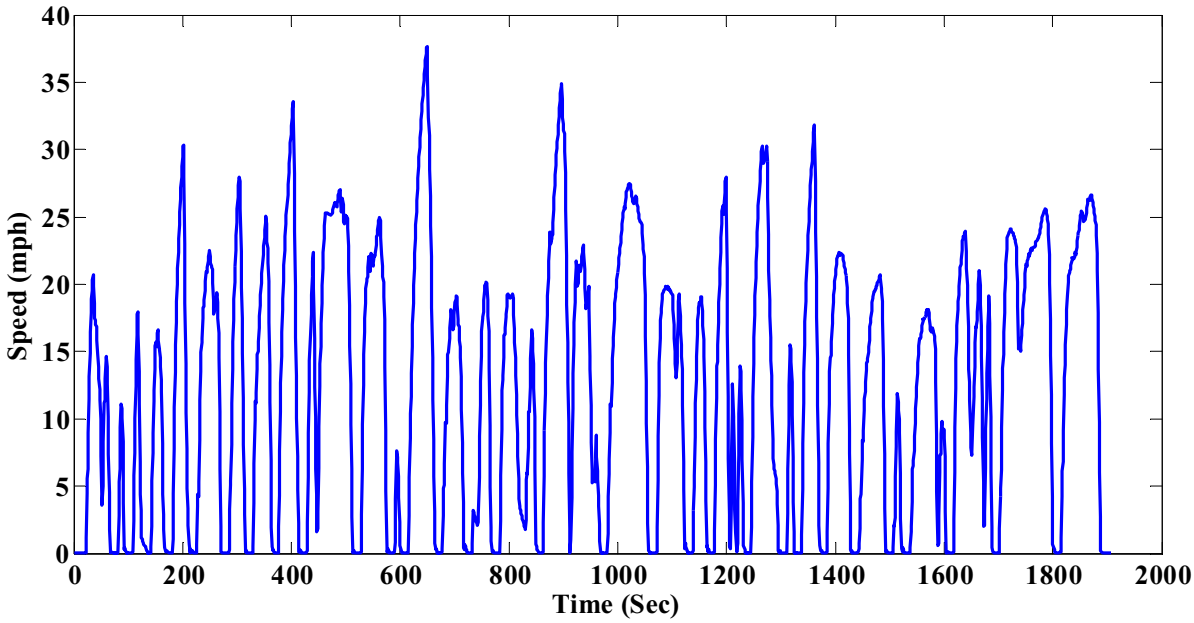

Figure A7: OCTA Cycle

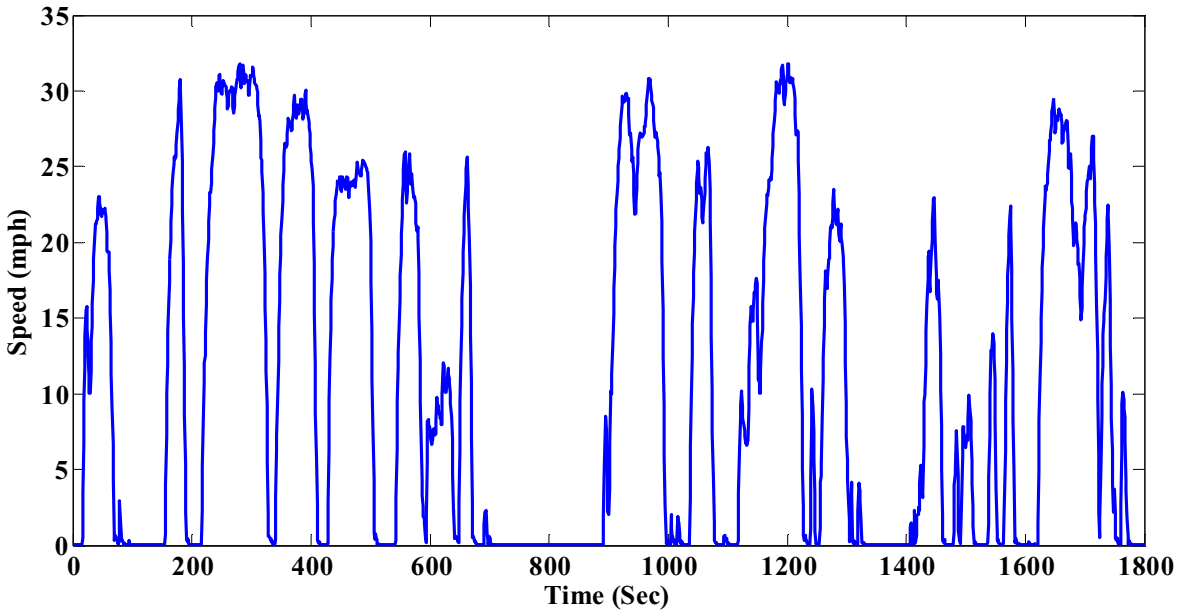

Figure A8: Houston Cycle

Appendix B: NO_x Emissions Model-LR Method

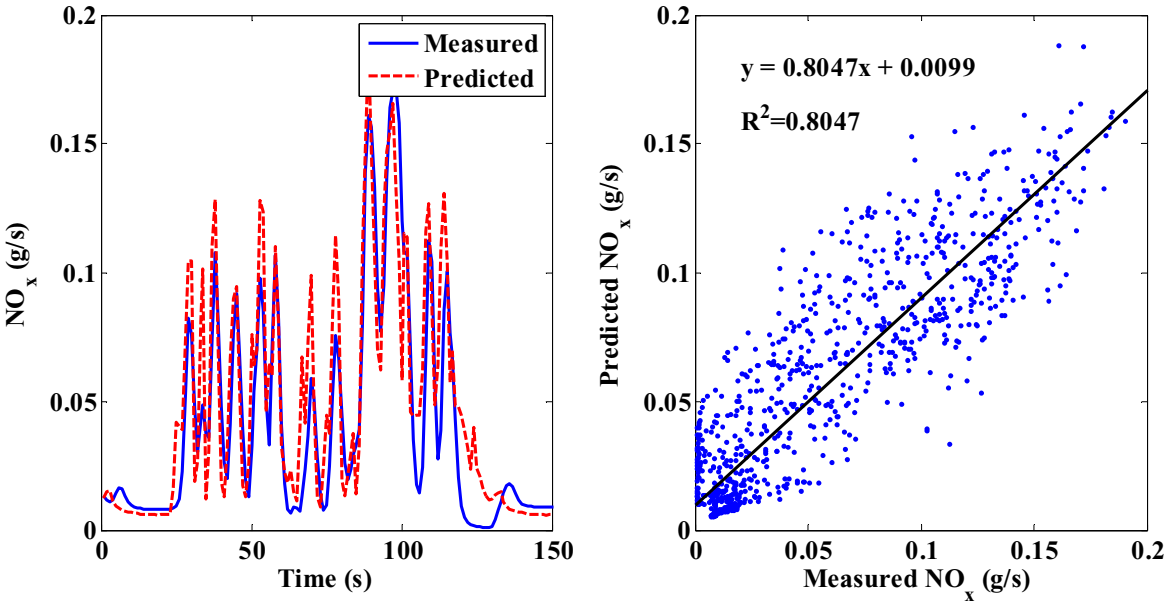

Figure B1: The comparison plot (over a selected 150 seconds) and parity plot of the measured and predicted NO_x of the 2005 LYNX transit bus using LR method from the UDDS training data

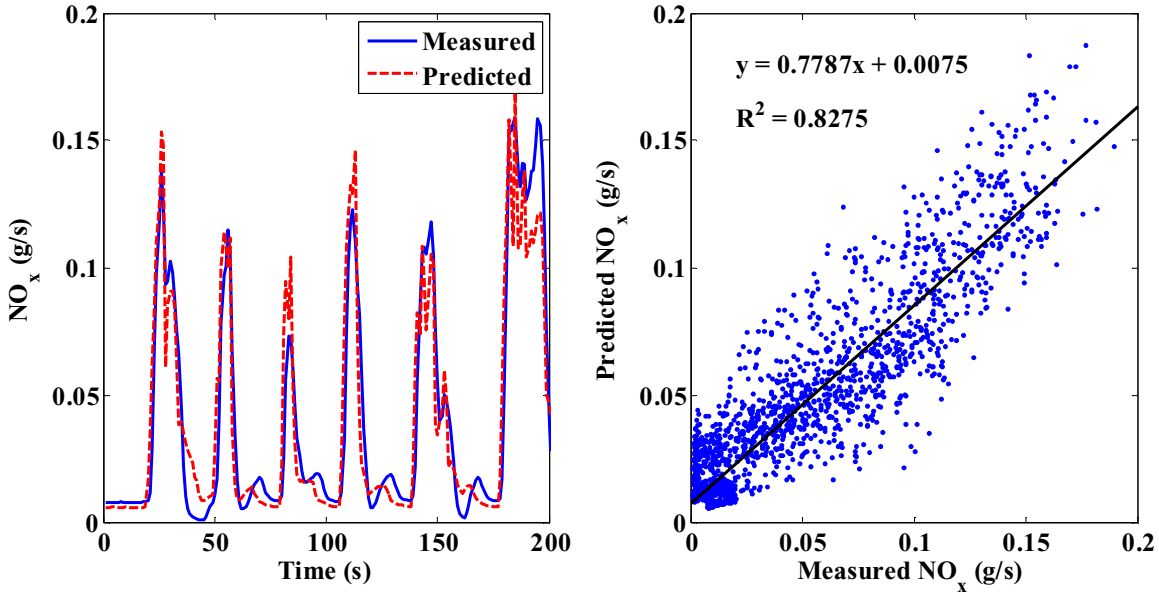

Figure B2: The comparison plot (over a selected 200 seconds) and parity plot of the measured and predicted NO_x of the 2005 LYNX transit bus using LR method from the OCTA cycle testing data

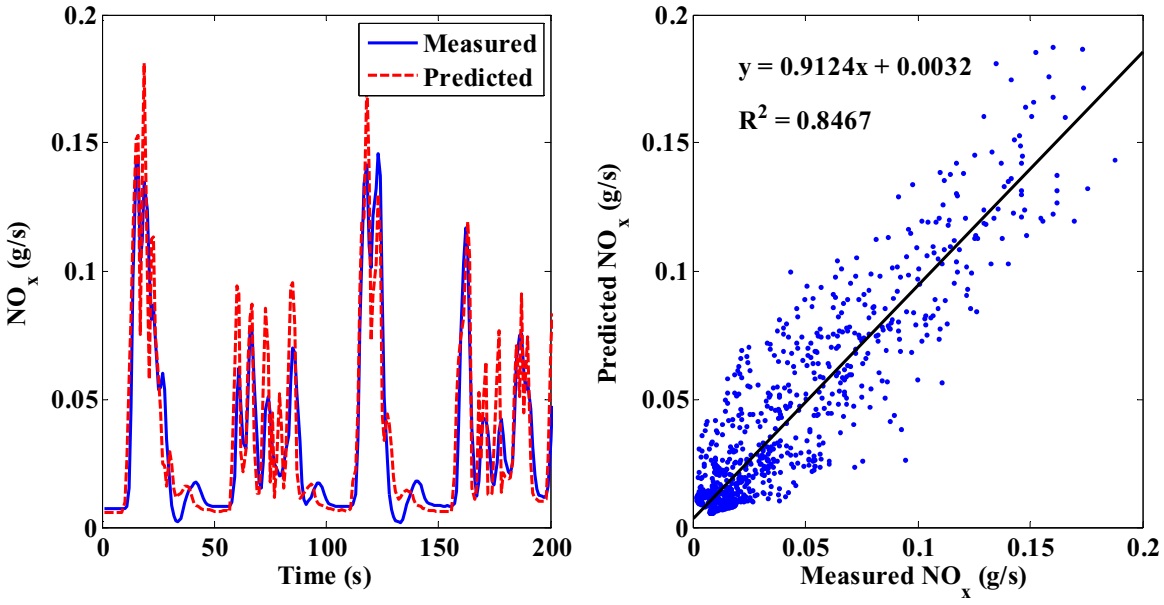

Figure B3: The comparison plot (over a selected 200 seconds) and parity plot of the measured and predicted NO_x of the 2005 LYNX transit bus using LR method from the Manhattan cycle testing data

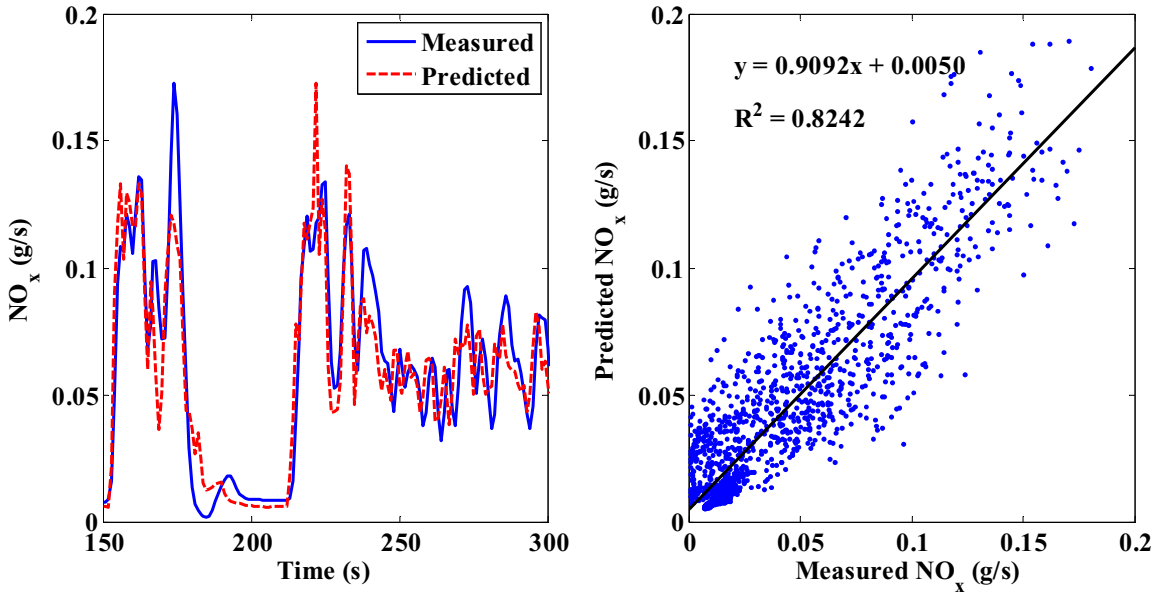

Figure B4: The comparison plot (over a selected 150 seconds) and parity plot of the measured and predicted NO_x of the 2005 LYNX transit bus using LR method from the Houston cycle testing

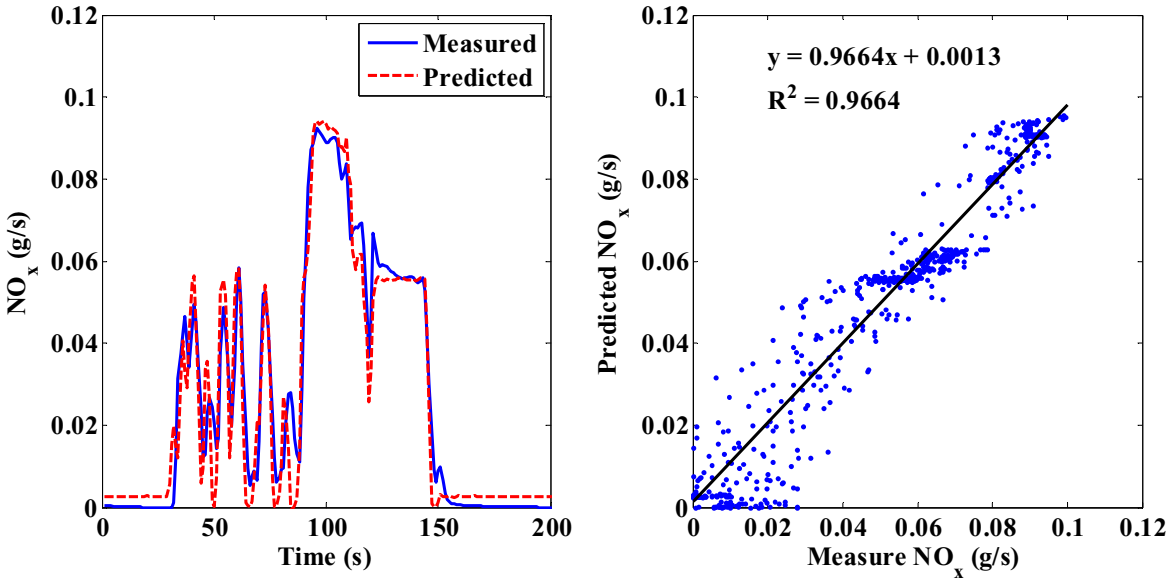

Figure B5: The comparison plot (over a selected 200 seconds) and parity plot of the measured and predicted NO_x of the 2007 MY ISE hybrid bus using LR method from the UDDS training data

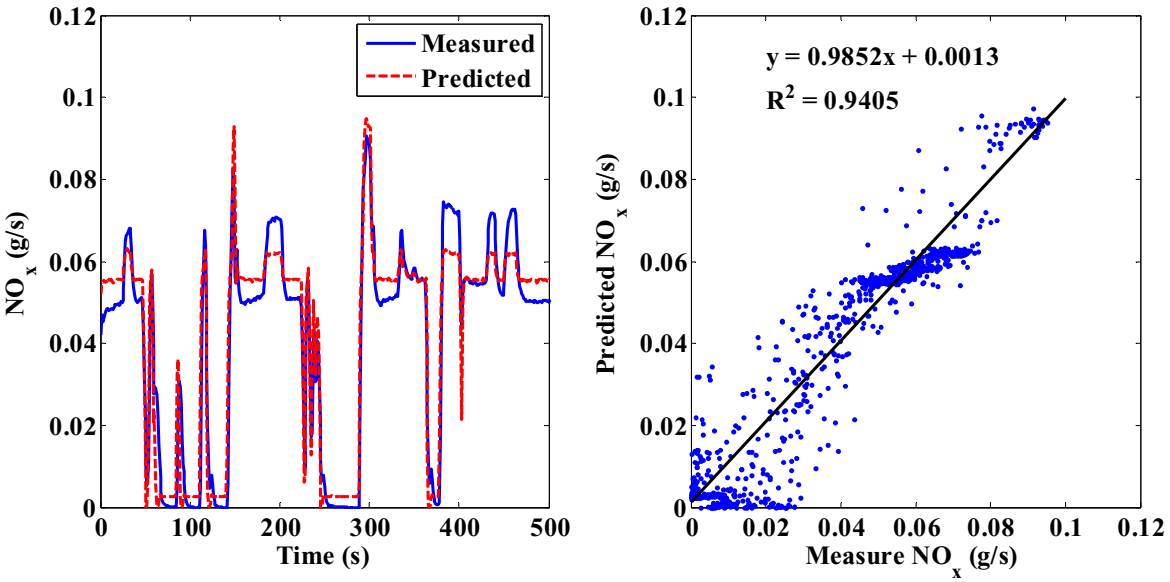

Figure B6: The comparison plot (over a selected 500 seconds) and parity plot of the measured and predicted NO_x of the 2007 MY ISE hybrid bus using LR method from the OCTA cycle testing data

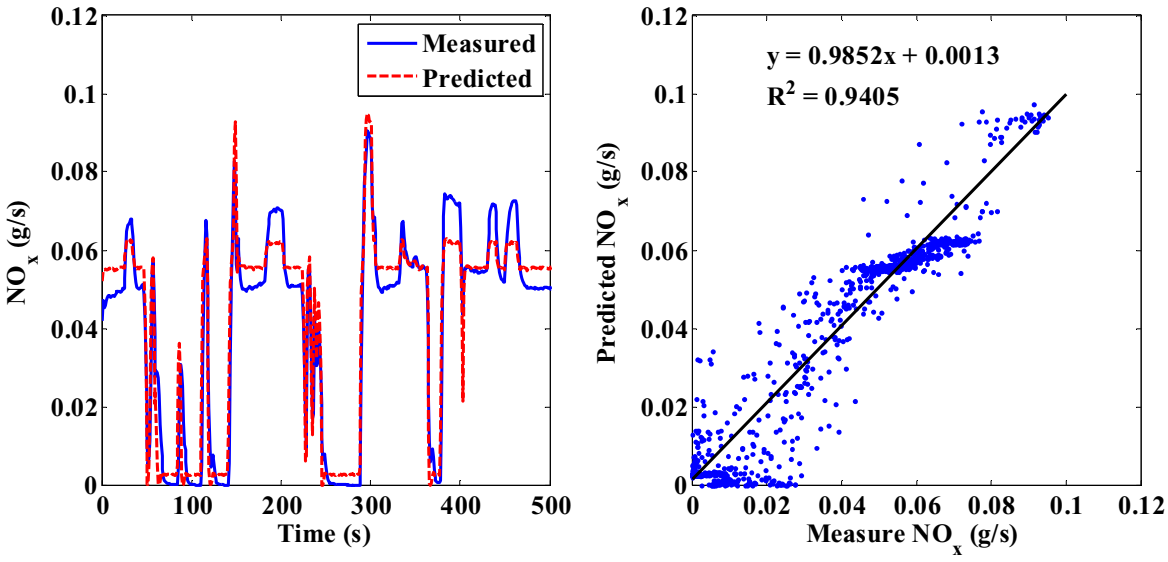

Figure B7: The comparison plot (over a selected 500 seconds) and parity plot of the measured and predicted NO_x of the 2007 MY ISE hybrid bus using LR method from the Manhattan cycle testing data

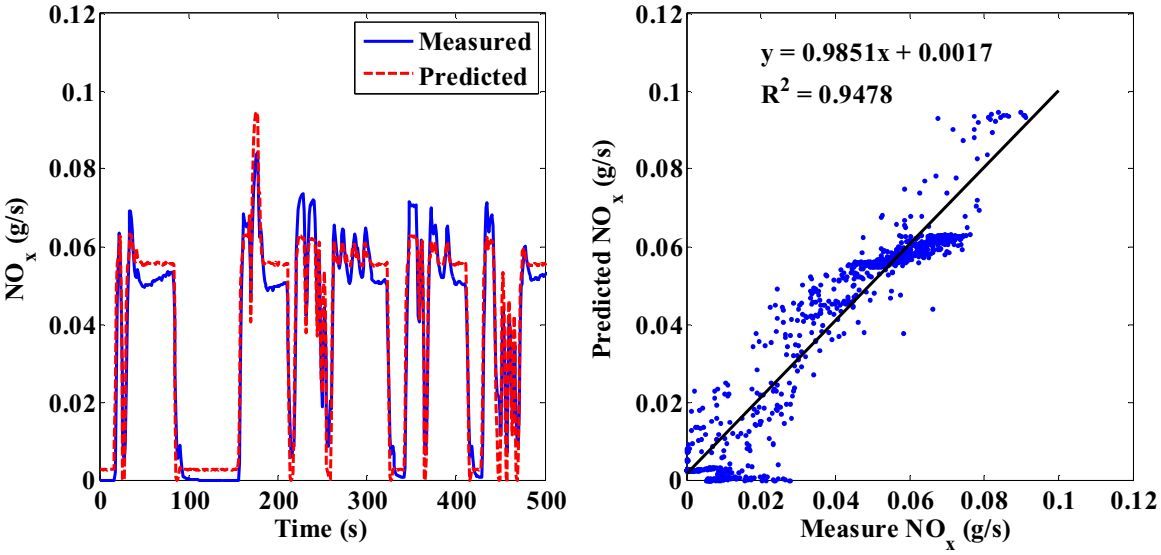

Figure B8: The comparison plot (over a selected 500 seconds) and parity plot of the measured and predicted NO_x of the 2007 MY ISE hybrid bus using LR method from the Houston cycle testing data

Appendix C: NO_x Emissions Model - ANN Method

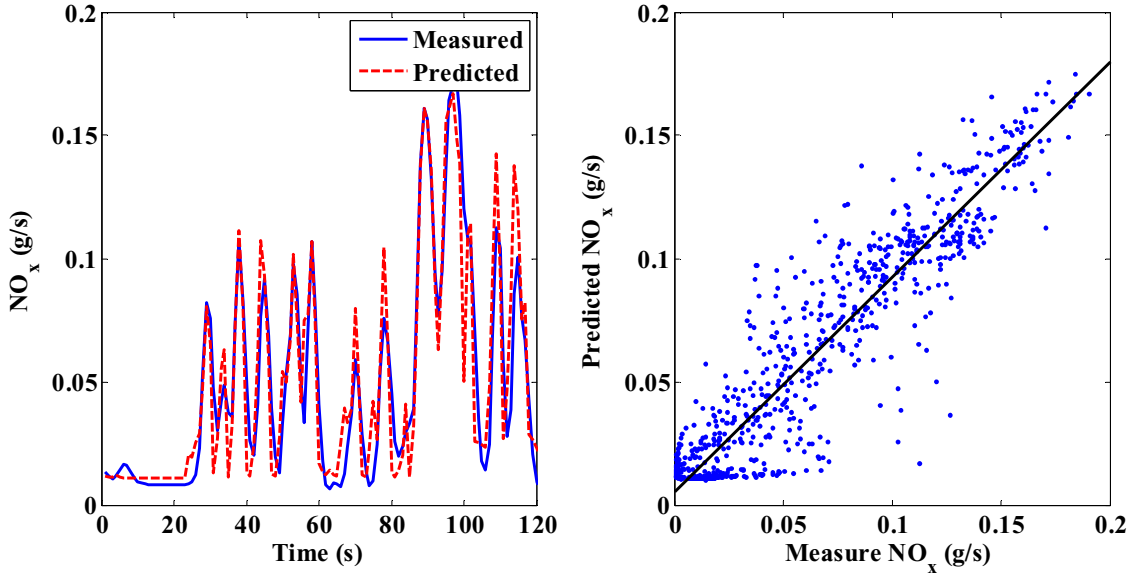

Figure C1: The comparison plot (over a selected 120 seconds) and parity plot of the measured and predicted NO_x of the 2005 LYNX transit bus using ANN method from the UDDS training data

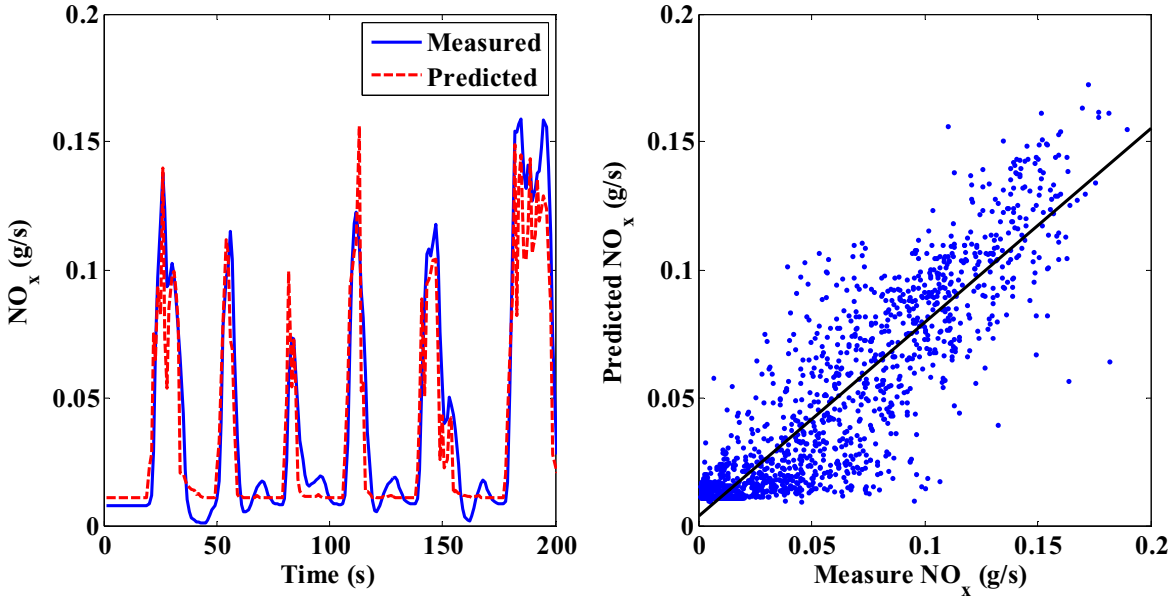

Figure C2: The comparison plot (over a selected 200 seconds) and parity plot of the measured and predicted NO_x of the 2005 LYNX transit bus using ANN method from the OCTA cycle testing data

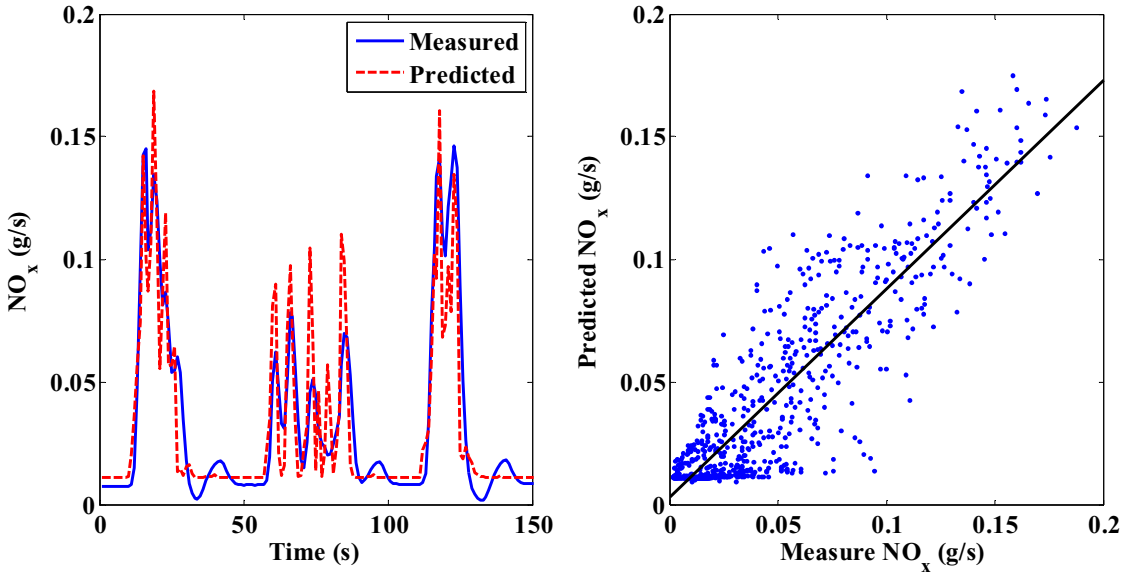

Figure C3: The comparison plot (over a selected 150 seconds) and parity plot of the measured and predicted NO_x of the 2005 LYNX transit bus using ANN method from the Manhattan cycle testing data

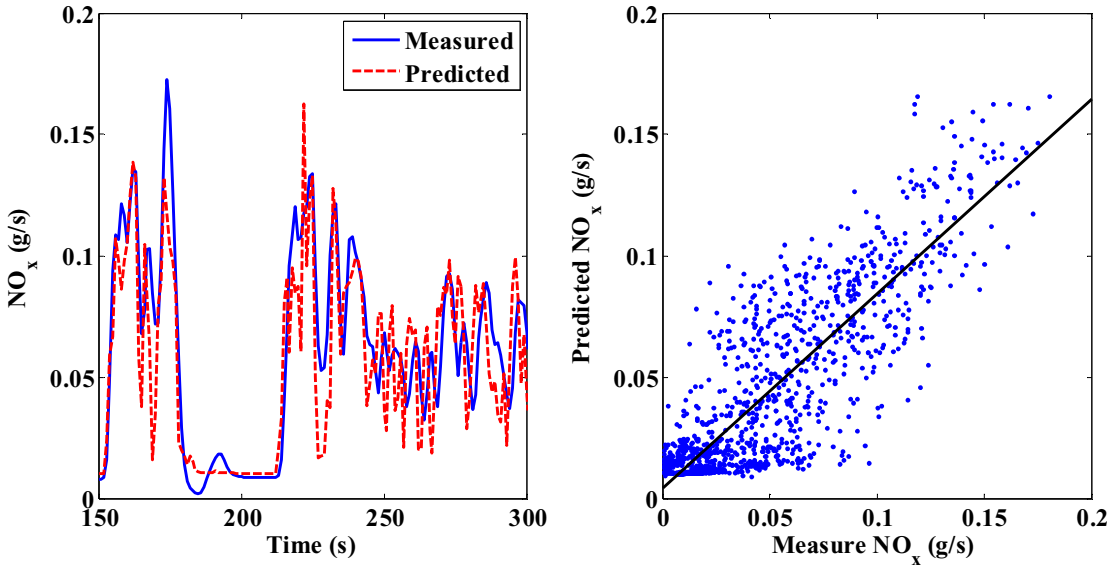

Figure C4: The comparison plot (over a selected 150 seconds) and parity plot of the measured and predicted NO_x of the 2005 LYNX transit bus using ANN method from the Houston cycle testing data

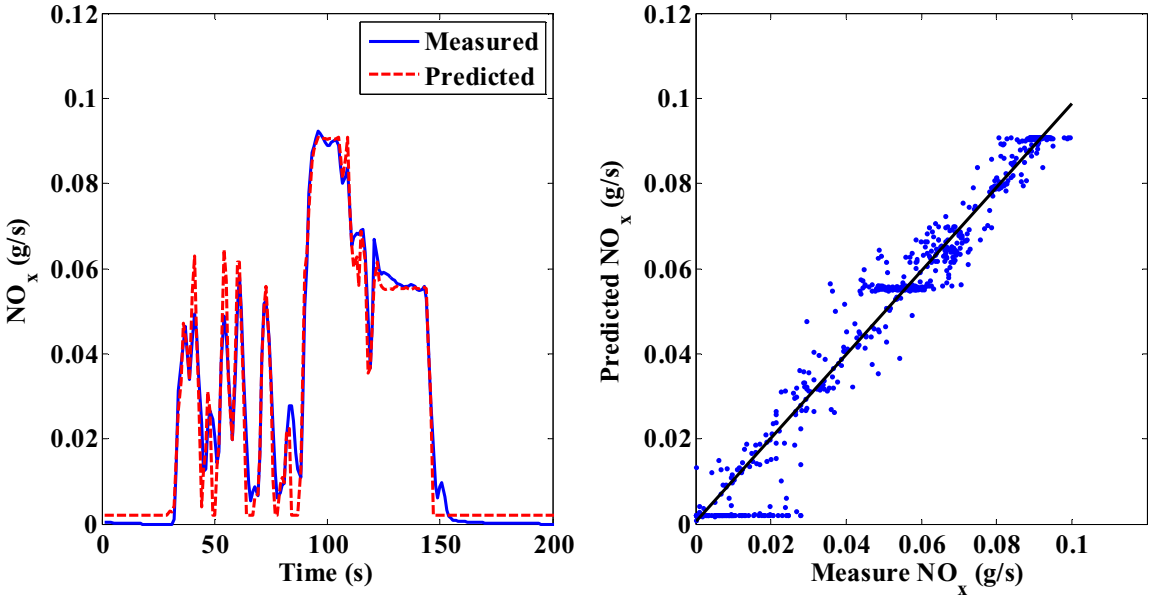

Figure C5: The comparison plot (over a selected 200 seconds) and parity plot of the measured and predicted NO_x of the 2007 MY ISE hybrid bus using ANN method from the UDDS training data

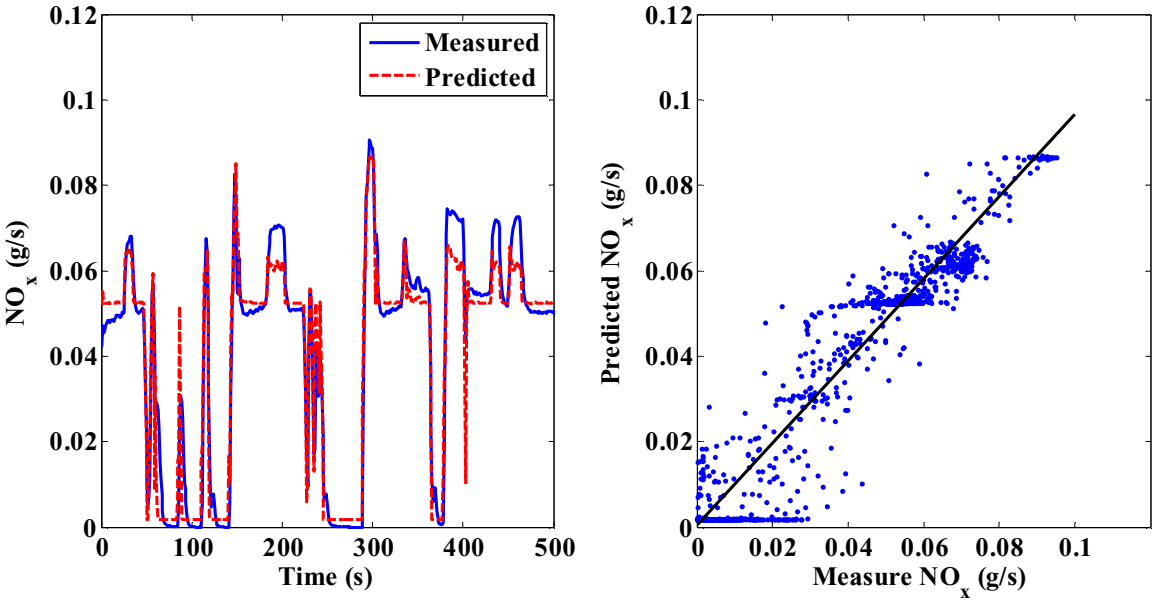

Figure C6: The comparison plot (over a selected 500 seconds) and parity plot of the measured and predicted NO_x of the 2007 MY ISE hybrid bus using ANN method from the OCTA cycle testing data

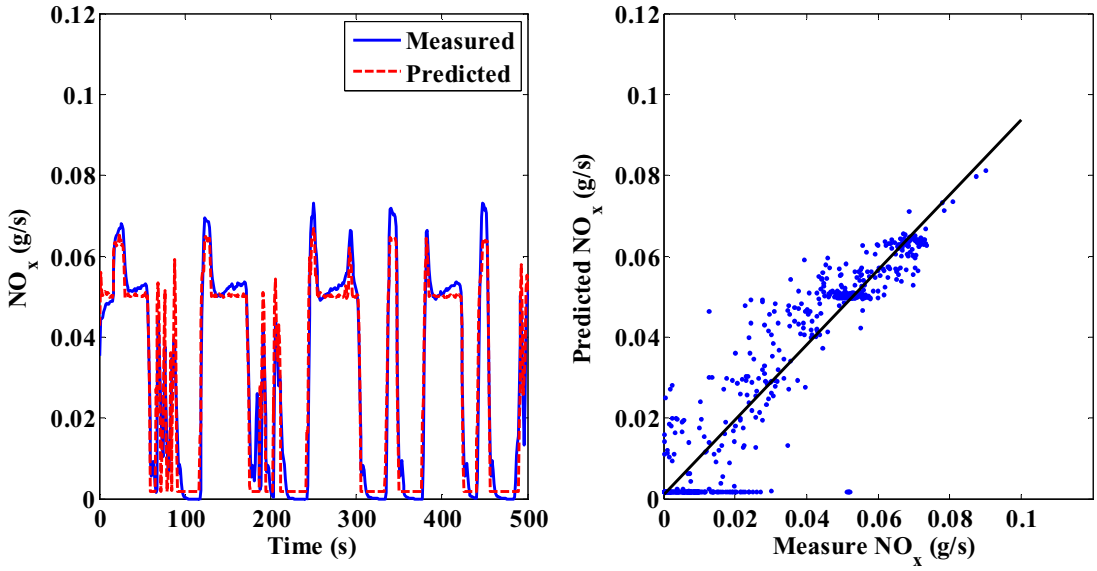

Figure C7: The comparison plot (over a selected 500 seconds) and parity plot of the measured and predicted NO_x of the 2007 MY ISE hybrid bus using ANN method from the Manhattan cycle testing data

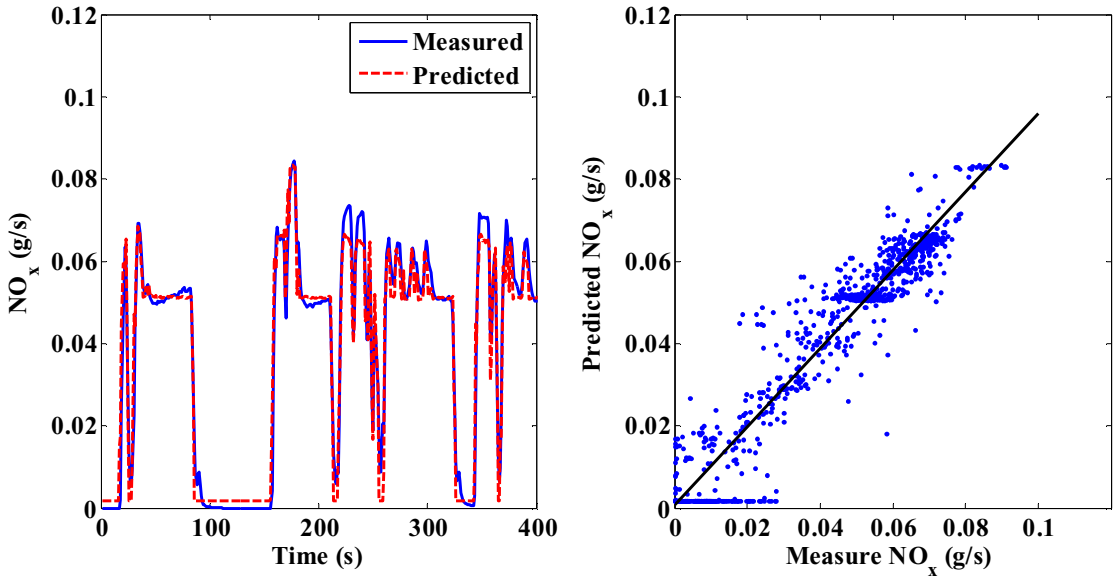

Figure C8: The comparison plot (over a selected 400 seconds) and parity plot of the measured and predicted NO_x of the 2007 MY ISE hybrid bus using ANN method from the Houston cycle testing data